Modeling of ignition and flame propagation in lean and rich hydrogen-air mixtures

Modellierung der Zündung und Flammenpropagation in mageren und fetten Wasserstoff-Luft Mischungen

Zur Erlangung des akademischen Grades Doktor-Ingenieur (Dr.-Ing.)
Genehmigte Dissertation von Hannes Böttler aus Marktredwitz
Tag der Einreichung: 15.01.2024, Tag der Prüfung: 23.04.2024

1. Gutachten: Prof. Dr.-Ing. Christian Hasse
2. Gutachten: Prof. Zheng Chen, Ph.D.
Darmstadt, Technische Universität Darmstadt

TECHNISCHE UNIVERSITÄT DARMSTADT

STFS Simulation of reactive Thermo-Fluid Systems

Mechanical Engineering Department

Modeling of ignition and flame propagation in lean and rich hydrogen-air mixtures
Modellierung der Zündung und Flammenpropagation in mageren und fetten Wasserstoff-Luft Mischungen

Accepted doctoral thesis by Hannes Böttler

Date of submission: 15.01.2024
Date of thesis defense: 23.04.2024

Darmstadt, Technische Universität Darmstadt

Let's get H_2yped!

Preface

The work presented in this dissertation was conducted during my time as a doctoral candidate at the Institute for Simulation of reactive Thermo-Fluid Systems (STFS) at the Technical University of Darmstadt. The gained scientific insights were published in internationally recognized journals with peer review. In chronological order, these publications are:

- [P1] **H. Böttler**, A. Scholtissek, X. Chen, Z. Chen, and C. Hasse. Premixed flames for arbitrary combinations of strain and curvature. In: Proc. Combust. Inst. 38 (2021), 2031–2039. DOI: 10.1016/j.proci.2020.06.312
- [P2] X. Chen, **H. Böttler**, A. Scholtissek, C. Hasse, and Z. Chen. Effects of stretch-chemistry interaction on chemical pathways for strained and curved hydrogen/air premixed flames. In: Combust. Flame 232 (2021), 111532. DOI: 10.1016/j.combustflame.2021.111532
- [P3] **H. Böttler**, X. Chen, S. Xie, A. Scholtissek, Z. Chen, and C. Hasse. Flamelet modeling of forced ignition and flame propagation in hydrogen-air mixtures. In: Combust. Flame 243 (2022), 112125. DOI: 10.1016/j.combustflame.2022.112125
- [P4] **H. Böttler**, H. Lulic, M. Steinhausen, X. Wen, C. Hasse, and A. Scholtissek. Flamelet modeling of thermo-diffusively unstable hydrogen-air flames. In: Proc. Combust. Inst. 39 (2023), 1567–1576. DOI: 10.1016/j.proci.2022.07.159
- [P5] **H. Böttler**, D. Kaddar, T. J. P. Karpowski, F. Ferraro, A. Scholtissek, H. Nicolai, and C. Hasse. Can flamelet manifolds capture the interactions of thermo-diffusive instabilities and turbulence in lean hydrogen flames?—An a-priori analysis. In: Int. J. Hydrogen Energy 56 (2024), 1397–1407. DOI: 10.1016/j.ijhydene.2023.12.193

During my time as a research associate at STFS, I co-authored additional publications, which are not directly included in this cumulative dissertation, but have a close scientific connection to it. These publications are listed in chronological order:

- [A1] X. Wen, T. Zirwes, A. Scholtissek, **H. Böttler**, F. Zhang, H. Bockhorn, and C. Hasse. Flame structure analysis and composition space modeling of thermodiffusively unstable premixed hydrogen flames — Part I: Atmospheric pressure. In: Combust. Flame (2021), 111815. DOI: 10.1016/j.combustflame.2021.111815
- [A2] X. Wen, T. Zirwes, A. Scholtissek, **H. Böttler**, F. Zhang, H. Bockhorn, and C. Hasse. Flame structure analysis and composition space modeling of thermodiffusively unstable premixed hydrogen flames — Part II: Elevated pressure. In: Combust. Flame (2021), 111808. DOI: 10.1016/j.combustflame.2021.111808
- [A3] S. Xie, X. Chen, **H. Böttler**, A. Scholtissek, C. Hasse, and Z. Chen. Forced Ignition of a Rich Hydrogen/Air Mixture in a Laminar Counterflow: A Computational Study. In: Flow Turbul. Combust. 110 (2023), 441–456. DOI: 10.1007/s10494-022-00374-2
- [A4] M. Bolla, M. Papp, C. Olm, **H. Böttler**, T. Nagy, I. G. Zsély, and T. Turányi. Comparison and Analysis of Butanol Combustion Mechanisms. In: Energy & Fuels 36 (2022), 11154–11176. DOI: 10.1021/acs.energyfuels.2c01529
- [A5] X. Chen, S. Xie, **H. Böttler**, A. Scholtissek, W. Han, D. Yu, C. Hasse, and Z. Chen. Effects of electrodes and imposed flow on forced ignition in laminar premixed hydrogen/air mixtures with large Lewis number. In: Proc. Combust. Inst. 39 (2023), 1967–1976. DOI: 10.1016/j.proci.2022.07.217
- [A6] Y. Luo, F. Ferraro, A. Breicher, **H. Böttler**, A. Dreizler, D. Geyer, C. Hasse, and A. Scholtissek. A novel flamelet manifold parametrization approach for lean CH4–H2-air flames. In: Int. J. Hydrogen Energy 48 (2023), 407–421. DOI: 10.1016/j.ijhydene.2022.09.233
- [A7] X. Chen, **H. Böttler**, S. Xie, A. Scholtissek, W. Han, C. Hasse, and Z. Chen. On the flow-facilitated ignition in a mixture with low Lewis number. In: Combust. Flame 258 (2023), 113091. DOI: 10.1016/j.combustflame.2023.113091
- [A8] Y. Wang, S. Xie, **H. Böttler**, Y. Wang, X. Chen, A. Scholtissek, C. Hasse, and Z. Chen. Forced ignition of premixed cool and hot DME/air flames in a laminar counterflow. In: Combust. Flame 259 (2024), 113169. DOI: 10.1016/j.combustflame.2023.113169

This work has been funded by the Deutsche Forschungsgemeinschaft (DFG, German Research Foundation) – project number 411275182, the European Union's Horizon 2020 research and innovation program under the Center of Excellence in Combustion (CoEC) project, grant agreement No 952181 and the Federal Ministry of Education and Research (BMBF) and the state of Hesse as part of the NHR4CES Program.

Numerical simulations for this research were conducted on the Lichtenberg II High-Performance Computer of the Technical University of Darmstadt and the GCS Supercomputer SuperMUC-NG at Leibniz Supercomputing Centre.

Abstract

Green hydrogen holds significant promise as a sustainable alternative to traditional fossil fuels in mitigating global warming. Its direct thermal conversion via combustion is one of the most cost-efficient ways of power generation. To advance the development of technical combustion chambers for green hydrogen, detailed knowledge of its combustion dynamics, which differ significantly from that of conventional fuels, is required. Simulation-aided design processes that incorporate predictive and computationally efficient models have become indispensable in the development of combustion chambers. To enable simulation-aided design processes for hydrogen, established models must be adapted to the distinct characteristics of hydrogen flames. In particular, the high reactivity and diffusivity of hydrogen cause mixture inhomogeneities near the reaction zones due to an imbalance in the diffusive mass and heat fluxes, known as differential diffusion. This also leads to a strong sensitivity to flame front distortions known as flame stretch, which in turn can be classified into strain and curvature effects. In lean hydrogen-air flames, the interplay of differential diffusion and stretch effects leads to strongly corrugated flame fronts with cellular structures, as they are subject to thermo-diffusive instabilities. These instabilities change the flame dynamics and are not yet captured by the existing models.

In this thesis, various physical phenomena in premixed hydrogen-air flames are analyzed, focusing on differential diffusion, flame stretch, and thermo-diffusive instabilities. Flames with arbitrary combinations of strain and curvature are systematically investigated using a composition space model that reveals sensitive changes in global flame properties, flame structures and reaction pathways. Based on this analysis, a novel flamelet-based modeling approach is developed that incorporates a tabulated manifold, differential diffusion, and a coupling method through the transport of major species. Rigorous evaluations demonstrate the accuracy of the model in predicting ignition characteristics, flame propagation and flame structure in different hydrogen-air mixtures. The model shows significantly improved predictions for the flame structure observed in laminar and turbulent thermo-diffusively unstable hydrogen-air flames when extended by strain and curvature variations. In summary, this work introduces a novel model that showcases improved predictability of premixed hydrogen-air flames in different configurations and marks a substantial advancement toward the predictive simulation of technical hydrogen combustors.

Kurzfassung

Grüner Wasserstoff ist eine vielversprechende nachhaltige Alternative zu herkömmlichen fossilen Brennstoffen, um die globale Erwärmung zu begrenzen. Eine der kosteneffizientesten Arten der Energieerzeugung basiert auf seiner direkten thermischen Umwandlung durch Verbrennung. Um die Entwicklung technischer Brennkammern für grünen Wasserstoff voranzutreiben, sind jedoch detaillierte Kenntnisse seiner Verbrennungsdynamik erforderlich, die sich deutlich von der konventioneller Brennstoffe unterscheidet. Dabei sind simulationsgestützte Entwurfsprozesse, die prädiktive und recheneffiziente Modelle einbeziehen, unverzichtbar geworden. Allerdings müssen etablierte Modelle kritisch überprüft und möglicherweise an die Eigenschaften von Wasserstoffflammen angepasst werden. Insbesondere die hohe Reaktivität und Diffusivität von Wasserstoff führen zu Mischungsinhomogenitäten in der Nähe der Reaktionszonen, die als differentielle Diffusion bekannt sind. Dies führt auch zu einer starken Sensitivität gegenüber Änderungen der Flammenoberfläche, die als Flammenstreckung bezeichnet werden und wiederum in Streckungs- und Krümmungseffekte unterteilt werden können. In mageren Wasserstoff-Luft Flamen führt das Zusammenspiel von differentieller Diffusion und Streckung zu stark gewellten Flammenfronten mit zellularen Strukturen, da sie thermo-diffusiven Instabilitäten unterliegen. Diese Instabilitäten verändern die Flammendynamik und werden von den bestehenden Modellen noch nicht erfasst.

In dieser Arbeit werden verschiedene physikalische Phänomene in vorgemischten Wasserstoff-Luft-Flammen analysiert, wobei der Schwerpunkt auf differentieller Diffusion, Flammenstreckung und thermo-diffusiven Instabilitäten liegt. Flammen mit beliebigen Kombinationen von Streckung und Krümmung werden systematisch unter Verwendung eines „Composition space“-Modells untersucht, das sensitive Änderungen in globalen Flammeneigenschaften, Flammenstrukturen und Reaktionswegen aufzeigt. Auf der Grundlage dieser Analyse wird ein neuartiger Flamelet-Modellierungsansatz entwickelt, der eine tabellierte Mannigfaltigkeit, differentielle Diffusion und eine Kopplungsmethode durch den Transport der wichtigsten Spezies umfasst. Rigorose Bewertungen zeigen die Genauigkeit des Modells bei der Vorhersage von Zündungscharakteristiken, Flammendynamik und Flammenstrukturen in verschiedenen Wasserstoff-Luft-Gemischen. Das Modell zeigt signifikant verbesserte Vorhersagen für die Flammenstruktur in laminaren und turbulenten thermo-diffusiv instabilen Wasserstoff-Luft Flammen, wenn es um Streckungs- und Krümmungsvariationen erweitert wird. Durch die Demonstration der Leistungsfähigkeit des neuartigen Modells in verschiedenen Flammenkonfigurationen stellt diese Arbeit einen wesentlichen Fortschritt in der prädiktiven Simulation von technischen Wasserstoffbrennern dar.

Table of contents

1 Introduction

To minimize greenhouse gas emissions and transition to a zero-carbon energy system, green hydrogen produced from renewable sources emerges as a promising alternative to traditional fossil fuels. This holds significant scientific and technological importance [1]. For power generation, hydrogen can be either further processed into synthetic fuels or directly used as a fuel. While the direct usage of hydrogen leads to higher overall efficiencies, it also comes with major challenges in technical combustors. The higher diffusivity and reactivity of hydrogen results in a drastic change in combustion characteristics compared to conventional carbon-based fuels [2], which can lead to safety issues due to the faster flame speed and the reduced minimum ignition energy [3]. Hence, both hydrogen's flame and ignition characteristics must be understood to safely initiate and control combustion processes. Further, a lean premixed combustion mode is desirable for low pollutant emissions but faces challenges from thermo-diffusive instabilities leading to highly corrugated flame fronts and an increased flame speed [4]. Moreover, technical combustors are usually operated in turbulent conditions. The interaction with the turbulent flow leads to highly wrinkled flames. Therefore, it is hard to distinguish between wrinkling due to turbulence and due to intrinsic instabilities. This introduces additional challenges when modeling these types of flames since even synergistic interactions between turbulence and intrinsic instabilities exist [5, 6]. Still, many physical phenomena of hydrogen-air mixtures are not yet fundamentally understood but detailed knowledge is indispensable for the design of efficient and safe hydrogen combustion systems.

To gain deep insights into the underlying physical phenomena, Computational fluid dynamics (CFD) simulations of combustion processes have become an important tool for optimizing combustion processes concerning safety, control, efficiency, and pollutant formation. Fully resolved simulations (FRSs)[1] using detailed chemistry (DC) inherently capture the physical phenomena by resolving all relevant time and length scales concerning both the flow field and chemical reactions but are computationally expensive and hence, restricted to generic configurations [7]. For the simulation of technical combustors, modeling approaches that reduce the computational cost need to be derived. However, the models utilized in these simulations need to capture the most relevant physical effects. In this context, flamelet-based manifold models provide the prediction accuracy of detailed chemistry simulations by solving only a reduced set of control variables each representing certain physical effects [11, 12]. Flamelet-based modeling approaches are well established for

[1] In this thesis, FRS are seen equally to direct numerical simulation (DNS) but usually do employ numerical schemes of lower order than specialized DNS codes [7]. The FRSs within this thesis are performed using Open∇FOAM® [8, 9]. It is noted that Open∇FOAM®-based FRSs have proven to agree with other DNS codes. Further information is provided by Zirwes et al. [10].

conventional fuels and have been extended to problems of increasing physical complexity [12–20]. However, many flamelet-based manifold models for conventional fuels rely on the assumption of equal diffusivities for all species. Hence, the applicability of existing models to hydrogen is questionable as its high diffusivity requires an assessment of existing models and the development of improved models. In particular, a focus on differential diffusion, flame stretch effects and intrinsic instabilities is required as they are pronounced in hydrogen-air flames.

Differential diffusion describes mixture inhomogeneities in the vicinity of the reaction zone which alters the mixture composition and subsequently the characteristics of the flame [21]. This effect is caused by the unequal diffusivities of different species. Small molecules, such as hydrogen, diffuse faster than larger ones. The diffusion of a species k can be characterized by the Lewis number Le_k which is defined by the ratio of thermal to mass diffusion. Fast (slow) diffusing species exhibit Le numbers smaller (larger) than unity. The Le number not only provides insight into the diffusion characteristics but also serves as a key parameter reflecting the overall characteristics of premixed hydrogen-air flames, which significantly change with the equivalence ratio as their effective Le number increases from lean to rich: $0.3 \leq \mathrm{Le} \leq 2.3$ [21, 22]. This change in Le number affects not only the flame structure but also the flame propagation and transport processes. In particular, the Le number characterizes the flame response to flame stretch effects resulting from changes in the flame surface area, which subsequently alters the mixture composition and the reaction intensities depending on the local conditions [23–27]. The flame stretch $K = (1/A)\,\mathrm{d}A/\mathrm{d}t$ is defined by changes of the flame surface area A [23]. It is positive (negative) if the flame surface increases (decreases). The two effects leading to flame stretch are (1) the propagation of a curved flame front and (2) an imposed flow, which is also referred to as strain. In general, in response to flame stretch, mixtures with $\mathrm{Le} < 1$ ($\mathrm{Le} > 1$) show higher reaction intensities in areas of positive (negative) stretch. This is also referred to as the Le number effect. However, the detailed prediction of flame responses to stretch and mixture characteristics is challenging and spans the broad field of stretch-chemistry interaction [P2, 28, 29].

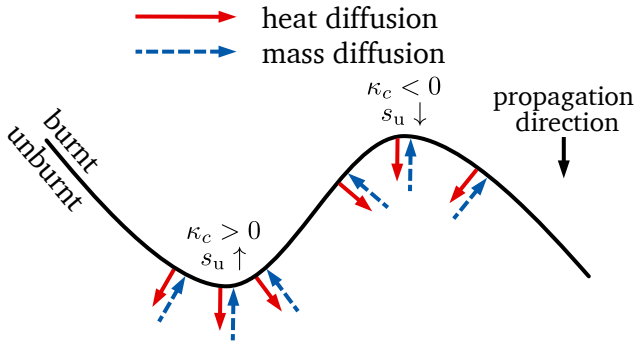

Fig. 1.1: Schematic depiction of the intrinsic instability mechanism observed in lean hydrogen-air flames ($\mathrm{Le} < 1$). The figure is adapted from [21].

The Le number effect is further elaborated based on the curvature variations that lead to intrinsically unstable flame dynamics and highly corrugated flame fronts[2] in lean hydrogen-air flames ($\mathrm{Le} < 1$).

[2]This work focuses mainly on characteristics resulting from thermo-diffusive instabilities. However, it is noted that various instability mechanisms exist. More detailed information on other mechanisms can be found in [30, 31].

In Fig. 1.1, the mechanism leading to unstable flame propagation is schematically depicted. A perturbed flame front segment is shown together with the fluxes of heat and mass diffusion. The convexly curved flame segment (to the burned side) corresponds to positive curvatures ($\kappa_c > 0$), while concave curvature leads to negative values ($\kappa_c < 0$). In the positively curved segment, a strong accumulation of hydrogen is observed due to the inwardly focused mass diffusion, while heat diffuses away at a reduced speed. This leads to intensified reaction rates and a locally increased flame speed ($s_\mathrm{u} \uparrow$) since hydrogen is the deficient reactant. In contrast, hydrogen is further depleted in the area of negative curvature. This results in a locally slower flame ($s_\mathrm{u} \downarrow$) since the depletion of hydrogen by mass diffusion is stronger than the preheating by the focused heat diffusion. Further, with the overall flame propagating downwards, this perturbation will grow with time as the leading edge is propagating faster than the trailing one. This indicates the intrinsic amplification of the perturbation leading to the evolution of a thermo-diffusive instability [21, 30].

In the pursuit of simulating practical hydrogen combustors, it becomes evident that the models employed must accurately capture differential diffusion, stretch effects and intrinsic instabilities. This thesis marks a substantial advancement in this regard by developing a novel flamelet-based model for premixed hydrogen combustion and evaluating the model performance in different flame configurations such as igniting and thermo-diffusively unstable flames.

Objectives and structure of this thesis

As outlined above, premixed hydrogen flames are subject to various physical phenomena that need to be incorporated into existing combustion models to allow for a reliable prediction of hydrogen combustion systems. Within the scope of this thesis, several steps of modeling premixed hydrogen combustion are addressed in multiple flame configurations with increasing complexity.

A schematic overview of the scientific objectives and the contributions of the publications related to this thesis is depicted in Figure 1.2. The overview is structured by the level of modeling from bottom to top. First, the physical phenomena are analyzed based on which models are developed and finally, their performance is evaluated. Additionally, the investigated configurations are classified by their complexity, increasing from left to right. Namely, the investigated configurations are forced ignition, laminar flame propagation, intrinsic instabilities and turbulent flame propagation. The different publications related to this thesis are grouped in boxes that indicate their respective contribution to the level of modeling and the investigated configuration. The color-coding of the boxes depicts the connection of the publications to the scientific objectives. The objectives of this thesis are:

O1 Analysis of strain and curvature effects: The stretch-chemistry interaction is analyzed in detail for lean and rich hydrogen-air mixtures including both canonical flames and flames with arbitrary combinations of strain and curvature, which are computed with a recently developed composition space model (CSM) [P1, P2]. In these studies, not only the global flame characteristics and flame structures but also the interaction of strain and curvature effects on chemical pathways are investigated.

O2 Model development and evaluation of igniting H_2 flames: The forced ignition and early flame propagation in lean and rich hydrogen-air flames is analyzed [A3, A5, A7]. Based on these findings a computationally efficient flamelet-based model capturing non-adiabatic effects, resulting from forced ignition, and differential diffusion in lean and rich hydrogen-air mixtures is developed and successfully applied to several igniting canonical flame configurations concerning the flame structure, flame propagation and ignition characteristics [P3].

O3 Model development and evaluation of thermo-diffusively unstable H_2 flames: The physical phenomena of thermo-diffusively unstable hydrogen-air flames are analyzed [P5, A1, A2]. Based on these findings the previously developed flamelet-based model is extended to better capture laminar thermo-diffusively unstable hydrogen flames by considering large curvature variations (positive and negative) in the manifold [P4]. Finally, the model for laminar thermo-diffusively unstable flames is extended to turbulent conditions by capturing both strain and curvature variations in the manifold to accurately predict the synergistic effects between turbulence and intrinsic instabilities [P5].

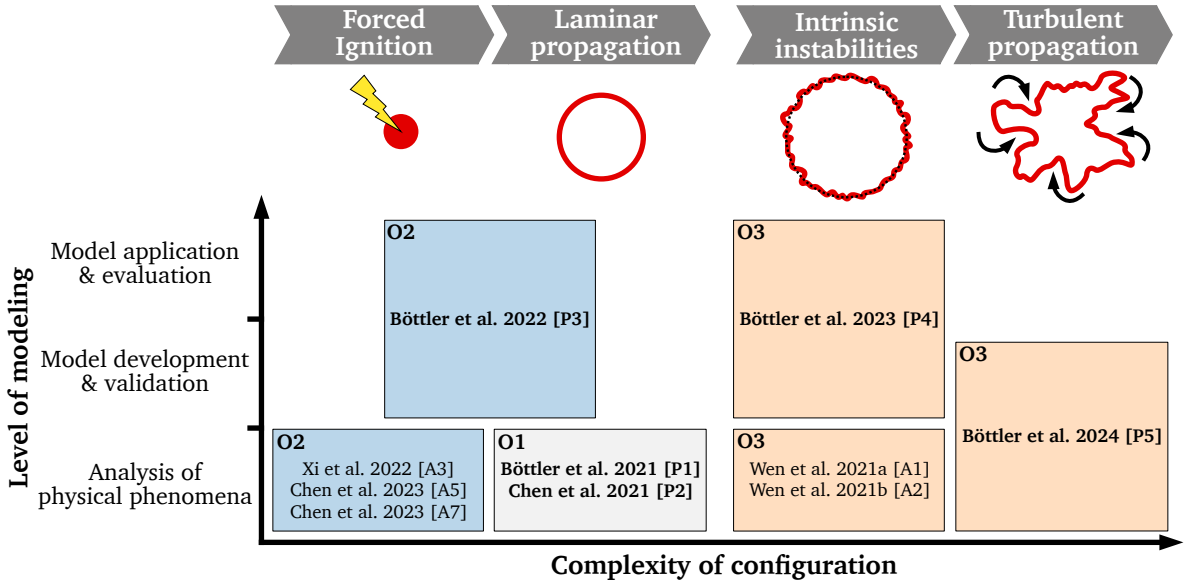

Fig. 1.2: Overview of scientific objectives and publications related to this thesis classified by the complexity of configuration and the level of modeling. The main publications are written in bold. The ones written in regular font depict related co-author publications. The contribution of each publication to the respective scientific objective is highlighted by the color-coding of the boxes.

In the remainder of this thesis, the most relevant theoretical background is briefly outlined in Chapter 2. Chapter 3 presents the characteristics of the newly developed flamelet-based model for premixed hydrogen-air flames. In Chapter 4, the key findings concerning the different flame configurations are discussed. The discussion of each configuration is structured by an initial assessment of relevant physical phenomena, followed by an assessment of manifold specifics and subsequent model extensions. Finally, the model performance is rigorously evaluated for the respective flame configuration. The thesis ends with a conclusion and outlook (Chapter 5).

2 Theoretical background

In this chapter, the theoretical background relevant to the scientific objectives of this thesis is presented. First, the governing equations of chemical reacting flows are briefly discussed (Sec. 2.1). Thereafter, an introduction to the theory of flame stretch is given (Sec. 2.2) and the composition space model (CSM) is introduced (Sec. 2.3). Finally, the fundamentals of flamelet modeling and the challenges of modeling hydrogen combustion are presented (Sec. 2.4).

2.1 Governing equations of chemical reacting flows

In chemical reacting flows, conservation equations for mass, momentum, species and energy are solved. The equations outlined in this section follow the book of Poinsot and Veynante [32] and the book of Kee et al. [33].

Mass and momentum conservation

Within the scope of this thesis, the transport of Newtonian fluids in the low Mach number limit is assumed and all body forces except gravity are neglected. The subsequently simplified equations for mass and momentum conservation read:

$$\frac{\partial \rho}{\partial t} + \frac{\partial u_i}{\partial x_i} = 0\,, \tag{2.1}$$

$$\frac{\partial (\rho u_j)}{\partial t} + \frac{\partial (\rho u_i u_j)}{\partial x_i} = -\frac{\partial p}{\partial x_j} + \frac{\partial \tau_{ij}}{\partial x_i} + \rho g_j\,, \tag{2.2}$$

with the density ρ, the flow velocity u, the pressure p, the gravity constant g and the stress tensor τ_{ij} which is defined as:

$$\tau_{ij} = \rho\nu \left(\frac{\partial u_j}{\partial x_i} + \frac{\partial u_i}{\partial x_j} \right) - \frac{2}{3}\rho\nu \frac{\partial u_k}{\partial x_k}\delta_{ij}\,, \tag{2.3}$$

where ν represents the kinematic viscosity and δ_{ij} is the Kronecker delta.

Species conservation

The conservation equation for species mass fractions Y_k describes chemically reacting systems and reads:

$$\frac{\partial \rho Y_k}{\partial t} + \frac{\partial}{\partial x_i}\left(\rho u_i Y_k\right) = -\frac{\partial}{\partial x_i}\left(\rho Y_k V_{k,i}\right) + \dot{\omega}_k \,, \tag{2.4}$$

where $\dot{\omega}_k$ is the source term of species k. For detailed information about its evaluation using detailed reaction mechanisms, the interested reader is referred to the book of Kee et al. [33]. Further, $\rho Y_k V_{k,i}$ represents the diffusive flux of the species k and $V_{k,i}$ is the diffusion velocity. In general, the diffusive flux can be modeled using Fick's Law of diffusion, which postulates a linear relation of the diffusive flux, the negative of a species gradient and a proportionality constant [33]. It is noted the proportionality constant of a species k can be analogously described by the diffusion coefficient D_k or the Lewis number Le_k, which can be converted into each other following the ratio of the thermal diffusivity to mass diffusivity as it defines the Lewis number:

$$\mathrm{Le}_k = \frac{\lambda}{\rho c_\mathrm{p} D_k} = \frac{\alpha}{\rho D_k} \,, \tag{2.5}$$

where λ is the thermal conductivity, c_p is the heat capacity, $\alpha = \lambda / c_\mathrm{p}$ is the thermal diffusivity. Further, the diffusive fluxes can be described by various models. Two popular diffusion models are:

Unity Lewis diffusion: The unity Lewis diffusion model assumes that all species and the temperature diffuse equally. Setting the Lewis numbers of all species to unity allows a direct evaluation of the diffusion coefficient using Eq. 2.5 and the subsequent expression for the diffusive flux reads:

$$\rho Y_k V_{k,i} = -\alpha \frac{\partial Y_k}{\partial x_i} \,. \tag{2.6}$$

This approach is utilized in several combustion modeling approaches concerning conventional fossil fuels where equal diffusivities are assumed for all species. However, this assumption is challenged by the broad variety of diffusivities in hydrogen combustion [21] and will be further elaborated in the remainder of this thesis.

Mixture-averaged diffusion: The mixture-averaged diffusion utilizes the Curtiss and Hirschfelder approximation [34]. The diffusive flux for mixture-averaged diffusion is expressed by:

$$\rho Y_k V_{k,i} = \rho Y_k V_{k,i}^\mathrm{D} + \rho Y_k V_{k,i}^\mathrm{T} + \rho Y_k V_i^\mathrm{C} \,, \tag{2.7}$$

where $V_{k,i}^\mathrm{D}$ represents the mixture-averaged diffusion velocity, $V_{k,i}^\mathrm{T}$ is the thermal diffusion velocity and V_i^C is the correction velocity. The mixture-averaged diffusion velocity describes the transport based on species gradients and can be either expressed using the species mole fraction X_k or the species mass fraction Y_k:

$$V_{k,i}^\mathrm{D} = -\frac{D_k^\mathrm{M}}{X_k}\frac{\partial X_k}{\partial x_i} = -\frac{D_k^\mathrm{M}}{Y_k}\frac{\partial Y_k}{\partial x_i} - \frac{D_k^\mathrm{M}}{\overline{M}}\frac{\partial \overline{M}}{\partial x_i} \,, \tag{2.8}$$

with the mixture averaged diffusion coefficient D_k^{M} and the mean molecular weight $\overline{M}$. The thermal diffusion velocity describes the transport based on temperature gradients and is defined by:

$$V_{k,i}^{\mathrm{T}} = -\frac{D_k^{\mathrm{T}}}{\rho Y_k T}\frac{\partial T}{\partial x_i}\,, \tag{2.9}$$

with D_k^{T} representing the thermal diffusion coefficient [35]. Thermal diffusion is also known as Soret diffusion. The correction velocity is required for mass conservation and reads:

$$V_i^{\mathrm{C}} = -\sum_{k=1}^{N_{\mathrm{s}}} Y_k \left(V_{k,i}^{\mathrm{D}} + V_{k,i}^{\mathrm{T}}\right)\,, \tag{2.10}$$

where N_{s} is the total number of species. In this work, the diffusion coefficients are either evaluated using Cantera [36] or the EGLIB transport library [35], which calculate the transport properties based on the kinetic theory of gases [33].

Energy conservation

Finally, the energy conservation is expressed by the enthalpy transport equation:

$$\frac{\partial}{\partial t}(\rho h) + \frac{\partial}{\partial x_i}\left(\rho u_i h\right) = \frac{\partial}{\partial x_i}\left(\lambda\frac{\partial T}{\partial x_i}\right) - \frac{\partial}{\partial x_i}\left(\sum_{k=1}^{N_{\mathrm{s}}} h_k \rho Y_k V_{k,i}\right) + q\,, \tag{2.11}$$

with T being the temperature, h_k is the enthalpy of the species k and q represents an external energy source. The first term on the right-hand side captures heat diffusion and the second one depicts the energy transport due to species diffusion. Note that the latter one is affected by differential diffusion effects. The viscous heating term is neglected. For a detailed derivation of the energy conservation, the interested reader is referred to [32].

2.2 Flame stretch

In the context of premixed flames, flame stretch K represents a fundamental phenomenon in understanding their local flame dynamics. A general definition was proposed by Williams [23] based on the flame surface area A:

$$K = \frac{1}{A}\frac{\mathrm{d}A}{\mathrm{d}t}\,. \tag{2.12}$$

This definition describes the change of a flame surface element which is schematically depicted in Tab. 2.1. The change of flame surface can be classified into two effects and can lead to an increase (reduction) of the flame surface which results in positive (negative) flame stretch. First, an imposed flow field affects the flame stretch if it contains a flame tangential component. The flame surface is increased if the streamlines are diverging since the flame tangential velocity component elongates the flame. In contrast, for converging streamlines the flame tangential velocity component results in a compression of the flame surface. The stretch resulting from an imposed flow is also referred

Tab. 2.1: Schematic overview of temporal flame surface evolutions ($t_1 > t_0$) causing flame stretch. Red arrows denote flame propagation and black arrows correspond to streamlines of an imposed flow.

	Effect of imposed flow	Effect of flame curvature
$\frac{\mathrm{d}A}{\mathrm{d}t} > 0$	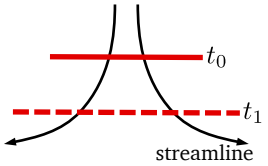	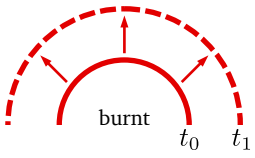
$\frac{\mathrm{d}A}{\mathrm{d}t} < 0$	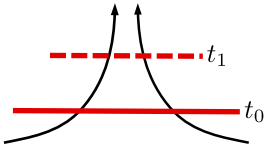	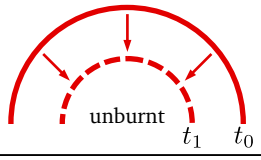

to as strain. Second, the overall flame topology affects the flame stretch even if there is no flow field imposed. The self-propagation of a curved flame segment affects the evolution of the flame surface area. The propagation of a convexly curved flame segment (curvature $\kappa_c > 0$) results in an increase of the flame surface, while the propagation of a concavely curved flame results in flame surface reduction. Stretch resulting from the self-propagation of a curved flame front are also referred to as curvature effects.

This phenomenological description of the flame surface evolution covers all effects leading to positive or negative flame stretch K. However, flame front segments in a multi-dimensional turbulent flame cannot be easily attributed to this classification since the imposed flow and the flame curvature interact with each other and the overall flame stretch in a turbulent flame contains contributions from both the imposed flow field and the flame curvature. To allow for a detailed assessment of stretch effects in complex flames, a mathematically more refined description is required which can be derived by considering a curvilinear coordinate system along the flame and an imposed instantaneous velocity vector $\mathbf{u}$ [21, 22, 24, 37]:

$$K = \nabla_\mathrm{t} \cdot \mathbf{u}_\mathrm{t} + (\mathbf{s}_\mathrm{u} \cdot \mathbf{n})(\nabla \cdot \mathbf{n})\,, \tag{2.13}$$

where $\nabla_\mathrm{t} \cdot \mathbf{u}_\mathrm{t}$ is the flame-tangential strain imposed by the flow, $\mathbf{s}_\mathrm{u}$ represents the flame speed, and $\mathbf{n} = \nabla Y_c / |\nabla Y_c|$ is the flame normal unit vector ($\mathbf{n}$ pointing towards the burnt gases). Finally, the flame speed can be decomposed into the flow velocity and the flame displacement speed, $\mathbf{s}_\mathrm{u} = \mathbf{u} - s_\mathrm{d}\,\mathbf{n}$, resulting in the following expression for the flame stretch K [27]:

$$K = \underbrace{\nabla_\mathrm{t} \cdot \mathbf{u}_\mathrm{t} - (\mathbf{u} \cdot \mathbf{n})\,\kappa_c}_{K_s} + \underbrace{s_\mathrm{d}\,\kappa_c}_{K_c}\,, \tag{2.14}$$

with $\kappa_c = -\nabla \cdot \mathbf{n}$ being the flame curvature[3], K_s is the strain imposed by the flow, and K_c is the stretch resulting from the propagation of a curved flame.

[3] Generally, the curvature can be evaluated based on any scalar field. In this thesis, it is calculated using the progress variable field. Hence, $\mathbf{n} = \nabla Y_c / |\nabla Y_c|$ represents the unit vector of the progress variable gradient.

A detailed understanding of stretch effects is required since they alter the overall transport mechanism of mass and heat in the flame and can lead to locally increased or reduced burning intensities in the flame front due to the interaction with transport and chemistry. The overall response of a flame to the flame stretch depends on the Lewis number of the mixture which is characterized by its deficient reactant. In general, mixtures with $\mathrm{Le} < 1$ (e.g., lean hydrogen-air flames) are strengthened (weakened) by positive (negative) stretch, while the opposite is true for $\mathrm{Le} > 1$ mixtures (e.g., rich hydrogen-air flames). This locally altered burning intensity affects the local flame speed and subsequently, the overall combustion dynamics of the flame, as already discussed for the mechanism leading to thermo-diffusive instabilities (see Fig. 1.1). However, the analysis of stretch effects in multidimensional (turbulent) flames can be challenging since many processes interact, which complicates the identification of the individual contributions of strain and curvature. Therefore, it is beneficial to analyze stretch effects and the stretch-chemistry interaction in simplified one-dimensional canonical flame configurations with well-defined boundary conditions, ensuring an accurate determination of flame stretch.

Tab. 2.2: Overview of stretch effects in canonical flames including a planar freely propagating (FP) flame, a stagnation flow (STAG) flame, an inwardly propagating flame (IPF) and a spherical expanding flame (SEF). Black lines indicate streamlines of an imposed flow while red arrows depict the direction of flame propagation. In addition, the classification by total stretch K and the contributions resulting from strain K_s and curvature stretch K_c are presented. This overview is adapted from [P1].

	FP	**STAG**	**IPF**	**SEF**
	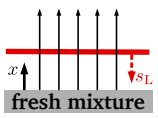	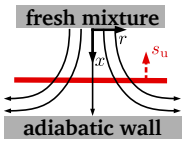	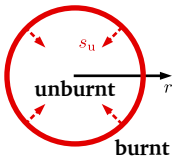	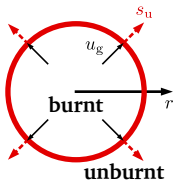
Stretch	$K = 0$	$K > 0$	$K < 0$	$K > 0$
Strain	$K_s = 0$	$K_s > 0$	$K_s = 0$	$K_s > 0$
Curvature stretch	$K_c = 0$	$K_c = 0$	$K_c < 0$	$K_c > 0$

In Tab. 2.2, a selection of canonical flames is shown schematically together with their overall flame stretch K and the contributions from strain K_s and curvature stretch K_c (see Eq. 2.14). The overall sign of stretch effects can be qualitatively derived when comparing the schematic flame configurations to the different effects causing a change in flame surface (see Tab. 2.1). Note that all these canonical flames include a symmetry condition that allows for a numerical solution along a one-dimensional coordinate. The simplest canonical flame configuration is the planar freely propagating (FP) flame which is unstretched [38]. A planar flame can be strained by placing it into a stagnation flow (STAG) towards a wall or an opposed stream with the same composition (twin flame configuration). A STAG flame is positively strained since the flow has an extending effect on the flame [39]. In general, negative strain could be studied in a reverse stagnation flow. However, such flames can neither be stabilized in experimental nor numerical setups which renders the assessment of negative strain difficult. Curved flames can be studied as inwardly propagating flames (IPFs) or spherical expanding flames (SEFs). An IPF is obtained by igniting a quiescent

mixture of fresh gases in a perfect spherical shape. The flame then propagates inwards consuming the remaining fresh gases and forming a negatively curved flame. This configuration allows the assessment of negative curvature stretch K_c while no strain is present. Although such an idealized flame can hardly be established in experiments, it can be computed numerically [40, 41]. Positively curved flames can be studied in the SEF configuration, which can be created by using an ignition source in a quiescent mixture of fresh gases. This flame is subject to positive curvature stretch due to the overall flame topology. However, it is also affected by strain due to the thermal expansion resulting from the burned gases enclosed by the flame. The thermal expansion inside the flame leads to an additional gas velocity u_g since the unburned mixture is pushed away from the flame. This flow has a qualitatively similar effect on the flame surface as the stagnation flow and therefore causes positive strain [42].

To highlight the qualitative impact of flame stretch on lean and rich hydrogen-air flames, the heat release rate profiles from the different canonical flames are depicted in Fig. 2.1. The flame stretch K of the selected flame structures is chosen as $K_{\mathrm{SEF}} > K_{\mathrm{STAG}} > K_{\mathrm{FP}} = 0 > K_{\mathrm{IPF}}$, to highlight the overall variations caused by flame stretch. Since these flames exhibit different topologies in physical space, the flame structures are spanned by the progress variable Y_c which is usually defined as a linear combination of species:

$$Y_c = \sum_{k=1}^{N_s} w_k Y_k \,, \tag{2.15}$$

and represents a flame-attached coordinate system for premixed flames that spans the composition space. Here, w_k denotes the weight of species k and Y_k is the species mass fraction. In this work, the progress variable is defined as $Y_c = Y_{\mathrm{H2O}} - Y_{\mathrm{H2}} - Y_{\mathrm{O2}}$. From Fig. 2.1, it becomes apparent that the heat release rate changes significantly between all canonical flame configurations for both lean and rich hydrogen-air flames. Not only the peak values but also the shapes of the profiles are altered by the flame stretch K. Overall the trends are analogous to the previously discussed flame propagation in combination with stretch and the Lewis number effect.

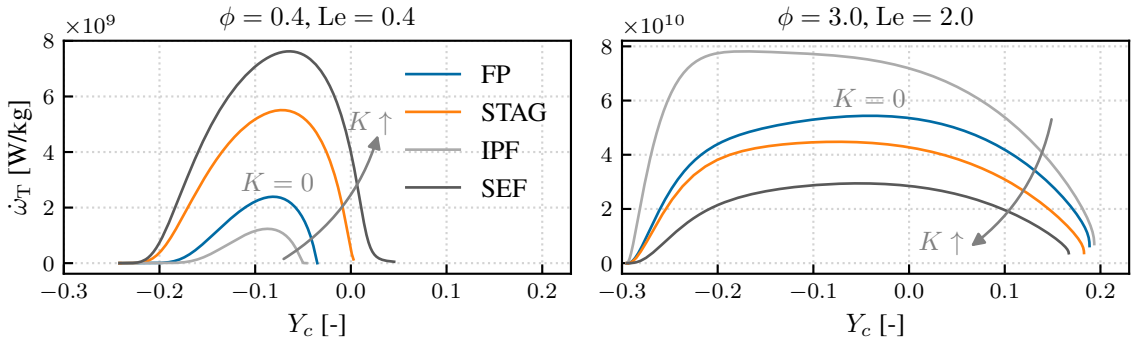

Fig. 2.1: Qualitative flame structure comparison of different canonical flame configurations for H_2-air flame with $\phi = 0.4$ and $\phi = 3.0$ at ambient conditions. The heat release rate $\dot{\omega}_{\mathrm{T}}$ is shown along the progress variable Y_c. The flame stretch K of the selected results are chosen as $K_{\mathrm{SEF}} > K_{\mathrm{STAG}} > K_{\mathrm{FP}} = 0 > K_{\mathrm{IPF}}$.

In short, lean (rich) hydrogen-air flames exhibit increased heat release in positively (negatively) stretched configurations which coincides with a varying maximum value of the progress variable Y_c.

Further, it is highlighted that canonical flame configurations only allow for assessing particular combinations of strain K_s and curvature κ_c. This is a result of the specific boundary conditions of these flames. However, in comparison, turbulent flames exhibit wider distributions for strain and curvature than those accessible in the canonical flame configurations, including also negative flame stretch [43]. Additionally, even reverted correlations between strain and curvature are found between laminar canonical flames and turbulent flames which result from different topological features in highly curved turbulent flame segments [44]. This motivated the development of a composition space model (CSM) [45, 46], which allows the assessment of flame structures with arbitrary combinations of strain and curvature. Thereby, a larger strain-curvature parameter space compared to canonical flame configurations can be investigated. This model is introduced in the next section.

2.3 Composition space model (CSM)

The composition space model (CSM) developed by Scholtissek et al. [45, 46] plays a central role in the investigations of this thesis since it is used to systematically analyze flame structures and to generate flamelet manifolds. In the following, the governing equations of the CSM are briefly discussed and the overall model characteristics are outlined. Thereafter, the CSM characteristics and possible parameter variations, which allow a systematic analysis of different flame structures, are highlighted.

Governing equations

Starting from a transport equation of the progress variable Y_c and a kinematic condition for the flame-attached coordinate system, the conservation equations for species mass fractions and temperature are transformed from physical space (x, t) to the composition space $(\tau, Y_c(t, x))$ using the following transformation rule for a generic scalar quantity φ:

$$\frac{\partial \varphi}{\partial t} = \frac{\partial \varphi}{\partial \tau} + \frac{\partial Y_c}{\partial t}\frac{\partial \varphi}{\partial Y_c}\,, \tag{2.16}$$

where τ is a flame-attached time defined by $\tau = t$. Further, an equation for the progress variable gradient $g_c = |\nabla Y_c|$ is derived, which is required for closure. The final set of equations reads [46]:

$$\begin{aligned}\rho\frac{\partial Y_k}{\partial \tau} = &\underbrace{-g_c\frac{\partial}{\partial Y_c}\left(g_c\,\rho Y_k\tilde{V}_k\right) + g_c\frac{\partial}{\partial Y_c}\left(g_c\,\rho Y_c\tilde{V}_c\right)\frac{\partial Y_k}{\partial Y_c}}_{\text{Diffusion}} \\ &+\underbrace{\rho g_c\,\kappa_c\left(Y_k\tilde{V}_k - Y_c\tilde{V}_c\frac{\partial Y_k}{\partial Y_c}\right)}_{\text{Diffusion}} - \underbrace{\dot{\omega}_c\frac{\partial Y_k}{\partial Y_c}}_{\text{Drift}} + \underbrace{\rho\dot{\omega}_k}_{\text{Source}}\,,\end{aligned} \tag{2.17}$$

$$\rho\frac{\partial T}{\partial \tau} = \underbrace{\frac{g_c}{c_p}\frac{\partial}{\partial Y_c}\left(g_c\lambda\frac{\partial T}{\partial Y_c}\right) + g_c\frac{\partial}{\partial Y_c}\left(g_c\,\rho Y_c\tilde{V}_c\right)\frac{\partial T}{\partial Y_c}}_{\text{Diffusion}}$$
$$\underbrace{-\rho g_c^2\sum_k^{n_s}\frac{c_{p,k}}{c_p}Y_k\tilde{V}_k\frac{\partial T}{\partial Y_c} - \rho g_c\,\kappa_c\left(\frac{\lambda}{\rho c_p}+Y_c\tilde{V}_c\right)\frac{\partial T}{\partial Y_c}}_{\text{Diffusion}} \underbrace{-\dot{\omega}_c\frac{\partial T}{\partial Y_c}}_{\text{Drift}} + \underbrace{\frac{\dot{\omega}_T}{c_p}}_{\text{Source}}\,, \tag{2.18}$$

$$0 = \underbrace{-g_c^2\frac{\partial^2}{\partial {Y_c}^2}\left(g_c\,\rho Y_c\tilde{V}_c\right) + g_c^2\frac{\partial}{\partial Y_c}\left(\kappa_c\,\rho Y_c\tilde{V}_c\right)}_{\text{Diffusion}} \underbrace{-\dot{\omega}_c\frac{\partial g_c}{\partial Y_c}}_{\text{Drift}} + \underbrace{g_c\frac{\partial\dot{\omega}_c}{\partial Y_c} + \rho K_s g_c}_{\text{Source}}\,, \tag{2.19}$$

where $\tilde{V}_k$ is the diffusion velocity in composition space which is calculated analogously to Eqs. 2.6 – 2.8 but includes the gradient along the progress variable Y_c instead of the physical space coordinate x. Further, $\dot{\omega}_c$ is the progress variable source term and $c_{\mathrm{p},k}$ is the heat capacity of species k. The different terms in this set of equations can be classified as diffusion, drift, and source terms. As diffusion and source terms are well-established and known from conventional transport equations, they are not further discussed here. However, the drift terms are less common. These terms scale the composition space and are crucial for the CSM framework as the burned side boundary condition is coupled to the progress variable gradient g_c, which subsequently scales the computational domain. This is an important feature of these equations as stretched flame structures can be studied by supplying strain K_s and curvature κ_c as external parameters. It was already shown in Fig. 2.1 that depending on the overall flame stretch (negative or positive) sub- or super-equilibrium states can be reached, which coincide with different burned side values for the progress variable. The drift terms ensure that this behavior is accurately described and that the CSM obtains the appropriate burned side value of the progress variable. Note that the equations for mass and momentum conservation are not required since they are included in the transformation to the flame-attached coordinate system. To solve the system of equations, boundary conditions need to be provided. On the unburned side, fixed-value conditions based on the temperature and composition of a certain mixture are prescribed. The burned-side boundary condition is defined as a moving boundary that is coupled to the progress variable gradient g_c through the drift terms.

Model characteristics

Given only this set of equations, the CSM can describe the flame structure of various canonical premixed flame configurations along with the limiting case of homogeneous ignition at constant pressure. The physical space coordinate x can be reconstructed based on:

$$x(Y_c) = \int_{Y_{c,\min}}^{Y_c}\frac{\mathrm{d}Y_c}{g_c}\,. \tag{2.20}$$

Further, the burning velocity s_u of a CSM solution can be estimated via the density-weighted displacement speed s_d:

$$s_\mathrm{u} = \frac{\rho s_\mathrm{d}}{\rho^0} = \frac{1}{\rho^0}\left(-\frac{\partial}{\partial Y_c}\left(\rho Y_c \tilde{V}_c\right) + \kappa_c \rho Y_c \tilde{V}_c + \frac{\dot{\omega}_c}{g_c}\right) . \tag{2.21}$$

This expression is evaluated at the maximum heat release peak, since it should be evaluated close to the burned side [27, 47] and is weighted by the fresh gas density ρ^0. The homogeneous ignition is recovered in the asymptotic limit of $g_c \to 0$ where all diffusive terms vanish [46]. It is also stressed that the progress variable definition is of utmost importance for the solution obtained by the CSM and needs to be specified in a way that it increases monotonically along the physical space coordinate.

Parameter variations

The CSM characteristics are utilized to analyze the stretch-chemistry interaction [P1, P2] and to generate the flamelet manifolds developed in [P3–P5]. Therefore, different parameter variations with the CSM are performed and the resulting flame characteristics are analyzed systematically. While different mixtures, pressure levels and temperatures can be investigated in any canonical flame configuration, the CSM is beneficial for studying strain and curvature effects as they can be supplied as external parameters. Thereby, one-dimensional flame structures with arbitrary combinations of strain and curvature can be computed using only a single set of equations (Eqs. 2.17 – 2.19). This model characteristic is used to perform a parameter variation for strain K_s and curvature κ_c [P1, P2]. Additionally, the asymptotic limit of $g_c \to 0$, where homogeneous ignition is recovered, is included in a parameter variation by increasing the unburned temperature to model the forced ignition and the subsequent flame propagation. Thereby, the CSM accounts inherently for the blending of premixed flame characteristics and homogeneous ignition which proved to be beneficial in the flamelet-based modeling approach developed in [P3]. Finally, this flamelet-based model is extended to include strain K_s and curvature κ_c effects in the flamelet-based model by performing a corresponding variation with the CSM to better predict strongly thermo-diffusively unstable hydrogen-air flames [P4, P5].

2.4 Flamelet-based manifold models

Flamelet-based models[4] are established on the separation of flow time scales τ_{fl} and chemistry time scales τ_{ch} [52]. This ratio of time scales defines the Damköhler number:

$$\mathrm{Da} = \frac{\tau_{\mathrm{fl}}}{\tau_{\mathrm{ch}}} \,. \tag{2.22}$$

In the case of large Damköhler numbers, hence, fast chemistry, the main gradients in temperature and species mass fractions occur in a thin flame sheet and align in the flame normal direction as only small changes appear in the flame tangential direction. This also implies that the flame structure is not affected by the flow and subsequently multidimensional (turbulent) flames can be considered a statistical ensemble of one-dimensional laminar flamelets [11]. Thereby, one-dimensional (canonical) flames can be pre-computed and tabulated in a flamelet manifold, which is parameterized by certain control variables that account for different physical effects. Commonly used control variables are the progress variable Y_c describing the reaction progress, the mixture fraction Z to account for mixture stratification, and enthalpy h to capture non-adiabatic effects [51]. Flamelet manifolds are then coupled to CFD simulations providing the full thermochemical state using detailed kinetic mechanisms but requiring only the transport of a reduced set of control variables resulting in a significant reduction of the computational cost. Comprehensive overviews of modeling concepts and their usage in turbulent applications can be found in [13, 53].

This section first discusses the workflow of flamelet-based models, highlighting the implications for model development. Thereafter, the challenges of modeling hydrogen-air flames with flamelet-based approaches are outlined and the state-of-the-art flamelet modeling of hydrogen-air flames is discussed based on the existing literature.

2.4.1 Workflow of flamelet-based manifold models

Flamelet-based models are mainly characterized by a pre-computed flamelet manifold which is accessed by a reduced set of control variables. In general, there are two options to assess the performance of flamelet-based models, namely the *a-priori* and *a-posteriori* analysis. Both types of analysis are performed within the remainder of this thesis to comprehensively evaluate the novel flamelet-based model developed in the next chapter. The workflow of these assessments is shown schematically in Fig. 2.2. For both analyses, a reference database consisting of an FRS using DC is utilized to assess the model performance since all relevant physical phenomena are resolved in these simulations.

In an *a-priori* analysis the reduced set of control variables of the flamelet manifolds is extracted or calculated from the thermochemical state of a reference simulation. Subsequently, these control variables are used to perform a lookup to retrieve the thermochemical state from the manifold. This thermochemical state is compared to the reference data by computing e.g., a relative error ϵ_{rel}

[4] Flamelet-based models are known by different established acronyms namely Flamelet/Progress Variable (FPV) approach [48], Flamelet Generated Manifolds (FGM) [12, 49], or the Flame Prolongation for ILDM (FPI) model [50, 51].

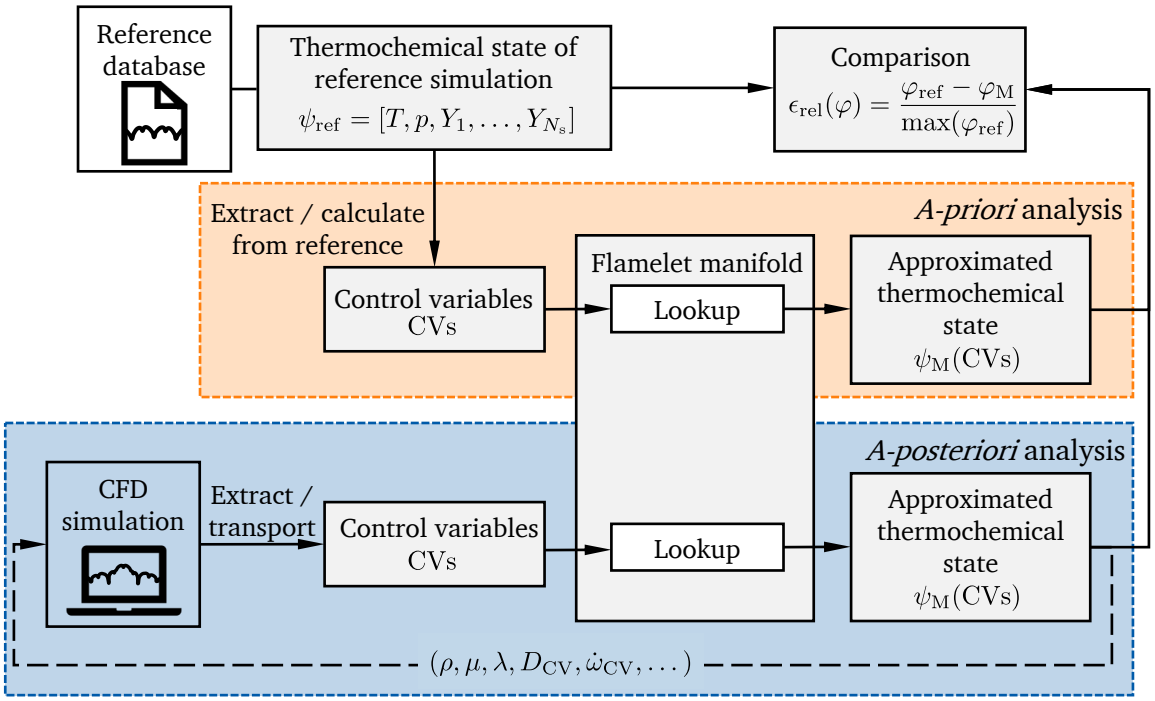

Fig. 2.2: Schematic overview of an *a-priori* and an *a-posteriori* analysis for flamelet-based models. This figure is adapted from [P5, 54].

between the reference data and the manifold prediction of a quantity of interest φ. Thereby, the overall deviations resulting from the approximated thermochemical state are assessed which corresponds also to the possibly best model performance to be expected in flamelet-coupled CFD simulations.

As a next step, an *a-posteriori* analysis can be performed, which includes the coupling of the CFD simulation and the manifold. Thereby, potential modeling errors resulting from the transport of the control variables can be investigated. It is emphasized that this coupling contains a feedback loop since the properties required for solving the transport equations are retrieved from the manifold and utilized in the CFD simulations. In particular, the source terms and diffusivities of the control variables are of utmost importance to capture the flame dynamics in fully coupled flamelet CFD simulations. Thereby, assumptions made in the respective transport equations can be critically evaluated when comparing the model predictions from *a-priori* and *a-posteriori* analyses.

2.4.2 Challenges for flamelet-based modeling of hydrogen-air flames

Next, the characteristics of the usual control variables of flamelet manifolds concerning hydrogen-air flames are outlined. Thereafter, the corresponding transport equations are discussed and the resulting challenges for modeling are highlighted.

Influence of differential diffusion effects

As already highlighted, differential diffusion effects play an important role in the context of hydrogen combustion. These differential diffusion effects mainly manifest in a mixture stratification across the flame front. To describe these effects, the Bilger mixture fraction Z_{Bilger} is frequently used [55, 56]. It is defined by coupling functions β between the fuel (index 1) and oxidizer (index 0) [57]:

$$Z_{\mathrm{Bilger}} = \frac{\beta - \beta_0}{\beta_1 - \beta_0} \,. \tag{2.23}$$

These coupling functions depend on the elemental mass fractions Z_l contained in the mixture,

$$\beta = \sum_{l=1}^{N_\mathrm{e}} \gamma_l Z_l = \sum_{l=1}^{N_\mathrm{e}} \gamma_l \sum_{k=1}^{N_\mathrm{s}} \frac{a_{l,k} M_l Y_k}{M_k} \,, \tag{2.24}$$

where N_e is the total number of elements, γ_l represents a weighting factor of element l, M_l (M_k) corresponds to the molecular weight of element l (species k), and $a_{l,k}$ to the number of element l in species k. Note that the weighting factors γ_l are not unique [58]. In this work, the weights are chosen in agreement with Bilger et al. [57].

To further highlight the implications of differential diffusion effects on flamelet-based models, the profiles of frequently used manifold control variables (Bilger mixture fraction Z_{Bilger}, enthalpy h and progress variable Y_c) are depicted along the physical space coordinate x for a stoichiometric unstretched hydrogen-air flame and different diffusion models in Fig. 2.3. The Bilger mixture fraction and the enthalpy experience a broad variation for the mixture averaged diffusion models while constant values are retrieved from the simulation with unity Lewis number diffusion. However, the progress variable profile ($Y_c = Y_{\mathrm{H2O}} - Y_{\mathrm{H2}} - Y_{\mathrm{O2}}$) is similar between all diffusion models. This indicates that the mixture fraction and enthalpy are strongly affected by differential diffusion effects. The consideration of Soret diffusion (see Eq. 2.9) amplifies the stratification of the Bilger mixture fraction but only a small influence is found for the enthalpy profile.

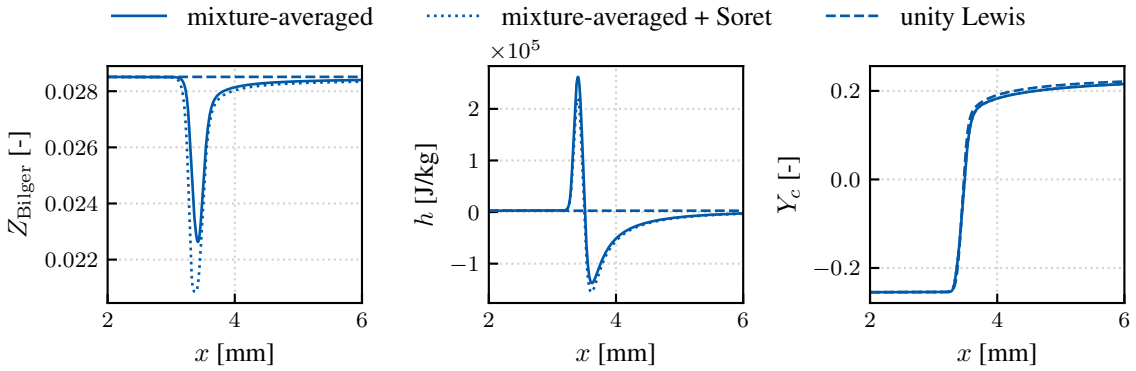

Fig. 2.3: Profiles of frequently used flamelet control variables along an FP flame front (H_2-air, $\phi = 1$, $p = 1\,\mathrm{atm}$, $T_\mathrm{u} = 300\,\mathrm{K}$) in physical space for different diffusion models.

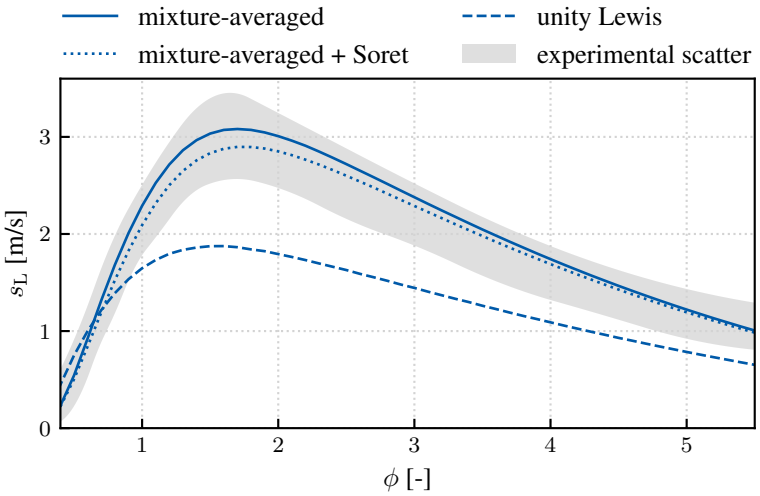

Fig. 2.4: Comparison of laminar burning velocities s_L for hydrogen-air mixtures with varying equivalence ratios at ambient conditions ($p = 1\,\mathrm{atm}$, $T_u = 300\,\mathrm{K}$). The blue lines correspond to unstretched planar flame calculations with different diffusion models and the grey shaded area is the experimental scatter extracted from [59, 60].

It becomes apparent that these fluctuations in Bilger mixture fraction Z_{Bilger} and enthalpy h need to be included in flamelet-based models addressing these hydrogen-air flames since they alter the combustion dynamics significantly e.g., the laminar burning velocity s_L is sensitive to the mixture stratification. In Fig. 2.4, the laminar burning velocity s_L along varying equivalence ratios ϕ is shown for simulation results of unstretched planar flames performing the same variation of diffusion models compared to Fig. 2.3. Additionally, the scatter of experimental data taken from [59, 60] is depicted by the grey-shaded area. It can be seen that the laminar burning velocity changes significantly between the different diffusion models. The unity Lewis model predicts significantly lower burning velocities compared to the mixture-averaged diffusion model. Overall, the simulations with mixture-averaged diffusion capture the experimental scatter very well, while including Soret diffusion leads only to slightly lower laminar burning velocities. This highlights the importance of differential diffusion effects for hydrogen-air flames since the overall flame dynamics are changed when neglecting differential diffusion indicating that flamelet-based models can only describe the flame dynamics if differential diffusion effects are incorporated in the flamelet manifold and the transport equations of the control variables.

Governing equations of control variables

Given this overall assessment of differential diffusion in the context of flamelet-based models, the transport equations of the control variables are discussed to outline the challenges when modeling differential diffusion effects with flamelet-based models. In the pioneering work of Peters [11, 61], a transport equation for the mixture fraction Z is derived in the context of non-premixed combustion:

$$\frac{\partial}{\partial t}(\rho Z) + \frac{\partial}{\partial x_i}(\rho u_i Z) = \frac{\partial}{\partial x_i}\left(\rho D_Z \frac{\partial Z}{\partial x_i}\right) . \tag{2.25}$$

Analogously, a transport equation for the progress variable was derived in the context of premixed combustion [49, 62]:

$$\frac{\partial}{\partial t}(\rho Y_c) + \frac{\partial}{\partial x_i}(\rho u_i Y_c) = \frac{\partial}{\partial x_i}\left(\rho D_c \frac{\partial Y_c}{\partial x_i}\right) + \dot{\omega}_c \,. \tag{2.26}$$

In these two transport equations, the diffusivity of mixture fraction D_Z and the one for progress variable D_c appear. Unlike the species diffusion coefficients, these quantities do not represent certain mixture properties since mixture fraction and progress variable are composed of several species each given its diffusion coefficient. Therefore, models are needed to estimate the diffusivities of the composed quantities based on the underlying species properties.

Alternatively, Sutherland et al. [58] proposed an exact transport equation for the Bilger mixture fraction Z_Bilger which does not require the modeling of any diffusivity:

$$\frac{\partial}{\partial t}(\rho Z_\mathrm{Bilger}) + \frac{\partial}{\partial x_i}(\rho u_i Z_\mathrm{Bilger}) = \frac{-1}{\beta_1 - \beta_0}\left(\sum_{l=1}^{N_\mathrm{e}} \gamma_l \left(\underbrace{\sum_{k=1}^{N_s} \frac{a_{l,k} M_l}{M_k} \frac{\partial}{\partial x_i}(\rho Y_k V_{k,i})}_{\text{Closure required}}\right)\right) . \tag{2.27}$$

However, in this transport equation the diffusive fluxes of all species, containing their respective gradients, need to be evaluated. But these are not inherently available in a reduced-order flamelet-based model and closure is required. It is noted that a similar closure is needed for the enthalpy transport (Eq. 2.11), which also contains the diffusive fluxes of all species.

Various approaches were proposed addressing the issue of capturing differential diffusion effects in flamelet-based models. These are briefly reviewed in the next section.

2.4.3 State-of-the-art flamelet-based modeling of hydrogen-air flames

Most of the extensions proposed for flamelet-based models for hydrogen combustion aim to improve the predictions of the mixture stratification due to differential diffusion effects and proposed closures for the diffusivities of mixture fraction and progress variable [63–65].

Swart et al. [63] developed a flamelet-based model for lean premixed methane-air flames, including a discussion on the effects of hydrogen addition. In their model, a differential diffusion coefficient for the progress variable is utilized and the closure of molecular diffusive fluxes is partly retrieved from the tabulated one-dimensional flames. Donini et al. [64] extended this model to include non-adiabatic conditions found in premixed laminar methane-air flames with heat loss and also turbulent gas turbine applications [66].

Another modeling approach was presented by Schlup and Blanquart [65], who investigated curvature effects in lean premixed hydrogen-air flames by extending the transport equation of the mixture fraction and using flamelet manifolds generated based on unstretched planar flamelets. By

assuming single-step chemistry, the authors could relate the diffusive flux of the mixture fraction to the diffusive transport of the progress variable. Thereby, the study focused on adiabatic premixed flames and hence, a manifold parameterized by mixture fraction and progress variable.

The modeling approaches above share the characteristic that the control variables are often composite quantities (e.g., mixture fraction and progress variable) that are transported directly in the CFD simulation. Therefore, additional modeling effort concerning their diffusivity is required as discussed in the previous section.

Progress has also been made with a hybrid transported-tabulated chemistry method (HTTC) to reduce the size of the flamelet manifold [67–69] where a reduced set of major species is transported and only intermediate species are tabulated using mixture fraction and progress variable as control variables. This model has been validated against freely propagating flames of large hydrocarbons (e.g., kerosene) [67] and a partially premixed methane-air flame [68, 69] using a mixture-averaged approach. Further, a manifold prolongation was utilized to account for effects beyond the flammability limits, but deviations remained in species profiles such as H_2O and CO [69]. Overall, this concept is promising to improve the prediction of flamelet-based approaches by transporting major species instead of conventional control variables. Gierth et al. [55] presented a similar approach for non-premixed combustion to capture differential diffusion effects in an LES of a non-piloted, non-premixed turbulent oxy-fuel flame fueled by a methane hydrogen blend. In this study, the transport of major species considerably improved the model predictions for the flame structure in comparison to conventional coupling strategies.

Although considerable progress has been made, no universally applicable solution has been presented for capturing differential diffusion in hydrogen-air flames with flamelet-based approaches. This gap is addressed in [P3] where a novel flamelet-based model based on the transport of major species and an approximated Bilger mixture fraction is developed to circumvent the closures for the mixture fraction Z and progress variable Y_c transport. Subsequent model extensions have been made in [P4, P5] to better capture thermo-diffusively unstable flames. In the next chapter, the fundamental characteristics of the new modeling approach are introduced.

3 Development of a flamelet-based model for premixed hydrogen combustion

The challenges for flamelet-based modeling of hydrogen-air flames and the state of the art of flamelet-based models have already been outlined in the previous chapter. One particular challenge in modeling hydrogen combustion is to accurately predict differential diffusion effects. First models were proposed to better predict the mixture stratification due to differential diffusion, however, no generic solution has been presented for capturing differential diffusion in premixed hydrogen-air flames. In particular, no flamelet-based models exist that address ignition or strain and curvature effects in the context of premixed hydrogen combustion. This gap is addressed in [P3–P5].

This chapter presents a novel coupling approach of the manifold and the CFD simulation used in [P3–P5] together with an overview of model characteristics which are subsequently adapted according to the modeling focus of the respective study.

3.1 Flamelet coupling approach based on transport of major species

In this thesis, additional models for diffusivities of mixture fraction and progress variable are avoided by transporting major species (H_2, O_2, H_2O) instead of the conventional control variables (Z_{Bilger}, Y_c). These three species are chosen since they capture the predominant part of the elemental mass fractions of H and O and have wide source terms, which are easy to resolve. The major species further correspond to reactants and products, respectively, and are indicative of the reaction progress. For each of the transported species, a respective conservation equation needs to be solved:

$$\frac{\partial \rho Y_k}{\partial t} + \frac{\partial}{\partial x_i}\left(\rho u_i Y_k\right) = -\frac{\partial}{\partial x_i}\underbrace{\left(-\frac{\alpha}{\mathrm{Le}_k}\frac{\partial Y_k}{\partial x_i}\right)}_{\rho Y_k V_{k,i}} + \dot{\omega}_k \,, \tag{3.1}$$

the diffusive flux $\rho Y_k V_{k,i}$ is described by a mixture-averaged diffusion model as highlighted in Eq. 2.8. It is noted that the diffusive fluxes are calculated based on the species mass fraction field while the gradient of the mean molecular mass is neglected due to its minor influence in comparison to the mass fraction gradient [P3]. For later usage in a coupled CFD simulation, the source terms and diffusivities of all major species are stored in a flamelet manifold, which is also discussed below.

To account for non-adiabatic effects the conservation equation for enthalpy h is solved (see Eq. 2.11). It is noted that this equation contains the temperature gradient, which is not inherently available in a flamelet-based CFD simulation. Therefore, the equation is reformulated to obtain a form that is only dependent on enthalpy and species gradients:

$$\frac{\partial}{\partial t}(\rho h) + \frac{\partial}{\partial x_i}(\rho u_i h) = \frac{\partial}{\partial x_i}\underbrace{\left[\alpha\frac{\partial h}{\partial x_i} - \sum_{k=1}^{N_s}\left(h_k\left(\rho Y_k V_{k,i} + \underbrace{\alpha\frac{\partial Y_k}{\partial x_i}}_{\text{Additional}}\right)\right)\right]}_{\text{Closure required}} + q\,, \tag{3.2}$$

where q represents a source term to model the energy deposition in the forced ignition process [P3, 70]. Further, an additional term, including the species gradient, is present compared to Eq. 2.11. Still, this formulation of the enthalpy equation is found to be numerically more robust. However, closure is required for the enthalpy transport since it contains the diffusive fluxes of all species. Although intermediate species like radicals do not contribute substantially to the elemental balance, they can contribute significantly to the mixture's enthalpy due to their high enthalpy of formation. Since only the gradients of the transported species are directly available in the CFD simulation, all other species gradients are approximated based on one-dimensional flamelets and stored in the flamelet manifold as indicated by the enthalpy closure $\nabla h_{\text{closure}}$:

$$\nabla h_{\text{closure}} = \sum_{k=1}^{N_\text{s}}\left(h_k\left(\rho Y_k V_{k,i} + \alpha\frac{\partial Y_k}{\partial x_i}\right)\right) \quad \forall k \notin \{\text{H}_2, \text{O}_2, \text{H}_2\text{O}\}\ . \tag{3.3}$$

It is noted that the gradients of these minor species mainly occur in the reaction zone where flamelet-based models yield accurate results and only a single additional field needs to be stored in the flamelet manifold. Thereby, the approach of transporting major species reduces the required closure significantly compared to the model of Mukundakumar et al. [71] who developed a flamelet-based model for hydrogen combustion solving conservation equations for mixture fraction, progress variable and enthalpy, which requires closure by one-dimensional flames in all equations to approximate their diffusivities. This indicates the flexibility of the novel model based on the transport of major species since fewer closures are required even though the number of transported scalars is slightly increased. While the overall computational cost is increased by transporting additional scalars, it was also found that this can improve the accuracy of flamelet-based models [56].

The number of transported scalars can result in some drawbacks concerning the manifold generation. When being used directly as control variables for the tabulated manifold, its dimensionality and subsequently the memory requirements are increased. To avoid any memory overhead of the new model, the structure of the flamelet manifold is kept consistent with conventional tabulation strategies by utilizing an approximate version of the Bilger mixture fraction, which is defined based on the transported species only. For the hydrogen-air flames examined in this thesis, the approximated Bilger mixture fraction recovers the same characteristics as the original version without

introducing significant modeling errors. However, it is emphasized that this approximation must be used consistently in both, the manifold parameterization, and the coupling of the CFD simulation and manifold. The progress variable can be directly calculated from the linear combination of the major species since it is defined as $Y_c = Y_{\mathrm{H2O}} - Y_{\mathrm{H2}} - Y_{\mathrm{O2}}$ in all works included in this thesis. Thereby, a self-contained coupling between the flamelet manifold and the CFD solver is achieved resulting in a speedup of one order of magnitude in comparison to FRSs of hydrogen-air flames using DC. The specifics of the described coupling between the CFD solver and the flamelet manifold are also schematically summarized in Fig. 3.1. This schematic workflow highlights the processing of the control variables based on the transported major species (H_2, O_2, H_2O) and the properties retrieved from the manifold. Properties like the Le_k numbers, and source terms $\dot{\omega}_k$ of the major species or the enthalpy closure $\nabla h_{\mathrm{closure}}$ are coupled back to the conservation equations of the transported quantities since they are required for their solution.

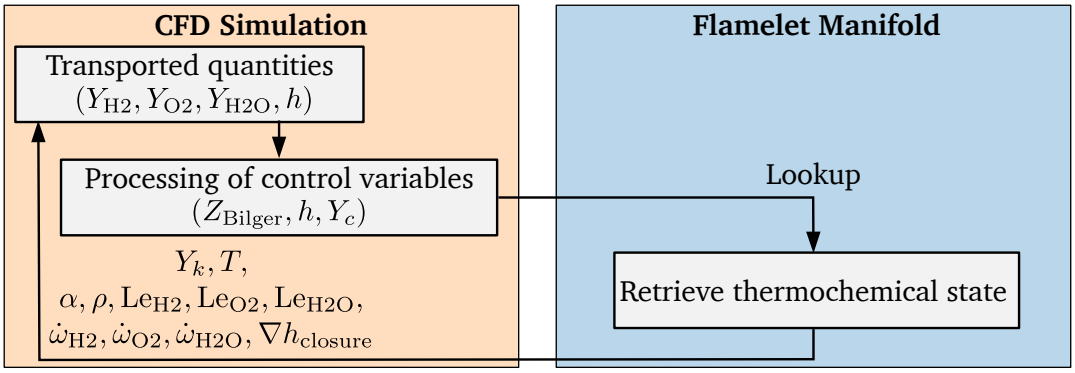

Fig. 3.1: Schematic overview of the novel flamelet coupling approach. This figure is adapted from [P3].

It is stressed that this modeling approach is not restricted to hydrogen combustion but also proved beneficial in the simulation of a Bunsen flame fueled by a hydrogen-methane blend where good agreement between experimental data and the model prediction is found when transporting six species in total [A6]. Here, an even higher reduction in computational cost is achieved compared to pure hydrogen combustion as detailed reaction mechanisms are much larger when capturing methane kinetics. Similar behavior is expected concerning ammonia-hydrogen blends or if $\mathrm{NO_x}$ formation is included in the model.

3.2 Overview of modeling specifics

The modeling approach introduced in the previous section was initially developed to describe the forced ignition and early flame propagation of lean and rich hydrogen-air flames [P3] and was extended to better capture laminar [P4] and turbulent [P5] thermo-diffusively (TD) unstable hydrogen-air flames. These model extensions mainly consist of different physical phenomena included in the respective manifold. In Tab. 3.1, an overview of the different models is presented which includes the flame configuration of the modeling focus and a model name to easily identify

the respective model extension. In addition, the manifold parameterization is given which contains the thermochemical state ψ obtained from certain parameter variations using the CSM (see Sec. 2.3) and the control variables which are used to parameterize the manifolds.

Tab. 3.1: Overview of flamelet-based models developed within the scope of this thesis.

Modeling focus	Model name	Manifold parameterization	Control variables	Used in publication
Igniting flames	M-h	$\psi(\phi, h, Y_c)$	$Z_{\mathrm{Bilger}}, h, Y_c$	[P3–P5]
Laminar TD unstable flames	M-κ_c	$\psi(\phi, Y_c, \kappa_c)$	$Z_{\mathrm{Bilger}}, Y_c, Y_{\mathrm{H}}$	[P4, P5]
Turbulent TD unstable flames	M-(K_s, κ_c)	$\psi(\phi, Y_c, \kappa_c, K_s)$	$Y_{\mathrm{H2}}, Y_{\mathrm{O2}}, Y_{\mathrm{H2O}}, Y_{\mathrm{H}}, h$	[P5]

Each manifold includes differential diffusion effects and presents a particular novelty concerning the captured physics. In short, the main characteristics of the manifolds are briefly outlined:

- The M-h manifold is initially developed for igniting hydrogen-air flames with a focus on forced ignition events. To model this process the manifold captures non-adiabatic effects, which result from the energy deposition during forced ignition events, by utilizing the enthalpy h as manifold dimension. The deposited energy then causes a thermal runaway which triggers the chemical reactions. The appropriate kinetics are captured in the manifold by CSM calculations in the ignition limit for high unburned temperatures (see Sec. 2.3), while the characteristics of unstretched planar flames are recovered for low unburned temperatures.
- The M-κ_c manifold is developed in the context of laminar thermo-diffusively unstable flames, where it was found that curvature effects are particularly important to describe the cellular flame structure. This manifold accounts for large curvature κ_c variations (positive and negative). Thereby, the characteristics of the CSM are exploited as curvature can be supplied as an external parameter which allows a broader variation compared to canonical flames.
- The M-(K_s, κ_c) manifold is a subsequent extension of the M-κ_c manifold and also takes strain K_s variations into account. This manifold is developed in the context of turbulent thermo-diffusively unstable hydrogen-air flames, where it is found that the previously developed manifolds cannot capture all physical phenomena.

More detailed information concerning the respective manifolds and their generation is presented in the next chapter together with the respective flame configurations.

4 Results and discussion

This chapter presents the main findings of the publications included in this thesis [P1–P5] together with related coauthor publications addressing hydrogen combustion [A1–A3, A5–A7]. It is structured according to the schematic overview of the scientific objectives of this thesis presented in Fig. 1.2. First, strain and curvature effects are systematically analyzed for lean and rich hydrogen-air flames using the CSM (see Sec. 2.3). Thereafter, two configurations are discussed concerning flamelet-based modeling, namely: (1) forced ignition and flame propagation of lean and rich hydrogen-air flames and (2) laminar and turbulent thermo-diffusively unstable hydrogen-air flames. These configurations include an analysis of physical phenomena followed by a discussion of modeling specifics concerning the tabulated manifold. Finally, the newly developed models are applied to the flame configuration and their performance is evaluated, respectively.

4.1 Analysis of strain and curvature effects

As highlighted in Chapter 2, stretch effects play an important role in premixed hydrogen-air flames. Hence, their detailed investigation is of high scientific interest. However, this remains a challenging task in multidimensional (turbulent) flames and simple canonical flames are restricted in their attainable strain and curvature effects due to their topology and boundary conditions (see Sec. 2.2). To this end, a recently developed composition space model (CSM) exhibits beneficial characteristics as strain K_s and curvature κ_c can be supplied as external parameters (see Sec. 2.3). Therefore, the CSM allows for an assessment of flames with arbitrary combinations of strain and curvature even beyond the limit of canonical flame configurations solved in physical space. The studies presented in [P1, P2] analyze such flames by performing (K_s, κ_c)-parameter variations with the CSM. In these works, the stretch-chemistry interaction for lean and rich hydrogen-air flames is studied focusing not only on global flame properties but also on detailed flame structures and reaction pathways and subsequently discussing the Lewis number effect. In the following, the main findings from [P1, P2] are outlined.

In Fig. 4.1, the (K_s, κ_c)-parameter spaces for hydrogen-air mixtures with $\phi = 0.4$ (top) and $\phi = 5.1$ (bottom) are shown and color-coded by stretch K, flame speed s_u and maximum temperature T_max. Additionally, the canonical flame solutions for IPF and SEF (see Fig. 4.4) are shown for reference. It is visible that the CSM spans a much larger (K_s, κ_c)-parameter space compared to the canonical flames and includes also negative values for strain and curvature. Further, it is noted that multiple combinations of strain and curvature can result in the same stretch level since the iso-lines for stretch K are not perpendicular to the respective axes. However, the flame characteristics change

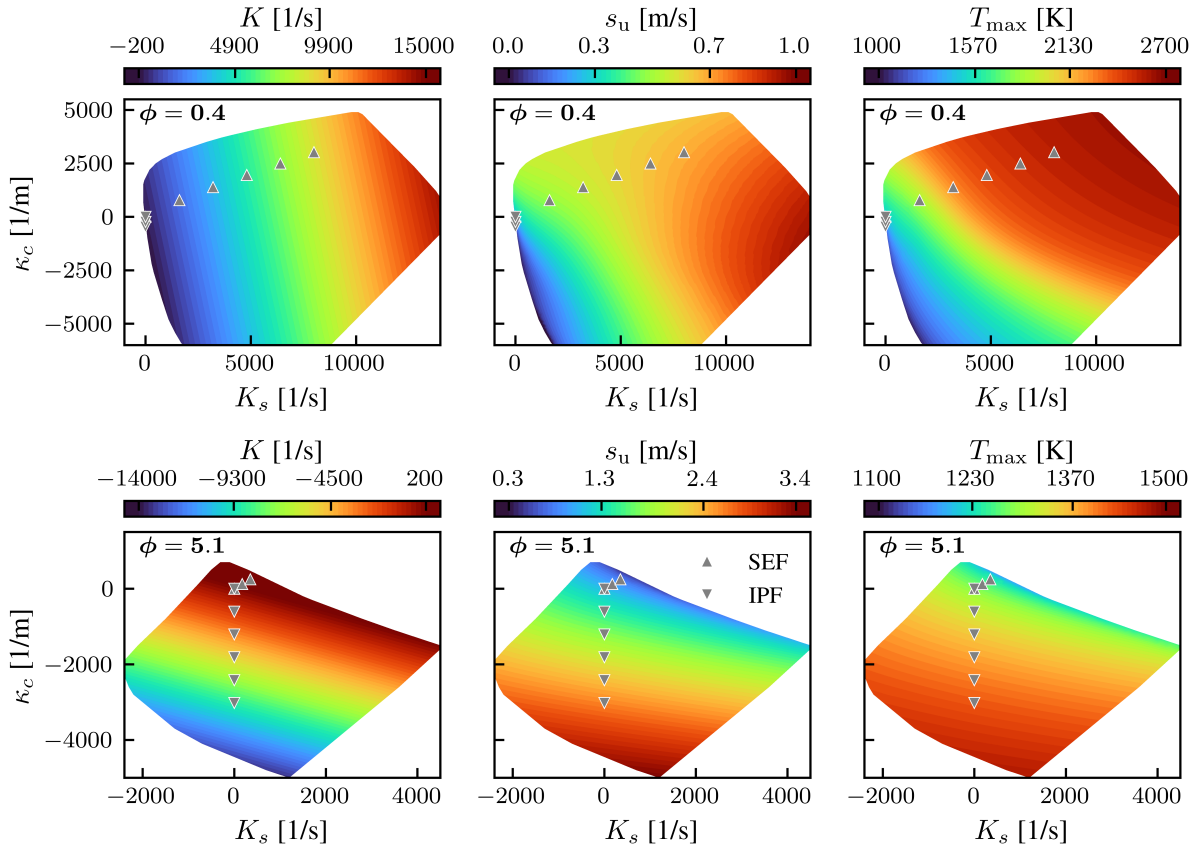

Fig. 4.1: (K_s, κ_c)-parameter space for lean ($\phi = 0.4$) and rich ($\phi = 5.1$) hydrogen-air flames at ambient conditions ($p = 1\,\mathrm{atm}$, $T_0 = 300\,\mathrm{K}$) attained by the CSM. The parameter space is characterized by stretch K, burning velocity s_u and maximum temperature T_{max}. Canonical flame solutions are shown for reference. This figure is adapted from [P1, P2].

significantly which can be seen from the change in flame speed s_u and maximum temperature T_{max} throughout the parameter space. For the lean hydrogen-air flames, the flame speed varies by a factor greater than five where low burning velocities are found in areas of negative stretch and subsequently increasing velocities are found for increasing strain and curvature values. A similar statement can be made concerning the maximum temperature which varies by approximately $1700\,\mathrm{K}$. However, opposite trends are found for rich hydrogen-air flames where lower flame speeds and lower maximum temperatures are found for positively stretched flames which increase for decreasing values of strain and curvature. This is consistent with the Lewis number effect.

Further, flame structures throughout the (K_s, κ_c)-parameter space are analyzed beyond the limit of canonical flames. In Fig. 4.2, the heat release rate $\dot{\omega}_T$ is depicted along the progress variable Y_c as a representative quantity of the flame structure for selected CSM calculations (H_2-air, $\phi = 0.4$) with increasing strain (left) and increasing curvature (right). It is visible that the maximum heat release rate more than doubles for both increasing strain K_s and increasing curvature κ_c. However,

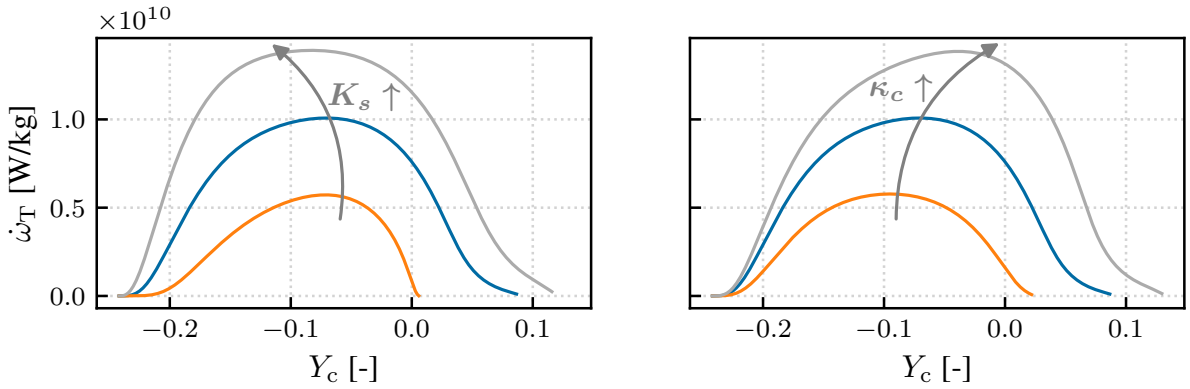

Fig. 4.2: Flame structure comparison at different locations within the (K_s, κ_c)-parameter space for lean hydrogen-air flames ($\phi = 0.4$, $p = 1\,\mathrm{atm}$, $T_0 = 300\,\mathrm{K}$). The heat release rate $\dot{\omega}_T$ is shown for CSM calculations with increasing strain (left: $\kappa_c = 0\,\mathrm{m}^{-1}$, $K_s = 1000/5000/10\,000\,\mathrm{s}^{-1}$) and with increasing curvature (right: $K_s = 5000\,\mathrm{s}^{-1}$, $\kappa_c = -2500/0/2500\,\mathrm{m}^{-1}$). This figure is adapted from [P1, P2].

increasing strain shifts the maximum heat release rate towards the unburned side, while it is shifted towards the burned side for increasing curvature. This highlights the different effects of strain and curvature on the flame structure and indicates that different combinations of strain and curvature can result in significantly different flame structures even if their net flame stretch is similar. These findings are comprehensively summarized in [P1, P2]. Additionally, these works present a detailed assessment of the different effects of strain and curvature on the reaction pathways of lean and rich hydrogen-air flames. Most importantly, these findings indicate that both strain and curvature effects are relevant to model development while incorporating only the total flame stretch cannot describe all effects. In the following, strain and curvature effects are further discussed for igniting hydrogen-air flames and thermo-diffusively unstable flames focusing also on aspects of flamelet-based modeling.

4.2 Ignition and flame propagation in lean and rich hydrogen-air mixtures

In this section, first, the physical phenomena of ignition and flame propagation in lean and rich hydrogen-air mixtures are discussed. Thereafter, modeling specifics concerning the tabulated manifold (M-h) are presented and finally, the model performance is evaluated [P3].

4.2.1 Physical phenomena

Ignition processes in technical combustors are often forced by supplying energy. These processes are very complex due to the interaction of chemical reactions with many different processes such

as energy deposition, heat loss to cold surfaces and their interaction with a turbulent flow field. Therefore, canonical flames are frequently used to study ignition processes in a more confined manner focusing particularly on differential diffusion and stretch effects.

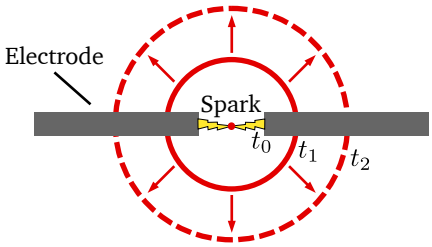

Fig. 4.3: Schematic of a spherical expanding flame configuration.

A commonly used canonical configuration to study forced ignition is the spherical expanding flame (SEF). Such flames can be studied experimentally in a constant-volume chamber that contains the unburned mixture. Ignition is achieved in a narrow gap between a pair of pointing electrodes, where a spark containing certain ignition energy E_{ign} can be created depending on the supplied voltage and the capacitance of the ignition circuit [72–76]. A schematic overview of this configuration is depicted in Fig. 4.3. In these experiments, the minimum ignition energy (MIE) but also burning velocities at high temperatures and high pressures are determined [77]. The measurements are either performed in quiescent mixtures or fan-stirred near-isotropic turbulence [74]. Thereby, the ignition characteristics can be studied in a broad operating range using different mixtures, ignition energies, electrode gap distances, electrode shapes and different turbulent intensities [76]. This experimental setup can also be described numerically in a one-dimensional configuration by solving mass, species and energy conservation in spherical coordinates [78]. Here, the non-adiabatic forced ignition process is usually modeled by energy deposition in a confined area similar to the spark between electrodes in the experimental setup [70]. The deposited energy results in a local temperature increase which causes a thermal runaway and subsequently initiates the combustion process. This model configuration recovers the most important characteristics such as minimum ignition energy, flame dynamics and reaction kinetics, while some effects like heat loss to the electrodes or turbulent flows cannot be captured due to the symmetry conditions included in the one-dimensional formulation. Additionally, numerically studying inwardly propagating flames (IPFs) is straightforward, whereas achieving such flames in experimental setups poses significant challenges [40, 41].

Spherical expanding flames have been investigated in several studies focusing on different aspects. Besides assessing minimum ignition energies, the early flame dynamics are of high scientific interest to gain further insights into the ignition process, since spherical ignition kernels are subject to pronounced flame stretch resulting from transient changes in flame surface area (see Sec. 2.2). Chen et al. [79] analyzed the dependence of the Lewis number effect during the ignition process for lean and rich hydrogen-air SEFs ($0.5 \leq \phi \leq 4.5$, $0.4 \leq \mathrm{Le} \leq 2.1$) and compared experimental data to results obtained from asymptotic theory and numerical one-dimensional simulations focusing on the early flame propagation. This study was later extended to different fuels and to IPFs investigating also effects of negative stretch [P1, P2, 41, 80]. These studies report significantly altered flame speeds depending on the overall flame stretch.

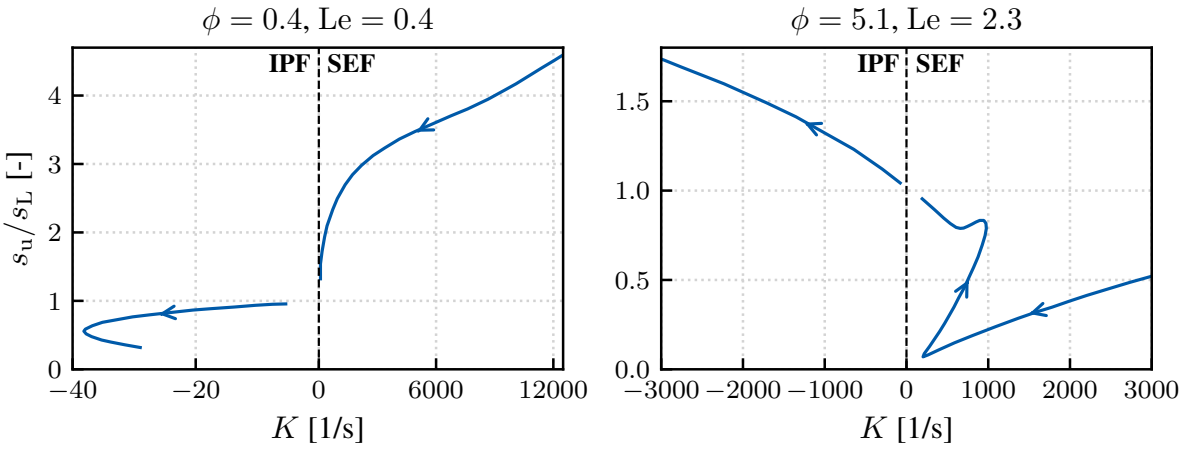

Fig. 4.4: Change of the normalized flame propagation speed s_u/s_L along flame stretch K during the spherical flame propagation in hydrogen-air mixtures with $\phi = 0.4$ (left) and $\phi = 5.1$ (right). The arrows indicate the direction of the transient flame propagation. This figure is adapted from [P2].

The change of flame speed s_u with stretch K during the spherical flame propagation is shown in Fig. 4.4 for a lean hydrogen-air flame with $\phi = 0.4$ (Le < 1) and a rich one with $\phi = 5.1$ (Le > 1). The flame propagation speed s_u is normalized by the laminar burning velocity s_L and the results for IPF and SEF are separated by the dashed line at $K = 0\,\mathrm{s}^{-1}$ since they correspond to negative and positive stretch, respectively. For lean hydrogen-air flames (Le < 1), the flame speed decreases with decreasing stretch K depicting a C-shaped curve for negative stretch due to the competition between the changes in flame speed and curvature [41, 80, 81]. In contrast, rich hydrogen-air flames (Le > 1) exhibit a different relation between propagation speed and stretch rate. In general, the flame speed increases with decreasing stretch. However, a non-monotonic relation between propagation speed and stretch is found for positive stretch rates which is attributed to the ignition process in the SEF. Initially, the highly positively stretched flame kernel propagates outwards due to the energy deposition causing fuel decomposition and radical formation. Subsequently, an unsteady flame transition, which is mainly driven by chemical reactions and local transport effects, is observed where the flame kernel exhibits a decrease in its flame thickness (increase in flame speed and stretch). Finally, a self-sustained flame propagates outwards resulting in an increase in propagation speed due to the decreasing stretch rate. Based on these relations between flame speed and stretch, the importance of the stretch-chemistry interaction and the Lewis number effect on the ignition process in SEFs becomes apparent. The ignition process can be defined by a critical flame radius, indicating the point at which the impact of the initial flame transition can be disregarded [79]. This critical radius increases with the Lewis number of the mixture. It is also found that the minimum ignition energy shows a linear increase with the cube of the critical radius which further outlines that mixtures with large critical radii (large Le numbers) are harder to ignite in the SEF configuration [82].

While forced ignition of quiescent mixtures already includes complex physical phenomena, several experimental [83–88] and numerical studies [89–91] investigated forced ignition in turbulent flow fields. Their overall findings depict an inhibiting effect of turbulence on the ignition process

since it causes stronger dissipation of the deposited energy. It was found that the MIE increases monotonically with the turbulent intensity and a MIE transition is observed where a steep increase of the MIE is found with increasing turbulent intensity. However, Wu et al. [72] observed that turbulence can facilitate ignition for mixtures with large Lewis numbers, namely a rich hydrogen-air mixture with $\phi = 5.1$ ($\mathrm{Le} \approx 2.3$) besides others. This effect of turbulent-facilitated ignition (TFI) is attributed to flame stretch since turbulence deforms the strongly positively curved flame kernel in various wrinkled flame segments resulting in negatively stretched flame sections. In these negatively stretched segments, the burning intensity is increased for $\mathrm{Le} > 1$ mixtures which can promote ignition. Further, several experimental works [73–75] found TFI for mixtures with large Lewis numbers, which also discuss the role of differential diffusion and the heat loss to cold electrodes narrowing down the prerequisites of TFI to mixtures with large Lewis numbers and small gap distances between the electrodes.

Uranakara et al. [92] performed fully resolved simulations of forced ignition in a turbulent hydrogen-air mixture with $\mathrm{Le} > 1$ at similar conditions where experiments report TFI ($\phi = 4$). They found that turbulence leads to locally positively stretched flame segments and did not find any facilitating effect of turbulent wrinkling on the ignition process. However, they did not account for the electrodes in their numerical simulations. In the study of Chen et al. [A5], the forced ignition of hydrogen-air mixtures is investigated including cold electrodes. To mimic a turbulent flow around the electrodes, a uniform laminar flow is imposed which transports the flame kernel away from the electrodes. In this configuration, flow-facilitated ignition (FFI) is observed for a rich hydrogen-air mixture ($\phi = 5.1$, $\mathrm{Le} \approx 2.3$) and a sufficiently small electrode gap. These FFI results are similar to the TFI phenomena observed in experiments and form an important step in identifying the physical phenomena relevant to TFI. It is found that the presence of electrodes does not only induce heat loss but also alters the shape of the flame kernel and subsequently its curvature and flame stretch. Compared to the forced ignition in quiescent mixtures, the imposed flow normal to the electrodes blows the flame kernel away from the electrodes which reduces the heat loss to the electrodes and reduces the flame curvature. Thereby, the imposed flow can facilitate the ignition process. Chen et al. [A7] extended this study to lean and stoichiometric hydrogen-air flames at a reduced pressure ($p = 0.3\,\mathrm{atm}$) including a variation of the electrode gap distance and the imposed flow velocity. Thereby, FFI is also found for a lean hydrogen-air mixture with $\phi = 0.4$ ($\mathrm{Le} \approx 0.4$) indicating that a mixture with a large Lewis number is not a prerequisite for FFI and rather a mixture with a large critical radius seems to be a necessary condition. However, these findings are contradictory to the current understanding of TFI and no experimental results exist that support the finding of FFI in mixtures with small Lewis numbers. Although the process of TFI and FFI is not yet fully understood, the relevance of the stretch-chemistry interaction for hydrogen-air flames even in relatively simple configurations like spherical expanding flames is highlighted. This forms a strong need for active research to further elucidate the physical phenomena relevant to turbulent facilitated ignition.

Given these recent findings on forced ignition in hydrogen-air mixtures, it becomes apparent that stretch effects play an important role during the ignition process as turbulent wrinkling can promote ignition in these mixtures, which is contradictory to the previous understanding. Here, the development of models based on the CSM might provide additional insights into the importance of strain and curvature effects. However, developing flamelet-based models capturing forced ignition

and early flame propagation in quiescent hydrogen-air mixtures (laminar flames) is already a challenging task. In the next section, the manifold characteristics of a model capturing differential diffusion and forced ignition are discussed before evaluating the model performance.

4.2.2 Manifold generation

Based on the previous discussion of the physical phenomena of forced ignition in spherical expanding flames, the key findings affecting the model development are:

- Differential diffusion effects in combination with the Lewis number effect are of utmost importance since the early flame propagation can be significantly affected by flame stretch and particularly mixtures with $\mathrm{Le} > 1$ (e.g., rich hydrogen-air mixtures) are harder to ignite due to stretch effects.
- Non-adiabatic effects need to be considered to model the energy deposition during the forced ignition process. Thereby, the relevant kinetics at high temperatures need to be captured to describe the thermal runaway and subsequently the minimum ignition energy appropriately.

It is emphasized that no flamelet-based models exist that describe both physical phenomena relevant to forced ignition in premixed hydrogen-air flames. This gap is addressed in [P3], where a respective manifold is developed following the coupling approach based on major species (see Chapter 3) and the model performance is evaluated in various igniting canonical flame configurations for lean and rich hydrogen-air flames ($0.7 \leq \phi \leq 1.4$)[5]. In the following, the modeling specifics of the utilized flamelet manifold are outlined.

The M-h manifold developed in [P3] grounds on a parameter variation of equivalence ratio ($0.35 \leq \phi \leq 2.0$) and unburned temperature ($300\,\mathrm{K} \leq T_u \leq 3500\,\mathrm{K}$) using the CSM. In Fig. 4.5, a representative subset of CSM calculations ($\phi = 0.7$) included in the manifold is depicted highlighting the different characteristics depending on the overall enthalpy level. The enthalpy h, the temperature T, and the mass fractions of H_2O and OH are shown along the progress variable. Overall, consistent variations in thermochemical quantities such as the temperature and species mass fractions are observed. Additionally, the profiles of the normalized progress variable gradient $g_c/g_{c,\max}$ and the enthalpy closure $\nabla h_{\text{closure}}$ are depicted. The enthalpy closure is evaluated for every CSM calculation according to Eq. 3.2 after reconstructing the physical space coordinate (see Eq. 2.20). The enthalpy closure shows increasing amplitudes for higher enthalpy levels as both the progress variable gradient and the amount of radical mass fractions change. The different line styles highlight certain characteristics of the CSM. Solid lines correspond to the deflagration limit, where the CSM recovers the characteristics of unstretched freely propagating flames (FP). The variations found along each CSM calculation in the enthalpy h and the enthalpy closure $\nabla h_{\text{closure}}$ highlight the relevance of differential diffusion effects for flames in the deflagration limit. In addition to the preheated FP calculations, CSM simulations with reduced enthalpy are performed taking exhaust

[5] This study presents a flamelet-based model applicable to a broad range of equivalence ratios. However, very rich hydrogen-air flames are beyond the scope of this study since they exhibit slightly non-monotonic progress variable profiles in the post-oxidation zone. Regularization methods to retrieve optimized Y_c definitions might enable modeling studies for very confined conditions like very rich hydrogen-air flames [93–95]. Such an assessment is subject to future work.

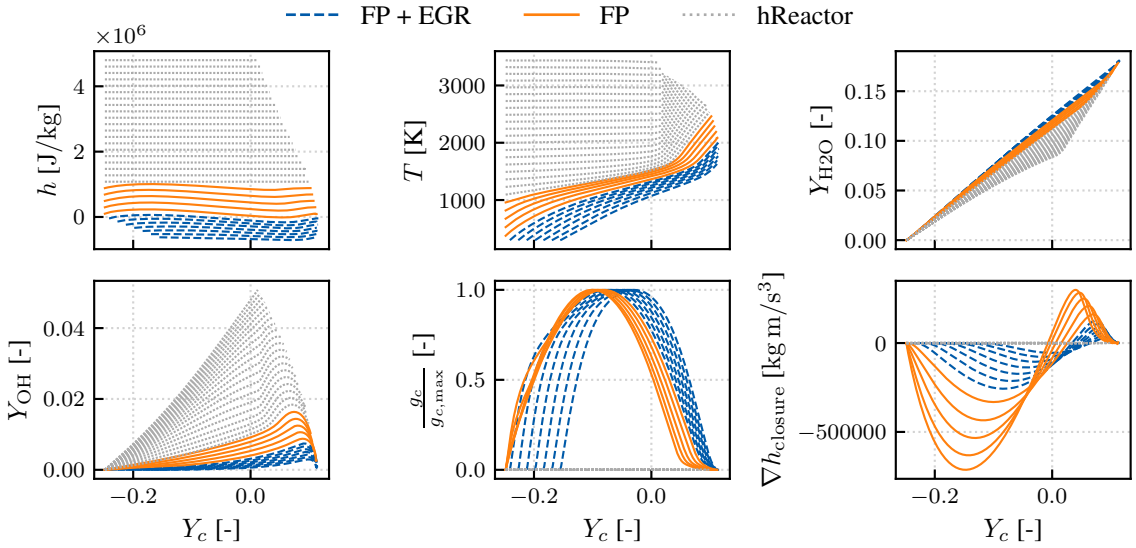

Fig. 4.5: Characteristics of CSM calculations with varying enthalpy levels and $\phi = 0.7$ which are used for manifold generation. Conceptual differences between flamelets are highlighted by different line styles for planar freely propagating flames with exhaust gas recirculation (FP+EGR, dashed lines), planar freely-propagating flames (FP, solid lines), and homogeneous ignition at constant pressure (hReactor, dotted lines). This figure is adapted from [P3].

gas recirculation (EGR) into account (dashed lines) [96]. These are required to ensure that all thermochemical states found in the investigated flame configuration are covered in the flamelet manifold since these flame topologies, subject to significant differential diffusion and flame stretch, can exhibit large enthalpy variations. At high enthalpy levels, the CSM transitions to the ignition limit ($g_c \to 0$). In the ignition limit, the CSM recovers the characteristics of a homogeneous reactor at constant pressure (hReactor) as all diffusion terms vanish (see Sec. 2.3). These CSM solutions are depicted by the dotted lines. It is noted that they are not affected by differential diffusion since all diffusion terms vanish. However, capturing the ignition limit in the manifold is required to model the thermal runaway during the forced ignition process, which is related to a different radical formation compared to the deflagration limit. The highest enthalpy levels mainly describe dissociation reactions as no significant temperature increase occurs along the CSM calculations.

4.2.3 Model validation and evaluation

The study [P3] includes a comprehensive evaluation of the model performance by comparing the propagation and flame structure of (1) unstretched planar flames and igniting (2) cylindrical expanding flames, (3) spherical expanding flames and (4) counterflow flames against reference simulations using detailed chemistry (DC). Additionally, different hydrogen-air mixtures ($\phi = 0.7; 1.0; 1.4$) and varying ignition energies E_{ign} are investigated and minimum ignition energies are

assessed. In the following, the main findings of the model evaluation are summarized. For brevity, only the SEF results with ($\phi = 0.7; 1.4$, $E_{\mathrm{ign}} = 0.15\,\mathrm{mJ}$) are discussed as the other reference cases show similar results [P3].

The transient evolution of the flame propagation speed from ignition to quasi-steady flame propagation obtained by the M-h model and the DC reference simulation is shown in Fig. 4.6. The flame propagation speed s_{u} in SEFs is a result of both thermal expansion and self-sustained flame propagation. It can be decomposed according to:

$$s_{\mathrm{u}} = \frac{\mathrm{d}R_{\mathrm{f}}}{\mathrm{d}t} = u_{\mathrm{g}} + s_{\mathrm{d}}\,, \tag{4.1}$$

where s_{d} is the flame displacement speed and u_{g} is the gas velocity that results from the thermal expansion of the hot products enclosed by the flame. It is defined as the peak velocity value found on the unburned side of the flame [42, 97]. To allow for a detailed assessment of the propagation dynamics all three velocities are shown in Fig. 4.6 for the lean and rich hydrogen-air flame, respectively. The propagation speed s_{u} depicts an initial increase which marks the point of ignition where thermal expansion (cf. u_{g}) and chemical reactions (cf. s_{d}) also show a strong increase. This is followed by a decay during the transition of the ignition kernel to the self-sustained flame propagation, where the flame propagation speed becomes constant. The gas velocity u_{g} also exhibits a rapid increase at the point of ignition. Afterward, it follows the overall trend of the propagation speed s_{u}. Overall, the onset of ignition, the flame displacement speed and the different time scales of flame transition for the lean and rich flame are accurately captured by the M-h model. Only small deviations in the propagation speed are found which can be attributed to the thermal expansion (cf. u_{g}) as it is slightly underpredicted for the lean flame.

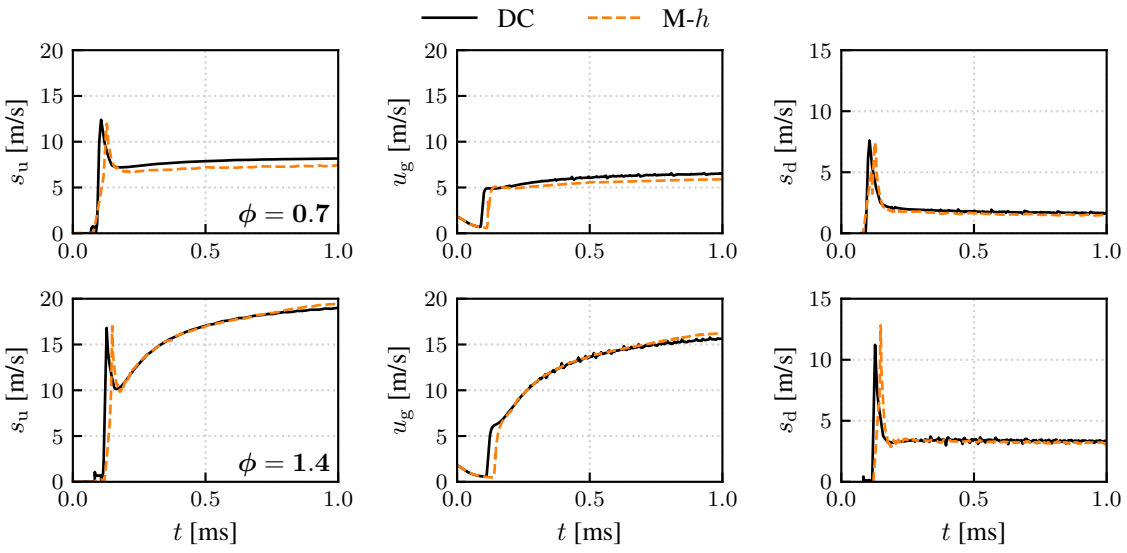

Fig. 4.6: Comparison of flame propagation speed s_{u}, gas velocity u_{g} and flame displacement speed s_{d} in spherical expanding flames ignited by an energy deposition of $E_{\mathrm{ign}} = 0.15\,\mathrm{mJ}$ with equivalence ratios of $\phi = 0.7$ and $\phi = 1.4$. This figure is adapted from [P3].

The differences in the gas velocity u_g are further elaborated by analyzing the flame structure. In Fig. 4.7, the profiles of the control parameters of the flamelet manifold (Z_{Bilger}, Y_c, h), the temperature T, the OH mass fraction Y_{OH}, and the velocity u are shown along the domain radius R for the lean SEF. In general, the variations of Bilger mixture fraction Z_{Bilger} and enthalpy h due to

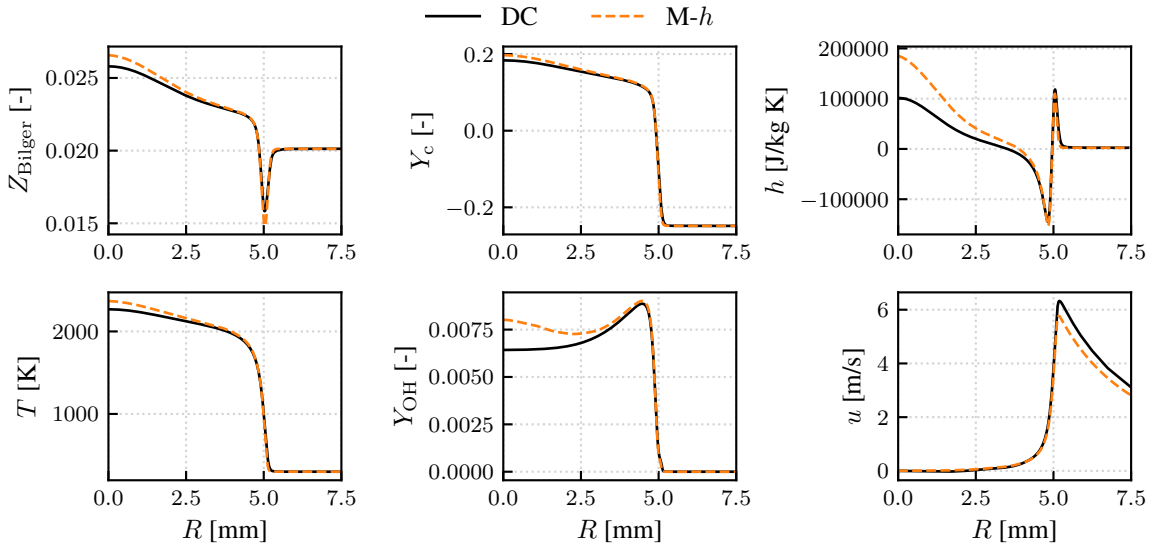

Fig. 4.7: Flame structure comparison of the SEF with $\phi = 0.7$ ignited by an ignition energy of $E_{\mathrm{ign}} = 0.15\,\mathrm{mJ}$. The Bilger mixture fraction Z_{Bilger}, the progress variable Y_c, the enthalpy h, the temperature T, the OH mass fraction Y_{OH} and the velocity u are shown along radial direction R. This figure is adapted from [P3].

differential diffusion are well recovered by the model. Only the thermodynamic state of the burned side mixture ($R < 2.5\,\mathrm{mm}$) is slightly overpredicted which can be attributed to the transient process, energy deposition and stretch effects during the ignition process, where small deviations can also cumulate over time. This further causes a small shift in the temperature and species composition. Subsequently, these minor deviations affect the thermal expansion during the transient evolution and thereby the gas velocity u_g. However, these deviations are considered insignificant given the complexity of the configuration, the good agreement found for the minimum ignition energy [P3], and the comparison across different CFD codes[6].

Overall, the novel flamelet model based on the transport of major species shows very good prediction accuracy. This is demonstrated by the good agreement concerning the ignition, flame propagation and flame structure of lean and rich hydrogen-air flames.

[6]The DC reference simulations of one-dimensional spherical flames are performed using the A-SURF code [79, 82], while all flamelet-based simulations are performed using Open∇FOAM® [8, 9]

4.3 Laminar thermo-diffusively unstable hydrogen-air flames

Moving on to more complex flame configurations (see Fig. 1.2), the characteristics of laminar thermo-diffusively unstable hydrogen-air flames are discussed and a suitable flamelet-based model is developed [P4, A1, A2]. In this Section, first, the relevant physical phenomena found in these flames are reviewed. Thereafter, modeling specifics concerning the tabulated manifold are presented and finally, the model performance is evaluated.

4.3.1 Physical phenomena

Thermo-diffusive instabilities arise from the imbalance of mass and heat diffusion in mixtures with low Lewis numbers (e.g., lean hydrogen-air flames) as already discussed based on Fig. 1.1. The strong differential diffusion of hydrogen causes the growth of minor perturbations in the flame front, resulting in highly wrinkled flame fronts which are characterized by a locally increased flame speed and substantial fluctuations in local reaction rates.

Recent studies on laminar reacting flows have explored these instabilities [P4, A1, 4, 30, 31, 98–105], revealing an increase in the overall fuel consumption rate. This can be attributed to both an enlarged flame surface area and increased consumption rates per unit of flame surface area. The gain in flame surface area results from the highly wrinkled flame front which depicts a cellular structure characterized by transitions between positively and negatively curved flame segments. The enhanced consumption rates are observed in positively curved flame segments of the cellular flame front, while negatively curved areas show almost no chemical reactions. Furthermore, thermo-diffusively unstable flames tend to exhibit characteristic cell sizes within their corrugated structure [4]. To investigate such instabilities, the linear stability analysis (LSA) was utilized by determining the so-called dispersion relation from either asymptotic theory [104] or numerical simulations [P4, 4, 101, 102]. The works on LSA exploit the fact that initially, the amplitude of the flame front perturbation increases linearly on a logarithmic scale as a predominant perturbation grows. This characteristic defines the linear regime. Thereafter, a non-linear regime is identified where different perturbations interact, leading to an even more corrugated flame front. While most of these numerical studies focused on perturbed planar flames, these different steps of instability development can also be found in lean hydrogen-air SEFs [P4, A1].

The main characteristics of the propagation regimes are summarized below based on the FRS using DC of a thermo-diffusively unstable SEF used in [P4, A1] and discussed hereafter based on Fig. 4.8. The transient flame front evolution of the thermo-diffusively unstable SEF (H_2-air, $\phi = 0.4$, $p = 1\,\mathrm{atm}$) is shown (left) and the temporal evolution of the mean flame radius $\overline{R}_\mathrm{f}$ of this flame is depicted (right). In addition, the temporal evolution of the flame radius of a one-dimensional SEF, where instabilities are suppressed by the numerical setup, is shown. The respective instantaneous flame fronts and the sections of the temporal evolution are color-coded by the propagation regimes:

- **Stable flame propagation**: Initially, after the ignition a stable flame propagation is observed where no flame front corrugations are visible. During this phase the flame radii of the DC reference simulation and the 1D SEF match since both predict the same flame propagation speed.

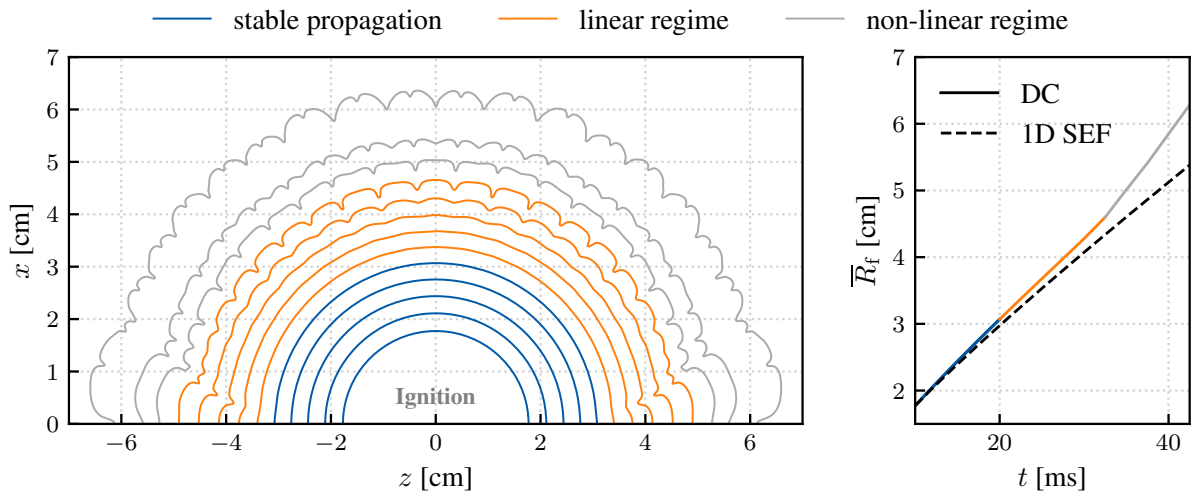

Fig. 4.8: Temporal evolution of the flame front obtained from the FRS of the thermo-diffusively unstable hydrogen-air SEF with $\phi = 0.4$ (left). Temporal evolution of the arithmetic mean flame radius $\overline{R}_\mathrm{f}$ of the SEF including an analogous evolution of the flame radius obtained from a one-dimensional SEF without instabilities (right). The propagation modes concerning instability development are highlighted: stable propagation (blue), linear regime (orange), and non-linear regime (grey). This figure is adapted from [P4, A1].

- **Linear regime**: Here, a predominant perturbation starts to develop which coincides with an increase of flame speed as $\overline{R}_\mathrm{f}$ grows faster in the two-dimensional DC simulation compared to the one-dimensional SEF. This regime is the focus of LSA.
- **Non-linear regime**: Finally, the flame propagates in a non-linear regime which is characterized by the interaction of different corrugations causing a highly wrinkled flame front and a significantly increased flame propagation speed.

The formation of a cellular flame front and the subsequently increased propagation speed indicate pronounced stretch effects in thermo-diffusively unstable flames. Due to the flame's response to positively (negatively) curved flame segments with subsequently strong (weak) reaction rates, cellular flame structures evolve [P4, A1]. The cellular structure also results in a non-uniform flow across the flame front coinciding with strain effects. These thermo-diffusively unstable flame fronts were studied by Wen et al. [A1, A2] in a flamelet-based manner. In these works, the importance of strain and curvature are outlined based on budget analyses and also by extracting one-dimensional flamelets from a thermo-diffusively unstable SEF and comparing these flame structures to CSM calculations with corresponding values for strain K_s and curvature κ_c [A1]. It is found that these flame structures can be described by the CSM even though they exhibit large curvature variations, which is not possible by using simple canonical flame configurations solved in physical space. The increased burning intensities in positively curved flame segments are mainly attributed to curvature-induced diffusion of H_2, and H indicating that these two species are particularly relevant when modeling thermo-diffusively unstable flames. It is emphasized that the sensitivity to curvature-induced diffusion is also reflected in the amount of H radical found in the flame front. Positively curved flame segments depict high amounts of H, while negligible

concentrations are observed for negative flame curvature. Further, the overall differential diffusion effects are even more pronounced at increased pressure [A2].

The findings of Wen et al. [A1, A2] provide an initial assessment of relevant effects to be incorporated in flamelet-based models. This is further elaborated in the next section based on the findings from [P4], where a novel flamelet-based model including curvature effects is developed and the performance of different flamelet-based models in describing the dynamics of thermo-diffusively unstable hydrogen-air flames are discussed in an *a-posteriori* manner.

4.3.2 Manifold generation

It was shown in the previous section that thermo-diffusive instabilities found in lean hydrogen-air flames ($\mathrm{Le} < 1$) cause highly wrinkled flame fronts which propagate with a substantially increased flame speed. These findings imply that curvature variations get increasingly important when modeling these types of flames since the local burning intensity varies within the cellular flame front, which coincides with variations in minor species e.g., the H radical. The study [P4] elaborates further on the assessment of these flames using flamelet-based models. It presents a novel flamelet-based model that takes curvature variations into account (M-κ_c) and compares the model performance of the new M-κ_c model and the M-h model in a thermo-diffusively unstable SEF with $\phi = 0.4$ utilizing the DC reference data from [A1]. Next, the modeling specifics of the novel M-κ_c manifold are introduced.

The basis of the M-κ_c manifold is a parameter variation with varying equivalence ratio ($0.275 \leq \phi \leq 0.6$) and curvature ($-1500\,1/\mathrm{m} \leq \kappa_c \leq 5000\,1/\mathrm{m}$) using the CSM, while the strain is fixed at $K_s = 500\,1/\mathrm{s}$. It is noted that the values for strain and curvature are estimated based on the reference simulation of the thermo-diffusively unstable SEF used in [P4].

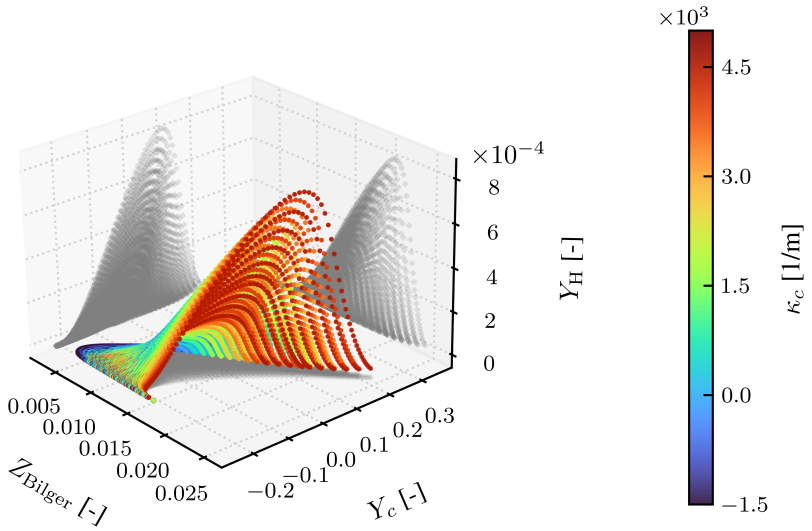

Fig. 4.9: State space obtained by CSM calculations with varying equivalence ratio ϕ and curvature κ_c parameterized by Bilger mixture fraction Z_{Bilger}, progress variable Y_c and H mass fraction Y_{H} color-coded by curvature κ_c.

The thermochemical state of the CSM calculations spanned by Bilger mixture fraction Z_{Bilger}, progress variable Y_c and H radical mass fraction Y_{H} is depicted in Fig. 4.9 and color-coded by the curvature κ_c. Curvature variations cause different local mixture compositions and maximum values of Y_c due to pronounced differential diffusion effects. Further, the H mass fraction Y_{H} shows an increase with curvature, which is also found in thermo-diffusively unstable flame fronts [A1]. High amounts of H radical are found for CSM calculations with positive curvature while almost no H mass fraction is observed for negative curvatures. This indicates a link to the cellular structure of laminar thermo-diffusively unstable flames which exhibit a similar variation of the burning intensity depending on the local flame curvature. It is noted that the H radical mass fraction was already used in previous works to include stretch effects in flamelet-based approaches [A1, 106]. Hence, the H radical is also chosen here to parameterize curvature effects. Subsequently, the M-κ_c manifold is parameterized by $\psi(Z_{\mathrm{Bilger}}, Y_c, Y_{\mathrm{H}})$ and a transport equation for the H radical needs to be solved together with the ones for the major species.

4.3.3 Model validation and evaluation

The improvement that results from capturing curvature effects in the manifold is directly assessed in [P4], by comparing both the previously developed M-h and novel M-κ_c model against a reference simulation of a thermo-diffusively unstable spherical expanding flame (H_2-air, $\phi = 0.4$) using detailed chemistry (DC) [A1]. In addition, linear stability analyses of perturbed planar flames are performed with the respective models. In the following, the main findings are discussed based on the thermo-diffusively unstable spherical expanding flame.

The temporal evolution of the flame front obtained from all three models is shown in Fig. 4.10 together with the evolution of the mean flame radius $\overline{R}_{\mathrm{f}}$. It can be seen from the DC reference simulation that the flame front gets wrinkled due to the evolution of thermo-diffusive instabilities as the flame propagates outwards. This coincides with an increase in the propagation speed as shown by the temporal evolution of the mean radius (bottom right). In general, all simulations depict similar characteristics, but slightly different flame shapes are apparent. The DC simulation exhibits an almost uniform cell size which is expected since laminar thermo-diffusively unstable flames exhibit a characteristic cell size [4]. These cell sizes are also present in the other calculations, however, for the M-h model, a smaller secondary cell size is also present causing a more corrugated flame front. The M-κ_c simulation also exhibits secondary cells which are larger compared to the M-h calculation. The dynamics of the cell formation are highlighted by the temporal evolution of the mean radius (Fig. 4.10 bottom right). Here, the different propagation regimes discussed in Fig. 4.8 are also observed: (I) stable propagation, (II) linear regime, and (III) non-linear regime. The increase in flame propagation due to intrinsic instabilities is confirmed since all simulations show a faster increase in the flame radius compared to the one-dimensional SEF where instabilities are suppressed by the boundary conditions. Overall, the flamelet-based models capture the evolution reasonably well in the linear regime while a faster propagation is observed in regime III, resulting in a deviation of $15\,\%$ for the largest flame radius. A faster flame propagation is expected since the flamelet-based models exhibit more corrugated flame fronts. Still, the agreement is considered remarkable given the complexity of the configuration including differential diffusion, curvature effects and the unsteady evolution of cellular structures. It is noted that the overall impression

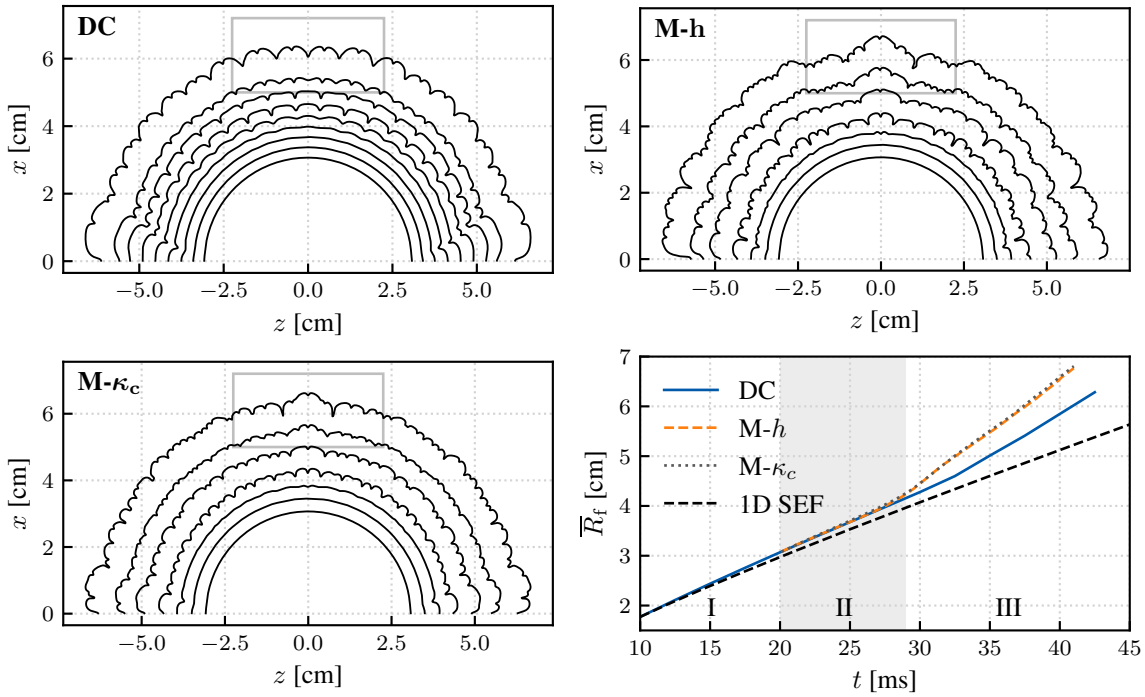

Fig. 4.10: Comparison of flame fronts obtained by different simulation approaches and various time steps for the thermo-diffusively unstable SEF. Further, the temporal evolution of the mean flame radius $\overline{R}_f$ is depicted for the respective calculations (bottom right). Additionally, the regimes of stable propagation (I), linear growth (II), and non-linear growth (III) are highlighted and the DC result of a one-dimensional SEF simulation is shown for reference as no instabilities can evolve due to the spatial confinement (black line) The gray boxes visualize the magnified region which will be investigated in detail in Fig. 4.11. This figure is adapted from [P4].

of the flame dynamics/cell formation is also quantified by a linear stability analysis of perturbed planar flames in [P4].

To elaborate further on the overall flame dynamics and cell formation, variations in the local flame structure are analyzed. In Fig. 4.11, a flame front segment (grey box in Fig. 4.10) is depicted and color-coded by Bilger mixture fraction Z_{Bilger}, temperature T, and OH mass fraction Y_{OH}. Richer (leaner) mixtures are found in regions of positive (negative) curvature, which is expected for lean hydrogen-air flames. While both manifold-based models show similar mixture stratification across the flame, they tend to predict richer mixtures on the burned side of the flame in comparison to the DC calculation. This coincides with a slightly overpredicted temperature. In contrast, leaner mixtures around negatively curved flame segments seem to be less prevalent in flamelet-based simulations. However, the mixture stratification depends on the size of the cellular structures, since smaller cells exhibit higher curvature variations and subsequently amplified differential diffusion effects. Further, the OH radical depicts a correlation with curvature and indicates the local reaction intensity. High (low) amounts of OH are found in positively (negatively) curved flame segments

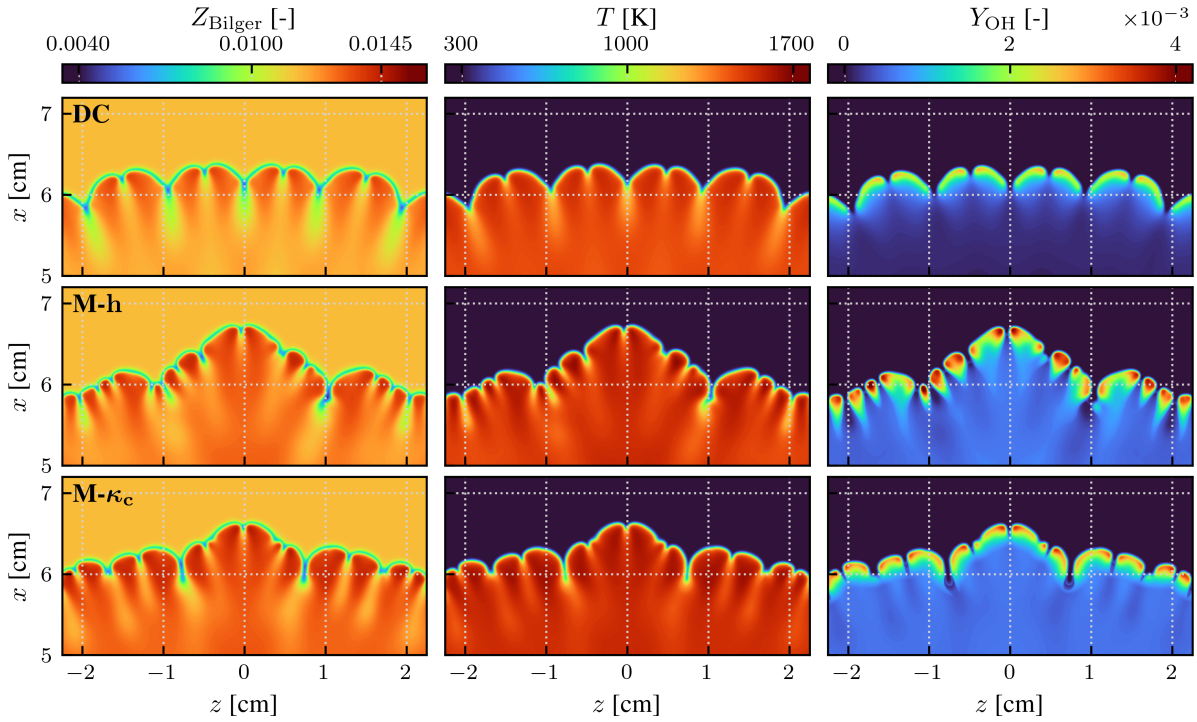

Fig. 4.11: Flame structure comparison for the DC reference, the M-h, and the M-κ_c model at a mean flame radius of $\overline{R}_{\mathrm{f}} \approx 6\,\mathrm{cm}$. The sections of the flame front are color-coded by Bilger mixture fraction Z_{Bilger}, temperature T, and OH mass fraction Y_{OH}. This figure is adapted from [P4].

of the DC reference simulation. The M-h model overpredicts the OH mass fraction and depicts a broader area with substantial amounts of OH. However, the M-κ_c model shows better agreement with the reference data for the OH mass fraction. Both, the area with substantial amounts of OH and the overall trends along the cellular flame front are well recovered. Only areas subject to very high positive curvatures exhibit slightly higher amounts of OH compared to the DC reference. This indicates that the M-κ_c model can describe minor species like OH in the reaction zone of the corrugated flame front.

Based on the discussed results, it is concluded that both models reproduce the global flame characteristics well while the M-κ_c model better predicts the microstructure of the flame. In particular, flame segments with high curvature (both negative and positive) are better described by the M-κ_c model where the characteristics of intermediate species like the OH radical are recovered. This highlights the importance of curvature effects when modeling thermo-diffusively unstable hydrogen-air flames.

4.4 Turbulent thermo-diffusively unstable hydrogen-air flames

Finally, the characteristics of turbulent thermo-diffusively unstable hydrogen-air flames concerning physical phenomena and model development are discussed [P5]. These flames correspond to the most complex configuration of this thesis (see Fig. 1.2). In the following, the relevant physical phenomena found in these flames are analyzed. Thereafter, modeling specifics concerning the tabulated manifold are presented and finally, the model performance is evaluated.

4.4.1 Physical phenomena

Recent numerical studies on FRSs of turbulent lean premixed hydrogen-air flames at various turbulent intensities suggest that thermo-diffusive instabilities persist in turbulent flames and are even amplified through synergistic interactions [5, 107, 108]. Hence, in lean turbulent hydrogen flames, both turbulence and thermo-diffusive instabilities contribute to flame wrinkling. Thereby the local reactivity and the fuel consumption rate are altered, which consequently affects the turbulent flame speed. The enhancing effects of turbulence on thermo-diffusive effects are linked to higher values of strain K_s and curvature κ_c due to turbulent wrinkling and steepened scalar gradients. Thereby, the differential diffusion of hydrogen is promoted resulting in strong mixture inhomogeneities across the flame front and super-adiabatic temperatures in the exhaust gas [5, 109]. The effects of intrinsic instabilities are further enhanced with increasing pressure [6, 107, 110, 111] and diffusion of molecular and atomic hydrogen still exhibit a leading order effect on the fuel consumption rates [107]. The strong effects of molecular diffusion in turbulent hydrogen flames differ significantly from hydrocarbon fuels, where turbulence-induced flame wrinkling solely determines the turbulent flame speed. Therefore, flamelet-based models have yet to be established for (lean) turbulent premixed hydrogen-air flames to enable reliable simulations at reduced computational cost. However, to achieve that physical phenomena such as differential diffusion and the impact of strain and curvature on the flame structure need to be understood in more detail. This gap is addressed in [P5] where an FRS of a lean turbulent premixed hydrogen-air slot flame with $\phi = 0.5$ at ambient conditions is performed and analyzed concerning strain and curvature effects in combination with thermochemical states.

In Fig. 4.12, the computational domain of the turbulent slot flame is visualized together with an instantaneous snapshot of the flame front. The fresh mixture is supplied through a central jet with a jet velocity $u_{\mathrm{Jet}} = 38\,\mathrm{m/s}$ ($\mathrm{Re} = (\mathrm{u_{Jet}\,L})/(\nu) = 10\,000$), which is enclosed by a laminar coflow of burned products ($u_{\mathrm{Coflow}} = 9.5\,\mathrm{m/s}$) and separated from the jet by cold walls. The domain spans across $12\,L$, $12\,L$, $2\,L$ in respective x, y, z directions, with $L = 5\,\mathrm{mm}$ being the width of the central jet. The uniform mesh resolution $\Delta = 30\,\mu\mathrm{m}$ is chosen to adequately resolve both the Kolmogorov length scale and the flame front, resulting in a resolution of 15 cells within the thermal flame thickness. The flame front is colored by its curvature to highlight intense wrinkling and areas of positive and negative curvature. In addition, a color-coding by the H mass fraction Y_{H} can be used as it correlates with curvature (see Sec. 4.3). This indicates the flame response on the local stretch as the H radical mass fraction varies significantly between positively and negatively curved flame segments [P4, A1, 106]. The variation of the H radical further implies a relation between locally

altered consumption rates and the thermochemical states in the turbulent flame. This relation is of utmost importance when aiming for the development of flamelet-based models.

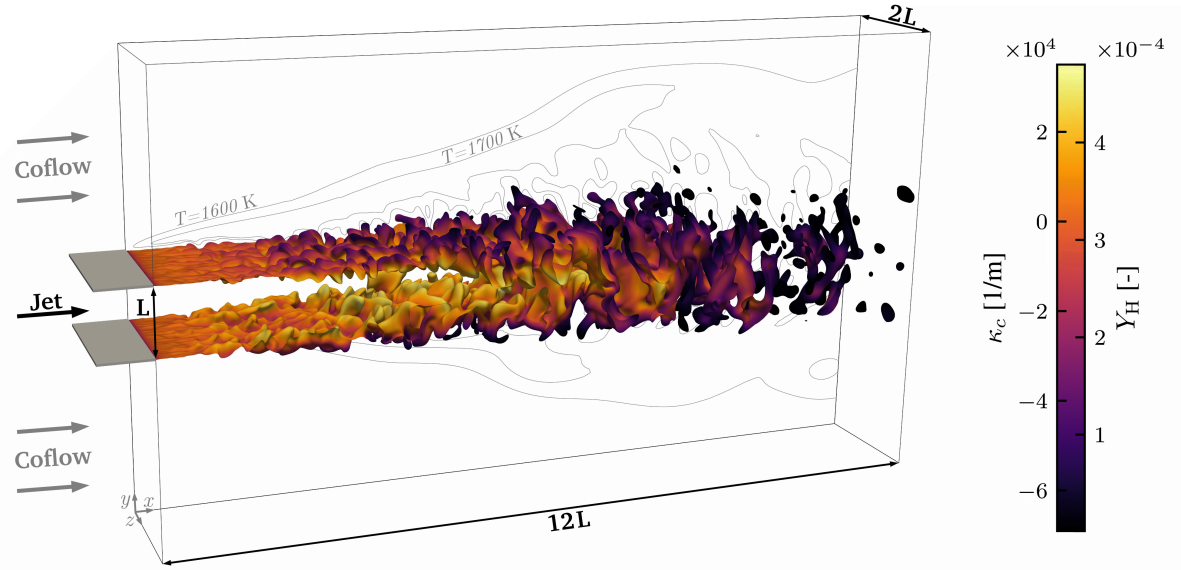

Fig. 4.12: Visualization of the computational domain of the turbulent slot flame (H_2-air, $\phi = 0.5$, $T_0 = 300\,\mathrm{K}$, $p = 1\,\mathrm{atm}$) and an instantaneous snapshot of flame front color-coded by curvature κ_c and H radical mass fraction Y_H. Additionally, temperature iso-lines are depicted in the background. This figure is adapted from [P5].

To elaborate on this, Fig. 4.13 shows the contour of thermochemical states spanned by the enthalpy h and the progress variable Y_c colored by the conditional mean of the Bilger mixture fraction Z_Bilger which can also be interpreted as a local equivalence ratio ϕ_local. These quantities are of particular interest since these are often used as control variables in flamelet-based models (see Sec. 2.4). In addition, CSM simulations with varying strain K_s and constant curvature κ_c are depicted as grey dashed lines in Fig. 4.13 (A) and CSM results with varying curvature but constant strain are shown analogously in Fig. 4.13 (B). The solid black line corresponds to the unstretched planar flame solution. The state space of the turbulent flame scatters broadly concerning the enthalpy and the Bilger mixture fraction along the progress variable. For low progress variable values ($Y_c < -0.07$), the enthalpy h varies significantly with higher mixture fraction values located in the center of the scatter and leaner mixtures (low values of the Bilger mixture fraction) are found towards the respective edges of the scatter (lower and higher enthalpy levels). However, for high values of the progress variable ($Y_c > 0$), the enthalpy scatter broadens even further and significantly lower enthalpy levels are found, depicting substantially higher mixture fraction values. The broadening of the scatter towards the burned side is related to the occurrence of super-equilibrium states, which coincide with increased values for the progress variable and are sensitive to the local flame stretch.

When comparing the scatter of the turbulent flame against the CSM calculations with varying strain or curvature, the predominant influences of strain and curvature become visible. For higher

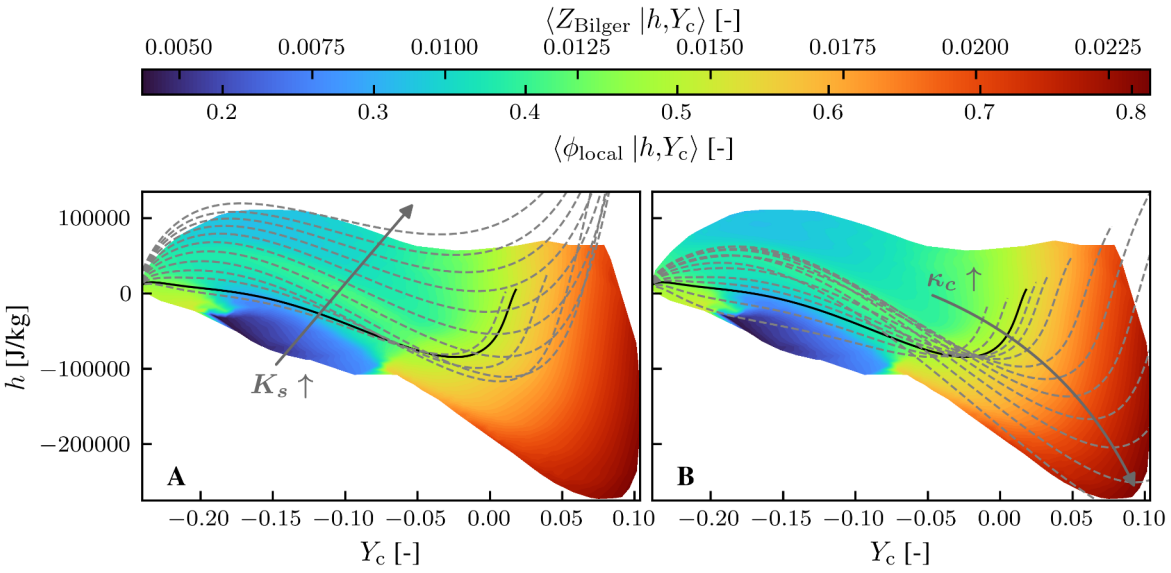

Fig. 4.13: Conditional mean of the Bilger mixture fraction Z_{Bilger} and the local equivalence ratio ϕ_{local} conditioned on the enthalpy h and the progress variable Y_c evaluated from the FRS of the turbulent slot flame. Additionally, CSM solutions with varying strain ($-100\,\mathrm{s}^{-1} \leq K_s \leq 28\,000\,\mathrm{s}^{-1}$; $\kappa_c = 0\,\mathrm{m}^{-1}$) are depicted as dashed grey lines (left) and CSM simulations with varying curvature ($-500\,\mathrm{m}^{-1} \leq \kappa_c \leq 8000\,\mathrm{m}^{-1}$; $K_s = 0\,\mathrm{s}^{-1}$) (right). The solid black line corresponds to the unstretched planar flame solution, respectively. All CSM results follow the global conditions of the turbulent flame ($T = 300\,\mathrm{K}, p = 1\,\mathrm{atm}, \phi = 0.5$). This figure is adapted from [P5].

enthalpy levels, the scatter of the turbulent flame is well captured by CSM simulations with increasing strain. It is highlighted that not only a comparable parameter space is spanned, but also the profiles of the CSM calculations resemble the overall shape of the scatter (Fig. 4.13 A). Similarly, for high values of progress variable and reduced levels of enthalpy, the range and shape of the scatter of the turbulent flame simulation are captured by CSM simulations with varying curvature (Fig. 4.13 B). This indicates that the broadening of the scatter toward the burned side with subsequent super-equilibrium states ($Y_c > 0$) is mainly caused by curvature effects. Only a small part of the scatter where the lowest values of Bilger mixture fraction occur are not directly captured by the CSM results where flame-tangential diffusion might become increasingly important [P4]. It is considered remarkable that the CSM calculations capture major parts of the scatter of the turbulent slot flame even though nominal values for strain and curvature in the FRS significantly exceed the strain-curvature parameter space attainable with the CSM. From a flamelet modeling perspective, it is a favorable outcome that one-dimensional flames and their respective boundary conditions have been identified since this is a prerequisite for generating a flamelet manifold. However, these manifolds get increasingly complex as both strain K_s and curvature κ_c effects need to be considered in flamelet-based models addressing turbulent premixed hydrogen combustion. This challenge has been addressed in [P5] and will be further elaborated in the next section.

4.4.2 Manifold generation

It was shown in the previous section that particularly the synergistic effects between turbulent wrinkling and the wrinkling due to thermo-diffusive instabilities are resulting from both, strain K_s and curvature κ_c effects. Further, it was demonstrated that CSM calculations with varying strain and curvature cover most of the state space of a turbulent lean premixed hydrogen-air slot flame. Building upon the findings from [P3, P4] the subsequently discussed study [P5] extends the flamelet-based modeling approach to better capture the thermochemical states of lean turbulent premixed hydrogen flames. The complexity is increased as the further extended M-(K_s, κ_c) manifold takes both strain and curvature variations into account. In the following, the characteristics of the M-(K_s, κ_c) manifold are highlighted.

The M-(K_s, κ_c) manifold grounds on a parameter variation with varying equivalence ratio ($0.275 \leq \phi \leq 0.85$), varying strain ($-400\,1/\mathrm{s} \leq K_s \leq 30\,000\,1/\mathrm{s}$) and varying curvature ($-2500\,1/\mathrm{m} \leq \kappa_c \leq 8000\,1/\mathrm{m}$) using the CSM. It is noted that this manifold is generated as an artificial neural network, to reduce the overall memory footprint of such high dimensional manifolds including differential diffusion effects[7].

Since it is increasingly challenging to find suitable parametrizations of high dimensional manifolds taking differential diffusion and stretch effects into account, an optimal estimator assessment is performed to identify a suitable manifold parameterization [5, 113]. In an optimal estimator assessment, a set of parameters ξ is used to parameterize a specific quantity (e.g., the progress variable source term $\dot{\omega}_c$) and is determined by an error norm known as irreducible error[8]. Further, this error is quantified by the quadratic error norm of the scatter of the progress variable source term $\dot{\omega}_c$ relative to the conditional mean $\langle \dot{\omega}_c | \xi \rangle$. Subsequently, this error is normalized by the maximum obtained from a respective unstretched FP flame [5]:

$$\epsilon^{\mathrm{norm}}_{\mathrm{irr},\dot{\omega}_c} = \frac{\langle (\dot{\omega}_c - \langle \dot{\omega}_c | \xi \rangle)^2 | Y_c \rangle}{\max\left(\dot{\omega}_c^{\mathrm{FP}}\right)^2} \,. \tag{4.2}$$

Thereby, low values for the normalized irreducible error $\epsilon^{\mathrm{norm}}_{\mathrm{irr},\dot{\omega}_c}$ indicate a suitable parameterization of the thermochemical states by the respective parameter set ξ. In Fig. 4.14, the irreducible error is shown for different combinations of parameters along the progress variable Y_c. The largest errors occur when parameterizing only by the progress variable. These errors are reduced when adding the Bilger mixture fraction Z_{Bilger} to the set of parameters. Including strain K_s, curvature κ_c, or both in the parameterization does not result in a significant error reduction. This is attributed to the fact that strain and curvature are highly instantaneous quantities that are closely linked to the flame's topology. However, they do not account for the temporal evolution of the thermochemical state [114]. Zirwes et al. [115, 116] found a phase shift between stretch effects and the subsequent flame response, which depends on the local flow time scale. They attributed this to memory effects in the local flame dynamics indicating that strain and curvature are not necessarily suitable

[7] A review of data-driven models in combustion research can be found in [112].

[8] The progress variable source term $\dot{\omega}_c$ is used in this study since it represents an important characteristic quantity that needs to be predicted by manifold-based models. In Addition, properly capturing the source term in the manifold poses usually one of the biggest challenges in flamelet-based modeling.

control variables for the manifold parameterization. As discussed in Sec. 4.3.2 and previous works [A1, 106], stretch effects can be represented in flamelet-based models using the H radical mass fraction Y_{H}. Further, to distinguish between strain and curvature effects the enthalpy h can be used as already indicated by Fig. 4.13, since CSM calculations with varying strain or curvature cover different parts of the state space of the turbulent slot flame. Adding Y_{H} or h to the parameter set ξ results in an additional error reduction. But the lowest irreducible error and, hence, the most suitable parameterization is obtained when using $\xi = [Y_c, Z_{\mathrm{Bilger}}, Y_{\mathrm{H}}, h]$.

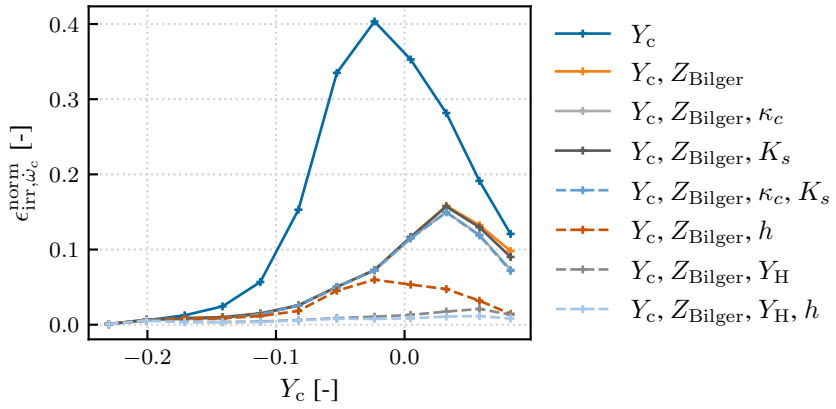

Fig. 4.14: Irreducible errors of the progress variable source term $\dot{\omega}_c$ for different sets of parameters evaluated from the FRS of the turbulent slot flame. This figure is adapted from [P5].

Finally, the novel M-(K_s, κ_c) manifold is parameterized by Y_{H2}, Y_{O2}, Y_{H2O}, Y_{H}, and enthalpy h. It is noted that the major species are used directly as control variables since data-driven approaches are more flexible concerning their dimensionality.

4.4.3 Model validation

In the study [P5], the model predictions of the M-h, M-κ_c and M-(K_s, κ_c) models are compared against an FRS using DC of a lean turbulent premixed hydrogen-air slot flame ($\phi = 0.5$, $T_{\mathrm{u}} = 300\,\mathrm{K}$, $p = 1\,\mathrm{atm}$, $\mathrm{Re} = 1000$, see Fig. 4.12) in an *a-priori* manner. The main findings of this model comparison are discussed next.

In Fig. 4.15, a snapshot of the temperature T, the OH mass fractions Y_{OH} and the hydrogen source term $\dot{\omega}_{\mathrm{H2}}$ fields of the turbulent flame are shown along a slice perpendicular to the z-axis at $z = 0\,\mathrm{mm}$ (top row). Further, the relative deviations ϵ_{rel} of all manifold predictions are depicted for the respective fields (bottom panel). The turbulent flame front is highly curved and various pockets containing unburnt mixture are observed, which are detached from the main flame front and can be found for $x > 30\,\mathrm{mm}$. Maximum temperatures higher than the equilibrium temperature of an unstretched flame occur near the flame front, indicating super-equilibrium states caused by the interplay of differential diffusion and flame stretch. Further, this region is intersected by areas of lower temperatures as a consequence of turbulent fluctuations. Besides the impact of local temperature fluctuations, the amount of the OH mass fraction also depends significantly

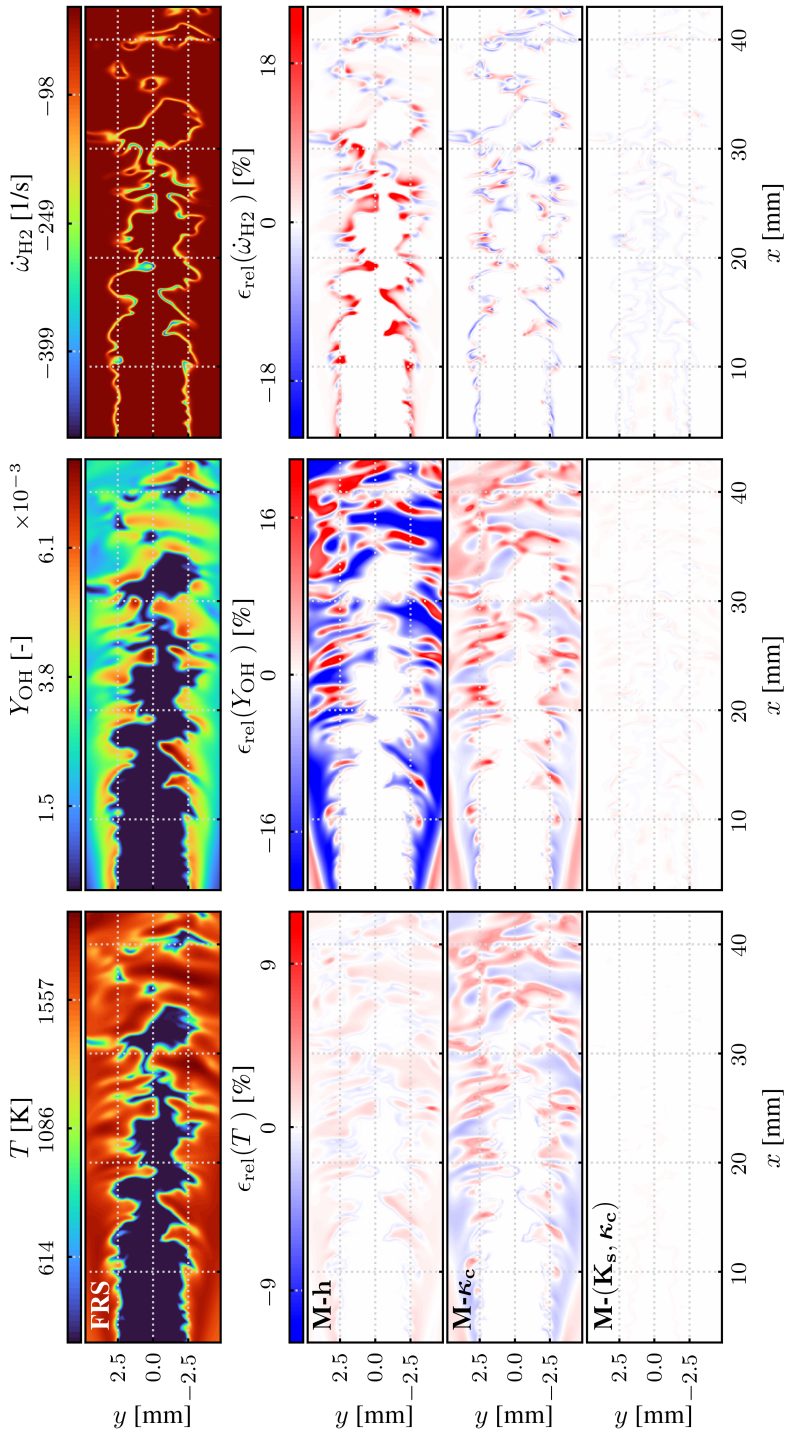

Fig. 4.15: *A-priori* comparison of the manifolds against the FRS for an instantaneous snapshot. The temperature T, the mass fractions of OH and the H_2 source term fields of the reference data are shown along a slice perpendicular to the z-axis at $z = 0\,\mathrm{mm}$ (top row). The manifold predictions are depicted as relative deviations ($\epsilon_{\mathrm{rel}}(\varphi) = (\varphi_{\mathrm{FRS}} - \varphi_{\mathrm{M}})/\max(\varphi_{\mathrm{FRS}})$) for the respective fields. This figure is adapted from [P5].

on curvature. In areas convexly shaped towards the burned side (positive curvature), increased amounts of OH are found, highlighting the increased burning rates due to the Lewis number effect. The hydrogen source term $\dot{\omega}_{\mathrm{H2}}$ exhibits similar characteristics in comparison to the OH mass fraction as its variation indicates the locally altered burning rate of the flame. The highest source terms are found in flame segments with positive curvature. This corresponds to negative values as H_2 gets consumed. Negatively curved flame segments depict lower source terms. These characteristics highlight the relevance of differential diffusion effects in this flame configuration and indicate the interplay of turbulent wrinkling and thermo-diffusive instabilities. The M-h manifold exhibits reasonable agreement with the reference data for the temperature field T, showing the highest deviations around the detached pockets of the unburned mixture. However, it depicts high deviations for the OH mass fraction and the relative errors are beyond $50\,\%$ for the H_2 source term. This indicates that the tabulation approaches based on unstretched flames cannot predict the radical species and source terms in this flame configuration. The prediction of the M-κ_c manifold shows deviations in the temperature field up to $10\,\%$. In particular, the temperatures close to the burned side exhibit larger deviations but it shows better agreement for the OH mass fraction. The highest deviations (up to $\approx 20\,\%$) are located close to negatively curved flame segments. Similar statements can be made for the hydrogen source term $\dot{\omega}_{\mathrm{H2}}$. Only the prediction of the M-(K_s, κ_c) manifold, taking both strain and curvature effects into account, results in negligible errors for all quantities.

Based on this error estimation for the different manifolds and the more detailed assessment provided in [P5], it is concluded that flamelet manifolds based on unstretched planar flames cannot predict the thermochemical states of the lean turbulent premixed hydrogen-air slot flame. Including only curvature effects in the manifold (M-κ_c) improves the predictions for minor species and source terms but also does not capture all relevant physics. Only if both positive and negative values for strain and curvature are considered in the manifold generation (M-(K_s, κ_c)) good agreement with the reference data is achieved. This highlights the benefits of the CSM concerning the assessment of strain and curvature effects since such flames cannot be approximated by canonical flame configurations solved in physical space. A final assessment requires an *a-posteriori* model evaluation based on fully coupled simulations which is the subject of future works. Additionally, when aiming for applications in the context of large eddy simulations, suitable sub-grid models for turbulent hydrogen combustion are of key importance.

5 Conclusion and outlook

In this thesis, fundamental phenomena of premixed hydrogen combustion are elucidated, focusing particularly on differential diffusion and stretch effects. The initial objective of this thesis is the analysis of strain and curvature effects in lean and rich hydrogen-air flames (**O1**). Thereafter, novel flamelet-based modeling approaches are developed and applied to different flame configurations. In particular, a flamelet-based model is developed that captures differential diffusion, forced ignition, and early flame propagation in lean and rich hydrogen-air mixtures (**O2**). This modeling approach is subsequently extended to better capture the characteristics of thermo-diffusively unstable hydrogen-air flames (**O3**). Following insights related to the scientific objectives of this thesis (see Fig. 1.2) are gained:

O1 Analysis of strain and curvature effects:
The response of global flame properties, flame structures and reaction pathways are systematically analyzed concerning strain and curvature effects. Publication [P1] is the first study analyzing arbitrary combinations of strain K_s and curvature κ_c in one-dimensional premixed flames by utilizing a recently developed composition space model (CSM), which enables a larger (K_s, κ_c)-parameter space compared to canonical flame configurations. Significant changes in flame speed and maximum temperature are found throughout the (K_s, κ_c)-parameter space. The overall trends are consistent with the Lewis number effect as lean hydrogen-air flames ($\mathrm{Le} < 1$) are strengthened by positive flame stretch and weakened by negative stretch while vice versa trends are observed for rich hydrogen-air flames ($\mathrm{Le} > 1$). Additionally, the different effects of strain and curvature variations concerning the flame structure are outlined (e.g., shifts in heat release profiles). These findings are further complemented by the assessment of reaction pathways in the (K_s, κ_c)-parameter space in [P2] depicting a strong sensitivity to stretch resulting from curvature.

O2 Model development and evaluation of igniting H_2 flames:
A flamelet-based model that accurately describes the ignition and flame propagation in lean and rich hydrogen-air flames is developed. This includes a flamelet manifold (M-h) that is generated using the CSM and includes both unstretched flame characteristics and igniting solutions in the limit of homogeneous reactor simulations. Further, a coupling strategy has been derived where major species and enthalpy are transported while the control variables of the manifold (Z_{Bilger}, Y_c) are reconstructed based on the transported scalars. Thereby, differential diffusion effects can be accurately described using a mixture-averaged diffusion approach. The performance of the model has been validated in *a-posteriori* analyses of different igniting canonical flame configurations (cylindrical expanding flames, spherical expanding flames and counterflow flames), including a broad variation of equivalence ratios

($0.7 \leq \phi \leq 1.4$) and subsequently mixtures with small and large Lewis numbers [P3]. The novel model shows good agreement for the flame structure, the flame propagation speed and the minimum ignition energy for various canonical configurations. Thereby, it is concluded that the model can partly account for flame stretch in the investigated flame configurations even though unstretched flames are tabulated in the manifold.

O3 Model development and evaluation of thermo-diffusively unstable H_2 flames:
The flamelet-based model is extended to better capture laminar and turbulent thermo-diffusively hydrogen flames. In [P4], the predictions of the previously developed M-h model and a novel flamelet manifold (M-κ_c) generated based on CSM calculations with large curvature variation (positive and negative) are compared to a DC reference simulation of a laminar thermo-diffusively unstable SEF taken from [A1]. The performance of the two flamelet manifolds is critically assessed in both *a-priori* and *a-posteriori* manner, showing that both models capture the global flame characteristics well, while the extended model accounting for curvature effects (M-κ_c) leads to an improved prediction of the local flame structure.

Finally, the performance of the flamelet-based models is assessed for a lean turbulent hydrogen-air slot flame which exhibits synergistic effects between turbulence and intrinsic instabilities [P5]. The model performance of the previously developed manifolds (M-h and M-κ_c) are evaluated in an *a-priori* manner together with a novel manifold (M-(K_s, κ_c)), taking both strain and curvature variations into account. The study reveals that the M-h and M-κ_c manifolds fall short in describing the thermochemical states of the turbulent slot flame. Only the extended M-(K_s, κ_c) model including both strain and curvature variation captures all physical phenomena found in the fully resolved reference simulation resulting in negligible modeling errors.

The systematic approach of consistently increasing the complexity of flame configurations and model capabilities has led to a novel flamelet-based model that captures the characteristics of a broad variety of premixed hydrogen-air flames. These results represent significant advancements concerning flamelet-based models for premixed hydrogen-air flames that accurately predict differential diffusion effects. Additionally, the benefits of the CSM for manifold generation concerning the modeling of forced ignition and stretch effects are outlined.

Future works should address practical combustors and hence, even more complex flame configurations. Therefore, flamelet-coupled CFD of lean turbulent (partially) premixed hydrogen-air flames should be performed and analyzed in an *a-posteriori* manner. This requires suitable sub-grid models when aiming for model applications in the context of large eddy simulations which must recover the effects of differential diffusion, flame stretch and intrinsic instabilities. Additionally, combining the models developed for forced ignition and turbulent hydrogen combustion is desirable and could potentially elucidate the phenomena leading to turbulent facilitated ignition, which are not yet fully understood. Moreover, incorporating $\mathrm{NO_x}$ chemistry into the novel modeling approach to predict pollutant formation would be a valuable contribution to the field. Furthermore, transferring the modeling approach to other research areas, such as flame-wall interaction, dual fuel systems, or combustors with effusion cooling is of great technical and scientific interest. However, this poses additional challenges for modeling hydrogen combustion.

Acknowledgements

This work would not have been possible without the support of many people. I would like to express my gratitude to:

Christian Hasse, for supervising my doctoral thesis and the numerous discussions that significantly contributed to my progress during my time as a doctoral candidate and his guidance, especially in the tough times,

Zheng Chen, for being the second examiner of my doctoral thesis, the warm welcome in his group at Peking University and the fruitful collaboration throughout the last years even though personal meetings were scarce due to the COVID-19 pandemic. I thoroughly enjoyed my research stay in Beijing,

All my coauthors of the publications leading to this thesis, for all the formal and informal discussions,

My colleagues at STFS, for the development of a shared code base and many memorable moments in and outside the office. Here, I want to express my special thanks to:

> Our IT admins, particularly Driss Kaddar for his fast replies and always granting additional quota when needed,
>
> Sebastian Popp, Sandro Gierth and Hendrik Nicolai for sharing their experience on flamelet-based models and many informal discussions solving rather technical issues,
>
> Philip Haspel, for the warm and humorous atmosphere in the office especially during my first months in Darmstadt,
>
> My dearest colleagues and friends, Matthias Steinhausen and Magnus Kircher. You made my time in Darmstadt enjoyable! This includes our open collaboration, the multiple barbecues, the memes shared and the rounds of cards played with Vinzenz Schuh in versatile pubs and local breweries. *“Our friendship is like a perfect cup of coffee — stimulating, uplifting, and sometimes a little too hot to handle” (Unknown)*.

Abschließend möchte ich meiner Familie, meinen Freunden und insbesondere Andrea meinen Dank aussprechen. Ihr habt mich stets tatkräftig unterstützt und mir ein Umfeld geschaffen, aus dem ich immer wieder neue Motivation ziehen und in dem ich auch mal Abstand von wissenschaftlichen Problemstellungen gewinnen konnte!

Bibliography

Publications included in this dissertation

[P1] **H. Böttler**, A. Scholtissek, X. Chen, Z. Chen, and C. Hasse. Premixed flames for arbitrary combinations of strain and curvature. In: Proc. Combust. Inst. 38 (2021), 2031–2039. DOI: 10.1016/j.proci.2020.06.312.

[P2] X. Chen, **H. Böttler**, A. Scholtissek, C. Hasse, and Z. Chen. Effects of stretch-chemistry interaction on chemical pathways for strained and curved hydrogen/air premixed flames. In: Combust. Flame 232 (2021), 111532. DOI: 10.1016/j.combustflame.2021.111532.

[P3] **H. Böttler**, X. Chen, S. Xie, A. Scholtissek, Z. Chen, and C. Hasse. Flamelet modeling of forced ignition and flame propagation in hydrogen-air mixtures. In: Combust. Flame 243 (2022), 112125. DOI: 10.1016/j.combustflame.2022.112125.

[P4] **H. Böttler**, H. Lulic, M. Steinhausen, X. Wen, C. Hasse, and A. Scholtissek. Flamelet modeling of thermo-diffusively unstable hydrogen-air flames. In: Proc. Combust. Inst. 39 (2023), 1567–1576. DOI: 10.1016/j.proci.2022.07.159.

[P5] **H. Böttler**, D. Kaddar, T. J. P. Karpowski, F. Ferraro, A. Scholtissek, H. Nicolai, and C. Hasse. Can flamelet manifolds capture the interactions of thermo-diffusive instabilities and turbulence in lean hydrogen flames?—An a-priori analysis. In: Int. J. Hydrogen Energy 56 (2024), 1397–1407. DOI: 10.1016/j.ijhydene.2023.12.193.

Additional publications as co-author

[A1] X. Wen, T. Zirwes, A. Scholtissek, **H. Böttler**, F. Zhang, H. Bockhorn, and C. Hasse. Flame structure analysis and composition space modeling of thermodiffusively unstable premixed hydrogen flames — Part I: Atmospheric pressure. In: Combust. Flame (2021), 111815. DOI: 10.1016/j.combustflame.2021.111815.

[A2] X. Wen, T. Zirwes, A. Scholtissek, **H. Böttler**, F. Zhang, H. Bockhorn, and C. Hasse. Flame structure analysis and composition space modeling of thermodiffusively unstable premixed hydrogen flames — Part II: Elevated pressure. In: Combust. Flame (2021), 111808. DOI: 10.1016/j.combustflame.2021.111808.

[A3] S. Xie, X. Chen, **H. Böttler**, A. Scholtissek, C. Hasse, and Z. Chen. Forced Ignition of a Rich Hydrogen/Air Mixture in a Laminar Counterflow: A Computational Study. In: Flow Turbul. Combust. 110 (2023), 441–456. DOI: 10.1007/s10494-022-00374-2.

[A4] M. Bolla, M. Papp, C. Olm, **H. Böttler**, T. Nagy, I. G. Zsély, and T. Turányi. Comparison and Analysis of Butanol Combustion Mechanisms. In: Energy & Fuels 36 (2022), 11154–11176. DOI: 10.1021/acs.energyfuels.2c01529.

[A5] X. Chen, S. Xie, **H. Böttler**, A. Scholtissek, W. Han, D. Yu, C. Hasse, and Z. Chen. Effects of electrodes and imposed flow on forced ignition in laminar premixed hydrogen/air mixtures with large Lewis number. In: Proc. Combust. Inst. 39 (2023), 1967–1976. DOI: 10.1016/j.proci.2022.07.217.

[A6] Y. Luo, F. Ferraro, A. Breicher, **H. Böttler**, A. Dreizler, D. Geyer, C. Hasse, and A. Scholtissek. A novel flamelet manifold parametrization approach for lean CH4–H2-air flames. In: Int. J. Hydrogen Energy 48 (2023), 407–421. DOI: 10.1016/j.ijhydene.2022.09.233.

[A7] X. Chen, **H. Böttler**, S. Xie, A. Scholtissek, W. Han, C. Hasse, and Z. Chen. On the flow-facilitated ignition in a mixture with low Lewis number. In: Combust. Flame 258 (2023), 113091. DOI: 10.1016/j.combustflame.2023.113091.

[A8] Y. Wang, S. Xie, **H. Böttler**, Y. Wang, X. Chen, A. Scholtissek, C. Hasse, and Z. Chen. Forced ignition of premixed cool and hot DME/air flames in a laminar counterflow. In: Combust. Flame 259 (2024), 113169. DOI: 10.1016/j.combustflame.2023.113169.

Other references

[1] K. Kohse-Höinghaus. Combustion in the future: The importance of chemistry. In: Proc. Combust. Inst. 38 (2021), 1–56. DOI: 10.1016/j.proci.2020.06.375.

[2] H. Kobayashi, A. Hayakawa, K. K. A. Somarathne, and E. C. Okafor. Science and technology of ammonia combustion. In: Proc. Combust. Inst. 37 (2019), 109–133. DOI: 10.1016/j.proci.2018.09.029.

[3] M. Ciniviz and H. Köse. Hydrogen use in internal combustion engine: A review. In: IJAET 1 (2012), 1–15.

[4] L. Berger, K. Kleinheinz, A. Attili, and H. Pitsch. Characteristic patterns of thermodiffusively unstable premixed lean hydrogen flames. In: Proc. Combust. Inst. 37 (2019), 1879–1886. DOI: 10.1016/j.proci.2018.06.072.

[5] L. Berger, A. Attili, and H. Pitsch. Synergistic interactions of thermodiffusive instabilities and turbulence in lean hydrogen flames. In: Combust. Flame 244 (2022), 112254. DOI: 10.1016/j.combustflame.2022.112254.

[6] T. Howarth, E. Hunt, and A. Aspden. Thermodiffusively-unstable lean premixed hydrogen flames: Phenomenology, empirical modelling, and thermal leading points. In: Combust. Flame 253 (2023), 112811. DOI: 10.1016/j.combustflame.2023.112811.

[7] P. Domingo and L. Vervisch. Recent developments in DNS of turbulent combustion. In: Proc. Combust. Inst. 39 (2023), 2055–2076. DOI: 10.1016/j.proci.2022.06.030.

[8] H. G. Weller, G. Tabor, H. Jasak, and C. Fureby. A tensorial approach to computational continuum mechanics using object orientated techniques. In: Comput. phys. 12 (1998), 620–631.

[9] I. Morev, B. Tekgül, M. Gadalla, A. Shahanaghi, J. Kannan, S. Karimkashi, O. Kaario, and V. Vuorinen. Fast reactive flow simulations using analytical Jacobian and dynamic load balancing in OpenFOAM. In: Phys. Fluids 34 (2022), 021801. DOI: 10.1063/5.0077437.

[10] T. Zirwes, M. Sontheimer, F. Zhang, A. Abdelsamie, F. E. H. Pérez, O. T. Stein, H. G. Im, A. Kronenburg, and H. Bockhorn. Assessment of Numerical Accuracy and Parallel Performance of OpenFOAM and its Reacting Flow Extension EBIdnsFoam. In: Flow Turbul. Combust. 111 (2023), 567–602. DOI: 10.1007/s10494-023-00449-8.

[11] N. Peters. Laminar Flamelet Concepts in Turbulent Combustion. In: Symp. (Int.) Combust. 21 (1988), 1231–1250. DOI: 10.1016/S0082-0784(88)80355-2.

[12] J. A. van Oijen, A. Donini, R. J. M. Bastiaans, J. H. M. ten Thije Boonkkamp, and L. P. H. de Goey. State-of-the-art in premixed combustion modeling using flamelet generated manifolds. In: Prog. Energy Combust. Sci. 57 (2016), 30–74. DOI: 10.1016/j.pecs.2016.07.001.

[13] B. Fiorina, D. Veynante, and S. Candel. Modeling Combustion Chemistry in Large Eddy Simulation of Turbulent Flames. English. In: Flow Turbul. Combust. 94 (2015), 3–42. DOI: 10.1007/s10494-014-9579-8.

[14] S. Popp, S. Hartl, D. Butz, D. Geyer, A. Dreizler, L. Vervisch, and C. Hasse. Assessing multi-regime combustion in a novel burner configuration with large eddy simulations using tabulated chemistry. In: Proc. Combust. Inst. 38 (2021), 2551–2558. DOI: 10.1016/j.proci.2020.06.098.

[15] H. Nicolai, L. Dressler, J. Janicka, and C. Hasse. Assessing the importance of differential diffusion in stratified hydrogen–methane flames using extended flamelet tabulation approaches. In: Phys. Fluids 34 (2022), 085118. DOI: 10.1063/5.0102675.

[16] M. Steinhausen, T. Zirwes, F. Ferraro, A. Scholtissek, H. Bockhorn, and C. Hasse. Flame-Vortex Interaction during Turbulent Side-Wall Quenching and Its Implications for Flamelet Manifolds. In: Proc. Combust. Inst. 39 (2023), 2149–2158. DOI: 10.1016/j.proci.2022.09.026.

[17] M. Kircher, S. Popp, S. Gierth, A. Pati, J. Schneider, M. Günther, and C. Hasse. Investigation of Engine Combustion and Auto-ignition of a Multicomponent Surrogate Fuel with NTC Behavior Under Knocking Conditions. In: Flow Turbul. Combust. 110 (2023), 149–169. DOI: 10.1007/s10494-022-00351-9.

[18] T. Tang, J. Yu, Z. Wang, D. Yang, M. Sun, H. Wang, G. Zhao, and Y. Yang. An improved flamelet/progress variable modeling in a hydrogen-fueled scramjet. In: Int. J. Hydrogen Energy (2023). DOI: 10.1016/j.ijhydene.2023.06.313.

[19] F. Vance, L. de Goey, and J. van Oijen. Prediction of flashback limits for laminar premixed hydrogen-air flames using flamelet generated manifolds. In: Int. J. Hydrogen Energy 48 (2023), 27001–27012. DOI: 10.1016/j.ijhydene.2023.03.262.

[20] F. Almutairi, K. R. Dinesh, and J. van Oijen. Modelling of hydrogen-blended dual-fuel combustion using flamelet-generated manifold and preferential diffusion effects. In: Int. J. Hydrogen Energy 48 (2023), 1602–1624. DOI: 10.1016/j.ijhydene.2022.10.078.

[21] C. K. Law. *Combustion Physics*. Cambridge University Press (CUP), 2006. DOI: 10.1017/cbo9780511754517.

[22] M. Matalon, C. Cui, and J. K. Bechtold. Hydrodynamic theory of premixed flames: effects of stoichiometry, variable transport coefficients and arbitrary reaction orders. In: J. Fluid Mech. 487 (2003), 179–210. DOI: 10.1017/S0022112003004683.

[23] F. A. Williams. A review of some theoretical considerations of turbulent flame structure. In: AGARD Conference Proceeding, 1975 (1975).

[24] S. Chung and C. Law. An invariant derivation of flame stretch. In: Combust. Flame 55 (1984), 123–125. DOI: 10.1016/0010-2180(84)90156-1.

[25] F. Williams. *Combustion Theory: The Fundamental Theory of Chemically Reacting Flow Systems*. Perseus Books, 1985. DOI: 10.1201/9780429494055.

[26] C. Law and C.-J. Sung. Structure, aerodynamics, and geometry of premixed flamelets. In: Prog. Energy Combust. 26 (2000), 459–505. DOI: 10.1016/S0360-1285(00)00018-6.

[27] G. R. A. Groot, J. A. van Oijen, L. P. H. de Goey, K. Seshadri, and N. Peters. The effects of strain and curvature on the mass burning rate of premixed laminar flames. In: Combust. Theor. Model. 6 (2002), 675–695. DOI: 10.1088/1364-7830/6/4/307.

[28] H. Wang, E. R. Hawkes, J. H. Chen, B. Zhou, Z. Li, and M. Aldén. Direct numerical simulations of a high Karlovitz number laboratory premixed jet flame – an analysis of flame stretch and flame thickening. In: J. Fluid Mech. 815 (2017), 511–536. DOI: 10.1017/jfm.2017.53.

[29] K. Aung, M. Hassan, and G. Faeth. Flame stretch interactions of laminar premixed hydrogen/air flames at normal temperature and pressure. In: Combust. Flame 109 (1997), 1–24. DOI: 10.1016/S0010-2180(96)00151-4.

[30] T. Howarth and A. Aspden. An empirical characteristic scaling model for freely-propagating lean premixed hydrogen flames. In: Combust. Flame 237 (2022), 111805. DOI: 10.1016/j.combustflame.2021.111805.

[31] D. Fernández-Galisteo, V. N. Kurdyumov, and P. D. Ronney. Analysis of premixed flame propagation between two closely-spaced parallel plates. In: Combust. Flame 190 (2018), 133–145. DOI: 10.1016/j.combustflame.2017.11.022.

[32] T. Poinsot and D. Veynante. *Theoretical and Numerical Combustion*. 3rd ed. Cerfacs, 2012.

[33] R. J. Kee, M. E. Coltrin, P. Glarborg, and H. Zhu. *Chemically Reacting Flow - Theory, Modeling, and Simulation*. 2nd ed. John Wiley & Sons, Inc, 2018.

[34] C. F. Curtiss and J. O. Hirschfelder. Transport Properties of Multicomponent Gas Mixtures. In: Chem. Phys. 17 (1949), 550–555. DOI: 10.1063/1.1747319.

[35] A. Ern and V. Giovangigli. *Multicomponent Transport Algorithms*. Springer Berlin Heidelberg, 1994. DOI: 10.1007/978-3-540-48650-3.

[36] D. G. Goodwin, R. L. Speth, H. K. nd Moffat, and B. L. Weber. *Cantera: An Object-oriented Software Toolkit for Chemical Kinetics, Thermodynamics, and Transport Processes*. 2021. DOI: 10.5281/zenodo.6387882.

[37] M. Matalon. On Flame Stretch. In: Combust. Sci. Technol. 31 (1983), 169–181. DOI: 10.1080/00102208308923638.

[38] R. J. Kee and J. A. Miller. Computational modeling of flame structure. In: Physica D 12 (1984). DOI: 10.1016/0167-2789(84)90524-4.

[39] R. J. Kee, J. A. Miller, G. H. Evans, and G. Dixon-Lewis. A computational model of the structure and extinction of strained, opposed flow, premixed methane-air flames. In: Symp. (Int.) Combust. 22 (1989). DOI: 10.1016/S0082-0784(89)80158-4.

[40] D. Bradley, P. H. Gaskell, and X. J. Gu. Burning velocities, markstein lengths, and flame quenching for spherical methane-air flames: A computational study. In: Combust. Flame 104 (1996), 176–198. DOI: 10.1016/0010-2180(95)00115-8.

[41] Z. Chen, X. Gou, and Y. Ju. Studies on the Outwardly and Inwardly Propagating Spherical Flames with Radiative Loss. In: Combust. Sci. Technol. 182 (2010), 124–142. DOI: 10.1080/00102200903299850.

[42] S. Balusamy, A. Cessou, and B. Lecordier. Direct measurement of local instantaneous laminar burning velocity by a new PIV algorithm. In: Exp. Fluids 50 (2011), 1109–1121. DOI: 10.1007/s00348-010-1027-5.

[43] G. Fru, G. Janiga, and D. Thévenin. Impact of Volume Viscosity on the Structure of Turbulent Premixed Flames in the Thin Reaction Zone Regime. In: Flow Turbul. Combust. 88 (2012), 451–478451–478. DOI: 10.1007/s10494-011-9360-1.

[44] A. Amato, M. Day, R. K. Cheng, J. Bell, D. Dasgupta, and T. Lieuwen. Topology and burning rates of turbulent, lean, H_2/air flames. In: Combust. Flame 162 (2015), 4553–4565. DOI: 10.1016/j.combustflame.2015.09.010.

[45] A. Scholtissek, P. Domingo, L. Vervisch, and C. Hasse. A self-contained progress variable space solution method for thermochemical variables and flame speed in freely-propagating premixed flamelets. In: Proc. Combust. Inst. 37 (2019), 1529–1536. DOI: 10.1016/j.proci.2018.06.168.

[46] A. Scholtissek, P. Domingo, L. Vervisch, and C. Hasse. A self-contained composition space solution method for strained and curved premixed flamelets. In: Combust. Flame 207 (2019), 342–355. DOI: 10.1016/j.combustflame.2019.06.010.

[47] G. K. Giannakopoulos, A. Gatzoulis, C. E. Frouzakis, M. Matalon, and A. G. Tomboulides. Consistent definitions of “Flame Displacement Speed” and “Markstein Length” for premixed flame propagation. In: Combust. Flame 162 (2015), 1249–1264. DOI: 10.1016/j.combustflame.2014.10.015.

[48] C. D. Pierce and P. Moin. Progress-variable approach for large-eddy simulation of non-premixed turbulent combustion. In: J. Fluid Mech. 504 (2004), 73–97. DOI: 10.1017/s0022112004008213.

[49] J. van Oijen and L. de Goey. Modelling of Premixed Laminar Flames using Flamelet-Generated Manifolds. In: Combust. Sci. Technol. 161 (2000), 113–137. DOI: 10.1080/00102200008935814.

[50] O. Gicquel, N. Darabiha, and D. Thévenin. Laminar premixed hydrogen/air counterflow flame simulations using flame prolongation of ILDM with differential diffusion. In: Proc. Combust. Inst. 28 (2000), 1901–1908. DOI: 10.1016/S0082-0784(00)80594-9.

[51] B. Fiorina, R. Baron, O. Gicquel, D. Thévenin, S. Carpentier, and N. Darabiha. Modelling non-adiabatic partially premixed flames using flame-prolongation of ILDM. In: Combust. Theor. Model. 7 (2003), 449–470. DOI: 10.1088/1364-7830/7/3/301.

[52] U. Maas and S. Pope. Simplifying chemical kinetics: Intrinsic low-dimensional manifolds in composition space. In: Combust. Flame 88 (1992), 239–264. DOI: 10.1016/0010-2180(92)90034-M.

[53] D. Veynante and L. Vervisch. Turbulent combustion modeling. In: Prog. Energy Combust. Sci. 28 (2002), 193–266. DOI: 10.1016/S0360-1285(01)00017-X.

[54] M. Steinhausen, T. Zirwes, F. Ferraro, A. Scholtissek, H. Bockhorn, and C. Hasse. Flame-vortex interaction during turbulent side-wall quenching and its implications for flamelet manifolds. In: Proc. Combust. Inst. 39 (2023), 2149–2158. DOI: 10.1016/j.proci.2022.09.026.

[55] S. Gierth, F. Hunger, S. Popp, H. Wu, M. Ihme, and C. Hasse. Assessment of differential diffusion effects in flamelet modeling of oxy-fuel flames. In: Combust. Flame 197 (2018), 134–144. DOI: 10.1016/j.combustflame.2018.07.023.

[56] W. Han, A. Scholtissek, F. Dietzsch, and C. Hasse. Thermal and chemical effects of differential diffusion in turbulent non-premixed H2 flames. In: Proc. Combust. Inst. 38 (2021), 2627–2634. DOI: 10.1016/j.proci.2020.06.049.

[57] R. Bilger, S. Stårner, and R. Kee. On reduced mechanisms for methane-air combustion in nonpremixed flames. In: Combust. Flame 80 (1990), 135–149. DOI: 10.1016/0010-2180(90)90122-8.

[58] J. C. Sutherland, P. J. Smith, and J. H. Chen. Quantification of differential diffusion in nonpremixed systems. In: Combust. Theor. Model. 9 (2005), 365–383. DOI: 10.1080/17455030500150009.

[59] A. Dahoe. Laminar burning velocities of hydrogen–air mixtures from closed vessel gas explosions. In: J. Loss Prev. Process Ind. 18 (2005), 152–166. DOI: 10.1016/j.jlp.2005.03.007.

[60] W. Han, P. Dai, X. Gou, and Z. Chen. A review of laminar flame speeds of hydrogen and syngas measured from propagating spherical flames. In: Appl. Energy Combust. Sci. 1-4 (2020), 100008. DOI: 10.1016/j.jaecs.2020.100008.

[61] N. Peters. Laminar diffusion flamelet models in non-premixed turbulent combustion. In: Prog. Energy Combust. Sci. 10 (1984), 319–339. DOI: 10.1016/0360-1285(84)90114-X.

[62] J. Janicka, W. Kolbe, and W. Kollmann. Closure of the Transport Equation for the Probability Density Funcfion of Turbulent Scalar Fields. In: J. Non-Equilib. Thermodyn. 4 (1979), 47–66. DOI: 10.1515/jnet.1979.4.1.47.

[63] J. A. M. de Swart, R. J. M. Bastiaans, J. A. van Oijen, L. P. H. de Goey, and R. S. Cant. Inclusion of Preferential Diffusion in Simulations of Premixed Combustion of Hydrogen/Methane Mixtures with Flamelet Generated Manifolds. In: Flow Turbul. Combust. 85 (2010), 473–511. DOI: 10.1007/s10494-010-9279-y.

[64] A. Donini, R. Bastiaans, J. van Oijen, and L. de Goey. Differential diffusion effects inclusion with flamelet generated manifold for the modeling of stratified premixed cooled flames. In: Proc. Combust. Inst. 35 (2015), 831–837. DOI: 10.1016/j.proci.2014.06.050.

[65] J. Schlup and G. Blanquart. Reproducing curvature effects due to differential diffusion in tabulated chemistry for premixed flames. In: Proc. Combust. Inst. 37 (2019), 2511–2518. DOI: 10.1016/j.proci.2018.06.211.

[66] A. Donini, R. M. Bastiaans, and J. van Oijen. A 5-D Implementation of FGM for the Large Eddy Simulation of a Stratified Swirled Flame with Heat Loss in a Gas Turbine Combustor. In: Flow Turbul. Combust. 98 (2017), 887–922. DOI: 10.1007/s10494-016-9777-7.

[67] B. Duboc, G. Ribert, and P. Domingo. Description of kerosene/air combustion with Hybrid Transported-Tabulated Chemistry. In: Fuel 233 (2018), 146–158. DOI: 10.1016/j.fuel.2018.06.014.

[68] B. Duboc, G. Ribert, and P. Domingo. Evaluation of chemistry models on methane/air edge flame simulation. In: Proc. Combust. Inst. 37 (2019), 1691–1698. DOI: 10.1016/j.proci.2018.05.053.

[69] B. Duboc, G. Ribert, and P. Domingo. Hybrid transported-tabulated chemistry for partially premixed combustion. In: Comput. Fluids 179 (2019), 206–227. DOI: 10.1016/j.compfluid.2018.10.019.

[70] W. Zhang, Z. Chen, and W. Kong. Effects of diluents on the ignition of premixed H_2/air mixtures. In: Combust. Flame 159 (2012), 151–160. DOI: 10.1016/j.combustflame.2011.05.017.

[71] N. Mukundakumar, D. Efimov, N. Beishuizen, and J. van Oijen. A new preferential diffusion model applied to FGM simulations of hydrogen flames. In: Combust. Theor. Model. 25 (2021), 1245–1267. DOI: 10.1080/13647830.2021.1970232.

[72] F. Wu, A. Saha, S. Chaudhuri, and C. K. Law. Facilitated Ignition in Turbulence through Differential Diffusion. In: Phys. Rev. Lett. 113 (2 2014), 024503. DOI: 10.1103/PhysRevLett.113.024503.

[73] S. S. Shy, M. T. Nguyen, S.-Y. Huang, and C.-C. Liu. Is turbulent facilitated ignition through differential diffusion independent of spark gap? In: Combust. Flame 185 (2017), 1–3. DOI: 10.1016/j.combustflame.2017.06.022.

[74] S. Shy, M. T. Nguyen, and S. Y. Huang. Effects of electrode spark gap, differential diffusion, and turbulent dissipation on two distinct phenomena: Turbulent facilitated ignition versus minimum ignition energy transition. In: Combust. Flame 205 (2019), 371–377. DOI: 10.1016/j.combustflame.2019.04.029.

[75] S. Shy, Y.-C. Liao, Y.-R. Chen, and S.-Y. Huang. Two ignition transition modes at small and large distances between electrodes of a lean primary reference automobile fuel/air mixture at 373 K with Lewis number » 1. In: Combust. Flame 225 (2021), 340–348. DOI: 10.1016/j.combustflame.2020.11.012.

[76] S. Shy. Spark ignition transitions in premixed turbulent combustion. In: Prog. Energy Combust. 98 (2023), 101099. DOI: 10.1016/j.pecs.2023.101099.

[77] L. Jiang, S. Shy, W. Li, H. Huang, and M. Nguyen. High-temperature, high-pressure burning velocities of expanding turbulent premixed flames and their comparison with Bunsen-type flames. In: Combust. Flame 172 (2016), 173–182. DOI: 10.1016/j.combustflame.2016.07.021.

[78] Z. Chen, X. Qin, B. Xu, Y. Ju, and F. Liu. Studies of radiation absorption on flame speed and flammability limit of CO_2 diluted methane flames at elevated pressures. In: Proc. Combust. Inst. 31 (2007), 2693–2700. DOI: 10.1016/j.proci.2006.07.202.

[79] Z. Chen, M. P. Burke, and Y. Ju. Effects of Lewis number and ignition energy on the determination of laminar flame speed using propagating spherical flames. In: Proc. Combust. Inst. 32 (2009), 1253–1260. DOI: 10.1016/j.proci.2008.05.060.

[80] Y. Wang, W. Han, and Z. Chen. Effects of fuel stratification on ignition kernel development and minimum ignition energy of n-decane/air mixtures. In: Proc. Combust. Inst. 37 (2019), 1623–1630. DOI: 10.1016/j.proci.2018.05.087.

[81] H. H. Kim, S. H. Won, J. Santner, Z. Chen, and Y. Ju. Measurements of the critical initiation radius and unsteady propagation of n-decane/air premixed flames. In: Proc. Combust. Inst. 34 (2013), 929–936. DOI: 10.1016/j.proci.2012.07.035.

[82] Z. Chen, M. P. Burke, and Y. Ju. On the critical flame radius and minimum ignition energy for spherical flame initiation. In: Proc. Combust. Inst. 33 (2011), 1219–1226. DOI: 10.1016/j.proci.2010.05.005.

[83] C. Huang, S. Shy, C. Liu, and Y. Yan. A transition on minimum ignition energy for lean turbulent methane combustion in flamelet and distributed regimes. In: Proc. Combust. Inst. 31 (2007), 1401–1409. DOI: 10.1016/j.proci.2006.08.024.

[84] S. Shy, C. Liu, and W. Shih. Ignition transition in turbulent premixed combustion. In: Combust. Flame 157 (2010), 341–350. DOI: 10.1016/j.combustflame.2009.08.005.

[85] C. Liu, S. Shy, H. Chen, and M. Peng. On interaction of centrally-ignited, outwardly-propagating premixed flames with fully-developed isotropic turbulence at elevated pressure. In: Proc. Combust. Inst. 33 (2011), 1293–1299. DOI: 10.1016/j.proci.2010.06.083.

[86] M.-W. Peng, S. Shy, Y.-W. Shiu, and C.-C. Liu. High pressure ignition kernel development and minimum ignition energy measurements in different regimes of premixed turbulent combustion. In: Combust. Flame 160 (2013), 1755–1766. DOI: 10.1016/j.combustflame.2013.03.030.

[87] C. Cardin, B. Renou, G. Cabot, and A. M. Boukhalfa. Experimental analysis of laser-induced spark ignition of lean turbulent premixed flames: New insight into ignition transition. In: Combust. Flame 160 (2013), 1414–1427. DOI: 10.1016/j.combustflame.2013.02.026.

[88] S. Shy, Y. Shiu, L. Jiang, C. Liu, and S. Minaev. Measurement and scaling of minimum ignition energy transition for spark ignition in intense isotropic turbulence from 1 to 5 atm. In: Proc. Combust. Inst. 36 (2017), 1785–1791. DOI: 10.1016/j.proci.2016.08.049.

[89] T. Poinsot. Using direct numerical simulations to understand premixed turbulent combustion. In: Symp. (Int.) Combust. 26 (1996), 219–232. DOI: 10.1016/S0082-0784(96)80220-7.

[90] M. Klein, N. Chakraborty, and R. S. Cant. Effects of Turbulence on Self-sustained Combustion in Premixed Flame Kernels: A Direct Numerical Simulation (DNS) Study. In: Flow Turbul. Combust. 81 (2008), 583–607. DOI: 10.1007/s10494-008-9149-z.

[91] C. Chi, A. Abdelsamie, and D. Thévenin. Direct Numerical Simulations of Hotspot-induced Ignition in Homogeneous Hydrogen-air Pre-mixtures and Ignition Spot Tracking. In: Flow Turbul. Combust. 101 (2018), 103–121. DOI: 10.1007/s10494-017-9883-1.

[92] H. A. Uranakara, S. Chaudhuri, and K. Lakshmisha. On the extinction of igniting kernels in near-isotropic turbulence. In: Proc. Combust. Inst. 36 (2017), 1793–1800. DOI: 10.1016/j.proci.2016.09.023.

[93] M. Ihme, L. Shunn, and J. Zhang. Regularization of reaction progress variable for application to flamelet-based combustion models. In: J. Comput. Phys. 231 (2012), 7715–7721. DOI: 10.1016/j.jcp.2012.06.029.

[94] Y.-S. Niu, L. Vervisch, and P. D. Tao. An optimization-based approach to detailed chemistry tabulation: Automated progress variable definition. In: Combust. Flame 160 (2013), 776–785. DOI: 10.1016/j.combustflame.2012.11.015.

[95] U. Prüfert, S. Hartl, F. Hunger, D. Messig, M. Eiermann, and C. Hasse. A Constrained Control Approach for the Automated Choice of an Optimal Progress Variable for Chemistry Tabulation. In: Flow Turbul. Combust. 94 (2015), 593–617. DOI: 10.1007/s10494-015-9595-3.

[96] M. Steinhausen, Y. Luo, S. Popp, C. Strassacker, T. Zirwes, H. Kosaka, F. Zentgraf, U. Maas, A. Sadiki, A. Dreizler, and C. Hasse. Numerical Investigation of Local Heat-Release Rates and Thermo-Chemical States in Side-Wall Quenching of Laminar Methane and Dimethyl Ether Flames. In: Flow, Turbul. Combust. 106 (2021), 681–700. DOI: 10.1007/s10494-020-00146-w.

[97] F. Egolfopoulos, N. Hansen, Y. Ju, K. Kohse-Höinghaus, C. Law, and F. Qi. Advances and challenges in laminar flame experiments and implications for combustion chemistry. In: Prog. Energy Combust. Sci. 43 (2014), 36–67. DOI: 10.1016/j.pecs.2014.04.004.

[98] O. Kwon, G. Rozenchan, and C. Law. Cellular instabilities and self-acceleration of outwardly propagating spherical flames. In: Proc. Combust. Inst. 29 (2002), 1775–1783. DOI: 10.1016/S1540-7489(02)80215-2.

[99] C. A. Hall, W. D. Kulatilaka, N. Jiang, J. R. Gord, and R. W. Pitz. Minor-species structure of premixed cellular tubular flames. In: Proc. Combust. Inst. 35 (2015), 1107–1114. DOI: 10.1016/j.proci.2014.05.108.

[100] C. Bauwens, J. Bergthorson, and S. Dorofeev. Experimental investigation of spherical-flame acceleration in lean hydrogen-air mixtures. In: Int. J. Hydrogen Energy 42 (2017), 7691–7697. DOI: 10.1016/j.ijhydene.2016.05.028.

[101] C. Altantzis, C. E. Frouzakis, A. G. Tomboulides, M. Matalon, and K. Boulouchos. Hydrodynamic and thermodiffusive instability effects on the evolution of laminar planar lean premixed hydrogen flames. In: J. Fluid Mech. 700 (2012), 329–361. DOI: 10.1017/jfm.2012.136.

[102] C. Altantzis, C. E. Frouzakis, A. G. Tomboulides, and K. Boulouchos. Direct numerical simulation of circular expanding premixed flames in a lean quiescent hydrogen-air mixture: Phenomenology and detailed flame front analysis. In: Combust. Flame 162 (2015), 331–344. DOI: 10.1016/j.combustflame.2014.08.005.

[103] C. E. Frouzakis, N. Fogla, A. G. Tomboulides, C. Altantzis, and M. Matalon. Numerical study of unstable hydrogen/air flames: Shape and propagation speed. In: Proc. Combust. Inst. 35 (2015), 1087–1095. DOI: 10.1016/j.proci.2014.05.132.

[104] F. Creta, P. E. Lapenna, R. Lamioni, N. Fogla, and M. Matalon. Propagation of premixed flames in the presence of Darrieus–Landau and thermal diffusive instabilities. In: Combust. Flame 216 (2020), 256–270. DOI: 10.1016/j.combustflame.2020.02.030.

[105] A. Attili, R. Lamioni, L. Berger, K. Kleinheinz, P. E. Lapenna, H. Pitsch, and F. Creta. The effect of pressure on the hydrodynamic stability limit of premixed flames. In: Proc. Combust. Inst. 38 (2021), 1973–1981. DOI: 10.1016/j.proci.2020.06.091.

[106] E. Knudsen, H. Kolla, E. R. Hawkes, and H. Pitsch. LES of a premixed jet flame DNS using a strained flamelet model. In: Combust. Flame 160 (2013), 2911–2927. DOI: 10.1016/j.combustflame.2013.06.033.

[107] M. Rieth, A. Gruber, F. A. Williams, and J. H. Chen. Enhanced burning rates in hydrogen-enriched turbulent premixed flames by diffusion of molecular and atomic hydrogen. In: Combust. Flame 239 (2022), 111740. DOI: 10.1016/j.combustflame.2021.111740.

[108] M. Rieth, A. Gruber, and J. H. Chen. The effect of pressure on lean premixed hydrogen-air flames. In: Combust. Flame 250 (2023), 112514. DOI: 10.1016/j.combustflame.2022.112514.

[109] V. Coulon, J. Gaucherand, V. Xing, D. Laera, C. Lapeyre, and T. Poinsot. Direct numerical simulations of methane, ammonia-hydrogen and hydrogen turbulent premixed flames. In: Combust. Flame 256 (2023), 112933. DOI: 10.1016/j.combustflame.2023.112933.

[110] Z. Yang, D. Li, and L. Wang. Research on the hot surface ignition of hydrogen-air mixture under different influencing factors. In: Int. J. Energy Res. 42 (2018), 3966–3976. DOI: 10.1002/er.4132.

[111] H. Chu, L. Berger, T. Grenga, Z. Wu, and H. Pitsch. Effects of differential diffusion on hydrogen flame kernel development under engine conditions. In: Proc. Combust. Inst. 39 (2023), 2129–2138. DOI: 10.1016/j.proci.2022.07.042.

[112] M. Ihme, W. T. Chung, and A. A. Mishra. Combustion machine learning: Principles, progress and prospects. In: Prog. Energy Combust. 91 (2022), 101010. DOI: 10.1016/j.pecs.2022.101010.

[113] A. Moreau, O. Teytaud, and J. P. Bertoglio. Optimal estimation for large-eddy simulation of turbulence and application to the analysis of subgrid models. In: Phys. Fluids 18 (2006), 105101. DOI: 10.1063/1.2357974.

[114] A. Y. Klimenko and A. G. Class. Propagation of Nonstationary Curved and Stretched Premixed Flames with Multistep Reaction Mechanisms. In: Combust. Sci. Technol. 174 (2002), 1–43. DOI: 10.1080/00102200290021317.

[115] T. Zirwes, F. Zhang, Y. Wang, P. Habisreuther, J. A. Denev, Z. Chen, H. Bockhorn, and D. Trimis. In-situ flame particle tracking based on barycentric coordinates for studying local flame dynamics in pulsating Bunsen flames. In: Proc. Combust. Inst. 38 (2021), 2057–2066. DOI: 10.1016/j.proci.2020.07.033.

[116] T. Zirwes, F. Zhang, and H. Bockhorn. Memory effects of local flame dynamics in turbulent premixed flames. In: Proc. Combust. Inst. 39 (2023), 2349–2358. DOI: 10.1016/j.proci.2022.07.187.

[117] L. Allen, A. O'Connell, and V. Kiermer. How Can We Ensure Visibility and Diversity in Research Contributions? How the Contributor Role Taxonomy (CRediT) Is Helping the Shift from Authorship to Contributorship. In: Learn. Publ. 32 (2019), 71–74. DOI: 10.1002/leap.1210.

List of figures

List of tables

Nomenclature

Abbreviations

A-SURF	Adaptive simulation of unsteady reacting flow
CEF	Cylindrical expanding flame
CFD	Computational fluid dynamics
CSM	Composition space model
CV	Control variable
DC	Detailed chemistry
DNS	Direct numerical simulation
EGR	Exhaust gas recirculation
FFI	Flow-facilitated ignition
FGM	Flamelet generated manifolds
FP	Freely propagating
FPI	Flame prolongation for ILDM
FPV	Flamelet/progress variable
FRS	Fully resolved simulation
hReactor	Homogeneous reactor at constant pressure
HTTC	Hybrid transported-tabulated chemistry
ILDM	Intrinsic low-dimensional manifold
IPF	Inwardly propagating flame

LSA	Linear stability analysis
M-$(K_s\kappa_c)$	Manifold with strain and curvature variation
M-κ_c	Manifold with curvature variation
M-h	Manifold with enthalpy variation
MIE	Minimum ignition energy
SEF	Spherical expanding flame
STAG	Stagnation flow
TD	Thermo-diffusive
TFI	Turbulent-facilitated ignition

Greek symbols

α	Thermal diffusivity
β	Coupling fucntion for Z_{Bilger} estimation
δ_{ij}	Kronecker delta
$\dot{\omega}_{\mathrm{T}}$	Heat release rate
$\dot{\omega}_c$	Progress variable source term
$\dot{\omega}_k$	Source term of species k
ϵ_{rel}	Relative error
$\epsilon^{\mathrm{norm}}_{\mathrm{irr},\dot{\omega}_c}$	Irreducible error of $\dot{\omega}_c$
γ_l	Weighting factor of element l used for Z_{Bilger} estimation
κ_c	Curvature
λ	Thermal conductivity
ν	Kinematic viscosity
ϕ	Equivalance ratio
ψ	Thermochemical state
ρ	Density

ρ^0	Fresh gas density
τ	Flame-attached time
τ_{ch}	Chemistry time scale
τ_{fl}	Flow time scale
τ_{ij}	Stress tensor
φ	Generic scalar quantity
ξ	Parameter set

Latin symbols

Da	Damköhler number
Le	Lewis number
Le_k	Lewis number of species k
Re	Reynolds number
$\mathbf{n}$	Normal vector of progess variable
$\mathbf{u}$	Velocity vector
$\nabla h_{\mathrm{closure}}$	Enthalpy closure in flamelet-based model
$\overline{M}$	Mean molecular weight
$\overline{R}_{\mathrm{f}}$	Mean flame radius
$\tilde{V}_c$	Diffusion velocity of progress variable in composition space
$\tilde{V}_k$	Diffusion velocity of species k in composition space
A	Flame surface area
$a_{l,k}$	Number of element l in species k
c_{p}	Heat capacity at constant pressure
$c_{\mathrm{p},k}$	Heat capacity of species k at constant pressure
D_k^{M}	Mixture-averaged diffusion coefficient of species k
D_k^{T}	Thermal diffusion coefficient of species k

D_{Z}	Diffusion coefficient of mixture fraction
D_c	Diffusion coefficient of progress variable
D_k	Diffusion coefficient of species k
E_{ign}	Ignition energy
g	Gravity constant
g_c	Progess variable gradient
h	Enthalpy
h_k	Enthalpy of species k
K	Stretch
k	Species index
K_c	Stretch resulting from curvature
K_s	Strain
L	Width of the central jet
l	Element index
M_k	Molecular weight of species k
M_l	Molecular weight of element l
N_{e}	Total number of elements
N_{s}	Total number of species
p	Pressure
q	External energy source
R	Radius
R_{f}	Flame radius
s_{d}	Flame displacement speed
s_{L}	Laminar burning velocity
s_{u}	Flame speed / Burning velocity

T	Temperature
t	Time
u	Flow velocity
u_{g}	Gas velocity
V_i^{C}	Correction velocity
$V_{k,i}$	Diffusion velocity of species k
$V_{k,i}^{\mathrm{D}}$	Mixture-averaged diffusion velocity of species k
$V_{k,i}^{\mathrm{T}}$	Thermal diffusion velocity of species k
w_k	Weight of species k in progress variable definition
x, y, z, r	Physical space coordinates
X_k	Mole fraction of species k
Y_c	Progess variable
Y_k	Mass fraction of species k
Z	Mixture fraction
Z_{Bilger}	Bilger mixture fraction

Publications

P1 Proc. Combust. Inst. 38 (2021), 2031–2039

H. Böttler, A. Scholtissek, X. Chen, Z. Chen, and C. Hasse. Premixed flames for arbitrary combinations of strain and curvature. In: Proc. Combust. Inst. 38 (2021), 2031–2039. DOI: 10.1016/j.proci.2020.06.312

Author contributions

Tab. P.1: Author contributions to publication [P1] following CRediT [117]

Hannes Böttler	Conceptualization of the numerical investigation (equal) Implementation and validation of a parallelization strategy for flame simulation Conduction of the numerical investigation (lead) Interpretation and discussion of the results (lead) Data analysis and visualization Writing – Original draft (equal) Main and corresponding author
Arne Scholtissek	Conceptualization of the numerical investigation (equal) Interpretation and discussion of the numerical results (supporting) Writing – Original draft (equal) Supervision of HB (equal)
Xinyi Chen	Numerical investigation of spherical expanding and inwardly propagating flames Interpretation and discussion of the numerical results (supporting)
Zheng Chen	Interpretation and discussion of the numerical results (supporting) Supervision of XC Funding acquisition
Christian Hasse	Conceptualization of the numerical investigation (equal) Interpretation and discussion of the numerical results (supporting) Supervision of HB (equal) Funding acquisition
All co-authors	Writing – Review & Editing

Use of publication contents in finalized and ongoing dissertations

This publication is part of the ongoing dissertation of Hannes Böttler at the Institute for Simulation of reactive Thermo-Fluid Systems at the Technical University of Darmstadt, Germany.

Available online at www.sciencedirect.com

ScienceDirect

Proceedings of the Combustion Institute 38 (2021) 2031–2039

Proceedings of the Combustion Institute

www.elsevier.com/locate/proci

Premixed flames for arbitrary combinations of strain and curvature

H. Böttler [a,*], A. Scholtissek [a], X. Chen [b], Z. Chen [b], C. Hasse [a]

[a] *Institute for Simulation of reactive Thermo-Fluid Systems, TU Darmstadt, Otto-Berndt-Straße 2, Darmstadt 64287, Germany*

[b] *SKLTCS, CAPT, BIC-ESAT, Department of Mechanics and Engineering Science, College of Engineering, Peking University, Beijing 100871, China*

Received 7 November 2019; accepted 28 June 2020
Available online 2 October 2020

Abstract

Many modeling strategies for combustion rely on laminar flamelet concepts to determine structure and properties of multi-dimensional and turbulent flames. Using flamelet tabulation strategies, the user anticipates certain aspects of the combustion process prior to the simulation and selects a flamelet model which mimics local flame conditions in the more complex configuration. Flame stretch, which can be decomposed into contributions from strain and curvature, is one of the conditions influencing a flame's properties, structure, and stability. The objective of this work is to study premixed flame structures in the strain-curvature space using a recently published composition space model (CSM) and three physical space models for canonical flame configurations (stagnation flame, spherical expanding flame and inwardly propagating flame). Flames with effective Lewis numbers both smaller and larger than unity are considered. For canonical laminar flames, the stretch components are inherently determined through boundary conditions and their specific flame configuration. Therefore, canonical flames can only represent a certain sub-set of stretch effects experienced by multi-dimensional and turbulent flames. On the contrary, the CSM allows arbitrary combinations of strain and curvature to be prescribed for premixed flames exceeding the conditions attainable with the canonical flame setups. Thereby, also influences of negative strain effects and large curvatures can be studied. A parameter variation with the CSM shows that flame structures still significantly change outside the region of the canonical flame configurations. Furthermore, limits in the strain-curvature space are discussed. The present paper highlights advantages of composition space modeling which is achieved by detaching the representation of the flame structure from a specific canonical flame configuration in physical space.

Keywords: Premixed flames; Composition space; Stretch effects; Negative strain; Curvature

* Corresponding author.
E-mail address: boettler@stfs.tu-darmstadt.de (H. Böttler).

https://doi.org/10.1016/j.proci.2020.06.312
1540-7489

1. Introduction

CFD simulations with flamelet-based chemistry tabulation, as utilized in flamelet-generated manifolds (FGM) [1] or flame-prolongiation of ILDM (FPI) [2], rely on the assumption that a turbulent flame can be considered a statistical ensemble of one-dimensional laminar flamelets [3]. These flamelets can be computed prior to the combustion simulation and tabulated as a function of a reduced set of scalars. During simulation runtime, thermochemical quantities and source terms are obtained from the table instead of computing them in every cell and time step. The application of the approach requires the user to anticipate certain aspects of the combustion process prior to the simulation and select a flamelet model which mimics local conditions for the turbulent flame as best as possible.

It is well-established, e.g. from studies of laminar and turbulent fully resolved numerical simulations, that flame physics are significantly affected by flame stretch, flame-wall interactions, multiple fuel streams, or multi-phase characteristics, among others. These effects potentially have to be considered in the flamelet tabulation to improve the overall model fidelity. For tabulation, the user can choose from physical space models, which represent canonical flame configurations subject to some of the aforementioned effects, or composition space models, which have been obtained by a mathematical transformation of the transport equations of species, temperature or enthalpy. However, these models do not necessarily cover the full parameter range or relevant scales which are to be expected in the combustion simulation. For instance, physical space flame configurations are inherently unstable at negative strain conditions (e.g. the rearward stagnation flame [4]). Furthermore, canonical curved flames, such as tubular flames [5], can only cover a limited curvature range due to geometrical restrictions (e.g. minimum realizable nozzle radius). On the contrary, it was shown for turbulent combustion that multi-dimensional flame configurations can experience a much wider range of stretch conditions, including substantial negative strain effects and large curvatures [6].

This serves as the motivation for this work where premixed flame structures are analyzed for a wide range of flame stretch conditions. Flames with effective Lewis numbers smaller and greater than unity are considered. Three physical space models for canonical flame configurations (stagnation flame, spherical expanding flame and inwardly propagating flame) and a recently published composition space model (CSM) [7,8] are utilized. For the latter, the representation of the flame structure is detached from a specific physical space flame configuration. In our previous work we showed that, when an additional equation for the progress variable gradient is being solved, arbitrary combinations of strain (K_s) and curvature (κ) can be prescribed as external parameters. Setting both parameters to zero, the CSM recovers the unstretched laminar burning velocity s_u^0. Here it is shown that the CSM can access a larger (K_s, κ)-parameter space exceeding the capabilities of canonical flame models, and that this can lead to significant differences for flame structures.

First, the required theory of flame stretch, the CSM, and the canonical flame models is briefly revisited. Then, different flame structures obtained for the canonical flame configurations are discussed and compared. Thereafter, composition space flame solutions are analyzed in the (K_s, κ)-region beyond the limits of canonical flame models. The paper ends with a summary.

2. Flame stretch effects

Flame stretch influences the structure and burning rate of a premixed flame and can lead to flame extinction if increased above a critical value. It is defined as the fractional area change of a flame surface element [9,10]

$$K = \frac{1}{A}\frac{\mathrm{d}A}{\mathrm{d}t} = \nabla_t \cdot \mathbf{u}_t + (\mathbf{s}_f \cdot \mathbf{n})(\nabla \cdot \mathbf{n}), \tag{1}$$

where $\nabla_t \cdot \mathbf{u}_t$ represents flame-tangential straining by the flow, $\mathbf{s}_f$ is the flame speed, and $\mathbf{n}$ is the flame-normal unit vector ($\mathbf{n}$ points towards the burnt gases). Introducing the decomposition of the flame speed into flow velocity and flame displacement speed, $\mathbf{s}_f = \mathbf{u} - s_d\,\mathbf{n}$, Eq. (1) can be reformulated [11]

$$K = \underbrace{\nabla_t \cdot \mathbf{u}_t - (\mathbf{u}\cdot\mathbf{n})\kappa}_{K_s} + \underbrace{s_d\,\kappa}_{K_c}, \tag{2}$$

where $\kappa = -\nabla \cdot \mathbf{n}$ is the flame curvature, K_s marks strain imposed on the flame by the flow, and K_c is a stretch component which originates from the self-propagation of the (curved) flame. This distinction is of importance here since the CSM presented in the next section requires K_s and the flow topology information κ as external parameters. On the contrary, K_c is tied to the flame displacement speed, which is obtained as a flame-response to the external flame parameters. The Markstein length $\mathcal{L}$ is often used to describe the relation between burning velocity s_u and stretch [12]

$$s_u = s_u^0 - \mathcal{L}\,K + H.O.T. \tag{3}$$

Its dimensionless form is denoted as Markstein number $\mathcal{M} = \mathcal{L}/l_f$ with the flame thickness l_f. However, the linear relation is limited to weakly stretched flames and higher order terms ($H.O.T$) gain importance with increasing stretch.

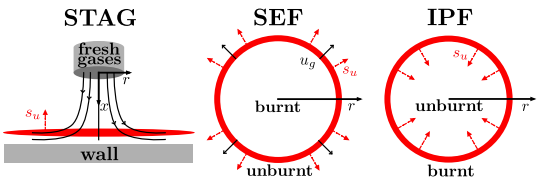

Fig. 1. Schematic models of the canonical flame configurations considered.

Table 1
Overview of stretch effects in the canonical flames considered.

Type	Stretch $K = K_s + K_c$	Strain K_s	Curvature stretch K_c
STAG	$K > 0$	$K_s > 0$	$K_c = 0$
SEF	$K > 0$	$K_s > 0$	$K_c > 0$
IPF	$K < 0$	$K_s = 0$	$K_c < 0$

3. Composition space model (CSM)

For a premixed flame, the reaction progress variable Y_c can be utilized as a flame-attached coordinate which spans the so-called progress variable space. Here, it is defined as a weighted sum of species, $Y_c = \sum_i^{n_s} \alpha_i Y_i$. With this, a transport equation for Y_c can be formulated

$$\rho \frac{\partial Y_c}{\partial t} + \rho \mathbf{u} \cdot \nabla Y_c = -\nabla \cdot (\rho Y_c \mathbf{V}_c) + \dot{\omega}_c \,, \tag{4}$$

where ρ is the density and $Y_c \mathbf{V}_c = \sum_i^{n_s} \alpha_i Y_i \mathbf{V}_i$ the diffusive flux of the progress variable, with $\mathbf{V}_i$ being the diffusion velocity of species i. Further, the source term is defined as a weighted sum of species source terms $\dot{\omega}_c = \sum_i^{n_s} \alpha_i \dot{\omega}_i$. The motion of the flame surface, represented by a collection of Y_c-isosurfaces, is then described by the kinematic condition [1,13]

$$\frac{\mathrm{d} Y_c}{\mathrm{d} t} = \frac{\partial Y_c}{\partial t} + \mathbf{s}_f \cdot \nabla Y_c = 0 \,, \tag{5}$$

and the unit vector along the flame-normal is defined as $\mathbf{n} = \nabla Y_c / |\nabla Y_c|$. The temperature and species balance equations can be transformed into Y_c-space given a suitable choice for the progress variable. Furthermore, an equation for the progress variable gradient $g_c = |\nabla Y_c|$ is required as a closure [7]. The final set of equations reads [8]

$$\begin{aligned} \rho \frac{\partial Y_i}{\partial \tau} &= -g_c \frac{\partial}{\partial Y_c}\left(g_c \rho Y_i \tilde{V}_i\right) + g_c \frac{\partial}{\partial Y_c}\left(g_c \rho Y_c \tilde{V}_c\right) \frac{\partial Y_i}{\partial Y_c} \\ &\quad + \rho g_c \kappa \left(Y_i \tilde{V}_i - Y_c \tilde{V}_c \frac{\partial Y_i}{\partial Y_c} \right) - \dot{\omega}_c \frac{\partial Y_i}{\partial Y_c} + \dot{\omega}_i \end{aligned} \tag{6}$$

$$\begin{aligned} \rho \frac{\partial T}{\partial \tau} &= \frac{g_c}{c_p} \frac{\partial}{\partial Y_c}\left(g_c \lambda \frac{\partial T}{\partial Y_c} \right) + g_c \frac{\partial}{\partial Y_c}\left(g_c \rho Y_c \tilde{V}_c\right) \frac{\partial T}{\partial Y_c} \\ &\quad - \rho g_c^2 \sum_k^{n_s} \frac{c_{p,k}}{c_p} Y_k \tilde{V}_k \frac{\partial T}{\partial Y_c} - \rho g_c \kappa \left(\frac{\lambda}{\rho c_p} + Y_c \tilde{V}_c \right) \frac{\partial T}{\partial Y_c} \\ &\quad - \dot{\omega}_c \frac{\partial T}{\partial Y_c} + \frac{\dot{\omega}_T}{c_p} \,, \end{aligned} \tag{7}$$

$$\begin{aligned} 0 &= -g_c^2 \frac{\partial^2}{\partial Y_c^2}\left(g_c \rho Y_c \tilde{V}_c\right) + g_c^2 \frac{\partial}{\partial Y_c}\left(\kappa \rho Y_c \tilde{V}_c\right) \\ &\quad - \dot{\omega}_c \frac{\partial g_c}{\partial Y_c} + g_c \frac{\partial \dot{\omega}_c}{\partial Y_c} + \rho K_s g_c \,, \end{aligned} \tag{8}$$

where $\tilde{V}_i$ represents the diffusion velocity of species i with respect to the Y_c-composition space, λ is the heat conductivity, c_p is the heat capacity and $\dot{\omega}_T$ is the heat release rate.

Solutions of these equations recover structure and characteristics of canonical flame configurations, and it has been shown that it is sufficient to approximate the external parameters strain K_s and curvature κ by representative values [8]. Setting strain and curvature to zero, the laminar burning velocity can be computed by solving the closed system of equations [7]. Homogeneous ignition is recovered by the CSM in the asymptotic limit of $g_c \to 0$ [7,8]. While the CSM can capture transient effects (ignition, flame structure of a spherical flame), it should be noted that it cannot account for very high transients or cases exhibiting multi-dimensional structures.

4. Canonical premixed flame configurations

Besides the composition space model (CSM), three physical space models for canonical flame configurations are considered which are shown schematically in Fig. 1. Planar stagnation flames (STAG) can be stabilized in a stream of premixed fresh gases towards a wall or an opposed stream of equivalent composition (twin-configuration). The governing equations can be found in Kee et al. [14]. In a quiescent mixture of fresh gases, a spherical expanding flame (SEF) can be created using an ignition source. This flame is stretched and curved at the same time and both quantities change as the flame evolves over time. Unlike SEF, an inwardly propagating flame (IPF) is obtained by igniting a quiescent mixture of fresh gases in perfect spherical shape. The flame then propagates inwards consuming the remaining fresh gases. Although such an idealized flame can hardly be established in experiments, it can be computed numerically [15,16]. Both spherical flames are computed using the code A-SURF [17]. Table 1 summarizes the stretch conditions for all three configurations.

5. Results

With the possibility to choose arbitrary combinations of strain and curvature, the CSM allows

studying the influence of K_s and κ on premixed flame structures systematically, which is the objective in the following. By contrast, strain and curvature are inherently determined through the boundary conditions and configuration for the canonical flames. Exemplary canonical flame solutions are analyzed and compared against the CSM in the (K_s, κ)-parameter space. As an estimate for the parameter variation, Fru et al. [6] found strain and curvature in the order of $K_s \approx \pm 10^4 \mathrm{s}^{-1}$ and $\kappa \approx \pm 10^4 \mathrm{m}^{-1}$ from direct numerical simulations of turbulent premixed flames in a periodic box. Although different values might be found in other multi-dimensional flame configurations, these orders of magnitude serve as an orientation here. After comparing the CSM against canonical flame solutions, flame structures beyond the limit of canonical flames are analyzed. Flame databases for two different fuels are created: (1) lean hydrogen/air flames ($\phi = 0.5$, $Le_{\mathrm{H_2}} \approx 0.3$, ≈ 12000 flame calculations) and (2) lean ethanol flames ($\phi = 0.7$, $Le_{\mathrm{C_2H_5OH}} \approx 1.6$, ≈ 6000 flame calculations). For the flames specified above, the fuel is the deficient reactant and its Lewis number is considered the effective Lewis number [18]. The applied progress variable definitions are $Y_c = Y_{\mathrm{H_2O}} - Y_{\mathrm{H_2}} - Y_{\mathrm{O_2}}$ for hydrogen and $Y_c = Y_{\mathrm{H_2O}} - Y_{\mathrm{O_2}} + Y_{\mathrm{CO_2}} + 10\, Y_{\mathrm{H_2}}$ for ethanol flames. A mixture averaged diffusion model is utilized [19] and thermal diffusion [20] is additionally considered for hydrogen-air flames.

5.1. *Le < 1 flames (H_2)*

Figure 2 shows the characteristics of lean H_2-air flames in the (K_s, κ)-parameter space obtained with the CSM. Reference solutions of canonical flames are included in the figure and it is observed that they only cover a small subset of the parameter range accessible by the composition space solutions. The plot on the left shows the burning velocity s_u. It is evaluated at the maximum heat release peak, which is in agreement with literature as it should be evaluated close to the burned side [11,12] and is weighted by the fresh gas density ρ^0, according to

$$s_u = \frac{\rho s_d}{\rho^0} = \frac{1}{\rho^0}\left(-\frac{\partial}{\partial Y_c}\left(\rho Y_c \tilde{V}_c\right) + \kappa \rho Y_c \tilde{V}_c + \frac{\dot{\omega}_c}{g_c}\right). \tag{9}$$

This equation can be obtained using the transformed Eqs. (4) and (5) [8]. Furthermore, Fig. 2 shows the inner layer temperature T_{il}, which is the temperature at the maximum heat release rate (middle), and the maximum temperature T_{max} (right). Moreover, the limits of the parameter space are indicated, as discussed further below.

Positive strain strengthens Le < 1 flames due to differential diffusion [18], as reflected in Fig. 2 illustrating that the burning velocity increases by a factor of approximately 5 from the left to the right boundary of the parameter space. Furthermore, the maximum temperature increases substantially with increasing K_s. The influence of strain on the flame structure is more significant than the effect resulting from curvature. This is also observed for the burning velocity, whereas the maximum temperature shows a moderate effect. On the other hand, both strain and curvature influence the inner layer temperature. T_{il} increases with increasing strain (decreasing curvature), which indicates that the heat release peak is shifted to lower (higher) temperatures, respectively.

Exemplary flame structures of canonical flame configurations are compared to corresponding results from the CSM in Fig. 3. Temperature, fuel and OH mass fractions are shown as a function of the progress variable. Overall, good agreement is observed between the canonical flame solutions and the CSM. Slight deviations occur at the right boundary for STAG flames resulting from restrainment effects which are discussed further below. For the SEF, small discrepancies can be observed in the

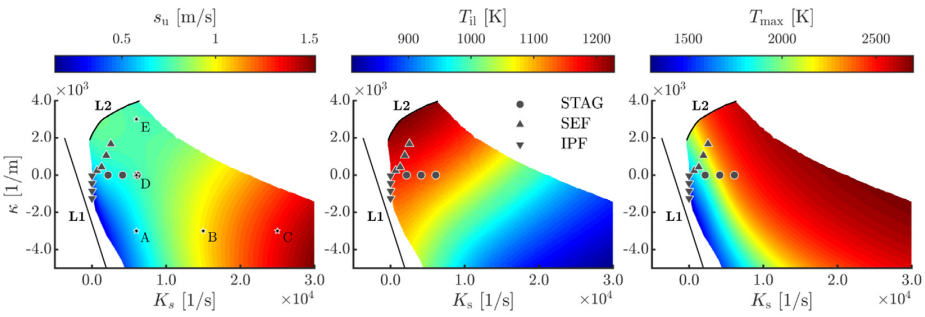

Fig. 2. (K_s, κ)-parameter space for lean H_2/air flames ($\phi = 0.5$, $p = 1$ atm, $T_0 = 300$ K) characterized by burning velocity s_u (left), inner layer temperature T_{il} (middle) and maximum temperature T_{max} (right). Canonical flame solutions are shown for reference. Furthermore, limits of the parameter space are indicated (L1: Strain-induced extinction limit, L2: Topological limit).

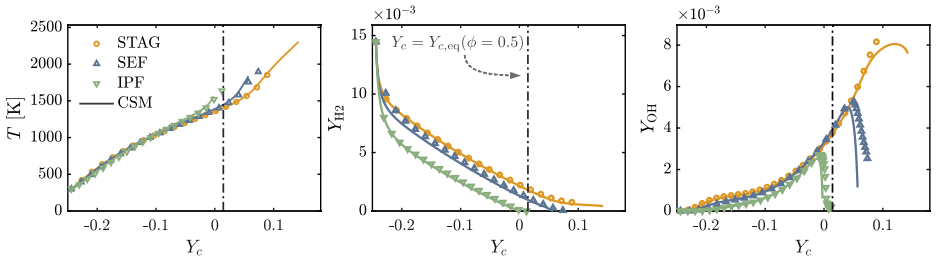

Fig. 3. Flame structure for lean H_2-air flames ($\phi = 0.5$, $p = 1$ atm, $T_0 = 300$ K) of canonical flames (symbols) compared to calculations with the CSM (lines). (STAG: $K_s = 4800\,\mathrm{s}^{-1}$ and $\kappa_c = 0\,\mathrm{m}^{-1}$, SEF: $K_s = 900\,\mathrm{s}^{-1}$ and $\kappa_c = 310\,\mathrm{m}^{-1}$, IPF: $K_s = 0\,\mathrm{s}^{-1}$ and $\kappa_c = -280\,\mathrm{m}^{-1}$).

hydrogen profile. These result from using representative values for strain and curvature in the CSM, and these are extracted at the maximum heat release peak for both spherical flames, while they vary in the physical space (SEF/IPF model). Nevertheless, the CSM can recover the flame structure of the SEF for an instant during its transient evolution [8]. The larger progress variable domain for the SEF is a direct consequence of the ignition process, which produces already burned products and a developed radical pool [21]. The flame structures of the IPF are captured well by the CSM. IPF solutions for large negative curvatures could not be matched by corresponding composition space solutions, presumably due to the fact that IPFs are weakly backsupported by hot products while propagating inwardly. This effect is not included in the CSM.

Restrainment of stagnation flames Although lean H_2-flames (Le < 1) are strengthened by positive strain, the corresponding STAG flames exhibit a positive strain extinction limit. According to Law [18], this extinction behavior is due to *restrainment* of the flame and not a stretch effect. Increasing the strain rate, extinction of STAG flames does not occur before the flame reaches the (adiabatic) stagnation plane. At the stagnation plane the flame is restrained, i.e. it cannot occupy enough space (limited flame thickness) and the residence times of reactants and intermediates are reduced. When the strain is further increased, chemical reactions remain incomplete and eventually the flame is extinguished. Restrainment is specific to the physical space STAG flame configuration. Such limitations are avoided in composition space. Instead, the CSM is defined such that both boundary conditions (fresh and burned gases) are far away from the reaction zone. This is readily understood from the boundary conditions for the gradient ($g_c = 0$), which represents the transformation between Y_c and coordinate $\mathrm{d}x = \mathrm{d}Y_c/g_c$ measured along the flame-normal in the physical space.

For further illustration, Fig. 4 shows STAG solutions subject to restrainment at elevated strain rates K_s and corresponding composition space so-

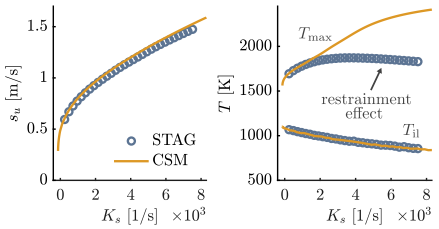

Fig. 4. Restrainment effect for premixed H_2-air STAG flames ($\phi = 0.5$, $p = 1$ atm, $T_0 = 300$ K) compared to the CSM.

lutions (unrestrained). Inner layer quantities, such as T_{il}, remain unaffected by restrainment until extinction of the STAG flames. On the contrary, the maximum temperature is affected as T_{max} is reached in the post-oxidation zone, which becomes restrained at the stagnation plane.

Flame structure analysis in composition space In Fig. 5 the temperature T, the local equivalence ratio ϕ_{local} and the heat release rate $\dot{\omega}_T$ are shown in composition space for three different cases with constant curvature and increasing strain from case A to C, respectively. The maximum of the progress variable increases with increasing strain indicating super equilibrium conditions ("hot spots") which have been identified for laminar and turbulent flames [22,23]. This is further affirmed by the maximum heat release peak and the increased local equivalence ratio, which both increase with K_s. Note that the integral of the heat release across the flame remains constant, the flame only becomes thinner and the gradient g_c assumes larger values (not shown).

Figure 6 shows the complementary result to Fig. 5. Here, the strain rate is fixed, while the curvature is varied. In accordance with the literature [18], the figure shows that positive curvature strengthens the flame, while negative curvature has the opposite effect. Interestingly, particularly the flame structure for case C can only be realized with the CSM, uti-

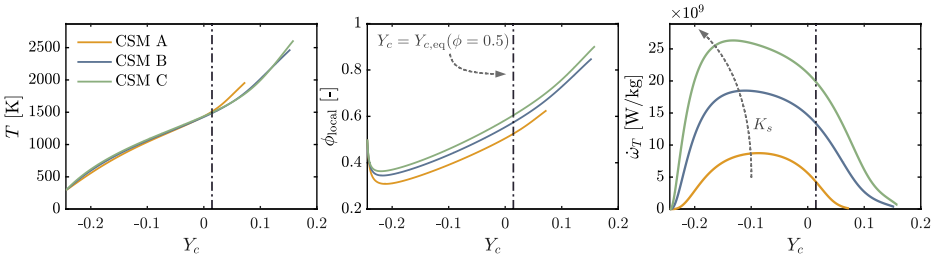

Fig. 5. Flame structure obtained with the CSM at different locations within the (K_s, κ)-parameter space for lean H_2-air flames ($\phi = 0.5$, $p = 1$ atm, $T_0 = 300$ K). The temperature profile (left), the local equivalence ratio ϕ_{local} (middle) and the heat release rate $\dot{\omega}_T$ (right) are shown in Y_c-space. The curvature is fixed at $\kappa = 3000\mathrm{m}^{-1}$ while strain K_s is increased for cases A/B/C according to $6000/15,000/25,000\mathrm{s}^{-1}$.

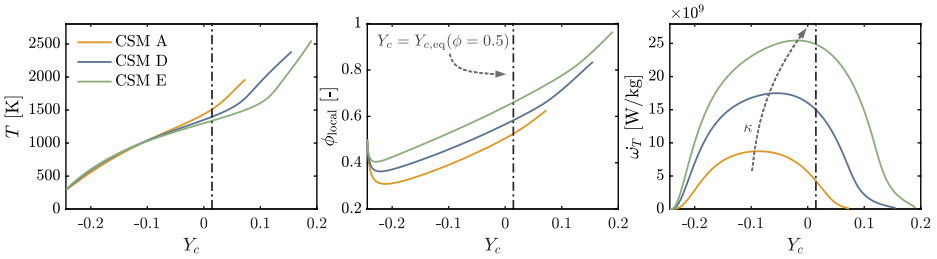

Fig. 6. Flame structure obtained with the CSM at different locations within the (K_s, κ)-parameter space for lean H_2-air flames ($\phi = 0.5$, $p = 1$ atm, $T_0 = 300$ K). The temperature profile (left), the local equivalence ratio ϕ_{local} (middle) and the heat release rate $\dot{\omega}_T$ (right) are shown as a function of Y_c. Strain is fixed at $K_s = 6000\mathrm{s}^{-1}$ while curvature κ is increased for cases A/D/E according to $-3000/0/3000\mathrm{m}^{-1}$.

lizing a compensation between opposing trends for positive strain and negative curvature effects. It is also found that the maximum heat release peak shifts towards fresh gases with increasing strain, while the opposite is true for increasing curvature.

Limits in strain-curvature parameter space It is indicated in Fig. 2 that the composition space solutions exhibit certain limits in the (K_s, κ)-parameter space. These limits originate from considerations about flame physics as outlined in the following.

L1: Strain-induced extinction limit Le < 1 flames are strengthened (weakened) by positive (negative) strain and vice versa for flames with Le > 1 [18]. Hence, strain can weaken a flame such that heat release rate and burning velocity become significantly reduced up to a point where the flame quenches. This strain-induced extinction limit L1 is estimated in (K_s, κ)-space by extrapolating the burning velocity to zero.

L2: Topological limit The CSM assumes that the flame structure is locally one-dimensional. However, considering a flame whose flame thickness is of the order of the curvature length scale (i.e. the flame radius, $l_\kappa = 1/\kappa$) implies a flame kernel structure rather than a flame surface. Solutions in the limit of the flame kernel structure require separate analyses and modeling, which is out of scope for this work. Therefore, a topological limit is introduced which restricts the flame thickness to be smaller than the curvature length scale by at least a factor of 3, $l_f < l_\kappa/3$. For this criterion the Zeldovich thickness is utilized $l_f = \lambda/(c_p\,\rho_u s_u)$ instead of a thickness definition based on the progress variable gradient, as this would introduce numerical uncertainties due to reconstruction of the physical space coordinate.

5.2. Le > 1 flames (C_2H_5OH)

Figure 7 shows the burning velocity (top) and inner layer temperature (bottom) for lean C_2H_5OH/air flames. The (K_s, κ)-parameter space attainable with the CSM is smaller and shaped differently than for H_2-air flames. There is only a small area with positive strain and positive curvature for ethanol flames and the strain induced extinction limit is found for positive strain. This is in agreement with theory [18] since Le > 1 flames are weak-

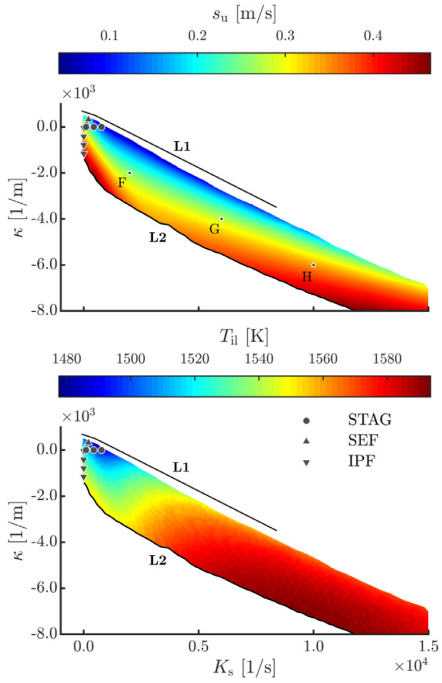

Fig. 7. (K_s, κ)-parameter space for lean C_2H_5OH/air flames ($\phi = 0.7$, $p = 1$ atm, $T_0 = 363$ K) characterized by burning velocity s_u (top) and inner layer temperature T_{il} (bottom). Further, canonical flame solutions and the respective limits (L1: Strain-induced extinction limit, L2: Topological limit) are shown.

ened by positive stretch. The burning velocity s_u increases by a factor of 4 and T_{il} increases by approximately 100K for increasing strain and decreasing curvature. The variations of maximum temperature (not shown) are comparable to the ones for T_{il}, with a slight decrease towards the upper boundary.

Similarly as for H_2-air flames, the CSM recovers the canonical flame structures for C_2H_5OH-air flames (not shown here, cf. [8]). Figure 8 shows temperature T, local equivalence ratio ϕ_{local} and the heat release rate $\dot{\omega}_T$ obtained for C_2H_5OH-air flames with the CSM from parameter variation (cases F-H, as indicated in Fig. 7). For Cases F to H, curvature decreases and strain rate increases. The maximum local equivalence ratio and the maximum heat release peak increases from F to H, which is expected for Le > 1 flames. On the other hand, the temperature profiles are almost identical and the shift of the maximum heat release peak is smaller compared to hydrogen. This underlines that stretch effects are less pronounced for C_2H_5OH-air flames, however, particularly the effects on s_u are significant (cf. Fig. 7).

5.3. Markstein numbers

Usually the Markstein length is obtained via a regression of burning velocity versus stretch [12]. In the (K_s, κ)-parameter space the Markstein length can be evaluated as the directional derivative of the burning velocity with respect to stretch $\mathcal{L} = \partial s_u / \partial K = \nabla s_u \cdot \nabla K / |\nabla K|^2$. Figure 9 shows the Markstein number for the whole parameter space. The Markstein number changes only slightly in the region of the canonical flames. This is in agreement with theory, since the Markstein number can be assumed constant for weakly stretched flames [11,12]. The Markstein number decreases towards the strain induced extinction limit as the burning velocity rapidly approaches zero. Overall, it is observed that the Markstein number changes significantly with respect to both, K_s and κ.

6. Summary and conclusions

In this work, stretch effects on premixed flame structures are investigated for flames with effective Lewis numbers smaller (lean H_2-air) and larger than unity (lean C_2H_5OH-air). Three canonical flame configurations (expressed and solved with respect to the physical space) and a recently published composition space model (CSM) are considered. The latter describes premixed flame structures in progress variable space and allows arbitrary combinations of strain and curvature to be chosen. By this means, the CSM recovers the canonical flame structures with one set of equations, while different models have to be used when computing the same flame structures in the physical space. Moreover, a larger region in the strain-curvature parameter space becomes attainable with the CSM. This has several reasons: (1) strain and curvature are inherently prescribed through boundary conditions for canonical flame configurations, and (2) canonical flame configurations are subject to certain limitations (e.g. with respect to the burner geometry, restrainment of stagnation flames).

The flame structure analysis for the lean H_2-air flames shows that strain effects can lead to burning velocities which differ by a factor of more than 5 and substantially different flame temperatures for the same thermochemical state of the fresh gases. For lean C_2H_5OH-air flames, the variability of these flame characteristics is smaller, but also significant. The evaluation of the Markstein number for hydrogen flames shows that this quantity changes only slightly in the region of the canonical flames, whereas significant changes are observed for higher strain and curvature.

It is noted, that canonical flames can only represent a small part of the strain-curvature parameter space and therefore only capture a certain portion of stretch effects on premixed flame

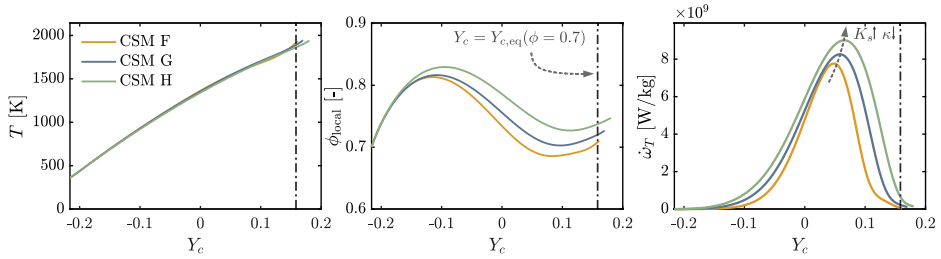

Fig. 8. Flame structure obtained with the CSM at different locations within the (K_s, κ)-parameter space of lean C_2H_5OH-air flames ($\phi = 0.7$, $p = 1$ atm, $T_0 = 363$ K). The temperature profile (left), the local equivalence ratio ϕ_{local} (middle) and the heat release rate $\dot{\omega}_T$ (right) are shown for three different cases as a function of Y_c (Case F: $K_s = 2000\,\mathrm{s}^{-1}$, $\kappa_c = -2000\,\mathrm{m}^{-1}$, Case G: $K_s = 6000\,\mathrm{s}^{-1}$, $\kappa_c = -4000\,\mathrm{m}^{-1}$, Case H: $K_s = 10000\,\mathrm{s}^{-1}$, $\kappa_c = -6000\,\mathrm{m}^{-1}$)

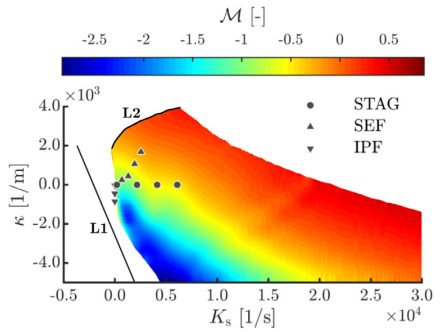

Fig. 9. Markstein number for lean H_2-air flames ($\phi = 0.5$, $p = 1$ atm, $T_0 = 300$ K) in the (K_s, κ)-parameter space.

structures. This could become relevant for multi-dimensional flame modeling in the context of tabulated chemistry approaches. These methods often rely on canonical flame solutions for the construction of look-up tables especially considering the significant changes of key quantities (such as the burning velocity) with strain and curvature. Hence, these modeling strategies could benefit from the CSM discussed here, incorporating a wider variability of stretch effects on premixed flame structures.

Declaration of Competing Interest

The authors declare that they have no known competing financial interests or personal relationships that could have appeared to influence the work reported in this paper.

Acknowledgments

Financial support is kindly acknowledged from the German Research Foundation (DFG) - Project no. 411275182 and the National Natural Science Foundation of China – Project no. 51861135309.

References

[1] J.A. van Oijen, A. Donini, R.J.M. Bastiaans, J.H.M. ten Thije Boonkkamp, L.P.H. de Goey, *Prog. Energy Combust. Sci.* 57 (2016) 30–74.
[2] O. Gicquel, N. Darabiha, D. Thévenin, *Proc. Combust. Inst.* 28 (2) (2000) 1901–1908.
[3] N. Peters, *Symp. (Int.) Combust.* 21 (1) (1988) 1231–1250.
[4] C. Law, C. Sung, *Prog. Energy Combust. Sci.* 26 (4–6) (2000) 459–505.
[5] R.W. Pitz, S. Hu, P. Wang, *Prog. Energy Combust. Sci.* 42 (0) (2014) 1–34.
[6] G. Fru, G. Janiga, D. Thévenin, *Flow Turb. Combust.* 88 (4) (2012) 451–478.
[7] A. Scholtissek, P. Domingo, L. Vervisch, C. Hasse, *Proc. Combust. Inst.* 37 (2018) 1529–1536.
[8] A. Scholtissek, P. Domingo, L. Vervisch, C. Hasse, *Combust. Flame* 207 (2019) 342–355.
[9] F.A. Williams, in: AGARD Conference Proceeding, 1975, 1975.
[10] S. Chung, C. Law, *Combust. Flame* 55 (1) (1984) 123–125.
[11] G.R.A. Groot, J.A. van Oijen, L.P.H. de Goey, K. Seshadri, N. Peters, *Combust. Theor. Model.* 6 (4) (2002) 675–695.
[12] G.K. Giannakopoulos, A. Gatzoulis, C.E. Frouzakis, M. Matalon, A.G. Tomboulides, *Combust. Flame* 162 (4) (2015) 1249–1264.
[13] M. Matalon, *Combust. Sci. Technol.* 31 (3–4) (1983) 169–181.
[14] R.J. Kee, J.A. Miller, G.H. Evans, G. Dixon-Lewis, *Symp. (Int.) Combust.* 22 (1) (1989) 1479–1494.
[15] D. Bradley, P.H. Gaskell, X.J. Gu, *Combust. Flame* 104 (1–2) (1996) 176–198.
[16] Z. Chen, X. Gou, Y. Ju, *Combust. Sci. Technol.* 182 (2) (2010) 124–142.

[17] Z. Chen, X. Qin, Y. Ju, Z. Zhao, M. Chaos, F.L. Dryer, *Proc. Combust. Inst.* 31 (1) (2007) 1215–1222.
[18] C.K. Law, in: Combustion Physics, Cambridge University Press (CUP), 2006.
[19] C.F. Curtiss, J.O. Hirschfelder, *J. Chem. Phys.* 17 (6) (1949) 550–555.
[20] A. Ern, V. Giovangigli, in: Multicomponent Transport Algorithms, Springer, Berlin Heidelberg, 1994.
[21] Y. Wang, W. Han, Z. Chen, *Proc. Combust. Inst.* 37 (2) (2019) 1623–1630.
[22] A.J. Aspden, M.S. Day, J.B. Bell, *J. Fluid Mech.* 680 (2011) 287–320.
[23] J. Schlup, G. Blanquart, *Proc. Combust. Inst.* (2018).

P2 Combust. Flame 232 (2021), 111532

X. Chen, **H. Böttler**, A. Scholtissek, C. Hasse, and Z. Chen. Effects of stretch-chemistry interaction on chemical pathways for strained and curved hydrogen/air premixed flames. In: Combust. Flame 232 (2021), 111532. DOI: 10.1016/j.combustflame.2021.111532

Author contributions

Tab. P.2: Author contributions to publication [P2] following CRediT [117]

Hannes Böttler	Numerical investigation of flamelet parameter spaces Conduction of the numerical investigation (supporting) Conceptualization of the numerical investigation (supporting) Writing – Original draft (supporting) Data analysis and visualization (equal)
Xinyi Chen	Conceptualization of the numerical investigation (lead) Numerical investigation of canonical flames configurations Interpretation and discussion of the numerical results (lead) Data analysis and visualization (equal) Writing – Original draft (lead) Main author
Arne Scholtissek	Supervision of HB (equal)
Christian Hasse	Supervision of HB (equal) Funding acquisition
Zheng Chen	Conceptualization of the numerical investigation (supporting) Corresponding author Supervision of XC Funding acquisition
All co-authors	Interpretation and discussion of the numerical results (supporting) Writing – Review & Editing

Use of publication contents in finalized and ongoing dissertations

Parts of this publication are used in the dissertation of Xinyi Chen at Peking University who conducted the numerical study and was the main author of the publication. (Xinyi Chen (2022): Numerical studies on forced ignition of premixed flames. Dissertation.)

This publication is part of the ongoing dissertation of Hannes Böttler at the Institute for Simulation of reactive Thermo-Fluid Systems at the Technical University of Darmstadt, Germany.

Other than the dissertation of Xinyi Chen and the ongoing dissertation of Hannes Böttler, this publication is not the subject of any further ongoing or completed dissertation.

Combustion and Flame 232 (2021) 111532

Contents lists available at ScienceDirect

Combustion and Flame

journal homepage: www.elsevier.com/locate/combustflame

Effects of stretch-chemistry interaction on chemical pathways for strained and curved hydrogen/air premixed flames

Xinyi Chen[a], Hannes Böttler[b], Arne Scholtissek[b], Christian Hasse[b], Zheng Chen[a,*]

[a] SKLTCS, CAPT, BIC-ESAT, Department of Mechanics and Engineering Science, College of Engineering, Peking University, Beijing 100871, China
[b] Institute for Simulation of reactive Thermo-Fluid Systems, TU Darmstadt, Otto-Berndt-Straße 2, 64287 Darmstadt, Germany

ARTICLE INFO

Article history:
Received 18 December 2020
Revised 26 May 2021
Accepted 26 May 2021

Keywords:
Stretch-chemistry interaction
Chemical pathway
Strain
Curvature
Hydrogen

ABSTRACT

In most combustion scenarios, stretch-chemistry interaction can directly alter the flame structure and combustion properties of a flammable mixture. In this study, the effects of stretch-chemistry interaction on chemical pathways of hydrogen oxidation are numerically investigated by considering laminar Inwardly Propagating Flames (IPF) and Outwardly Propagating Flames (OPF). One-dimensional transient simulations considering detailed chemistry and transport are conducted for different hydrogen/air mixtures with Lewis numbers well below and above unity. It is observed that the chemical pathways are affected by both flame stretch and flame propagation process. The relative roles of dominant elementary reactions vary with the Lewis number. In IPF and OPF, the negative and positive stretch rate are found to have opposite effects on the chemical pathway. When the relative importance of a reaction is enhanced by the positive stretch in OPF, it is weakened by the negative stretch in IPF. Furthermore, the chemical pathways obtained in this study are compared with other canonical flame configurations in previous work. It is observed that the relative importance of individual reaction is similar in different flame configurations, while disagreement is noticed in the quantitative contributions to the heat release and radical production. The disagreement is due to the different combinations of strain and curvature embodied in the stretch rate. To illustrate the individual role of the two stretch components respectively originating from hydrodynamic strain and flame curvature, a recently developed composition space model is used to decouple the influence of strain and curvature. It is found that these two stretch components have different effects upon chemical pathways. Overall, the hydrogen chemical pathway is more sensitive to the stretch originating from the curved flame propagation than to the flow field strain rate. Though the stretch rate is sufficient to characterize the flame chemistry for fuel-rich hydrogen/air flames with a negative stretch rate, more specific information on strain and curvature is required for fuel-lean and stoichiometric hydrogen/air flames.

1. Introduction

Turbulent premixed combustion is important in many applications. For example, fuel-lean premixed combustion can help to achieve high efficiency and low emissions in both automobile engines and gas turbines. Recent requirements for pollution control have further increased considerable interest in hydrogen combustion due to its promising applications in near future for zero carbon emission. Since understanding of chemical kinetics and flame dynamics of premixed turbulent hydrogen/air combustion is essential to developing advanced combustion engines, it has received great attention recently.

Turbulent premixed combustion in practical devices is complicated since it involves interaction among turbulence, molecular transport and chemical kinetics [1]. For example, turbulence is well known for its stretch effect on the large scale topology and flame front wrinkling [2]. Coupling with the Lewis number of the deficient reactant, the flame stretch affects the local temperature and reactant concentration distributions within the reaction zone [3] and thereby changes chemical reactions therein. On the other hand, the chemical reactions alter the flame structure and the flow field, resulting in changes in the local stretch rate. Therefore, combustion is affected by the two-way interaction between chemical kinetics and stretch rate. In hydrogen combustion, the fast diffusion of H_2 and H atoms strongly affects the flame due to its coupling with the stretch rate [4–6]. Therefore, it is essential to understand the effects of stretch-chemistry interaction in hydrogen combustion.

* Corresponding author.
E-mail address: cz@pku.edu.cn (Z. Chen).

https://doi.org/10.1016/j.combustflame.2021.111532
0010-2180/

Chemical reaction pathway assesses the relative roles of different reaction steps in heat release and radical production [7], and thereby it provides a global analysis to identify the direct influence of stretch rate on chemical kinetics. In the literature, many studies [7–9] have been conducted to understand the coupling between stretch and chemistry in laminar and turbulent hydrogen flames. For example, Dasgupta et al. [7] examined the influence of turbulence on chemistry for lean premixed hydrogen/air flames and found that the kinetics of highly turbulent, lean premixed hydrogen–air flames is not markedly different from their steady, unstretched 1D counterparts. Similar conclusions were obtained in their studies for other fuels such as methane [10] and n-dodecane [2]. However, in these studies, a global stretch rate defined by turbulence intensity was used and stretch effects are often assessed in a statistical manner for the entire turbulent flame. Therefore, the local changes in chemical pathways may not manifest themselves strongly when averaged over the entire flame in these studies. Furthermore, in turbulent flames multiple mechanisms exist through which the chemical pathway could be altered. For example, turbulence can enhance the transport of species along the flamelet and cause changes in local reaction pathways [8,9,11]. Besides, in the work of Aspden et al. [8], the enhanced radical pool due to turbulent stirring was observed in lean premixed hydrogen combustion. These studies indicate that turbulence can change chemical kinetics in a variety of ways and these effects are always coupled with each other in turbulent flame configurations. Currently, the stretch-chemistry interaction in hydrogen combustion is still not fully understood at a fundamental level.

Compared to turbulent flames, laminar flames can be used to get more detailed understanding of the stretch-chemistry interaction. Therefore, the first objective of this study is to assess the effects of stretch-chemistry interaction on chemical pathways without interference from turbulence. In Dasgupta et al.'s work [7], they also considered laminar steady stretched flames in a counterflow configuration which are subjected to positive tangential straining with zero curvature. However, it was shown for turbulent combustion that multi-dimensional flame configurations can experience a much wider range of stretch conditions including substantial negative strain effects and large curvatures [12]. Therefore, in our study, the laminar outwardly and inwardly propagating flame configurations with positive and negative flame curvature are considered. An outwardly propagating flame (OPF) is initiated from central ignition in a quiescent flammable mixture. During the transient evolution and propagation of the ignition kernel, the flame is exposed to a stretch rate ranging from 10^0 to $10^4\ s^{-1}$ [13,14]. An inwardly propagating flame (IPF) is difficult to establish practically in a laboratory, but it can be studied in numerical simulations [15,16]. Therefore, OPF and IPF can provide a wide positive and negative stretch rate parameter space for investigation. Here, one-dimensional (1D) numerical simulations, considering detailed chemistry and transport, are conducted for the transient IPF and OPF. For hydrogen/air mixtures, effective Lewis number well below and above unity can be achieved by changing the equivalence ratio. Therefore, stretch-chemistry interactions at different Lewis numbers can be studied. We shall explore how the hydrogen chemical pathway is altered when the premixed laminar flame is exposed to positive or negative stretch rate at different Lewis numbers.

Additionally, it is well-known that the total stretch rate, K, consists of two parts [17]: $K{=}K_s{+}K_c$, where K_s denotes the hydrodynamic strain by the flow field and K_c originates from the curved flame propagation. We have $K_s{=}\nabla_t \cdot \mathrm{u}_t - (\mathrm{u}\cdot\mathrm{n})\,\kappa$, where $\nabla_t \cdot \mathrm{u}_t$ represents flame-tangential straining by the flow and n is the flame-normal unit vector, and $K_c{=}S_d\,\kappa$, where S_d is the displacement speed and κ is the flame curvature. However, on the isosurface of a turbulent flame, strain and curvature are correlated with each other and flame stretch is often assessed in terms of a single-valued Karlovitz number [2,7,10]. It is not clear how these two stretch components individually affect the chemical pathway. Therefore, the second objective of present study is to investigate the individual effects of K_s and K_c upon flame chemistry. To this end, a recently proposed composition space model (CSM) [18–20], which can provide premixed flame structures for arbitrary combinations of strain and curvature, is used here to perform a systematic analysis for strained and curved laminar hydrogen/air flames.

2. Model and methods

We consider laminar premixed H_2/air flames at different stretch conditions. The unburned H_2/air mixtures are at $T_0 = 298$ K and $P_0 = 1$ atm. Fuel-lean ($\phi = 0.4$), stoichiometric, and fuel-rich ($\phi = 5.1$) H_2/air mixtures with Lewis numbers of Le = 0.43, 1.05 and 2.3 [21], respectively, are considered. The stretched flame structures are obtained by two methods: one is based on physical space model for propagating spherical flames, while the other is based on Composition Space Model (CSM) recently proposed by Scholtissek et al. [18,19]. These two methods are introduced below.

2.1. Physical space model

In physical space, we consider one-dimensional premixed spherical flame propagation in initially quiescent mixtures. Both outwardly and inwardly propagating spherical flames (OPF and IPF) are considered. An OPF can be initiated from a spark ignition in a quiescent mixture, and it is often used for accurate measurement of laminar flame speed (see [22] and references therein). The OPF simultaneously has positive strain and curvature, both decreasing during transient flame propagation. The IPF can be obtained by igniting a quiescent mixture in perfect spherical shape. It is difficult to be established experimentally but can be easily considered in simulations. Unlike OPF, IPF has zero strain rate and is only negatively curved [12].

The transient simulation of adiabatic spherical flame propagation in physical space is conducted using the in-house code A-SURF [23,24]. The finite volume method is used in A-SURF to solve the conservation equations for multi-component, reactive flow. Detailed chemistry and the mixture-averaged transport model [25] are considered in all simulations. Soret diffusion is important for H_2/air flames and it is therefore included in all simulations. The diffusion velocity for each species consists of three parts: the ordinary diffusion velocity due to fuel concentration gradient, the thermal (Soret) diffusion velocity due to temperature gradient [26], and the correction velocity [27] which is the same for all species and is included to ensure the compatibility of species and mass conservation equations. The CHEMKIN packages [28] are used to calculate the detailed thermal-transport properties and reaction rates. For hydrogen oxidation, we use the well-validated kinetic model developed by Li et al. [29]. A-SURF has been successfully used in previous studies on ignition [13,30], flame propagation [16], and detonation development [31,32]. More details about the governing equations, numerical schemes and code validation can be found in Refs. [23,24] and thereby are not repeated here.

Due to the spherical symmetry of OPF and IPF, the simulations are one-dimensional in a spherical coordinate. The radial coordinate is in the range of $0 \le r \le R_w$, where R_w is the computational domain size. The homogenous mixture is initially static, i.e., $u(r,\ t = 0) = 0$ cm/s, and uniformly distributed over the computational domain. Zero gradients of temperature and mass fractions are enforced at both boundaries at $r = 0$ and $r = R_w$. For OPF, the chamber radius is fixed to be $R_w = 50$ cm and the mixture is centrally ignited through the energy deposition term included in the energy equation [13,30]. When the spherical flame radius is less than $r = 5$ cm, the overall pressure rise is below 1‰ and

thereby the flame propagation process is nearly isobaric. For IPF, a premixed flame structure is initially imposed around $r = 10$ cm, inside (i.e. $0 < r < 10$ cm) and outside (i.e. $r > 10$ cm) of which are unburned and burned mixtures, respectively. The initial temperature and mass fraction profiles within the flame structure are obtained from one-dimensional unstretched planar flame solution by PREMIX [28]. For IPF, a very large computational domain of $R_w = 200$ cm is used to ensure that the flame propagation is nearly isobaric.

2.2. Composition space model

In addition to the canonical flames where the flame structure is resolved in a fixed coordinate system, the reaction progress variable Y_c can be used as a flame-attached coordinate for a premixed flame which spans the so-called progress variable space. We define it as a weighted sum of species, $Y_c = \sum_i^{n_s} \alpha_i Y_i$. The transport equation for Y_c is:

$$\rho \frac{\partial Y_c}{\partial t} + \rho \mathrm{u} \cdot \nabla Y_c = -\nabla \cdot (\rho Y_c \, \mathrm{V}_c) + \dot{\omega}_c \tag{1}$$

where ρ is the density and $Y_c \mathrm{V}_c = \sum_i^{n_s} \alpha_i Y_i \mathrm{V}_i$ is the diffusive flux of the progress variable, with V_i being the diffusion velocity of species i. The source term is defined as a weighted sum of species source terms, $\dot{\omega}_c = \sum_i^{n_s} \alpha_i \dot{\omega}_c$. The motion of the flame surface, represented by a collection of Y_c-isosurfaces, is then described by the kinematic condition [33,34]:

$$\frac{\mathrm{d}Y_c}{\mathrm{d}t} = \frac{\partial Y_c}{\partial t} + s_f \cdot \nabla Y_c = 0 \tag{2}$$

and the unit vector along the flame-normal is defined as $n = \nabla Y_c / |\nabla Y_c|$. The temperature and species balance equations can be transformed into Y_c-space given a suitable choice for the progress variable. Furthermore, an equation for the progress variable gradient $g_c = |\nabla Y_c|$ is required for closure [18]. The final set of equations reads [19]:

$$\begin{aligned}\rho \frac{\partial Y_i}{\partial \tau} = & -g_c \frac{\partial}{\partial Y_c}\left(g_c \, \rho Y_i \tilde{V}_i\right) + g_c \frac{\partial}{\partial Y_c}\left(g_c \, \rho Y_c \tilde{V}_c\right) \frac{\partial Y_i}{\partial Y_c} \\ & + \rho g_c \kappa \left(Y_i \tilde{V}_i - Y_c \tilde{V}_c \frac{\partial Y_i}{\partial Y_c}\right) - \dot{\omega}_c \frac{\partial Y_i}{\partial Y_c} + \dot{\omega}_i \end{aligned} \tag{3}$$

$$\begin{aligned}\rho \frac{\partial T}{\partial \tau} = & \frac{g_c}{c_p} \frac{\partial}{\partial Y_c}\left(g_c \lambda \frac{\partial T}{\partial Y_c}\right) + g_c \frac{\partial}{\partial Y_c}\left(g_c \, \rho Y_c \tilde{V}_c\right) \frac{\partial T}{\partial Y_c} \\ & - \rho g_c^2 \sum_k^{n_s} \frac{c_{p,k}}{c_p} \rho Y_k \tilde{V}_k \frac{\partial T}{\partial Y_c} - \rho g_c \kappa \left(\frac{\lambda}{\rho c_p} + Y_c \tilde{V}_c\right) \frac{\partial T}{\partial Y_c} \\ & - \dot{\omega}_c \frac{\partial T}{\partial Y_c} + \frac{\dot{\omega}_T}{c_p} \end{aligned} \tag{4}$$

$$\begin{aligned} 0 = & -g_c^2 \frac{\partial^2}{\partial Y_c^2}\left(g_c \, \rho Y_c \tilde{V}_c\right) + g_c^2 \frac{\partial}{\partial Y_c}\left(\kappa \rho Y_c \tilde{V}_c\right) \\ & - \dot{\omega}_c \frac{\partial g_c}{\partial Y_c} + g_c \frac{\partial \dot{\omega}_c}{\partial Y_c} + \rho K_s g_c \end{aligned} \tag{5}$$

where $\tilde{V}_i$ represents the diffusion velocity of species i with respect to the Y_c-composition space, λ is the heat conductivity, c_p is the heat capacity, and $\dot{\omega}_T$ is the heat release.

It has been shown that these equations can recover the structure and characteristics of canonical flame configurations, by prescribing representative values for the external parameters including strain K_s and curvature κ [19, 20]. Setting strain and curvature to be zero, the laminar flame speed can be computed by solving the closed system of equations [18]. Homogeneous ignition is recovered by the CSM in the asymptotic limit of $g_c \to 0$ [18,19]. The flame structure of OPF and IPF is recovered by prescribing constant values for strain and curvature in the CSM, while they vary in the physical space. These representative values are extracted at the maximum heat release peak in spherical flames. This parameterization of the CSM allows to study the influence of arbitrary combinations of strain and curvature [20].

In this study, three flame databases are created for hydrogen/air flames at different equivalence ratios of $\phi = 0.4$, 1.0 and 5.1. The progress variable is defined as $Y_c = Y_{H2O} - Y_{O2} - Y_{H2}$ for the lean case ($\phi = 0.4$, around 12,000 calculations) and rich case ($\phi = 5.1$, around 4000 calculations), while it is $Y_c = Y_{H2O} - Y_{O2} - 10\,Y_{H2}$ for the stoichiometric case ($\phi = 1.0$, around 18,000 calculations). In agreement with the physical space model, a mixture-averaged diffusion model [25] is utilized and thermal diffusion [26] is considered in this study.

2.3. Chemical pathway analysis

For premixed flames, the contribution of different elementary reactions to the heat release and the production/consumption of key radicals can be quantified through chemical pathway analysis [2,7,10].

In the physical space, the heat release from reaction k and the total global heat release across the spherical flame can be integrated as:

$$q_k = \int_{R_{in}}^{R_{out}} 4\pi r^2 Q_k(r) dr, \; q_{total} = \int_{R_{in}}^{R_{out}} 4\pi r^2 Q(r) dr \tag{6}$$

where $Q_k(r)$ is the heat release from reaction k and $Q = \sum_k Q_k$. The inner and outer bounds, R_{in} and R_{out}, are determined by the requirement of $Q = 0.001 Q_{max}$. The contribution of reaction k to the total heat release is q_k / q_{total}.

The net production of species i from reaction k and the total net production of species i across the flame are:

$$\omega_{ip,k} = \int_{R_{in}}^{R_{out}} 4\pi r^2 \omega_{ik}(r) dr, \; \omega_{ip} = \int_{R_{in}}^{R_{out}} 4\pi r^2 \omega_{\mathrm{i}}(r) dr \tag{7}$$

where $\omega_{ik}(r)$ is the formation of species i from reaction k and $\omega_i = \sum_k \omega_{ik}$. The contribution of reaction k to the total production is $\omega_{ip,k} / \omega_{ip}$.

Similarly, the net consumption of species i from reaction k and the total net consumption of species i across the flame are:

$$\omega_{ic,k} = \int_{R_{in}}^{R_{out}} 4\pi r^2 \omega_{ik}(r) dr, \;\; \omega_{ic} = \int_{R_{in}}^{R_{out}} 4\pi r^2 \omega_{\mathrm{i}}(r) dr \tag{8}$$

where $\omega_{ik}(r)$ is the consumption of species i from reaction k and $\omega_i = \sum_k \omega_{ik}$. The contribution of reaction k to the total consumption is $\omega_{ic,k} / \omega_{ic}$.

In CSM calculations, the physical space coordinate is not initially available as flame structures are solved in composition space. Therefore, the physical space coordinate r must be reconstructed from the composition space. The reconstruction can be done with the progress variable gradient g_c, since $\mathrm{d}r = dY_c / g_c$. Further details about the reconstruction are presented in appendix A. Based on the reconstructed physical space coordinate, the curvature profile can also be reconstructed. A comprehensive parameter study is shown in appendix B where the influence of reconstructed curvature profile on the flame structure is discussed. It is noted that the assumption of constant strain and curvature only holds for the laminar flames studied in this work. In turbulent flames, strain rate varies inside the flame front.

With the reconstructed flame coordinate r, the physical space integral for heat release of reaction k can be performed in composition space:

$$q_k = \int 4\pi r^2 \frac{Q_k(Y_c)}{g_c} \mathrm{d}Y_c \tag{9}$$

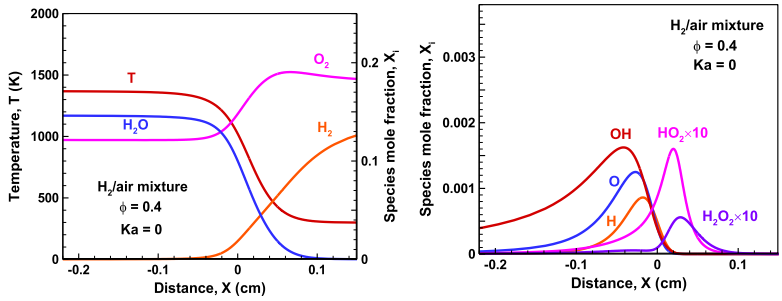

(a)

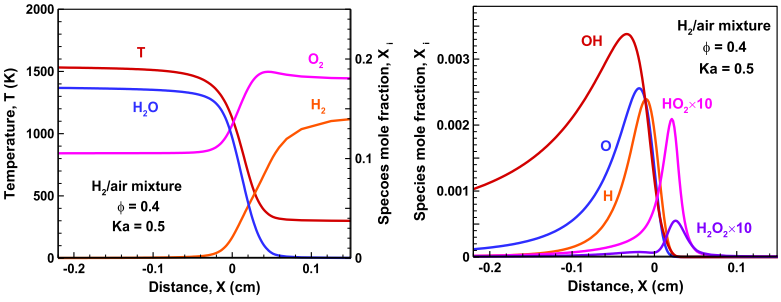

(b)

Fig. 1. Structures of (a) an unstretched ($Ka = 0$) and (b) a stretched ($Ka = 0.5$) fuel-lean hydrogen/air flame with $\phi = 0.4$.

Integrations performed for consumption and production rates of respective species follow the same structure as Eq. (9).

3. Results and discussion

3.1. Stretch-chemistry interaction in canonical flame configurations

In this subsection, we assess the stretch-chemistry interaction in canonical flame configurations. First, the flame structures and propagation speeds of OPF and IPF are examined. Then, the chemical pathways involved in OPF and IPF are analyzed. Finally, a comparison of chemical pathways in different flame configurations including both laminar and turbulent flames is performed.

We first study the change of flame structures and propagation speed with the stretch rate for OPF and IPF in H_2/air mixtures with different equivalence ratios. In simulations, the flame radius position, R_f, is defined as the position of maximum total heat release rate. The flame propagation speed is defined as $U = \mathrm{d}R_f/\mathrm{d}t$. In OPF and IPF, U represents the stretched flame speed relative to the static burned and unburned gas, respectively. For both OPF and IPF, the overall stretch rate is $K = 2U/R_f$. The Karlovitz number is defined as $Ka = K\delta/S_L$, where δ and S_L are respectively the flame thickness (defined based on maximum temperature gradient) and laminar flame speed of the one-dimensional, unstretched, adiabatic, planar flame, which can be obtained from PREMIX [28].

In order to get a fundamental understanding of stretch-chemistry interactions, structures of unstretched (obtained from PREMIX [28]) and stretched (during the propagation of OPF) laminar premixed H_2/air flames are first illustrated in Figs. 1–2 for fuel-lean and fuel-rich conditions, respectively.

For fuel-lean H_2/air flames with $\phi = 0.4$, due to the effects of preferential diffusion, faster diffusion of hydrogen compared to oxygen increases the local stoichiometry [35,36]. Therefore, the flame temperature for $Ka = 0.5$ is higher than that for the unstretched flame (roughly 1520 K for the stretched flame in Fig. 1(b), compared to roughly 1380 K for the unstretched flame in Fig. 1(a)). The increase in temperature correspondingly results in faster reaction rates and higher radical concentrations in the reaction zone of the stretched flame compared to the unstretched flame (e.g. the maximum mole fractions of OH and H are roughly 0.0035 and 0.0024 in the stretched flame in Fig. 1(b), but only 0.0018 and 0.0008 in the unstretched flame in Fig. 1(a)), thus enhancing the flame propagation speed for the stretched flame.

The effect of stretch on flame structure for fuel-rich H_2/air flame with $\phi = 5.1$ is opposite to the behavior of fuel-lean flame. As shown in Fig. 2, finite levels of stretch cause flame temperatures to be lower than for the unstretched flame (roughly 1300 K for the stretched flame in Fig. 2(b), compared to roughly 1350 K for the unstretched flame in Fig. 2(a)). This is because for fuel-rich flames, faster diffusion of hydrogen compared to oxygen causes the flame to become even richer [35,36]. As a result, the decreased temperature promotes slower reaction rates and lower radical concentrations in the reaction zone of stretched flame compared to the unstretched flame (e.g. the maximum mole fraction of H is roughly

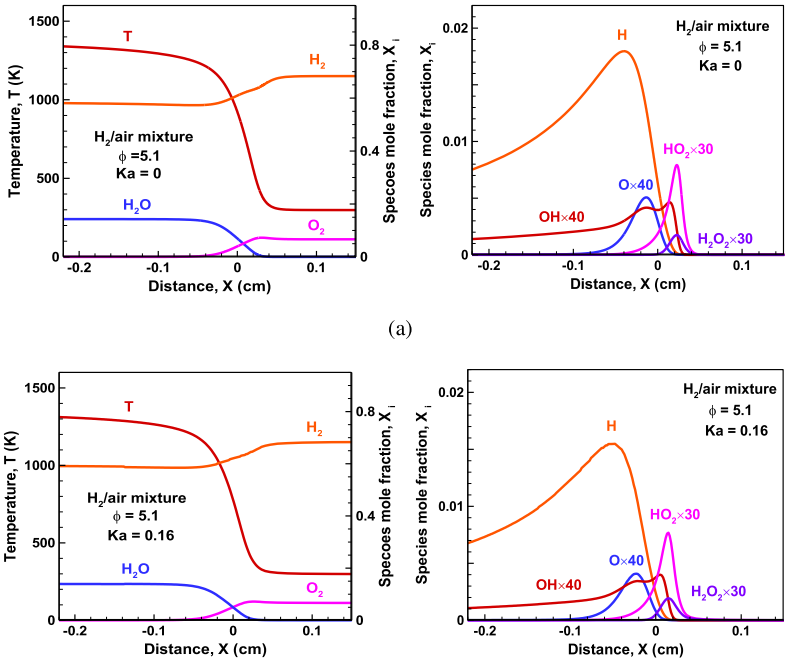

Fig. 2. Structures of (a) an unstretched ($Ka = 0$) and (b) a stretched ($Ka = 0.16$) fuel-rich hydrogen/air flame with $\phi = 5.1$.

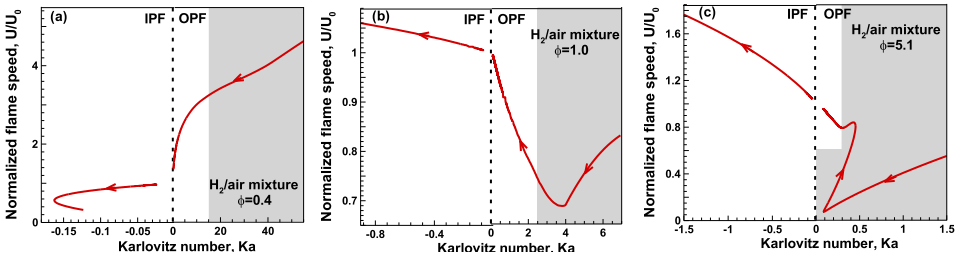

Fig. 3. Change of normalized flame propagation speed with Karlovitz number during the spherical flame propagation in H_2/air mixtures with (a) $\phi = 0.4$, (b) $\phi = 1.0$ and (c) $\phi = 5.1$. The arrows indicate the direction of flame propagation and the shaded regions represent ignition-influenced phase.

0.018 in the stretched flame in Fig. 2(b), but only 0.015 in the unstretched flame in Fig. 2(a)), resulting a lower flame propagation speed for the stretched flame.

Fig. 3 shows the normalized flame propagation speed as a function of Karlovitz number for OPF and IPF in fuel-lean, stoichiometric and fuel-rich H_2/air mixtures. Here U_0 is the flame propagation speed at zero stretch rate. In Fig. 3, the results for IPF and OPF are separated by the dashed line at $Ka = 0$ since IPF and OPF are exposed to negative and positive stretch rates, respectively. Fig. 3 clearly shows that the flame propagation speed of H_2/air strongly depends on the stretch. Besides, the change of the normalized flame propagation speed with Karlovitz number has opposite trends for $\phi = 0.4$ and $\phi = 1.0$ and 5.1. This is because the sensitivity of U to K depends on the Lewis number, which increases from $Le = 0.43$ for $\phi = 0.4$ to $Le = 2.3$ for $\phi = 5.1$ [3,37]. The OPF is initiated by energy deposition, and the initial ignition kernel has very large curvature. Therefore, the OPF starts from a very large Karlovitz number, at which the flame kernel propagation is mainly driven by the ignition energy deposition. For H_2/air $\phi = 5.1$ with Lewis number above unity, Fig. 3(c) shows that there are different regimes during the ignition kernel and spherical flame propagation. These regimes were discussed by Wang et al. [13] in their study on the ignition process in fuel-lean n-decane/air mixtures. After the unsteady transition, the OPF can propagate in a quasi-steady manner approaching zero stretch rate. Unlike OPF, IPF starts from a large flame radius corresponding to a small negative stretch

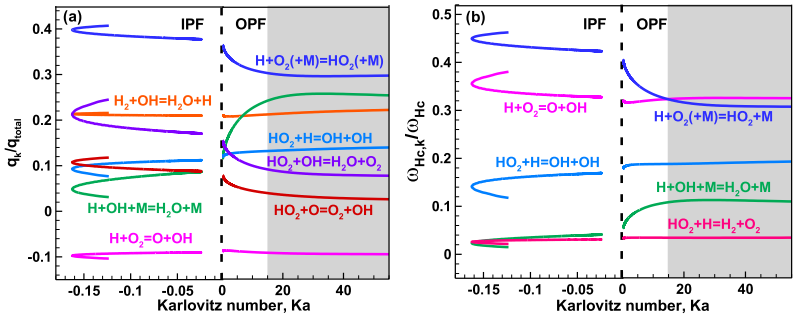

Fig. 4. Change of (a) Fractional heat release and (b) H radical consumption with Karlovitz number during the spherical flame propagation in a fuel-lean H_2/air mixture with $\phi = 0.4$. The shaded regions represent ignition-influenced phase.

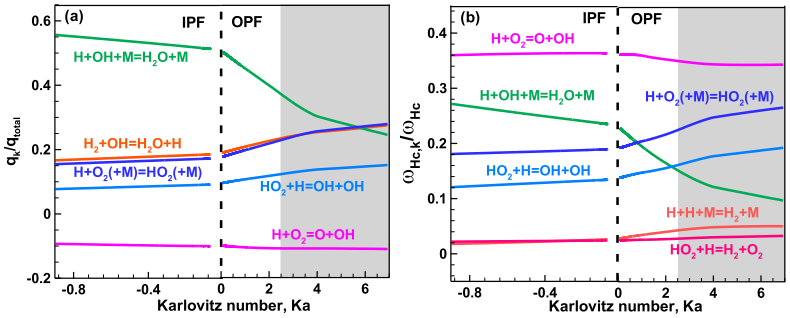

Fig. 5. Change of (a) fractional heat release and (b) H radical consumption with Karlovitz number during the spherical flame propagation in a stoichiometric H_2/air mixture. The shaded regions represent ignition-influenced phase.

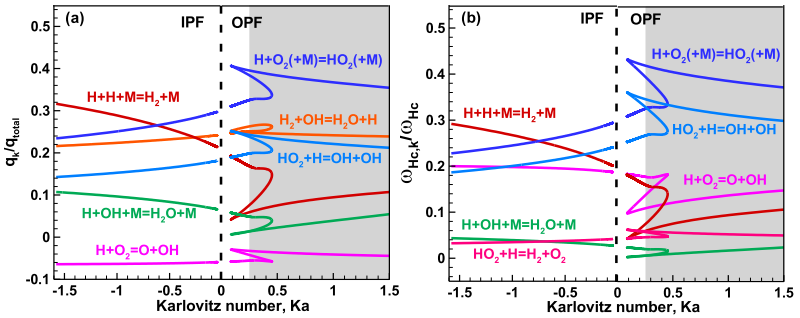

Fig. 6. Change of (a) fractional heat release and (b) H radical consumption with Karlovitz number during the spherical flame propagation in a fuel-rich H_2/air flame with $\phi = 5.1$. The shaded regions represent ignition-influenced phase.

rate at the beginning. During the inward propagation, the magnitude of the stretch rate imposed on IPF increases and so do the stretch effects. For the IPF in fuel-lean H_2/air ($\phi = 0.4$) mixture with $Le = 0.43$, Fig. 3(a) shows a C-shaped curve for IPF, indicating that the magnitude of the stretch rate first increases and then decreases. This is due to the competition between the changes in flame propagation speed and flame curvature. The present results on OPF and IPF are consistent with those in previous studies [13,14,16].

To assess the stretch-chemistry interaction, we conduct the chemical pathway analysis at each time step during the spherical flame propagation. Figs. 4–6 plot the fractional heat release (normalized by the total heat release, i.e. q_k/q_{total}) and H radical consumption (normalized by the total H radical consumption, i.e. $\omega_{Hc,k}/\omega_{Hc}$) associated with different elementary reactions. Only reactions with relatively large contributions, i.e., $q_k/q > 10\%$ or $\omega_{Hc,k}/\omega_{Hc} > 10\%$, are shown here. It is noted that for OPF, the high Karlovitz number corresponds to the ignition-influenced phase.

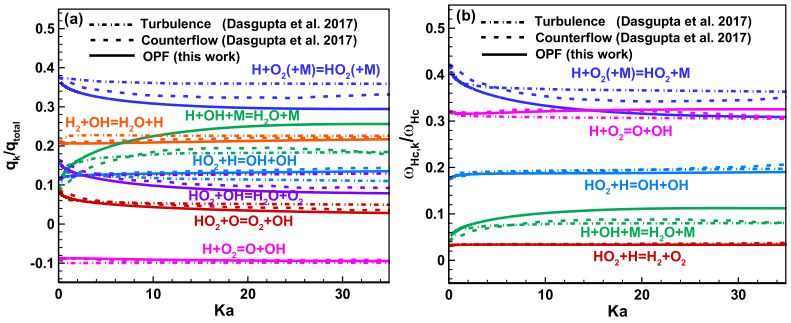

Fig. 7. Change of (a) fractional heat release and (b) H radical consumption with Karlovitz number for different flames propagating in a fuel-lean H_2/air mixture with $\phi = 0.4$. The results for laminar counterflow flame and turbulent flame are from Dasgupta et al. [7].

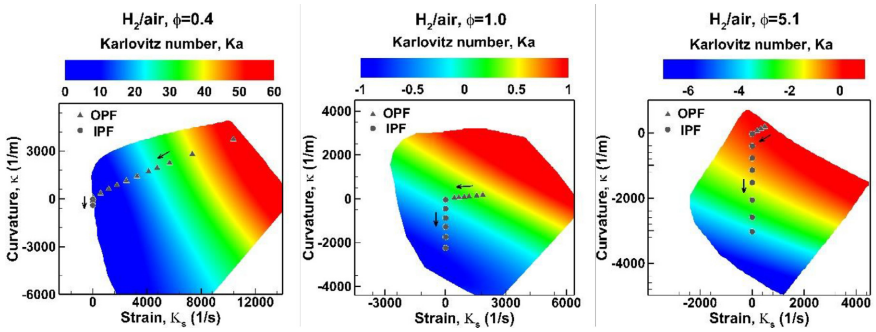

Fig. 8. Strain-curvature parameter space for H_2/air flames with $\phi = 0.4$, 1.0 and 5.1 ($T_0 = 298$ K and $P = 1$ atm) characterized by Karlovitz number. Canonical flame solutions (symbols) are shown for reference. The arrows indicate the direction of flame propagation.

The chemical pathway during this phase is affected by the initialization of energy deposition (e.g., heat source, size, intensity, timing, etc.). Therefore, the following discussion of stretch-chemistry interactions are limited to the flame phase with relatively low Karlovitz number (i.e. the monotonic part without the interference from ignition, which are $0<Ka<15$ for $\phi = 0.4$, $0 < Ka < 2.5$ for $\phi = 1.0$ and $0 < Ka < 0.25$ for $\phi = 5.1$). The chemical pathway during ignition-influenced phase is only briefly addressed here and needs to be explored in future studies.

For fuel-lean H_2/air flame with $\phi = 0.4$, the trends of the fractional values in Fig. 4 are similar to the trend in the *U-Ka* plot in Fig. 3(a). For the OPF, the relative contributions change monotonically with the stretch rate. However, C-shaped curves are obtained for the IPF and there are two flame structures for the same value of *Ka* in certain range. This indicates that the chemical pathway depends not only on the stretch rate but also on the flame propagation process. For the IPF, the flame stretch is due to the self-propagation of the curved flame, i.e., $K=K_c=S_d\kappa$; and the same stretch rate can be reached for two sets of (S_d, κ). Furthermore, Fig. 4 shows that the negative and positive stretch have opposite effects on the chemical pathway. When the relative importance of the reaction is enhanced in OPF, it is weakened by the negative stretch of IPF; and vice versa. At zero stretch rate, the fractional heat release and H radical consumption of IPF and OPF approaches the same value corresponding to an unstretched planar flame.

Fig. 4(a) shows that the reaction H + O_2 (+*M*) = HO_2 (+*M*) is the most dominant exothermic reaction. Other main exothermic reactions are those involved in OH consumption: H_2+OH = H_2O+H, HO_2+OH = H_2O+O_2 and H+OH+*M* = H_2O+*M*. For H radical consumption, H + O_2(+*M*) = HO_2(+*M*) is the most important reaction and the next two most dominant reactions are H + O_2 = O+OH and HO_2+H = OH+OH. Fig. 4 shows that the IPF only experiences a narrow negative stretch range with $-0.16 < Ka < -0.02$. Therefore, the relative importance of these reactions remains to be in the same order for $Ka < 0$. Nevertheless, the negative stretch has an obvious impact on the fractional heat release and H radical consumption; and the relative difference from the corresponding value at zero stretch is in the range of 10%~50%. The OPF exhibits a significantly larger range of stretch rate than the IPF since the initial ignition kernel is highly stretched. Consequently, the fractional heat release from reaction H+OH+*M* = H_2O+*M* at $Ka = 15$ is about two and a half times of that at $Ka = 0$. Additionally, the fractional H consumption from reaction H+OH+*M* = H_2O+*M* increases around 100% when *Ka* increases from 0 to 15.

Fig. 5 shows the results for a stoichiometric H_2/air mixture. Similar to the fuel-lean case, the fractional heat release and H radical consumption from reaction H+OH+*M* = H_2O+*M* are both strongly affected by stretch rate in the OPF while they show much smaller variations in the IPF. From the fuel-lean case to the stoichiometric case, the oxygen concentration decreases and thereby the main heat release reaction shifts from H + O_2(+*M*) = HO_2(+*M*) to H+OH+*M* = H_2O+*M*. Similar to the fuel-lean case, the H radical in stoichiometric H_2/air flame is still mainly consumed by reac-

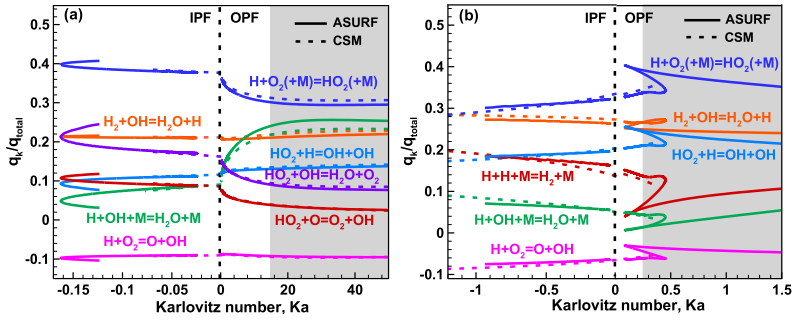

Fig. 9. Chemical pathway for (a) lean H_2/air flame with $\phi = 0.4$ and (b) rich H_2/air flame with $\phi = 5.1$ of canonical flames (solid lines) compared to calculations with the CSM (dashed lines). The shaded regions represent ignition-influenced phase.

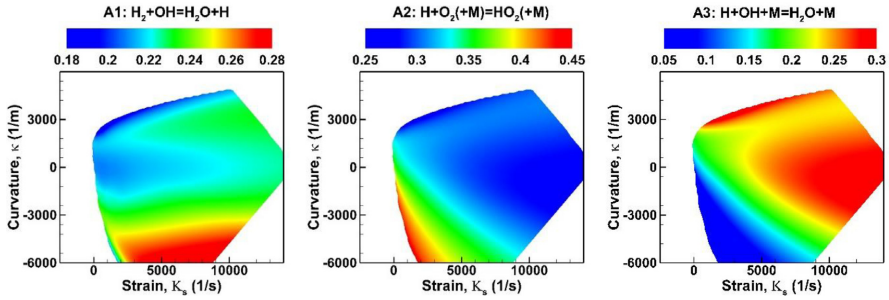

Fig. 10. Contours of fractional heat release from reactions A1-A3 over the strain-curvature parameter space for fuel-lean H_2/air flame with $\phi = 0.4$.

tions H + $O_2(+M)$ = $HO_2(+M)$ and H + O_2 = O+OH. Besides, the reaction H+OH+M = H_2O+M starts to play an essential role in H radical consumption, especially at negative stretch rate.

The results for fuel-rich H_2/air flame with $\phi = 5.1$ are shown in Fig. 6. Similar to Fig. 3(c), the contributions of the given reactions change monotonically with negative *Ka* for IPF; while non-monotonic change is observed for OPF. It is observed that the stretch rate has great impact on both fractional heat release and H radical consumption by different elementary reactions. Note that the OPF is strongly affected the ignition energy deposition and so is the chemical pathway. For fuel-rich H_2/air flames, there is a large amount of H radicals at relatively high flame temperature. Therefore, the reaction H + H + M = H_2+M starts to dominate in the contribution to total heat release and H radical consumption at high negative stretch rate, which strengthens the flame and increases the flame temperature. For positively stretched flame, reaction H + O_2 $(+M)$ = HO_2 $(+M)$ is still the most dominant one in terms of heat release and H radical consumption.

The above results are for OPF and IPF in H_2/air mixtures. Dasgupta et al. [7] considered the laminar counterflow flame and turbulent flame in the fuel-lean H_2/air mixture with $\phi = 0.4$. The present results and those from Dasgupta et al. [7] are compared in Fig. 7. Qualitative agreement is observed. Nevertheless, quantitative difference is seen for the most dominant exothermic reaction H + O_2 $(+M)$ = HO_2 $(+M)$ and H radical consumption reaction H + O_2=O+OH. Such discrepancy could be caused, in part, by two possible reasons. One is that the ignition energy deposition during the initiation of OPF affects the flame propagation at high stretch rate (i.e., small flame radius). The other one is that both stretch components originating from hydrodynamic strain and flame curvature contribute to the flame stretch rate, while they may not have identical effects upon chemical pathway. Therefore, even for the same Karlovitz number, the flame structure is not unique due to the various combinations of K_s and K_c. This scenario is more pronounced in a turbulent flame which, in the flamelet regime, can be considered as a statistical ensemble of laminar flamelets subjected to different combinations of K_s and K_c. Therefore, the fractional heat release and H radical consumption of turbulent flames are interpreted in a statistical manner. This can be further demonstrated by the low sensitivity of fractional values to flame stretch in Fig. 7 (dashed-dot line).

Based on above discussion, it is noted that the study of stretch-chemistry interaction in canonical flame configurations (i.e. IPF and OPF) is subject to certain limitations: 1) The influences of K_s and K_c are embodied in a single-valued Karlovitz number in canonical flames; 2) Canonical flames have limited range of stretch and thereby can only capture a small part of stretch effects on chemical pathway. Therefore, the composition space model (CSM), which allows arbitrary combinations of strain and curvature to be chosen, is used in the following discussion to assess the individual effects of K_s and K_c on chemical pathways. Besides, the large flame database provided by the CSM allows investigating a much wider range of stretch conditions which is beyond the limit of canonical flame solutions.

3.2. Stretch-chemistry interaction in CSM

In this subsection, we assess the individual effects of K_s and K_c on chemical pathways using the composition space model.

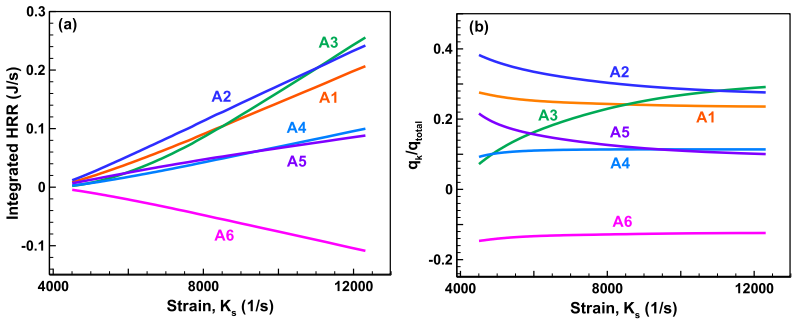

Fig. 11. Change of (a) integrated heat release and (b) fractional heat release by dominant reactions with K_s along isoline K_c=−2000 1/s for fuel-lean H_2/air flame with ϕ = 0.4. The dominant reactions are A1: H_2+OH=H_2O+H, A2: H + O_2(+M)=HO_2(+M), A3: H+OH+M = H_2O+M, A4: HO_2+H=OH+OH, A5: HO_2+OH=H_2O+O_2, A6: H + O_2=O+OH.

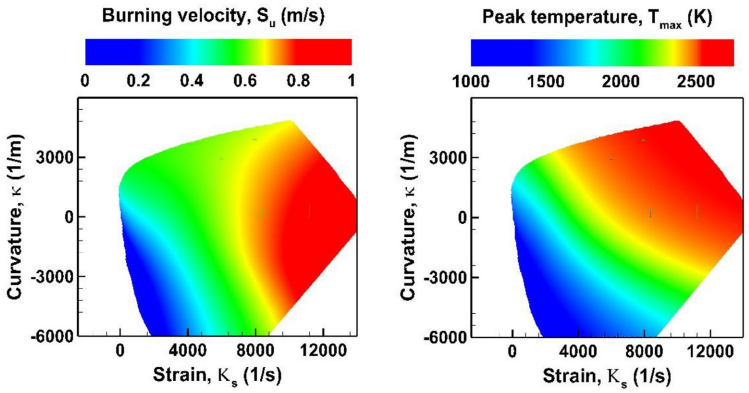

Fig. 12. Strain-curvature parameter space for fuel-lean H_2/air flame with ϕ = 0.4 characterized by burning velocity (left) and peak temperature (right).

Table 1
Key reactions relevant to the laminar flame speed and heat release for H_2/air flames at different equivalence ratios and T_0 = 298 K and P_0 = 1 atm.

Equivalence ratio	Key reactions relevant to S_u and q_{total}
ϕ = 0.4	A1: H_2+OH=H + H_2O
	A2: H + O_2 (+M)=HO_2 (+M)
	A3: H+OH+M = H_2O+M
ϕ = 1.0	B1: H_2+OH=H + H_2O
	B2: H + O_2=O+OH
	B3: H+OH+M = H_2O+M
	B4: H + O_2(+M)=HO_2(+M)
ϕ = 5.1	C1: H + O_2=O+OH
	C2: H+HO_2=2OH
	C3: H + O_2 (+M)=HO_2 (+M)
	C4: H_2+OH=H + H_2O
	C5: H + H + M = H_2+M

3.2.1. Parameter space and CSM validation

Fig. 8 shows the Karlovitz number in the attainable strain-curvature parameter space obtained with the CSM for different equivalence ratios. The parameter space is restrained by certain physical limits as discussed by Böttler et al. [20]. The canonical flame solutions are also plotted in Fig. 8 for reference. It is observed that IPF and OPF can only cover a small subset of the parameter range obtained by the CSM. Besides, the shape of the parameter space is shown to be strongly affected by the Lewis number. For fuel-lean H_2/air mixture with ϕ = 0.4 and Le = 0.43, the flame is weakened by negative stretch and strengthened by positive stretch. Therefore, the attainable parameter space is wider on positive Karlovitz number side. On the contrary, a wide negative Ka range is obtained for fuel-rich H_2/air flame with ϕ = 5.1 and Le = 2.3. For stoichiometric flames with Lewis number close to unity, the attainable positively and negatively stretched flames are comparable.

To validate the CSM, chemical pathways of IPF and OPF predicted by A-SURF in the physical space are compared with the corresponding results predicted by the CSM in Fig. 9. Overall, good agreement is observed between the canonical flame solutions and CSM results. The slight discrepancy results from the difference in boundary conditions: in CSM, both fresh and burned gases are defined far away from the reaction zone; while for OPF and IPF in physical space, the burned boundary conditions are close to the flame. During the ignition process of OPF, burned products and radical pool are generated in the ignition kernel, which causes diffusive fluxes and modifies the flame structure in the following propagation process. Similarly, in IPF heat conduction from the burned region to the reaction zone (i.e., the back-support effect) helps flame propagation at highly negative curvature where no CSM solution exists for fuel-lean H_2/air flames. The flame struc-

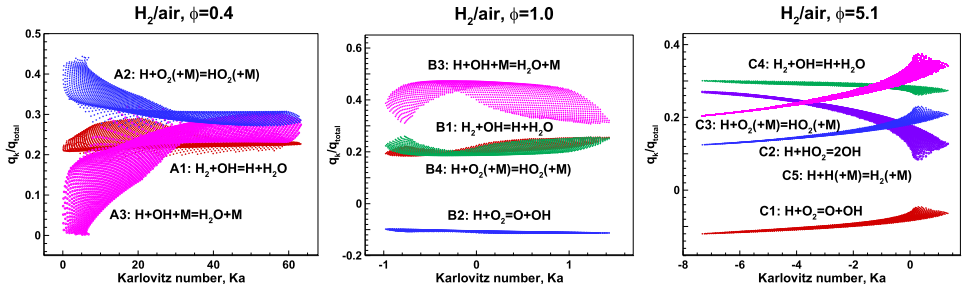

Fig. 13. Scatter of fractional heat release for key reactions involved in the H_2/air flames with the equivalence ratio of ϕ = 0.4, 1.0 and 5.1.

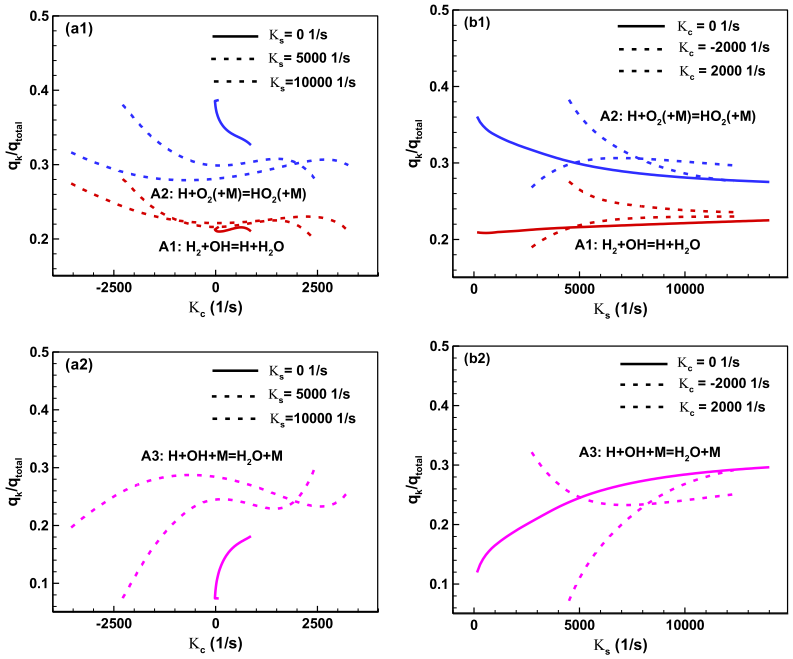

Fig. 14. Change of fractional heat release from key reactions along (a) K_s and (b) K_c isolines for fuel-lean H_2/air flame with ϕ = 0.4.

ture analysis is shown in Appendix C, where the ignition effect and back support effect are demonstrated. Besides, one limitation of the CSM for fuel-rich H_2/air flames is addressed here. The post oxidation zone of the fuel-rich flame tends to be very long. This region is dominated by reaction H + H + M = H_2+M, which slowly approaches the equilibrium state. The integral quantities defined in subSection 2.3 are very sensitive to this region. Therefore, for fuel-rich flames, the integration is only performed until heat release has decayed to 3% of the maximum on the burned side.

3.2.2. Effects of strain and curvature on chemical pathways

In this subsection, the CSM is used to assess the individual effects of K_s and K_c on chemical pathways. In following we shall address two questions:

1) Does the Karlovitz number already provide enough information to characterize flame chemistry?
2) Is the flame chemistry more sensitive to K_s or K_c?

There are around twenty elementary reactions involved in the hydrogen oxidation. Here we focus on the key reactions relevant to the laminar flame speed S_u and total heat release q_{total}. These reactions are identified through sensitivity analysis and listed in Table 1.

Fig. 10 shows the contours of fractional heat release from reactions A1: H_2+OH=H + H_2O, A2: H + O_2 (+M)=HO_2 (+M) and A3: H+OH+M = H_2O+M in the strain-curvature parameter space obtained by the CSM for fuel-lean H_2/air flames. It seems that the fractional heat release from reaction A1 is more sensitive to the curvature change than to the change of strain rate. From the bot-

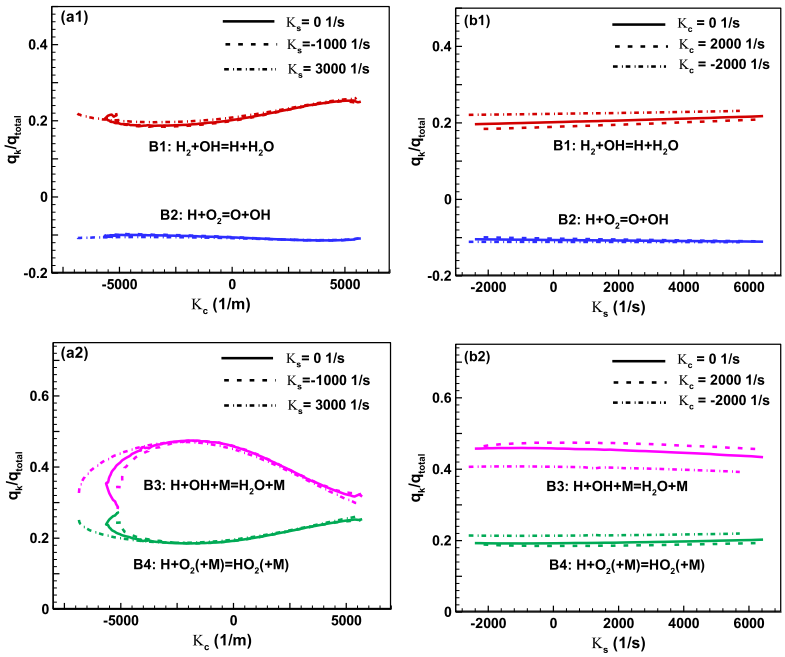

Fig. 15. Change of fractional heat release from key reactions along (a) K_s and (b) K_c isolines for stoichiometric H_2/air flame.

tom to the top boundary of the parameter space, the fractional heat release of reaction A1 is increased by 50%. Reactions A2: H + O_2 (+M)=HO_2 (+M) and A3: H+OH+M = H_2O+M are both radical-radical recombination reactions. Therefore, both strain and curvature have similar effects on the fractional heat release from reactions A2 and A3. From the bottom-left to the top-right boundary, the fractional heat release from reaction A2 decreases by a factor around 2 and the fractional heat release from reaction A3 increases by a factor around 6. Similar results are obtained for stoichiometric and fuel-rich H_2/air flames and the contours are not shown here.

These results indicate that the relative importance of different reaction steps in heat release alters under the influence of strain and curvature. It is not surprising that the reaction rates change under the effects of stretch rate and preferential diffusion, but the question is that why do relative importance of certain reactions increase and others decrease? To illustrate it, we transform the κ-K_s parameter space into K_s -K_c parameter space and plot the change of integrated heat release rate (HRR) (i.e. q_k) and fractional HRR (i.e. q_k/q_{total}) by dominant reactions with K_s along isoline $K_c = -2000$ 1/s in Fig. 11. The total stretch rate K=K_s+K_c increases with K_s along the K_c isoline. As shown before in Fig. 1, for fuel-lean flames with Lewis number smaller than unity, the temperature and radical concentrations are increased by finite levels of stretch rate. Therefore, the reaction rate as well as the integrated HRR by each reaction increases monotonically with K_s along K_c isoline in Fig. 11(a). However, since the reaction rates have different dependencies on the temperature and radical concentrations, the integrated HRR by each reaction shows different sensitivities to the change of stretch rate. For example, the integrated HRR by A3 increases more rapidly than all the other reactions. That is because for reaction A3: H+OH+M = H_2O+M, the reaction rate depends largely on the H and OH radical concentrations. As shown in Fig. 1, the mole concentrations of H and OH have the largest increase among all the radicals when stretch rate is increased. Therefore, the relative importance of A3 in heat release increases with the strain rate, while the fractional heat releases of other reactions decrease with the strain rate (see Fig. 11(b)). This indicates that reaction A3 plays more important role in heat release under higher stretch rates. In the work of Aspden et al. [8], the different sensitivities of reaction rates to the radical concentration change were also observed at different temperatures, which caused a decorrelation between fuel consumption and heat release. Besides, a similar enhancement in A3 was also observed for high Karlovitz numbers.

In summary, the stretch-chemistry interactions alter chemical pathway by following steps: First, the stretch and preferential diffusion effects alter local composition and temperature within the reaction zone. Then, the altered temperature and radical concentrations change the reaction rates of chemical reactions. Due to different dependencies, reaction rates show different sensitivities to the temperature and radical concentration change. Therefore, the relative importance of different reactions and chemical pathways change.

The important flame properties, burning velocity and peak temperature, of fuel-lean H_2/air flames in the strain-curvature parameter space are further illustrated in Fig. 12. Burning velocity is crucial to the combustion efficiency and the peak flame temperature is closely related to NOx emission in hydrogen combustion.

Due to the differential diffusion effects, positive stretch strengthens flames with Lewis number less than unity. As shown in Fig. 12, the burning velocity is strongly correlated with strain

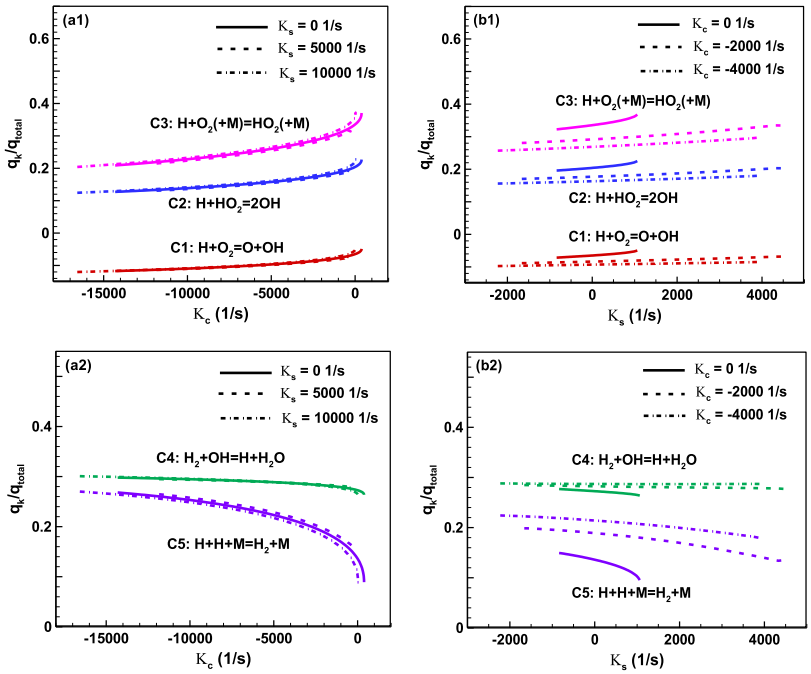

Fig. 16. Change of fractional heat release from key reactions along (a) K_s and (b) K_c isolines for fuel-rich H_2/air flame with $\phi = 5.1$.

rate while it shows a relatively weak response with curvature. From the left to the right boundary of the parameter space, the burning velocity is increased by a factor of 5. Furthermore, it is observed that the peak temperature increases substantially with increasing K_S and κ.

Fig. 13 shows the scatter plot of fractional heat release for key reactions of H_2/air flames with different equivalence ratios. The scatter is equidistantly extracted from strain-curvature parameter space and plotted as a function of Karlovitz number, which consists of the influence of both flame curvature and flow field strain rate (i.e. $Ka = K\delta/S_L$ where $K = K_S+K_c$). It is observed that the fractional heat release of reactions A1-A3 have large scatter for fuel-lean H_2/air flames. This implies that K_s and K_c have distinct effects upon flame chemistry and the fractional heat release of key reactions is sensitive to the combination of K_s and K_c. Figs. 13(b) and Fig. 13(c) show that the points collapse into a smaller region for the stoichiometric case and even into a single curve at negative Ka for fuel-rich H_2/air flames. This phenomenon could be caused by two reasons. First, the region of negative curvature is narrower for stoichiometric and fuel-rich H_2/air flames than for the fuel-lean case, which can be observed in Fig. 8. Second, the displacement speed increases with negative flame stretch for flames with Lewis number greater than unity. With a larger value of S_d, curvature has more dominant effect on flame chemistry since the curvature induced stretch is K_c=$S_d\kappa$. Nevertheless, it is noted that large scatter is observed around zero Karlovitz number for fuel-rich flames in Fig. 13(c). This implies that the effects of K_s and K_c on chemical pathway are still not identical. Fig. 13 indicates that a single-valued Karlovitz number is sufficient to characterize the flame chemistry for fuel-rich flames with a negative flame stretch, while more specific information is needed in terms of strain and curvature for the fuel-lean and stoichiometric H_2/air flames.

To demonstrate the individual influence of K_s and K_c, we transform the κ-K_s parameter space into the K_s-K_c parameter space and plot the fraction heat release from key reactions along the K_s and K_c isolines. Fig. 14 shows the results for H_2/air flames with $\phi = 0.4$. At zero strain rate of $K_s = 0\ s^{-1}$ and zero curvature of $K_c = 0\ s^{-1}$ (solid lines in Fig. 14), the flame is subjected to a stretch rate only due to propagation of curved flame and flow strain rate, respectively. It is shown that the fractional heat release of reaction A1 is dominated by K_c, while that of reactions A2 and A3 are affected both by K_s and K_c. This conclusion still holds for $K_s = 5000$ and 10,000 s^{-1} and $K_c = -2000$ and 2000 s^{-1}, where the stretch rate has contributions from both K_s and K_c.

Similar analysis is performed for stoichiometric H_2/air flames. Fig. 15(b) indicates that the strain rate has little effect on the fractional heat release from reactions B1-B4 for different K_c. This is further demonstrated by Fig. 15(a) where results for different strain rates of $K_s = 0$, -1000 and $3000\ s^{-1}$ almost collapse into a single curve. Therefore, the fractional heat release is nearly independent of the flow field strain rate. For reactions B1 and B2, slight variation is observed in the change of fractional heat release with K_c; while obvious change is observed for reactions B3 and B4 in Fig. 15(a).

Fig. 16 shows similar results for fuel-rich H_2/air flame with $\phi = 5.1$. The fractional heat release from reactions C1, C2 and C4 is shown to have low sensitivity to both K_s and K_c. The fractional heat release from reactions C3 and C5 is obviously affected by K_c: when the flame curvature increases from $K_c = -17{,}000\ s^{-1}$ to $K_c = 0\ s^{-1}$, the fractional heat release from reactions C3 increases

by about 100% and the fractional heat release from reactions C5 increases to about 1/3.

The above results in Figs. 14–16 indicate that for fuel-lean H_2/air flames, both K_s and K_c have a non-negligible effect on the flame chemistry; for stoichiometric flames, K_c has a more significant effect than K_s; while for fuel-rich flames, both K_s and K_c have moderate effects on the flame chemistry. Overall, flame chemistry shows a higher sensitivity to the stretch originating from the curved flame propagation than flow field strain rate. This is reasonable as the flame curvature is related to the direction of species concentration gradient around the reaction zone and is primarily correlated with mass diffusion rates [38]. Therefore, highly diffusive species such as H and H_2 can be easily focused by curvature effects to enhance the reaction rates and to alter the chemical pathway. The curvature effect induced by the high diffusivities of H_2 and H is further justified by transport budget analysis in Appendix D.

Usually data from counterflow flame solutions are used in turbulent combustion modelling [38]. However, the counterflow flame only has positive strain while it has zero curvature. On the isosurface of the turbulent flame, local flame segments can be subjected to different combinations of strain and curvature [7]. Therefore, the above results indicate that for hydrogen/air flame, it might be invalid to use steady strained flames with zero curvature to describe the local chemistry in turbulent flames.

4. Conclusions

In this study, one-dimensional simulations in physical space considering detailed chemistry and transport are conducted to assess the effects of stretch-chemistry interaction on chemical pathways in premixed H_2/air flames. Both inwardly and outwardly propagating spherical flames (IPF and OPF) with negative and positive stretch rate, respectively, are investigated for H_2/air mixtures with different equivalence ratios (or different effective Lewis numbers). Due to the coupling between preferential diffusion (characterized by the Lewis number) and stretch rate, the spherical flame propagation speed strongly depends on the stretch rate. For different equivalence ratios, the change of fractional heat release and radical production with the stretch rate is found to follow the same trend as the spherical flame propagation speed. The relative roles of dominant elementary reactions such as $H + O_2 (+M) = HO_2 (+M)$, H_2+OH=H + H_2O and $H + O_2 = O$+OH vary with the Lewis number. In IPF and OPF, the negative and positive stretch rates have opposite effects on the chemical pathway. Besides, the chemical pathways obtained for OPF are compared with these for laminar counterflow flame and turbulent flame. Qualitative agreement is observed though there is quantitative difference due to the different combinations of strain and curvature embodied in the stretch rate.

To further analyze the individual effects of the stretch components originating from hydrodynamic strain and curved flame propagation on the chemical pathway, a composition space model is used. It is demonstrated that K_s and K_c have different effects on flame chemistry. Due to the high diffusivity of H_2 and H, the chemical pathway shows a higher sensitivity to K_c than K_s. A single-valued Karlovitz number is sufficient to characterize the flame chemistry for fuel-rich flames with negative flame stretch, while more specific information is required in terms of strain and curvature for modelling the fuel-lean and stoichiometric H_2/air flames.

Here we only consider the oxidation pathway of hydrogen. In future works, it would be interesting to consider hydrocarbon fuels, for which the chemical pathways might have different sensitivity to K_s and K_c. Besides, it is noted that flame chemistry is also affected by excess energy deposition during the forced-ignition process, which is not included in the CSM. Hence, it would be of great interest take into account the influence of ignition in the composition space and to study the stretch effects on flame chemistry during the forced ignition process. Furthermore, it is noted that we consider atmospheric pressure in this work. It is well known that the hydrogen oxidation and the reaction pathway strongly depend on pressure. Therefore, it would be interesting to take into account the influence of pressure on the stretch-chemistry interaction and chemical pathway in future works.

Declaration of Competing Interest

The authors declare that they have no known competing financial interests or personal relationships that could have appeared to influence the work reported in this paper.

Acknowledgements

This work is jointly supported by the National Natural Science Foundation of China (NSFC, no. 51861135309) and the German Research Foundation (DFG, no. 411275182).

Appendix A. Physical space reconstruction

Physical space reconstruction is done by inverting the transformation between progress variable Y_c and physical coordinate r':

$$r' = \int_{Y_{c,\min}}^{Y_{c,\max}} \frac{\mathrm{d}Y_c}{g_c} \tag{A1}$$

Special attention should be paid to the upper and lower limits of the integral since the progress variable gradient g_c is equal to zero at the boundaries of the CSM, resulting in infinite value of the integral. Though this reconstructed coordinate does not account for curvature effect, the topological information is already contained in the CSM by the prescribed curvature value. The flame coordinate r can be obtained by superposing the curvature value and the reconstructed physical coordinate is:

$$r = \frac{2}{\kappa} + \left(r'|_{\dot{\omega}_T,max} - r'\right) \tag{A2}$$

where $r'|_{\dot{\omega}_T,max}$ corresponds to the radius at the maximum heat release rate. This value is taken as reference since the representative value for curvature κ is also extracted at the position of maximum heat release rate in spherical flames.

Appendix B. Curvature reconstruction

In CSM, the flame structure of OPF and IPF is recovered by prescribing constant values for strain and curvature in Eqs. (3–5), while they are different in the physical space. Here we demonstrate that the modelling assumption of using constant representative values for strain and curvature is valid in determining the flame structure. The curvature profile can be reconstructed via the reconstructed flame radius r:

$$\kappa_{re} = \frac{2}{r} \tag{B1}$$

Fig. B1(a) shows the profiles of constant curvature and reconstructed curvature in composition space. The reconstructed curvature remains constant in most parts of the progress variable domain and only shows differences in the preheat and post oxidation

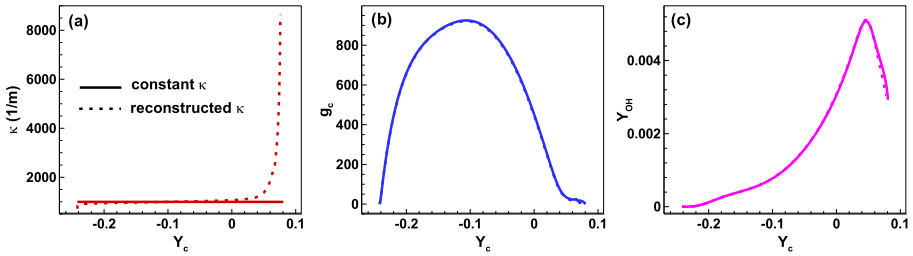

Fig. B1. Change of (a) flame curvature κ, (b) progress variable gradient g_c, and (c) OH mass fraction Y_{OH} with the progress variable with constant curvature (solid lines) and reconstructed curvature (dashed lines).

zone. Furthermore, Fig. B1(b) and Fig. B1(c) show that using the reconstructed curvature profile as input parameter has negligible influence on the flame structure in the composition space. Therefore, using constant curvature values in the composition space is valid while the reconstructed profile is only needed for the transformation back to physical space.

Appendix C. Flame structure analysis

Here we compare flame structures of canonical flame configurations to corresponding results from the CSM and assess the ignition effect and back support effect. Fig. C1 shows temperature, heat release rate, H_2 mass fraction and H mass fraction profiles for OPF with very small flame radii (corresponding to large Karlovitz numbers). In general, good agreement is observed between the canonical flame solutions in the physical space and those from the CSM, indicating that constant values for strain and curvature can be used in CSM. The ignition effect is visible in H and H_2 mass fraction profiles. At the center with strong ignition effect, H_2 diffuses toward the high temperature region at the center (i.e. $r = 0$ m). Diffusive flux turns around when the center cools down. This effect is not included in the CSM, and thereby discrepancy is observed in H_2 mass fractions in preheat zone and also in front of the preheat zone for stoichiometric and fuel-rich H_2/air flames. For fuel-lean case, higher H radical concentration at the center is caused by ignition energy deposition. The ignition effect is important during the early propagation of OPF and has a large effect on the chemical pathways at large Karlovitz numbers, which can be seen in Fig. 7.

Fig. C2 shows the flame structure analysis results for IPF. Due to the back support by hot products, more H_2 is observed in the flame structure for H_2/air flames with $\phi = 5.1$. Back support effect is less pronounced than ignition effect. Therefore, much better agreement is obtained for fuel-lean and stoichiometric IPF, which can be seen from the flame structure analysis in Fig. C2 and the chemical pathway comparison in Fig. 7.

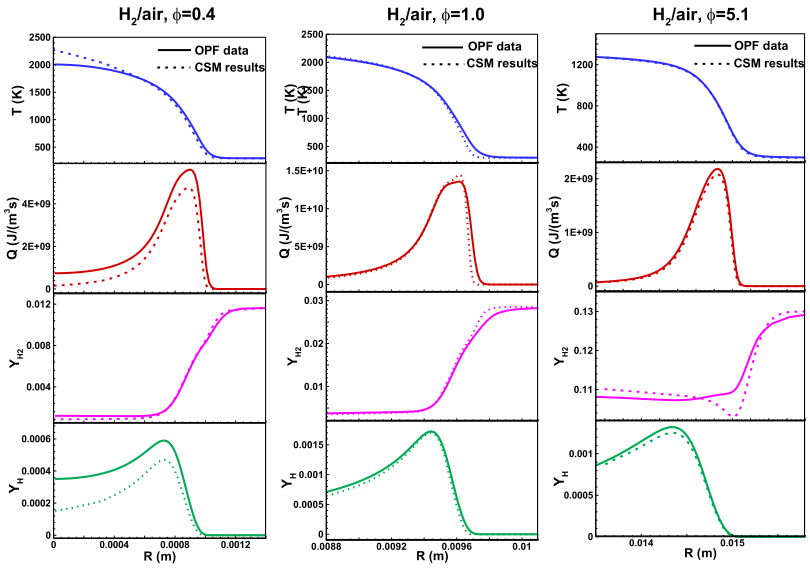

Fig. C1. Flame structures for H_2/air flames with $\phi = 0.4$, 1.0 and 5.1. The solid lines are results for OPF in the physical space while the dashed lines represent results from the CSM.

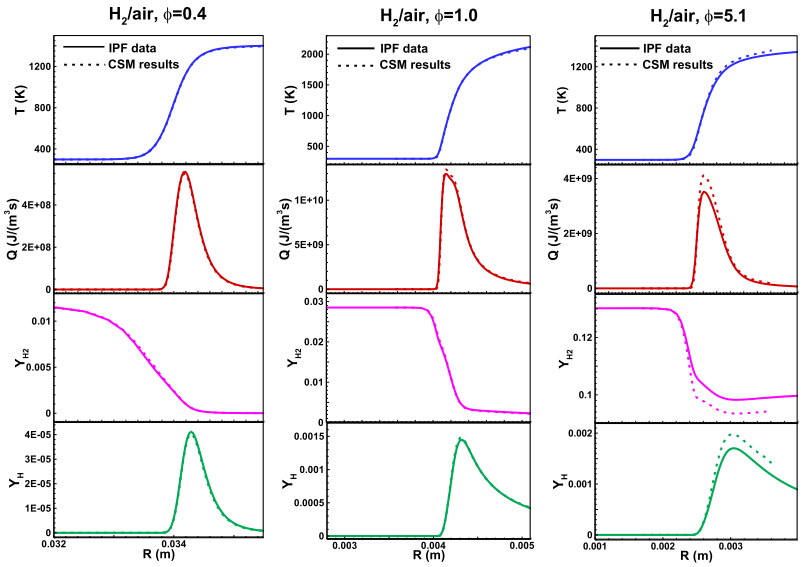

Fig. C2. Flame structures for H_2/air flames with $\phi = 0.4$, 1.0 and 5.1. The solid lines are results for IPF in the physical space while the dashed lines represent results from the CSM.

Appendix D. Transport budget analysis

In this appendix, we conduct a transport budget analysis to show the curvature effect induced by high diffusivities of H_2 and H. Here, the transport equation for the *i th* species is considered:

$$\rho\frac{\partial Y_i}{\partial \tau} = -g_c\frac{\partial}{\partial Y_c}\left(g_c\ \rho Y_i\tilde{V}_i\right) + g_c\frac{\partial}{\partial Y_c}\left(g_c\ \rho Y_c\tilde{V}_c\right)\frac{\partial Y_i}{\partial Y_c} + \rho g_c\kappa\left(Y_i\tilde{V}_i - Y_c\tilde{V}_c\frac{\partial Y_i}{\partial Y_c}\right) - \dot{\omega}_c\frac{\partial Y_i}{\partial Y_c} + \dot{\omega}_i \quad \text{(D1)}$$

where $-g_c\frac{\partial}{\partial Y_c}(g_c\ \rho Y_i\tilde{V}_i) + g_c\frac{\partial}{\partial Y_c}(g_c\ \rho Y_c\tilde{V}_c)\frac{\partial Y_i}{\partial Y_c}$ and $\rho g_c\kappa(Y_i\tilde{V}_i - Y_c\tilde{V}_c\frac{\partial Y_i}{\partial Y_c})$ denote the flame normal diffusion and curvature induced diffusion, respectively. $-\dot{\omega}_c\frac{\partial Y_i}{\partial Y_c}$ is a drift term and $\dot{\omega}_i$ represents the contribution from reaction.

Figures D1–3 show the budget analysis results of H_2, H and H_2O for fuel-rich H_2/air flames with different stretch conditions. For a steady flame, the terms on the right-hand side are well balanced with each other. The flame curvature is related to the direction of species concentration gradient around the reaction zone and is primarily correlated with mass diffusion rates. Therefore, curvature induced diffusion plays an important role in the transport of highly diffusive species such as H and H_2. However, for large molecules such as H_2O, the curvature induced diffusion term almost equals zero, as shown in Fig. D3.

For fuel-rich mixtures with Lewis number greater than unity, flames are weakened by positive stretch. In Figures D1–3, the Lewis number effect is clearly visible. When the strain rate is decreased from $K_S = 0$ 1/s to −1000 1/s (from Figs. D1–3(b) to Figs. D1–3(a)), the absolute value of source term increases. When the curvature is increased from κ=−2000 1/m to 300 1/m (from Figs. D1–3(b) to Figs. D1–3(c)), the absolute value of source term decreases. Therefore, the diffusion terms and drift terms change accordingly. It is noted that for H_2 and H, the relative importance of curvature in-

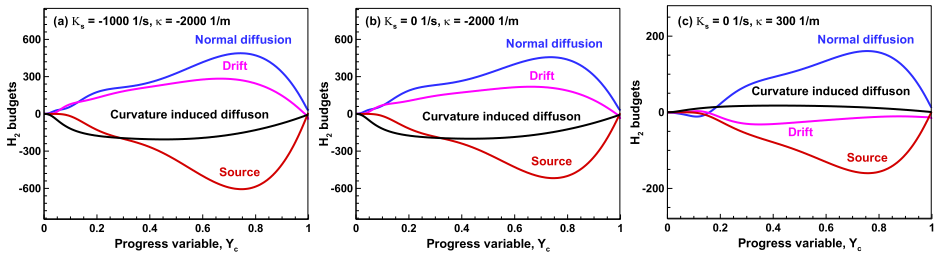

Fig. D1. H_2 budget analysis for fuel-rich H_2/air flames with $\phi = 5.1$. (a) $K_s = -1000$ 1/s, $\kappa = -2000$ 1/m, (b) $K_s = 0$ 1/s, $\kappa = -2000$ 1/m, (c) $K_s = 0$ 1/s, $\kappa = 300$ 1/m.

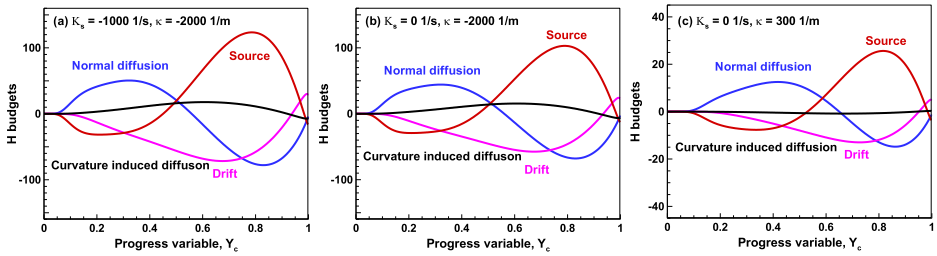

Fig. D2. H budget analysis for fuel-rich H_2/air flames with $\phi = 5.1$. (a) $K_s = -1000$ 1/s, $\kappa = -2000$ 1/m, (b) $K_s = 0$ 1/s, $\kappa = -2000$ 1/m, (c) $K_s = 0$ 1/s, $\kappa = 300$ 1/m.

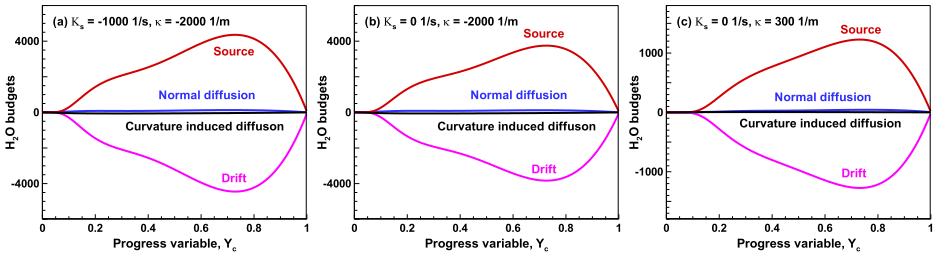

Fig. D3. H_2O budget analysis for fuel-rich H_2/air flames with $\phi = 5.1$. (a) $K_s = -1000$ 1/s, $\kappa = -2000$ 1/m, (b) $K_s = 0$ 1/s, $\kappa = -2000$ 1/m, (c) $K_s = 0$ 1/s, $\kappa = 300$ 1/m.

duced diffusion term is more sensitive to the change of curvature than strain rate, while for H_2O, the curvature induced diffusion term almost equals zero for all the stretch conditions considered.

References

[1] M. Baum, T.J. Poinsot, D.C. Haworth, N. Darabiha, Direct numerical simulation of $H_2/O_2/N_2$ flames with complex chemistry in two-dimensional turbulent flows, J. Fluid Mech. 281 (1994) 1–32.

[2] D. Dasgupta, W. Sun, M. Day, A.J. Aspden, T. Lieuwen, Analysis of chemical pathways and flame structure for n-dodecane/air turbulent premixed flames, Combust. Flame 207 (2019) 36–50.

[3] C.K. Law, Combustion Physics, Cambridge University Press, 2006.

[4] A.L. Sanchez, F.A. Williams, Recent advances in understanding of flammability characteristics of hydrogen, Prog. Energy Combust. Sci. 41 (2014) 1–55.

[5] J.H. Chen, H.G. Im, Stretch effects on the burning velocity of turbulent premixed hydrogen/air flames, Proc. Combust. Inst. 28 (2000) 211–218.

[6] A.J. Aspden, M.S. Day, J.B. Bell, Turbulence-chemistry interaction in lean premixed hydrogen combustion, Proc. Combust. Inst. 35 (2015) 1321–1329.

[7] D. Dasgupta, W. Sun, M. Day, T. Lieuwen, Effect of turbulence–chemistry interactions on chemical pathways for turbulent hydrogen–air premixed flames, Combust. Flame 176 (2017) 191–201.

[8] A.J. Aspden, M.S. Day, J.B. Bell, Turbulence-chemistry interaction in lean premixed hydrogen combustion, Proc. Combust. Inst. 35 (2015) 1321–1329.

[9] H. Carlsson, R. Yu, X.-S. Bai, Direct numerical simulation of lean premixed CH4/air and H2/air flames at high Karlovitz numbers, Int. J. Hydrog. Energy 39 (2014) 20216–20232.

[10] D. Dasgupta, W. Sun, M.S. Day, T.C. Lieuwen. Turbulence effects on the chemical pathways for premixed Methane/Air flames, AIAA Sci. Tech. Forum, 2017-1782.

[11] H. Carlsson, R. Yu, X.S. Bai, Flame structure analysis for categorization of lean premixed CH_4/air and H_2/air flames at high Karlovitz numbers: direct numerical simulation studies, Proc. Combust. Inst. 35 (2015) 1425–1432.

[12] G. Fru, G. Janiga, D. Thévenin, Impact of Volume Viscosity on the Structure of Turbulent Premixed Flames in the Thin Reaction Zone Regime, Flow Turbul. Combust. 88 (2012) 451–478.

[13] Y. Wang, W. Han, Z. Chen, Effects of fuel stratification on ignition kernel development and minimum ignition energy of n-decane/air mixtures, Proceed. Combust. Inst. 37 (2019) 1623–1630.

[14] H.H. Kim, H.W. Sang, J. Santner, Z. Chen, Y. Ju, Measurements of the critical initiation radius and unsteady propagation of n -decane/air premixed flames, Proceed. Combust. Inst. 34 (2013) 929–936.

[15] D. Bradley, P.H. Gaskell, X.J. Gu, Burning velocities, Markstein lengths, and flame quenching for spherical methane-air flames: a computational study, Combust. Flame 104 (1996) 176–198.

[16] Z. Chen, X. Gou, Y. Ju, Studies on the Outwardly and Inwardly Propagating Spherical Flames with Radiative Loss, Combust. Sci. Technol. 182 (2010) 124–142.

[17] G.R.A. Groot, J.A.V. Oijen, L.P.H.D. Goey, K. Seshadri, N. Peters, The effects of strain and curvature on the mass burning rate of premixed laminar flames, Combust. Theory Modelling 6 (2002) 675–695.

[18] A. Scholtissek, P. Domingo, L. Vervisch, C. Hasse, A self-contained progress variable space solution method for thermochemical variables and flame speed in freely-propagating premixed flamelets, Proc. Combust. Inst. 37 (2018) 1529–1536.

[19] A. Scholtissek, P. Domingo, L. Vervisch, C. Hasse, A self-contained composition space solution method for strained and curved premixed flamelets, Combust. Flame 207 (2019) 342–355.

[20] H. Bottler, A. Scholtissek, X. Chen, Z. Chen, C. Hasse, Premixed flames for arbitrary combinations of strain and curvature, Proc. Combust. Inst. (2020).

[21] F. Wu, A. Saha, S. Chaudhuri, C.K. Law, Facilitated Ignition in Turbulence through Differential Diffusion, Phys. Rev. Lett. 113 (2014) 024503.

[22] Z. Chen, On the accuracy of laminar flame speeds measured from outwardly propagating spherical flames: methane/air at normal temperature and pressure, Combust. Flame 162 (2015) 2442–2453.

[23] Z. Chen, M.P. Burke, Y. Ju, On the critical flame radius and minimum ignition energy for spherical flame initiation, Proc. Combust. Inst. 33 (2011) 1219–1226.

[24] Z. Chen, M.P. Burke, Y. Ju, Effects of Lewis number and ignition energy on the determination of laminar flame speed using propagating spherical flames, Proc. Combust. Inst. 32 (2009) 1253–1260.

[25] C.F. Curtiss, J.O. Hirschfelder, Transport properties of multicomponent gas mixtures, J. Chem. Phys. 17 (1949) 550–555.

[26] G. Vincent, Multicomponent transport in laminar flames, Proc. Combust. Inst. 35 (2015) 625–637.

[27] T.P. Coffee, J.M. Heimerl, Transport algorithms for premixed, laminar steady-state flames, Combust. Flame 43 (1981) 273–289.

[28] R.J. Kee, J.F. Grcar, M.D. Smooke, A FORTRAN Program for Modeling Steady Laminar One-Dimensional Premixed Flames, Sandia National Laboratories Report SAND (1985) 85–8240.

[29] J. Li, Z. Zhao, A.F. Kazakov, F.L. Dryer, An updated comprehensive kinetic model of hydrogen combustion, Int. J. Chem. Kinet. 36 (2004) 566–575.

[30] W. Zhang, Z. Chen, W. Kong, Effects of diluents on the ignition of premixed H_2/air mixtures, Combust. Flame 159 (2012) 151–160.

[31] P. Dai, Z. Chen, S. Chen, Y. Ju, Numerical experiments on reaction front propagation in n-heptane/air mixture with temperature gradient, Proc. Combust. Inst. 35 (2015) 3045–3052.

[32] P. Dai, Z. Chen, Supersonic reaction front propagation initiated by a hot spot in n-heptane/air mixture with multistage ignition, Combust. Flame 162 (2015) 4183–4193.

[33] V. Oijen, J. A., A. Donini, R.J.M. Bastiaans, T. Boonkkamp, J.H.M. Ten, D. Goey, L. P. H., State-of-the-art in premixed combustion modeling using flamelet generated manifolds, Prog. Energy Combust. Sci. 57 (2016) 30–74.

[34] M. Matalon, On Flame Stretch, Combust. Sci. Technol. 31 (1983) 169–181.
[35] K.T. Aung, M.I. Hassan, G.M. Faeth, Flame stretch interactions of laminar premixed hydrogen/air flames at normal temperature and pressure, Combust. Flame 109 (1997) 1–24.
[36] W. Liang, C.K. Law, Z. Chen, Ignition of hydrogen/air mixtures by a heated kernel: role of Soret diffusion, Combust. Flame 197 (2018) 416–422.
[37] P. Clavin, Dynamic behavior of premixed flame fronts in laminar and turbulent flows, Prog. Energy Combust. Sci. 11 (1985) 1–59.
[38] T. Echekki, J.H. Chen, Unsteady strain rate and curvature effects in turbulent premixed methane-air flames, Combust. Flame 106 (1996) 184–190.

P3 Combust. Flame 243 (2022), 112125

H. Böttler, X. Chen, S. Xie, A. Scholtissek, Z. Chen, and C. Hasse. Flamelet modeling of forced ignition and flame propagation in hydrogen-air mixtures. In: Combust. Flame 243 (2022), 112125. DOI: 10.1016/j.combustflame.2022.112125

Author contributions

Tab. P.3: Author contributions to publication [P3] following CRediT [117]

Hannes Böttler	Conceptualization of the numerical investigation (equal) Methodology of the flamelet manifold and coupling to the numerical solver Implementation and validation of the flamelet model (lead) Numerical investigation of flamelet-based simulations Interpretation and discussion of the results (lead) Data analysis and visualization Writing – Original draft (lead) Main author
Xinyi Chen	Numerical investigation of spherical and cylindrical flames with detailed chemistry Interpretation and discussion of the numerical results (supporting)
Shumeng Xie	Numerical investigation of counterflow flames with detailed chemistry Interpretation and discussion of the numerical results (supporting)
Arne Scholtissek	Conceptualization of the numerical investigation (equal) Interpretation and discussion of the numerical results (supporting) Writing – Original draft (supporting) Corresponding author Supervision of HB (equal)
Zheng Chen	Interpretation and discussion of the numerical results (supporting) Supervision of XC and SX Funding acquisition
Christian Hasse	Conceptualization of the numerical investigation (supporting) Interpretation and discussion of the numerical results (supporting) Supervision of HB (equal) Funding acquisition
All co-authors	Writing – Review & Editing

Use of publication contents in finalized and ongoing dissertations

This publication is part of the ongoing dissertation of Hannes Böttler at the Institute for Simulation of reactive Thermo-Fluid Systems at the Technical University of Darmstadt, Germany.

Combustion and Flame 243 (2022) 112125

Contents lists available at ScienceDirect

Combustion and Flame

journal homepage: www.elsevier.com/locate/combustflame

Flamelet modeling of forced ignition and flame propagation in hydrogen-air mixtures

H. Böttler[a], X. Chen[b], S. Xie[b], A. Scholtissek[a,*], Z. Chen[b], C. Hasse[a]

[a] Technical University of Darmstadt, Department of Mechanical Engineering, Simulation of reactive Thermo-Fluid Systems, Otto-Berndt-Str. 2, 64287 Darmstadt, Germany
[b] SKLTCS, CAPT, Department of Mechanics and Engineering Science, College of Engineering, Peking University, Beijing 100871, China

ARTICLE INFO

Article history:
Received 12 October 2021
Revised 18 March 2022
Accepted 18 March 2022
Available online 28 April 2022

Keywords:
Premixed flames
Composition space
Forced ignition
Hydrogen
Differential diffusion

ABSTRACT

Modeling hydrogen-air flames is challenging for several reasons. Due to its high diffusivity and reactivity, the combustion properties of hydrogen are substantially different from conventional hydrocarbon fuels. Besides differential diffusion and flame stretch, which play an important role in hydrogen combustion, the prediction of ignition events is also relevant for the safety and control of combustors operating with hydrogen. To address these effects with a manifold-based method, a novel flamelet progress variable (FPV) model is presented which consists of a tabulated manifold and a coupling strategy. In contrast to prior work, the manifold is coupled to the CFD simulation by transporting major species and enthalpy instead of transporting the flamelet control variables only. A closure approach is developed to employ a mixture-averaged diffusion model accounting for exact diffusion coefficients. Furthermore, a novel tabulation strategy is presented which is based on a recently published composition space model (CSM). The CSM is used for computing and tabulating flamelets which are consistently blended with constant-pressure homogeneous ignition solutions at elevated temperatures. The FPV model is validated for planar and curved hydrogen-air premixed flames across a range of equivalence ratios ($0.7 \leq \phi \leq 1.4$). The latter are ignited by an energy deposition followed by an outward propagation as cylindrical or spherical expanding flames. It is shown that the FPV model accurately recovers the characteristics of the forced ignition process in both quiescent mixtures and a counterflow configuration, as well as the flame structures and propagation speed of the outwardly propagating hydrogen-air flames.

1. Introduction

For the transition towards zero-carbon energy systems, hydrogen is an intensively discussed energy carrier of increasing relevance [1]. When generated with renewable energy sources via electrolysis, so-called *green hydrogen* can be directly used as a fuel or further processed to create synthetic fuels such as dimethyl ether (DME) and ammonia [1–3]. As a fuel, hydrogen leads to a drastic change in combustion characteristics due to its high diffusivity and reactivity [3]. This entails not only changes in the combustor equipment but also challenges for the modeling approaches that are used to design such devices [1,2].

Computational fluid dynamics (CFD) has become an essential tool in optimizing combustion facilities not only with regard to improving efficiency, control, and safety but also to reduce pollutants [1]. However, simulations of practical combustion devices resolving all relevant scales and employing detailed reaction mechanisms (direct numerical simulation, DNS) will remain an exception due to their tremendous computational cost. Therefore, DNS studies are restricted to academic configurations and will remain so in the near future [4], which has motivated the development of a variety of modeling approaches [5–10]. While approaches are available to reduce chemical reaction mechanisms [11], flamelet-based models are a promising alternative to account for detailed kinetics at a reasonable computational cost. Popular methods are the Flamelet/Progress Variable (FPV) approach [12], Flamelet Generated Manifolds (FGM) [10], or the Flame Prolongation for ILDM (FPI) model [6]. In general, these models are based on the assumption that a turbulent flame can be considered a statistical ensemble of one-dimensional laminar flamelets [5]. By this means, flamelet manifolds are coupled to CFD simulations providing detailed kinetic information but requiring only the transport of a reduced set of scalars. These flamelet manifolds are usually generated by pre-computing one-dimensional flame structures which are param-

* Corresponding author.
E-mail address: scholtissek@stfs.tu-darmstadt.de (A. Scholtissek).

https://doi.org/10.1016/j.combustflame.2022.112125
0010-2180/

eterized by variables accounting for different physical effects, and these parameters are used for tabulation. Commonly used variables are the mixture fraction Z, the progress variable Y_c and often also enthalpy h to capture non-adiabatic effects [13].

Comprehensive overviews of modeling concepts and their usage in turbulent applications can be found elsewhere [4,8].

Flamelet models were originally developed for non-premixed combustion [5,14], while FGM has its origins in premixed combustion [10]. First derived for unity Lewis number diffusion, both approaches were later extended to cover differential diffusion effects, which describe the separation of initially correlated scalars in a flow due to different molecular diffusion properties [6,7,9,15–17]. This effect is particularly important in mixtures containing hydrogen [16,18]. Capturing differential diffusion with flamelet-based modeling approaches still poses a considerable challenge. Comprehensive diffusion models which are capable of describing differential diffusion, such as the mixture-averaged diffusion model, require gradient information for all species to accurately predict the species' molecular diffusion fluxes. This is a particular challenge in flamelet-based approaches since not all species gradients are available and only a reduced set of scalars is transported in the coupled CFD simulation. Therefore, closures are required.

Next, previous manifold-based modeling approaches are reviewed which have attempted to incorporate differential diffusion effects for premixed flames. Thereafter, modeling approaches for ignition phenomena are discussed. de Swart et al. [15] developed a FGM model for lean premixed methane-air flames including a discussion on the effects of adding hydrogen. In their model, the authors utilize a preferential diffusion coefficient for the progress variable and the closure of molecular diffusive fluxes is partly realized by obtaining gradient information of the control variables from tabulated 1D flames. Donini et al. [19] extended this model to include non-adiabatic conditions found in premixed laminar methane/air flames with heat loss and also turbulent gas turbine applications [20]. Later, Zhang et al. [21] discussed stratification effects in lean and stoichiometric methane-air flames and compared the approach developed by Donini et al. [20] to a FGM model where stretch effects are expressed by a second mixture fraction instead of accounting for enthalpy variations in the flamelet manifold. Recently, the modeling approaches utilized by [15,19] were revisited by Mukundakumar et al. [22] to describe differential diffusion effects in laminar 2D hydrogen-air premixed flames. The authors introduced improvements compared to the previous model by Donini et al. [19] and compared both models to direct chemistry solutions with non-unity but constant Lewis numbers. Although the new model exhibited a better performance, significant deviations in important flame characteristics such as the flame height and heat release rate were still found. Another modeling approach was presented by Schlup and Blanquart [17], who captured curvature effects in lean premixed hydrogen-air flames by extending the transport equation of the mixture fraction and using flamelet manifolds based on unstretched flamelets. With the assumption of single-step chemistry, the authors were able to relate the diffusive flux of the mixture fraction to the diffusive transport of the progress variable. In their study, Schlup and Blanquart [17] focused on adiabatic premixed flames and did not include enthalpy as a flamelet parameter. The aforementioned modeling approaches share the common attribute that the control parameters, often composite variables such as the mixture fraction and progress variable, are transported directly in the CFD, which requires additional modeling effort with respect to their diffusivity (or Lewis number). Recently, progress has been made with a hybrid transported-tabulated chemistry method (HTTC) in order to reduce the size of the flamelet manifold [23–25]. In this model, a reduced set of major species is transported and only intermediate species are tabulated using mixture fraction and progress variable as control variables. The reduced manifold is coupled to a compressible CFD solver where mixture properties are calculated based on the retrieved species composition. This model was validated against freely propagating flames of large hydrocarbons (e.g. kerosene) [23] and a partially premixed methane-air flame [24,25] using a mixture-averaged approach. A manifold prolongation was utilized to account for effects beyond the flammability limits, however, deviations remained in species profiles such as H_2O and CO [25]. The concept is promising to improve the prediction of flamelet-based models by transporting major species instead of conventional control variables. Gierth et al. [16] presented a similar approach for non-premixed combustion in order to capture differential diffusion effects in an LES of a non-piloted, non-premixed turbulent oxy-fuel flame. Noting that the fuel consisted of two components with significantly different diffusivities (45 vol-% CH_4 and 55 vol-% H_2), the transport of major species considerably improved the model predictions for the flame structure in comparison to conventional coupling strategies. In summary, although considerable progress has been made, no generic solution has been presented for capturing differential diffusion with flamelet-based approaches.

With respect to ignition phenomena, the majority of flamelet-based models were developed in the context of non-premixed combustion. While recent experiments [26–28] and direct numerical simulations [29–32] comprehensively discussed forced ignition processes in laminar and turbulent premixed combustion, flamelet modeling of premixed ignition phenomena is not addressed as extensively in the literature. Recently, Malé et al. [33] discussed the characteristics of an unsteady representative flamelet model by means of a-priori analysis for premixed propane jets ignited by hot products. Tang et al. [34] developed a comprehensive ignition model which was validated for methane-air non-premixed flames in cross flow configurations and later also for alternative jet fuels [35]. In their work, the authors developed an advanced tabulation method combining flamelets from both counterflow flames and homogeneous reactors, further incorporating the stochastic nature of ignition processes by using a Monte-Carlo method in their coupled calculations. Although the the model by Tang et al. [34] performed well for modeling the ignition of hydrocarbon flames, it relies on unity Lewis number assumptions and is therefore not directly applicable to hydrogen ignition. Differential diffusion aspects in flamelet modeling of auto-igniting non-premixed flames were discussed by Abtahizadeh et al. [36]. The authors extended the transport equations for mixture fraction and progress variable and used their model to investigate the auto-ignition of non-premixed hydrogen-enriched methane flames.

In this work, we present a novel flamelet-based model which captures forced ignition and flame propagation in hydrogen-air mixtures for equivalence ratios ranging from $0.7 \leq \phi \leq 1.4$. To the authors' knowledge, so far no studies have been carried out focusing on the flamelet modeling of the forced ignition of premixed hydrogen-air mixtures with detailed diffusion modeling. The coupling of the flamelet manifold to the CFD simulation is realized by the transport of major species and enthalpy instead of transporting the conventional flamelet control variables (in a similar manner as [16,25]). The major species are then utilized to reconstruct the Bilger mixture fraction Z_{Bilger} [37] and the progress variable Y_c to access the tabulated manifold. By this means, the model captures differential diffusion and curvature effects. Figure 1 shows the range of effective Lewis numbers [38] covered by the investigated cases: for the lean hydrogen-air mixture, hydrogen is the deficient reactant and $\text{Le}_{\text{eff}} \approx 0.5$. For the rich hydrogen-air mixtures, oxygen is the deficient reactant, leading to an effective Lewis number larger than unity ($\text{Le}_{\text{eff}} \approx 1.4$). Additionally, a stoichiometric case with $\text{Le}_{\text{eff}} \approx 0.95$ is studied.

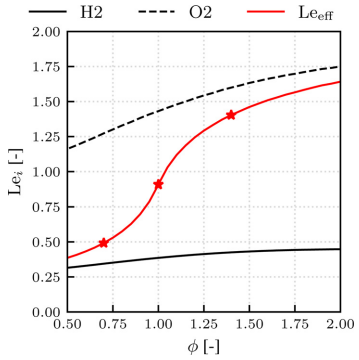

Fig. 1. Effective Lewis number Le_{eff} of hydrogen-air mixtures with varying equivalence ratios evaluated from the inner layer of unstretched planar flames according to the asymptotic theory of Matalon et al. [38]. The effective Lewis numbers of the mixtures addressed in this work are highlighted by red stars.

The flamelet manifold is constructed using a recently developed composition space model (CSM) [39–42] which allows to blend systematically between unstretched premixed flames and constant pressure ignition for the tabulation.

The paper is structured as follows: first, transport equations for species and enthalpy are derived and discussed with respect to required closures. Second, modeling aspects are outlined regarding the tabulation strategy and the generation of the flamelet manifold. Thereafter, the model is validated against a set of hydrogen-air flame configurations such as quasi-steady planar flames and transient expanding curved flames in both quiescent mixtures and the counterflow configuration. Both global combustion properties and local flame structures of flames with different equivalence ratios are discussed. The paper ends with a conclusion.

2. Numerical methodology

In this section, the governing equations of the transported quantities are presented and the required closures are discussed. Thereafter, the parametrization and the generation of the tabulated manifold is described. Finally, the CFD setup is briefly explained.

2.1. Flamelet coupling

For the standard FPV model [12], one-dimensional flame structures are tabulated and parameterized by the mixture fraction Z and progress variable Y_c. While the transport equations of these control variables can easily be derived for unity Lewis number diffusion, considerable modeling effort is required when describing differential diffusion using more complex diffusion models [15,17,19,22]. The utilization of the Bilger mixture fraction [37], which is based on elemental mass fractions, improves the performance of flamelet approaches [16,17,19,22]. However, as the mixture fraction and progress variable are variables that are defined based on several reactive species, it is challenging to describe their transport without introducing additional modeling assumptions [9,17].

An exact transport equation for the Bilger mixture fraction was presented by Sutherland et al. [43]. However, this formulation contains diffusive fluxes of all species, meaning that its numerical solution requires either a-priori knowledge about the scalar fields of all species or a closure based on assumptions about the flame structure [17,22]. Hence, by prescribing additional simplifications it is possible to derive transport equations for the mixture fraction which do not contain any source terms. However, this can lead to a decoupling of the local species composition from the mixture fraction, which can introduce additional modeling errors in flames impacted by strong differential diffusion effects.

Contrary to previous flamelet-based approaches, in this work equations for major species (H_2, O_2, H_2O) are solved instead of transporting the control variables mixture fraction and progress variable. These three species are chosen, since they comprise the predominant part of the elemental mass fractions of H and O. The species further correspond to reactants and products, respectively, and are thereby indicative of the reaction progress. For more complex fuels mathematical criteria can be utilized to identify the relevant major species [23]. The conventional species transport equation reads:

$$\frac{\partial \rho Y_k}{\partial t} = -\frac{\partial}{\partial x_i}(\rho u_i Y_k) - \frac{\partial}{\partial x_i}\left(\rho Y_k V_{k,i}\right) + \dot{\omega}_k, \tag{1}$$

with the density ρ, velocity u_i, diffusive flux $\rho Y_k V_{k,i}$ and source term $\dot{\omega}_k$. For a mixture-averaged diffusion model, the diffusive flux can be expressed as:

$$\rho Y_k V_{k,i} = -\frac{\alpha}{\mathrm{Le}_k}\frac{\partial Y_k}{\partial x_i} - \frac{\alpha}{\mathrm{Le}_k}\frac{Y_k}{\bar{M}}\frac{\partial \bar{M}}{\partial x_i}, \tag{2}$$

with the mean molecular mass of the mixture $\bar{M}$ and the thermal diffusivity $\alpha = \lambda / c_p$ where λ corresponds to the thermal conductivity and c_p the heat capacity of the mixture. Furthermore, to compute the Lewis number $\mathrm{Le}_k = \alpha/(\rho D_{m,k})$, the mixture-averaged diffusion coefficient of species k, $D_{m,k}$, is used. For later application in the coupled CFD simulation, the source terms and Lewis numbers for all major species are stored in the tabulated manifold described below. The gradient of $\bar{M}$ is found to be negligible compared to the mass fraction gradient and is therefore not taken into account in this work. This assumption was similarly made by other authors [17]. Thermal diffusion is not taken into consideration since Liang et al. [31] showed that it has a negligible effect on ignition characteristics and leads only to small changes in flame propagation for the range of equivalence ratios investigated here.

To describe non-adiabatic effects during the forced ignition process, a transport equation for enthalpy is solved:

$$\frac{\partial}{\partial t}(\rho h) + \frac{\partial}{\partial x_i}(\rho u_i h) = \tag{3}$$
$$\frac{\partial}{\partial x_i}\left[\alpha\frac{\partial h}{\partial x_i} - \sum_{k=1}^{N_s}\left(h_k\left(\rho Y_k V_{k,i} + \alpha\frac{\partial Y_k}{\partial x_i}\right)\right)\right] + q_{\mathrm{ign}},$$

where q_{ign} represents a source term which is formulated as [44]:

$$q_{\mathrm{ign}}(r,t) = \begin{cases} \dfrac{E_{\mathrm{ign}}}{\pi^{\frac{n}{2}} r_{\mathrm{ign}}^n \tau_{\mathrm{ign}}} \exp\left[-\left(\dfrac{r}{r_{\mathrm{ign}}}\right)^2\right] & \text{if } t < \tau_{\mathrm{ign}}, \\ 0 & \text{if } t \geq \tau_{\mathrm{ign}}. \end{cases} \tag{4}$$

It is parameterized by the energy E_{ign} deposited during the time τ_{ign} in the region spanned by the radius r_{ign}. The exponent n is needed to account for different hotspot topologies, where $n = 2$ corresponds to cylindrical hotspots and $n = 3$ to spherical hotspots. The change in topology also affects the unit of the supplied energy E_{ign}, which is J/m (J) for cylindrical (spherical) configurations.

Note that closure is needed for the enthalpy since its transport is affected by all species. Although radicals (e.g. H) contribute little to the elemental balance, they can contribute substantially to the mixture's enthalpy of formation. Therefore, all species gradients need to be considered for the closure of the enthalpy equation. While gradients of transported species are directly available in the CFD calculation, all other species gradients are tabulated using 1D

flamelets and stored in the lookup table. Major radical concentrations, as well as their respective gradients, are primarily found in the reaction zone. Hence, although the enthalpy closure relies on 1D flamelet structures, this closure is particularly required in the vicinity of thin reaction zones where flamelet modeling yields accurate results.

In the proposed modeling approach, differential diffusion effects outside the thin reaction zone are captured by the transport of major species. It has been shown by Han et al. [18] that the performance of flamelet models can be improved by transporting additional scalars. However, not all transported scalars should be used to parameterize the flamelet manifold since this would lead to substantial memory requirements due to the increased manifold dimensionality. Therefore, the structure of the flamelet manifold is kept consistent with conventional tabulation strategies by utilizing an approximate version of the Bilger mixture fraction, which is defined based on the transported species only. Conceptually, a similar approach was used by Butz et al. [45], who compared LES results to Raman/Rayleigh measurements of methane-air flames showing multi regime characteristics. In their work, the authors approximated the Bilger mixture fraction by Raman species. Furthermore, Gierth et al. [16] showed that the approximation of the Bilger mixture fraction by transporting major species leads to an improved prediction of differential diffusion effects in flamelet LES of non-premixed oxy-fuel flames. For the hydrogen-air flames examined in this work, the approximated Z_{Bilger} is found to recover the same characteristics as the original version. It is emphasized that no significant modeling error is introduced by using this modified control parameter, since the two variants of the Bilger mixture fraction are closely correlated. A consistent coupling of the flamelet manifold to the CFD solver is then realized by also using the approximated Bilger mixture fraction as the control variable for the tabulation of the manifold. Furthermore, the progress variable can be directly evaluated from the transported species. Thereby, the transported scalars lead to self-contained coupling between the CFD solver and the flamelet manifold. Note that the progress variable is defined as the linear combination $Y_c = Y_{\mathrm{H_2O}} - Y_{\mathrm{H_2}} - Y_{\mathrm{O_2}}$. This definition was found to be suitable over a large range of equivalence ratio with slight non-monotonicity in the post-oxidation zones for very rich flames. This aspect could be further improved by applying regularization methods to retrieve optimized Y_c definitions for certain operating conditions [46–48], which is however beyond the scope of this study.

2.2. Flamelet manifold generation and tabulation

In this work, a composition space model (CSM) is used to generate the flamelet manifold. The CSM can describe the flame structures of different canonical premixed flame configurations as well as the limiting case of homogeneous ignition at constant pressure with only one set of equations [39,40]. Compared to canonical flames, which are expressed and solved in physical space, the governing equations of the CSM are solved directly along the reaction progress variable Y_c, which spans the composition space [40,41]. The set of equations contains equations for the mass fractions of the species (Eq. 5), the temperature equation (Eq. 6), and an equation for the progress variable gradient g_c (Eq. 7). The latter links the physical space and the composition space coordinate to the flame surface [40]:

$$\rho\frac{\partial Y_k}{\partial \tau} = -g_c\frac{\partial}{\partial Y_c}\left(g_c\,\rho Y_k\tilde{V}_k\right) + g_c\frac{\partial}{\partial Y_c}\left(g_c\,\rho Y_c\tilde{V}_c\right)\frac{\partial Y_k}{\partial Y_c} + \rho g_c\,\kappa\left(Y_k\tilde{V}_k - Y_c\tilde{V}_c\frac{\partial Y_k}{\partial Y_c}\right) - \dot{\omega}_c\frac{\partial Y_k}{\partial Y_c} + \dot{\omega}_k\,, \tag{5}$$

$$\rho\frac{\partial T}{\partial \tau} = \frac{g_c}{c_p}\frac{\partial}{\partial Y_c}\left(g_c\lambda\frac{\partial T}{\partial Y_c}\right) + g_c\frac{\partial}{\partial Y_c}\left(g_c\,\rho Y_c\tilde{V}_c\right)\frac{\partial T}{\partial Y_c} - \rho g_c^2\sum_k^{n_s}\frac{c_{\mathrm{p},k}}{c_{\mathrm{p}}}Y_k\tilde{V}_k\frac{\partial T}{\partial Y_c} - \rho g_c\,\kappa\left(\frac{\lambda}{\rho c_p} + Y_c\tilde{V}_c\right)\frac{\partial T}{\partial Y_c} - \dot{\omega}_c\frac{\partial T}{\partial Y_c} + \frac{\dot{\omega}_T}{c_p}\,, \tag{6}$$

$$0 = -g_c^2\frac{\partial^2}{\partial {Y_c}^2}\left(g_c\,\rho Y_c\tilde{V}_c\right) + g_c^2\frac{\partial}{\partial Y_c}\left(\kappa\,\rho Y_c\tilde{V}_c\right) - \dot{\omega}_c\frac{\partial g_c}{\partial Y_c} + g_c\frac{\partial\dot{\omega}_c}{\partial Y_c} + \rho K_s g_c\,, \tag{7}$$

where $\tilde{V}_i$ represents the diffusion velocity of species i with respect to the Y_c-composition space, λ is the heat conductivity, c_{p} is the heat capacity and $\dot{\omega}_T$ is the heat release rate. Further, strain $K_s = \nabla_t\cdot\mathbf{u}_t - (\mathbf{u}\cdot\mathbf{n}_c)\kappa_c$, and curvature $\kappa_c = -\nabla\cdot\mathbf{n}_c$ can be supplied as external parameters, where $\nabla_t\cdot\mathbf{u}_t$ represents flame-tangential straining by the flow and $\mathbf{n}_c$ is the flame-normal unit vector [40–42]. In this work, the CSM is utilized to tabulate unstretched flames ($g_c > 0$) and homogeneous ignition with constant pressure. The set of equations describes homogeneous ignition in the limit of $g_c \to 0$ when all diffusive terms vanish [39].

A large set of hydrogen-air flames is calculated across a range of equivalence ratios $0.35 \le \phi \le 2.0$ and temperature levels $300\mathrm{K} \le \mathrm{T_u} \le 3500\mathrm{K}$. Additionally, the enthalpy of the fresh gases is reduced using exhaust gas recirculation (EGR) [49]. For diffusion modeling, a mixture-averaged approach [50] is used. For low temperatures in the fresh gas, the CSM recovers the properties of an unstretched premixed flame (deflagration limit, eigenvalue s_{L}), but at higher temperatures, it transitions toward the ignition limit. In this context, the g_c solution represents the relation between composition space and physical space. The one-dimensional physical space coordinate x can be reconstructed from the progress variable gradient as:

$$x(Y_c) = \int_{Y_{c,\min}}^{Y_c}\frac{\mathrm{d}Y_c}{g_c}\,. \tag{8}$$

It is noted that single CSM solutions can be directly compared to canonical flame configurations by means of this coordinate. In more complex flame configurations, such comparisons could be realized by reconstruction of a flame-attached coordinate following the progress variable gradient. On the other hand, solutions corresponding to homogeneous reactors represent an asymptotic limit resulting in a zero-dimensional structure where all diffusive terms vanish at the limit $g_c \to 0$ [40,41]. In this case, similarly to the reconstruction of the physical space coordinate, a temporal coordinate can be reconstructed by the integration of the progress variable source term.

Figure 2 shows examples of flamelets which are used to generate the tabulated manifold.

The equivalence ratio is kept constant ($\phi = 0.7$) to focus on enthalpy variation along the progress variable dimension. Further, the line styles are varied according to the characteristics of the flamelets. For high enthalpy levels, the conditions correspond to constant-pressure homogeneous ignition (dotted lines). Note that very high fresh gas temperatures above 3000K would suggest the use of the more complex plasma physics. However, plasma chemistry species quickly recombine to electrically neutral species and are therefore neglected in this work [51]. At these conditions the flamelet solutions mainly correspond to dissociation reactions without significant temperature increase. Preheated unstretched flamelets, which correspond to freely propagating flames (FP), are

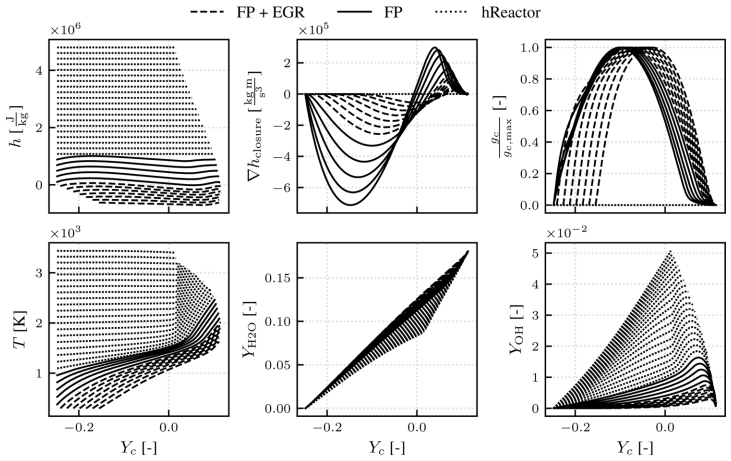

Fig. 2. Characteristics of flamelets with varying enthalpy levels and $\phi = 0.7$ which are used for table generation. Conceptual differences between flamelets are highlighted by different line styles for planar freely propagating flames with exhaust gas re-circulation (FP+EGR, dashed lines), planar freely propagating flames (FP, solid lines), and homogeneous ignition at constant pressure (hReactor, dotted lines).

indicated by solid lines. Finally, the lower enthalpy boundary is extended by adding unstretched flamelets with EGR. The latter is required to ensure that all thermo-chemical states found in the addressed flame configuration are covered in the flamelet manifold, since flame topologies subject to significant differential diffusion can exhibit large enthalpy variations. Overall, a consistent variation in thermo-chemical quantities such as the temperature and species mass fractions is observed. Additionally, the normalized progress variable gradient profiles are shown which are also affected by enthalpy variation and illustrate the relationship between physical and composition space (see Eq. 8). This can also be observed in the enthalpy gradient $\nabla h_{\text{closure}}$ used for the closure of Eq. 3:

$$\nabla h_{\text{closure}} = \sum_{k=1}^{N_s} \left(h_k \left(\rho Y_k V_{k,i} + \alpha \frac{\partial Y_k}{\partial x_i} \right) \right) \forall k \notin \{H_2, O_2, H_2O\}. \quad (9)$$

It is computed for every flamelet using the reconstructed physical coordinate x. This gradient shows increasing amplitudes for higher enthalpy levels as both the progress variable gradient and the amount of radical mass fractions change. Note that, despite increasing enthalpy gradients, no intersections between neighboring flamelet solutions are found.

The size of multidimensional tabulated manifolds can easily exceed the available memory. This can be circumvented without any loss of accuracy by using a memory abstraction layer, for which the flamelet manifold needs to be generated along normalized variables [52,53]. To generate the flamelet manifold along the desired control variables, the initial set of flame calculations ($\psi(\phi, h, Y_c)$) is first mapped to the approximate Bilger mixture fraction. It is defined by a coupling function between the fuel (index 1) and oxidizer (index 0) [37]:

$$Z_{\text{Bilger}} = \frac{\beta - \beta_0}{\beta_1 - \beta_0} \quad (10)$$

These coupling functions depend on the elemental mass fractions Z_l contained in the mixture,

$$\beta = \sum_{l=1}^{N_e} \gamma_l \sum_{k=1}^{N_s} \frac{a_{l,k} M_l Y_k}{M_k} \quad (11)$$

where γ_l represents a weighting factor of element l, M_l (M_k) corresponds to the molecular weight of element l (species k), and $a_{l,k}$ to the number of element l in species k. Note that the weighting factors γ_l are not unique [43]. In this work, the weights are chosen in agreement with Bilger et al. [37]. Furthermore, only major species, which are also transported in the CFD calculation, are used to calculate the coupling function β.

Second, the enthalpy h is mapped to the normalized enthalpy H_{norm}:

$$H_{\text{norm}} = \frac{h - h_{\text{min}}(Z_{\text{Bilger}}, Y_c)}{h_{\text{max}}(Z_{\text{Bilger}}, Y_c) - h_{\text{min}}(Z_{\text{Bilger}}, Y_c)}. \quad (12)$$

Finally, the flamelet manifold is mapped to a normalized progress variable:

$$c = \frac{Y_c - Y_{c,\text{min}}(Z_{\text{Bilger}}, H_{\text{norm}})}{Y_{c,\text{max}}(Z_{\text{Bilger}}, H_{\text{norm}}) - Y_{c,\text{min}}(Z_{\text{Bilger}}, H_{\text{norm}})}. \quad (13)$$

This leads to the final flamelet manifold parametrization $\psi(Z_{\text{Bilger}}, H_{\text{norm}}, c)$.

The variation in enthalpy over the progress variable directly affects the table lookup, since the minimum and maximum values are interdependent and can only be estimated iteratively, resulting in a time-consuming lookup procedure [10]. On the other hand, when unity Lewis number diffusion is used, a two-step lookup can be used for tabulated manifolds built along the same variables due to the decoupled normalization of enthalpy and the progress variable [54]. Establishing a similar procedure, flamelet manifolds that account for differential diffusion must be constructed such that the minimum and maximum enthalpy values can be determined independently of the progress variable. Therefore, to increase the efficiency of the lookup, the lower boundary of the table is extrapolated to there is a constant minimum enthalpy level. The upper limit of the enthalpy dimension is already independent of the progress variable since it corresponds to CSM calculations of homogeneous ignition, which exhibit constant enthalpy levels.

Finally, a patch for the source terms of the major species is introduced which is analogous to modeling approaches utilized for non-premixed ignition phenomena [34,55,56]. A non-zero source term $\dot{\omega}_i > 0$ is imposed for the transported species at the fresh gas boundary of the manifold ($c = 0$) to obtain an accurate prediction

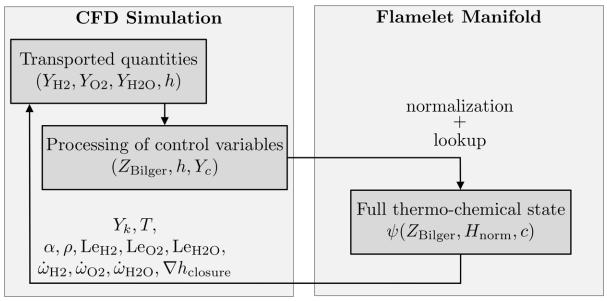

Fig. 3. Schematic overview of the coupling between transported quantities in a low-Mach CFD simulation and flamelet manifold.

of the ignition process. A conceivable alternative approach could be to extend the size of the tabulated manifold, e.g. by resolving an ignition progress variable based on ignition markers such as HO_2 and H_2O_2 [34], which would add considerable memory overhead and is avoided by the aforementioned approach. The patched source terms are determined from an integration method developed for non-premixed ignition by Sun et al. [56, Sec. 3.2.4.] which is adapted here for premixed ignition phenomena:

$$\dot{\omega}^*_{i,\text{init}}(Z_{\text{Bilger}}, H_{\text{norm}} \geq H_{\text{norm,crit}}) = \frac{\int_0^{c_{\text{init}}} \dot{\omega}_{i,\text{trans}}(Z_{\text{Bilger}}, H_{\text{norm}}, c)\,\mathrm{d}c}{\int_0^{c_{\text{init}}} \mathrm{d}c} \quad \forall c \in [0, c_{\text{init}}], \tag{14}$$

where c_{init} represents a threshold that is set to a small value (here, $c_{\text{init}} = 10^{-9}$ is used). By this means, ignitable mixtures can ignite even if chemical source terms of the transported species are zero for fresh gas conditions and would not lead to an ignition event otherwise [56]. The source term patch according to Eq. (14) is restricted to high enthalpy levels only ($H_{\text{norm,crit}}$) which correspond to the conditions relevant for ignition.

The aforementioned modeling specifics are schematically summarized in Fig. 3, showing the coupling between the transported scalars and the flamelet manifold. The figure also outlines tabulated quantities (e.g. Lewis numbers and source terms of major species) which are required for the transport equations solved in low-Mach CFD simulation. Note that, coupling flamelet manifolds to compressible CFD solvers require more refined modeling approaches [25,57].

2.3. Numerical setup

In this work, two different modeling approaches are used: the new flamelet model is applied in coupled simulations (FPV) and, for comparison, fully resolved direct chemistry calculations (DC) are conducted. The DC simulations serve as reference results to validate the new FPV model.

The FPV simulations are performed in an OpenFOAM framework [16,49,58] using second-order discretization in time and space. First, one-dimensional planar flames are computed to verify the modeling approach. These flames are initialized by burned products at equilibrium at one end of the domain and by fresh mixture ($T_u = 300$K, $p = 1$atm) in the remaining domain. The evolving flame then propagates through the domain with a length of $L = 3$cm discretized by 4000 uniform cells. Second, the ignition and the flame propagation of cylindrical and spherical expanding flames in quiescent mixtures is investigated. Finally, the ignition of the spherical flame is also studied in a counterflow flow field. The computational domains are shown schematically in Fig. 4. The 2D domains, which are used to study the ignition in quiescent mixtures, exhibit an edge length of $L = 15$mm and 1350 equidistant cells in both directions, resulting in a uniform mesh with 1.82 million cells and a cell size of $\Delta_{\text{mesh}} = 11\,\mu$m. While the same grid sizes are used for cylindrical and spherical flames, the specific flame configurations are realized by applying different symmetry conditions.

Cylindrical flames are computed in a 2D plane, applying cyclic boundary conditions at the edges along of which the flame evolves ($x = 0$, $y = 0$). Spherical flames are obtained by applying axisymmetric boundary conditions to a wedge-shaped domain at $y = 0$ and planar symmetry at $x = 0$. For both cases an atmospheric outlet condition is applied at $x = L$ and $y = L$. The computational domain used to study ignition in a counterflow flow field exhibits an edge length of $L = 20$mm in axial and $R = 30$mm in radial direction and a uniform mesh with a cell size of $\Delta_{\text{mesh}} = 25\,\mu$m is used. Inlet boundary conditions are applied along both radial patches ($x = L/2$ and $x = -L/2$), by prescribing a uniform inlet velocity U_{in} and the composition of the fresh mixture. Axisymmetric boundary conditions are applied at the domain center ($y = 0$) and an atmospheric outlet condition is prescribed at $y = R$. The hotspot used to ignite the mixture is defined according to Eq. 4 with a size of $r_{\text{ign}} = 0.2$mm for $\tau_{\text{ign}} = 0.2$ms. For a quantitative comparison, flame structures are extracted along the diagonal of the domain.

The fully resolved DC simulations are performed utilizing established one-dimensional models. A one-dimensional in-house flame solver [59] is used to compute direct chemistry reference solutions for planar flames, while the A-SURF code is used for curved flames [60,61]. The governing equations are revisited in the supplementary material. Additionally, the two-dimensional counterflow DC data is generated based on OpenFOAM [62,63], which is coupled with Cantera [64] for the evaluation of the reaction rates and transport properties. For all calculations, a detailed hydrogen reaction mechanism [65] is used in combination with a mixture-averaged diffusion model [50] However, it is noted that thermal/Soret diffusion can become increasingly important for very lean H_2-air flames [66].

3. Results and discussion

The proposed FPV model is validated against a set of flame configurations by comparing both global flame properties and local flame structures with corresponding calculations using direct chemistry (DC) simulations. The complexity of the flames is successively increased, starting with one-dimensional freely-propagating planar flames (Sec. 3.1). Then, 2D cylindrically expanding flames (Sec. 3.2), spherically expanding flames (Sec. 3.3) and ignition counterflow flames (Sec. 3.4) are addressed and in all configurations ignition is initiated with a fixed energy deposition.

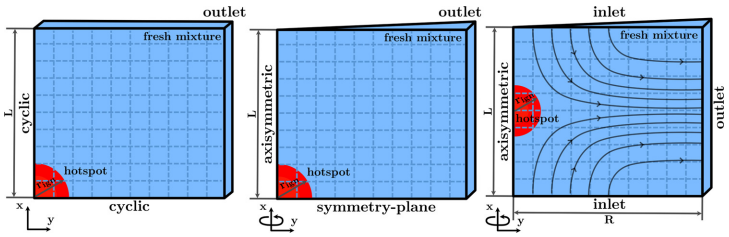

Fig. 4. Schematic representation of the computational domains used in OpenFOAM. Cylindrical flame on the left, spherical flame in the middle and the counterflow flame on the right.

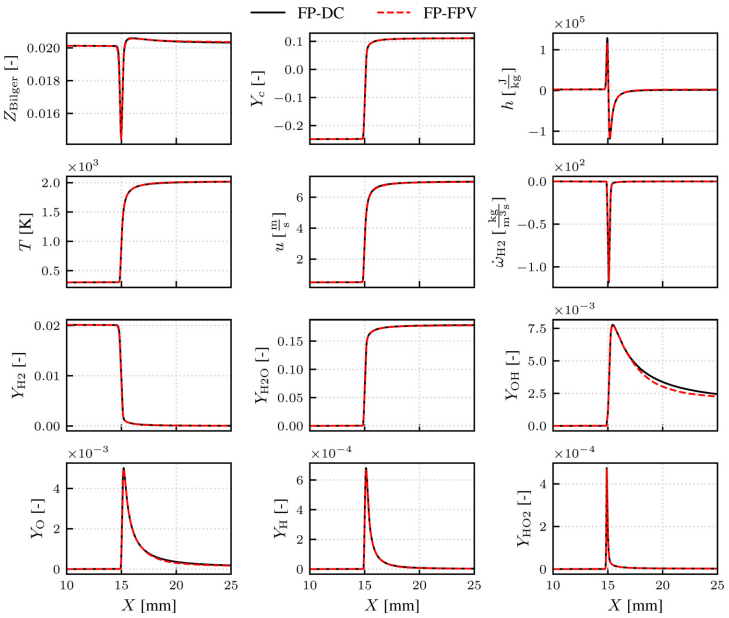

Fig. 5. Flame structure comparison between the fully-coupled FPV model (red) and the DC solution (black) of a freely propagating planar hydrogen-air flame with $\phi = 0.7$. The profiles along the physical space coordinate X are shown for the control parameters of the flamelet manifold ($Z_{\mathrm{Bilger}}, h, Y_c$; top row), the temperature T, the velocity u and the hydrogen source term $\dot{\omega}_{\mathrm{H2}}$ (second row) and various species mass fractions (bottom rows).

Finally, the capability of the FPV model to predict the minimum ignition energy (Sec. 3.5) is evaluated. In these configurations the FPV model led to a reduction of the computational cost by an order of magnitude. Even though the number of transport equations being solved is only halved, the interpolation of mixture properties and source terms from the manifold is faster than their estimation based on a detailed reaction mechanism.

3.1. Freely propagating planar flames

Characteristics of freely propagating flames are investigated in order to verify and validate the FPV model. While local flame structures are discussed here, it is noted that the flamelet approach also predicts the laminar burning velocity in the investigated range of equivalence ratios $0.7 \leq \phi \leq 1.4$ (cf. supplementary material).

In Fig. 5, the flame structures of a lean hydrogen-air flame ($\phi = 0.7$) obtained by the FPV model and the DC simulation are compared.

Here, the profiles for the flamelet control variables ($Z_{\mathrm{Bilger}}, h, Y_c$) are shown along the physical space coordinate X. Additionally, the temperature T and the velocity profile u are shown together with the hydrogen source term $\dot{\omega}_{\mathrm{H2}}$ and different species (H_2, H_2O, OH, O, H, HO_2). In general, very good agreement is observed for all quantities. Specifically, the mixture stratification due to differential diffusion is captured well by the FPV model, since the variation of both the Bilger mixture fraction and the enthalpy across the flame is correctly described. This indicates the feasibility of the closures proposed for mixture fraction and enthalpy and highlights the model's general capability to account for differential diffusion effects. Only minor deviations can be found in the absolute values of the OH mass fraction on the burned side. Similarly, very good agreement between the FPV model and DC calculations is observed

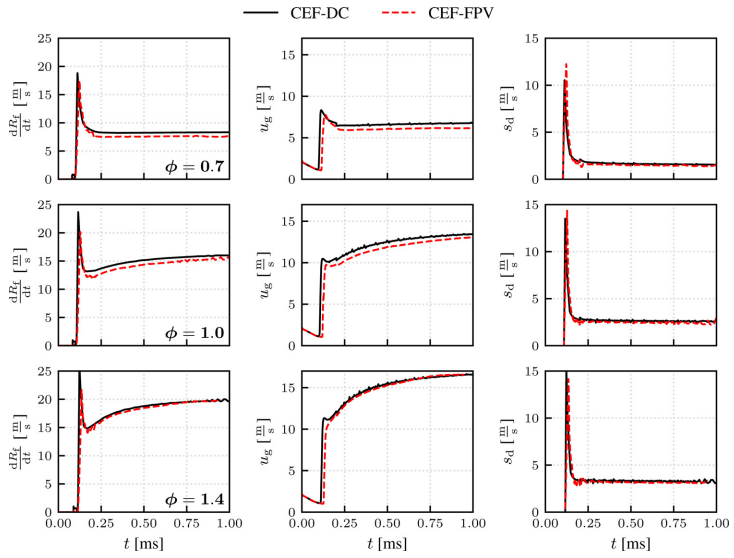

Fig. 6. Comparison of flame propagation speed $\frac{dR_f}{dt}$ (left), gas velocity u_g (middle) and flame displacement speed s_d (right) in cylindrical expanding flames ignited by an energy deposition of $E_{ign} = 35$nJ/m with equivalence ratios of $\phi = 0.7$, $\phi = 1.0$ and $\phi = 1.4$.

for flame structures across the entire range of investigated equivalence ratios ($0.7 \leq \phi \leq 1.4$), which are shown for reference in the supplementary material.

3.2. Cylindrical expanding flames

The complexity of the flame configuration is increased when cylindrical expanding flames (CEFs) are examined; the numerical configuration is shown in Fig. 4 (left). Notable differences compared to the freely propagating flame are the unsteadiness, the appearance of curvature and also non-adiabatic effects caused by the energy deposition used to ignite the mixture. Additionally, the propagation of the CEF is affected by thermal expansion of the burned gases enclosed by the flame front. From a modelling point of view, the thermo-chemical state of the burned gases needs to be correctly predicted, while it also affects the unburned side of the flame through the flow field. Further modeling challenges include the prediction of ignition caused by energy deposition and capturing the development from the hotspot to a self-sustained flame.

The transient evolution of the flame propagation speed from ignition to a quasi-steady flame propagation, which is obtained by the FPV model and the DC simulations, is shown in Fig. 6. Each row corresponds to different equivalence ratios and ignition is initiated with a fixed energy deposition $E_{ign} = 35$nJ/m in all cases.

The flame propagation speed dR_f/dt (Fig. 6, left) observed in expanding flames is a result of both thermal expansion and self-sustained flame propagation. It can be decomposed according to:

$$\frac{dR_f}{dt} = u_g + s_d, \tag{15}$$

where u_g is the gas velocity (unburned side) which results from thermal expansion of the hot products (Fig. 6, middle) and s_d is the flame displacement speed (Fig. 6, right) [67]. Here, dR_f/dt is estimated by tracking the location of the maximum progress variable source term. The gas velocity is defined as the peak velocity value found on the unburned side of the flame, while the combustion products have a zero velocity [67]. The flame displacement speed results from the difference in the other two velocities.

In Fig. 6, the initial increase in flame propagation speed marks the point of ignition where thermal expansion and chemical reactions also show a strong increase. This is followed by a decay during the transition of the ignition kernel to the self-sustained flame propagation, where the flame propagation speed becomes constant.

In general, favorable agreement is observed between the FPV model and the DC reference solution for all propagation phases and for all addressed equivalence ratios. Further, the onset of ignition is captured accurately by the FPV model, while the peak velocities are slightly underestimated. The FPV model tends to slightly underpredict the propagation speed during the transition from ignition to self-sustained flame propagation. It is highlighted that the observed offset can be related to thermal expansion (cf. u_g), since the flame displacement speed shows very good agreement. Hence, the underpredicted gas velocity leads to the lower flame propagation speed $\frac{dR_f}{dt}$. However, the deviation in the flame propagation speed is less than 1 % for the rich CEF, while a slightly larger deviation can be observed for the lean and stoichiometric cases. Given that modeling errors do accumulate during the transient evolution from ignition kernel formation to self-sustained flame propagation, the highest difference of 7 % in the gas velocity for the lean hydrogen-air flame is considered to be small.

The cause of this offset is investigated in the supplementary material, where the detailed flame structure is analyzed. In case of the FPV result, it is found that the temperature profile is shifted towards leaner mixtures, with the largest shift close to the unburned side, which indicates a close link between the slightly underpredicted gas velocity and the observed deviations in mixture com-

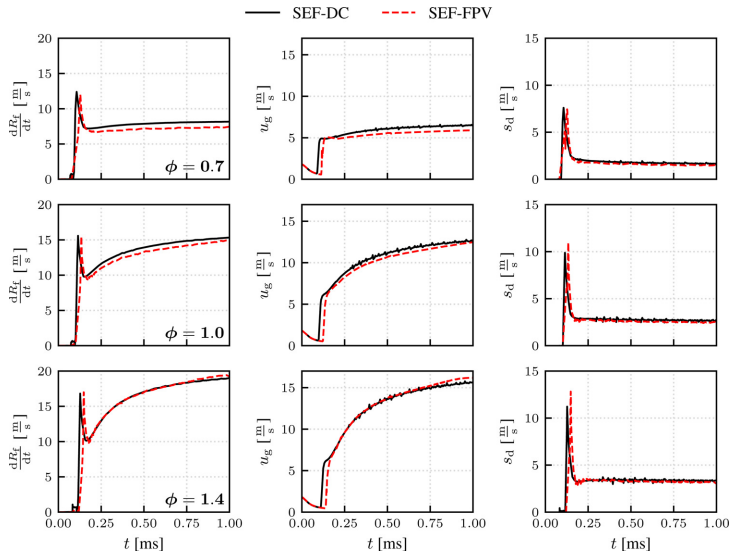

Fig. 7. Comparison of flame propagation speed $\frac{dR_f}{dt}$, gas velocity u_g and flame displacement speed s_d in spherical expanding flames ignited by an energy deposition of $E_{ign} = 0.15mJ$ with equivalence ratios of $\phi = 0.7$, $\phi = 1.0$ and $\phi = 1.4$.

position. The small deviation in Z_{Bilger} results in a shift in density, which then affects the velocity on the unburned side of the flame. While similar shifts in the mixture composition are observed for the rich case, the deviations in the flame propagation are smaller, since smaller density gradients are found across the flame front (flame structures for the stoichiometric and the rich CEF can also be found in the supplementary material).

In general, good agreement is found between the FPV model and the DC simulations not only for flame propagation, but also for the local flame structure, with minor deviations in the preheat zone. This validates the flamelet-based ignition model and the model's capability to describe non-adiabatic effects.

3.3. Spherical expanding flames

The FPV model is compared against DC reference results for spherical expanding flames (SEFs) with an analogous variation in the equivalence ratio from lean to rich; the numerical configuration is shown in Fig. 4 (middle). Compared to cylindrical flames, spherical flames are subject to increased flame stretch.

In Fig. 7, the flame speed obtained with the FPV model and the DC reference are compared for the transient evolution of the SEFs with varying equivalence ratio. The same ignition energy of $E_{ign} = 0.15$mJ is used for all flames. While CEFs and SEFs approach the same quasi-steady flame propagation, there are notable differences in the transition from ignition to propagation. For CEFs, the gas velocity exhibits a peak, while only a small plateau is observed for SEFs. This is related to the larger increase in the flame surface compared to cylindrical flames. The onset of ignition is slightly overestimated by the FPV model, as is the position of the peak value of the flame propagation speed $\frac{dR_f}{dt}$. Despite this small deviation, the FPV model reproduces the temporal evolution of the propagation of both CEFs and SEFs very well. As previously shown for CEFs, differences in propagation speed are caused by the underpredicted gas velocity u_g and the flame displacement speed shows very good agreement. Here, a similar observation can be made for the SEFs.

These differences are further investigated by performing a detailed flame structure analysis. In Fig. 8, the profiles of the control parameters of the flamelet manifold, the temperature T, velocity u, and hydrogen source term $\dot{\omega}_{H2}$ obtained by the flamelet model and the direct chemistry solution are compared for the lean SEF ($\phi = 0.7$). Further, various species profiles including both major and minor species are depicted. While the overall variation in the mixture fraction is larger compared to the CEF due to more dominant stretch effects, the FPV model in general reproduces the flame structure very well compared to the DC simulation. Similarly to the CEF structure, where small deviations are found in the mixture fraction on the burned side and in the velocity profile of the unburned side, analogous shifts are also found in the flame structure of the SEF. This confirms that a similar relation between the mixture composition, density, and velocity exists for the SEFs. The differences between the flame structures of the two topologies (cylindrical vs. spherical) can be attributed to the volume enclosed on the burned side of the flame. For SEFs, the volume of the burned side is smaller, while the area in which the flame propagates is larger. This can also be seen in the mass fraction of OH and the temperature at the center of the flame, which both exhibit smaller values compared to the CEF structure. The SEF structure obtained with the FPV model also agrees well with the DC reference calculations for stoichiometric and rich conditions. A detailed analysis is provided in the supplementary material.

In general, good agreement is found between the flamelet approach and the DC simulations for the flame propagation and local flame structure of spherical expanding flames. The observed deviations result from similar effects to those discussed for CEFs. Note that relative deviations found for SEFs do not differ significantly from those for CEFs despite the increase in flame stretch. The maximum deviation in the flame propagation speed is about 8 % for the lean case and less than 2 % for the other cases. Therefore, it can

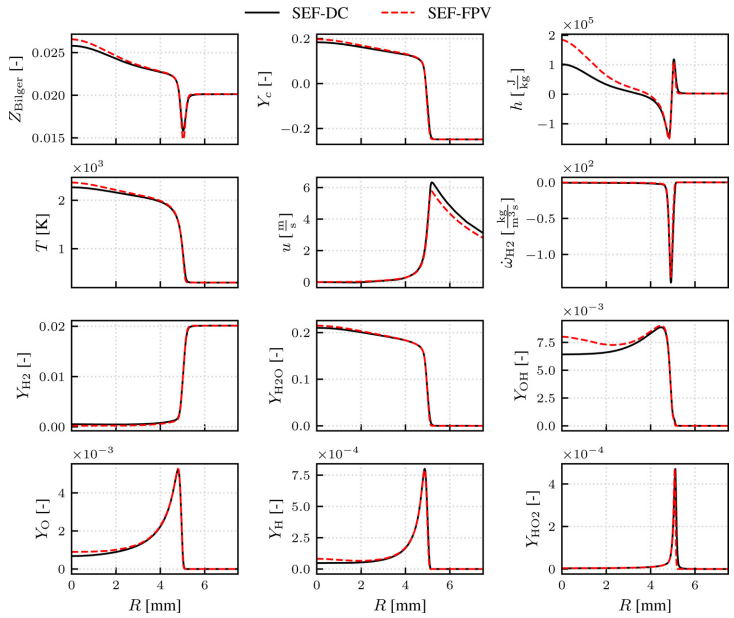

Fig. 8. Flame structure comparison of a spherical expanding flame with $\phi = 0.7$ ignited by an ignition energy of $E_{\mathrm{ign}} = 0.15\mathrm{mJ}$. The profiles along the radial coordinate R are shown for the input parameters of the tabulated manifold ($Z_{\mathrm{Bilger}}, h, Y_c$; top row), the temperature T, the velocity u and the hydrogen source term $\dot{\omega}_{\mathrm{H2}}$ (second row) and various species mass fractions (bottom rows).

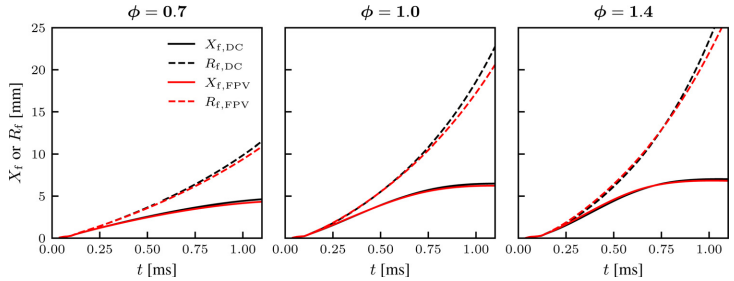

Fig. 9. Comparison of the temporal evolution of flame positions along the axial (X_{f}) and radial (R_{f}) direction for the igniting counterflow flames with equivalence ratios of $\phi = 0.7$, $\phi = 1.0$ and $\phi = 1.4$ predicted by the DC calculation (black) and the FPV model (red).

be concluded that the transport of major species leads to a flexible and robust flamelet model, as all effects caused by the variation in the equivalence ratio and the flame topology are reproduced well.

3.4. Igniting counterflow flames

While the previously discussed flame configurations are used to investigate ignition processes in quiescent mixtures, in the following igniting counterflow flames are considered. In comparison to the CEF and SEF, the counterflow leads to a deformation of the flame kernel with curvature variations along the flame front, additional straining of the flame due to the imposed flow field, and an asymmetric flame front in axial and radial direction. The numerical configuration is shown in Fig. 4 (right). Note that initially a converged numerical solution is computed for the steady non-reactive counterflow before the ignition process is initiated by the energy deposition (Eq. 4). Further, the global strain rate $a_{\mathrm{g}} = 4U_{\mathrm{in}}/L$ [68] is set to a constant value of $a_{\mathrm{g}} = 1000\mathrm{s}^{-1}$ for all following calculations and the same equivalence ratios are considered as before ($\phi = 0.7$, 1.0 and 1.4).

In Fig. 9, the temporal evolution of the flame position in axial (X_{f}) and radial direction (R_{f}) is shown for the DC reference simulations (black) with varying equivalence ratios and compared to the predictions of the FPV model (red). Note that all flames are ignited by an ignition energy of $E_{\mathrm{ign}} = 0.15\mathrm{mJ}$, analogously to the SEFs studied in Sec. 3.3.

The evolution of the axial flame position X_f indicates that the flame stabilizes against the imposed flow field, since it asymptot-

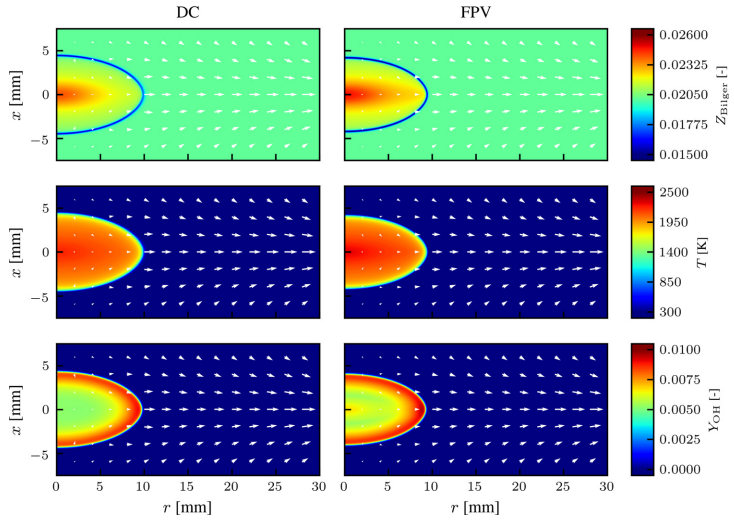

Fig. 10. Flame structure comparison of a counterflow flame flame with $\phi = 0.7$ ignited by an ignition energy of $E_{\mathrm{ign}} = 0.15mJ$. The flame is extracted at the time $t = 1$ms and color-coded by the Bilger mixture fraction Z_{Bilger}, temperature T, and the OH mass fraction Y_{OH} with color bars given for each row. The flow field is depicted by the white arrows.

ically approaches a limit around $t = 1$ms. On the other hand, the flame propagates outwards in the radial direction R_{f} and gets accelerated by the imposed flow field. The comparison of the flame positions between the DC calculation and the FPV model shows consistent trends compared to the flame configurations in quiescent mixtures. The FPV model also predicts a slightly slower flame propagation speed for the counterflow flames, since minor deviations are visible for the radial flame position. A similar conclusion can be drawn from the axial flame position, since the flames predicted by the FPV model stabilize slightly closer to the domain center, corresponding to a slightly lower axial velocity of the imposed flow field. However, given the challenging flame physics involving ignition, transient flame propagation, flame curvature, differential diffusion, and the interaction with an imposed flow, the observed agreement is remarkable.

Next, the flame structure of the evolving counterflow flame is analyzed. In Fig. 10, the contours of the Bilger mixture fraction Z_{Bilger}, temperature T and the OH radical mass fraction Y_{OH} are shown for the DC simulation and the FPV calculation for the lean flame($\phi = 0.7$) at the time $t = 1$ms. Additionally, the flow field is depicted by white arrows.

The FPV model predicts a very similar flame shape as observed in the DC simulation. This good agreement is also reflected in the velocity field which includes the interaction of the flame with the counterflow and represents an integral response to all modelling assumptions. Furthermore, all scalar fields shown are in good agreement with the DC reference data and observed deviations are minor, which is consistent with the previously discussed flame configurations. Also, in the counterflow configuration, the FPV model predicts slightly higher values for Z_{Bilger} on the burned side and the OH mass fraction is slightly overpredicted around the stagnation plane ($x = 0$). The higher OH mass fraction is directly related to the shift in Z_{Bilger}, while the temperature does not depict a sensitive response. A detailed analysis concerning the stoichiometric and the rich case is provided in the supplementary material, where a similar good agreement is obtained. These findings indicate that also multidimensional effects, which originate from the imposed counterflow, can be well recovered by the FPV model.

3.5. Prediction of the minimum ignition energy

It is shown in the previous sections that the FPV model recovers the onset of ignition, the subsequent flame propagation and the flame structure. Next, the model is used to determine the minimum ignition energy (MIE), which is the threshold value of E_{ign} (cf. Eq. 4) below which no ignition is possible. It is determined by performing multiple calculations with varying E_{ign} in a bisectional approach. The MIE is an important quantity which is related to safety aspects (ignition propensity of a gas mixture) and combustor design; for instance, is can be used to determine whether ignition will occur reliably. From a modeling perspective, the near-limit ignition event is particularly challenging because of high unsteadiness, enthalpy gradients and strong curvature during ignition kernel formation.

In Fig. 11, the MIEs obtained with the FPV model are compared to the direct chemistry solution for all equivalence ratios investigated and for flame configurations (CEF and SEF). Note that the MIE obtained in the counterflow configuration is almost identical to the one obtained from the SEF (not shown). The MIE is seen to increase with an increasing equivalence ratio. The FPV model reproduces this trend for both cylindrical and spherical flames, only slightly overestimating the absolute values compared to the direct chemistry reference solutions. Good agreement is found for the MIE of the stoichiometric mixtures ($\mathrm{Le}_{\mathrm{eff}} \approx 0.95$) and the rich mixtures ($\mathrm{Le}_{\mathrm{eff}} \approx 1.4$). Deviations are observed to increase towards the lean mixture ($\phi = 0.7$, $\mathrm{Le}_{\mathrm{eff}} \approx 0.5$) for both cylindrical and spherical expanding flames. This trend may be related to strong positive stretch effects in small spherical ignition kernels associated with Lewis numbers smaller than unity. Nevertheless, it is noteworthy that the FPV model recovers the MIE with only minor deviations, showing that the model can capture stretch effects even during ignition kernel formation in this near-limit case.

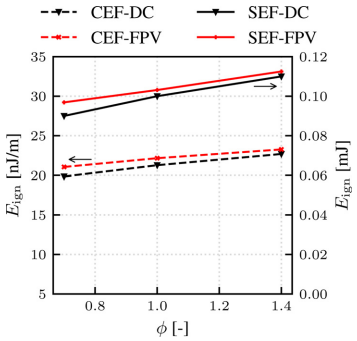

Fig. 11. Comparison of minimum ignition energies for different equivalence ratios and flame configurations.

4. Conclusions

In this work, a novel flamelet-based modeling approach is presented which accurately recovers forced ignition and flame propagation for planar and curved premixed hydrogen-air flames. The model is coupled to a three-dimensional flamelet manifold which is parametrized by an approximate Bilger mixture fraction Z_{Bilger}, progress variable Y_c and enthalpy h. The table is constructed with a recently developed composition space model (CSM) which allows to blend between unstretched premixed flamelets and constant pressure homogeneous ignition. Unlike common flamelet approaches, enthalpy and a set of major species are transported in the CFD. The approximate Bilger mixture fraction and the progress variable are determined from the transported species and then utilized for the look-up. While transporting the composite scalars Z_{Bilger} and Y_c requires additional modeling effort with respect to their diffusivity (or Lewis number), the new approach can circumvent such assumptions by tabulating the exact species diffusion coefficients. Furthermore, transporting species instead of control variables is advantageous for accurately predicting mixing processes away from the thin reaction zone.

The numerical results verify that the flamelet model can predict differential diffusion effects, curvature effects, and the forced ignition of premixed hydrogen-air flames across a range of equivalence ratios (lean to rich) with effective Lewis numbers smaller and greater than unity. This is shown by comparing detailed flame structures, the transient flame evolution (flame speed, displacement speed), and the ignition delay times to detailed chemistry reference calculations. Minor discrepancies only occur in the prediction of the gas velocity which originates from thermal expansion and in the flame structure at the radial flame tip of the igniting counterflow flames. It is further highlighted that the model accurately captures the minimum ignition energies (MIEs, deviations below 3 %) required to ignite cylindrical or spherical expanding hydrogen-air flames. Considering the strong diffusivity of hydrogen, which represents a challenge for flamelet-based modeling, these results underline the fidelity of the modeling approach.

It is further noted that the method is not restricted to hydrogen but can also be transferred to other fuels, which requires modifications to the tabulated flames and transported species. While three transported species appear to be sufficient for hydrogen flames, it is conceivable that the method requires more transported species in case of more complex fuels, which is still significantly less than the total amount of species in a detailed reaction mechanism. In turn, the computational cost increases compared to conventional flamelet-based models (usually 2-3 control variables). Ultimately, advantages in accuracy need to be weighed against model performance which should be carefully examined in future work.

In summary, this work shows that the FPV model exhibits promising predictive capabilities for hydrogen flames, where differential diffusion needs to be considered. Future studies should investigate the model's performance for hydrogen-rich fuel blends (e.g., CH_4/H_2, NH_3/H_2) or large hydrocarbons. Besides this, closures for turbulence-chemistry interactions are required when transferring the modeling approach to turbulent combustion (e.g. Large Eddy Simulations, LES) which represents a challenging subject for future research.

Declaration of Competing Interest

The authors declare that they have no known competing financial interests or personal relationships that could have appeared to influence the work reported in this paper.

Acknowledgments

Financial support is kindly acknowledged from the German Research Foundation (DFG) – Project No. 411275182 and the National Natural Science Foundation of China – Project No. 51861135309. Calculations for this research were conducted on the Lichtenberg II High Performance Computer of the Technical University of Darmstadt. We thank Drs. Thorsten Zirwes, Feichi Zhang, and Henning Bockhorn at Karlsruhe Institute of Technology for providing us their EBI-DNS code.

Supplementary material

Supplementary material associated with this article can be found, in the online version, at doi:10.1016/j.combustflame.2022.112125

References

[1] K. Kohse-Höinghaus, Combustion in the future: The importance of chemistry, Proceedings of the Combustion Institute 38 (1) (2021) 1–56.
[2] K. Kohse-Höinghaus, Clean combustion: Chemistry and diagnostics for a systems approach in transportation and energy conversion, Progress in Energy and Combustion Science 65 (2018) 1–5.
[3] H. Kobayashi, A. Hayakawa, K. Somarathne, E. Okafor, Science and technology of ammonia combustion, Proc. Combust. Inst. 37 (1) (2019) 109–133.
[4] B. Fiorina, D. Veynante, S. Candel, Modeling combustion chemistry in large eddy simulation of turbulent flames, Flow Turbul. Combust. 94 (1) (2015) 3–42.
[5] N. Peters, Laminar flamelet concepts in turbulent combustion, Symp. (Int.) Combust. 21 (1) (1988) 1231–1250.
[6] O. Gicquel, N. Darabiha, D. Thévenin, Laminar premixed hydrogen/air counterflow flame simulations using flame prolongation of ILDM with differential diffusion, Proc. Combust. Inst. 28 (2) (2000) 1901–1908.
[7] H. Pitsch, Unsteady flamelet modeling of differential diffusion in turbulent jet diffusion flames, Combust. Flame 123 (3) (2000) 358–374.
[8] D. Veynante, L. Vervisch, Turbulent combustion modeling, Prog. Energy Combust. Sci. 28 (3) (2002) 193–266.
[9] G. Lodier, L. Vervisch, V. Moureau, P. Domingo, Composition-space premixed flamelet solution with differential diffusion for in situ flamelet-generated manifolds, Combust. Flame 158 (10) (2011) 2009–2016.
[10] J.A. van Oijen, A. Donini, R.J.M. Bastiaans, J.H.M. ten Thije Boonkkamp, L.P.H. de Goey, State-of-the-art in premixed combustion modeling using flamelet generated manifolds, Prog. Energy Combust. Sci. 57 (2016) 30–74.
[11] T. Turányi, A.S. Tomlin, Analysis of Kinetic Reaction Mechanisms, Springer Science + Business Media, 2014.
[12] C.D. Pierce, P. Moin, Progress-variable approach for large-eddy simulation of non-premixed turbulent combustion, J. Fluid Mech. 504 (2004) 73–97.
[13] B. Fiorina, R. Baron, O. Gicquel, D. Thévenin, S. Carpentier, N. Darabiha, Modelling non-adiabatic partially premixed flames using flame-prolongation of ILDM, Combust. Theor. Model. 7 (3) (2003) 449–470.
[14] N. Peters, Laminar diffusion flamelet models in non-premixed turbulent combustion, Prog. Energy Combust. Sci. 10 (3) (1984) 319–339.
[15] J.A.M. de Swart, R.J.M. Bastiaans, J.A. van Oijen, L.P.H. de Goey, R.S. Cant, Inclusion of preferential diffusion in simulations of premixed combustion of hydrogen/methane mixtures with flamelet generated manifolds, Flow, Turbulence and Combustion 85 (3-4) (2010) 473–511.

[16] S. Gierth, F. Hunger, S. Popp, H. Wu, M. Ihme, C. Hasse, Assessment of differential diffusion effects in flamelet modeling of oxy-fuel flames, Combust. Flame 197 (2018) 134–144.
[17] J. Schlup, G. Blanquart, Reproducing curvature effects due to differential diffusion in tabulated chemistry for premixed flames, Proc. Combust. Inst. (2018).
[18] W. Han, A. Scholtissek, F. Dietzsch, C. Hasse, Thermal and chemical effects of differential diffusion in turbulent non-premixed h2 flames, Proceedings of the Combustion Institute 38 (2) (2021) 2627–2634.
[19] A. Donini, R. Bastiaans, J. van Oijen, L. de Goey, Differential diffusion effects inclusion with flamelet generated manifold for the modeling of stratified premixed cooled flames, Proc. Combust. Inst. 35 (1) (2015) 831–837.
[20] A. Donini, R. M. Bastiaans, J. van Oijen, A 5-d implementation of fgm for the large eddy simulation of a stratified swirled flame with heat loss in a gas turbine combustor, Flow Turbulence Combust 98 (2017) 887–922.
[21] W. Zhang, S. Karaca, J. Wang, Z. Huang, J. van Oijen, Large eddy simulation of the cambridge/sandia stratified flame with flamelet-generated manifolds: Effects of non-unity lewis numbers and stretch, Combustion and Flame 227 (2021) 106–119.
[22] N. Mukundakumar, D. Efimov, N. Beishuizen, J. van Oijen, A new preferential diffusion model applied to fgm simulations of hydrogen flames, Combustion Theory and Modelling 0 (0) (2021) 1–23.
[23] B. Duboc, G. Ribert, P. Domingo, Description of kerosene / air combustion with hybrid transported-tabulated chemistry, Fuel 233 (2018) 146–158.
[24] B. Duboc, G. Ribert, P. Domingo, Evaluation of chemistry models on methane/air edge flame simulation, Proceedings of the Combustion Institute 37 (2) (2019a) 1691–1698.
[25] B. Duboc, G. Ribert, P. Domingo, Hybrid transported-tabulated chemistry for partially premixed combustion, Computers & Fluids 179 (2019b) 206–227.
[26] F. Wu, A. Saha, S. Chaudhuri, C.K. Law, Facilitated ignition in turbulence through differential diffusion, Phys. Rev. Lett. 113 (2014) 024503.
[27] S. Shy, M.T. Nguyen, S.Y. Huang, Effects of electrode spark gap, differential diffusion, and turbulent dissipation on two distinct phenomena: Turbulent facilitated ignition versus minimum ignition energy transition, Combust. Flame 205 (2019) 371–377.
[28] S. Shy, Y.-C. Liao, Y.-R. Chen, S.-Y. Huang, Two ignition transition modes at small and large distances between electrodes of a lean primary reference automobile fuel/air mixture at 373 k with lewis number $>>$ 1, Combustion and Flame 225 (2021) 340–348.
[29] H.H. Kim, S.H. Won, J. Santner, Z. Chen, Y. Ju, Measurements of the critical initiation radius and unsteady propagation of n-decane/air premixed flames, Proc. Combust. Inst. 34 (1) (2013) 929–936.
[30] H.A. Uranakara, S. Chaudhuri, K. Lakshmisha, On the extinction of igniting kernels in near-isotropic turbulence, Proc. Combust. Inst. 36 (2) (2017) 1793–1800.
[31] W. Liang, C.K. Law, Z. Chen, Ignition of hydrogen/air mixtures by a heated kernel: Role of soret diffusion, Combust. Flame 197 (2018) 416–422.
[32] Y. Wang, W. Han, Z. Chen, Effects of fuel stratification on ignition kernel development and minimum ignition energy of n-decane/air mixtures, Proc. Combust. Inst. 37 (2) (2019) 1623–1630.
[33] Q. Malé, O. Vermorel, F. Ravet, T. Poinsot, Direct numerical simulations and models for hot burnt gases jet ignition, Combustion and Flame 223 (2021) 407–422.
[34] Y. Tang, M. Hassanaly, V. Raman, B. Sforzo, J. Seitzman, A comprehensive modeling procedure for estimating statistical properties of forced ignition, Combust. Flame 206 (2019) 158–176.
[35] Y. Tang, M. Hassanaly, V. Raman, B.A. Sforzo, J. Seitzman, Probabilistic modeling of forced ignition of alternative jet fuels, Proceedings of the Combustion Institute 38 (2) (2021) 2589–2596.
[36] E. Abtahizadeh, P. de Goey, J. van Oijen, Development of a novel flamelet-based model to include preferential diffusion effects in autoignition of ch4/h2 flames, Combustion and Flame 162 (11) (2015) 4358–4369.
[37] R. Bilger, S. Stärner, R. Kee, On reduced mechanisms for methane-air combustion in nonpremixed flames, Combust. Flame 80 (2) (1990) 135–149.
[38] M. Matalon, C. Cui, J.K. Bechtold, Hydrodynamic theory of premixed flames: effects of stoichiometry, variable transport coefficients and arbitrary reaction orders, J. Fluid Mech. 487 (2003) 179–210.
[39] A. Scholtissek, P. Domingo, L. Vervisch, C. Hasse, A self-contained progress variable space solution method for thermochemical variables and flame speed in freely-propagating premixed flamelets, Proc. Combust. Inst. 37 (2018) 1529–1536.
[40] A. Scholtissek, P. Domingo, L. Vervisch, C. Hasse, A self-contained composition space solution method for strained and curved premixed flamelets, Combust. Flame 207 (2019) 342–355.
[41] H. Bttler, A. Scholtissek, X. Chen, Z. Chen, C. Hasse, Premixed flames for arbitrary combinations of strain and curvature, Proceedings of the Combustion Institute 38 (2) (2021) 2031–2039.
[42] X. Chen, H. Böttler, A. Scholtissek, C. Hasse, Z. Chen, Effects of stretch-chemistry interaction on chemical pathways for strained and curved hydrogen/air premixed flames, Combustion and Flame 232 (2021) 111532.
[43] J.C. Sutherland, P.J. Smith, J.H. Chen, Quantification of differential diffusion in nonpremixed systems, Combust. Theor. Model. 9 (2) (2005) 365–383.
[44] W. Zhang, Z. Chen, W. Kong, Effects of diluents on the ignition of premixed h2/air mixtures, Combustion and Flame 159 (1) (2012) 151–160.
[45] D. Butz, S. Hartl, S. Popp, S. Walther, R.S. Barlow, C. Hasse, A. Dreizler, D. Geyer, Local flame structure analysis in turbulent ch4/air flames with multi-regime characteristics, Combustion and Flame 210 (2019) 426–438.
[46] M. Ihme, L. Shunn, J. Zhang, Regularization of reaction progress variable for application to flamelet-based combustion models, J. Comput. Phys. 231 (23) (2012) 7715–7721.
[47] Y.-S. Niu, L. Vervisch, P.D. Tao, An optimization-based approach to detailed chemistry tabulation: Automated progress variable definition, Combust. Flame 160 (4) (2013) 776–785.
[48] U. Prüfert, S. Hartl, F. Hunger, D. Messig, M. Eiermann, C. Hasse, A constrained control approach for the automated choice of an optimal progress variable for chemistry tabulation, Flow, Turbulence and Combustion 94 (3) (2015) 593–617.
[49] M. Steinhausen, Y. Luo, S. Popp, C. Strassacker, T. Zirwes, H. Kosaka, F. Zentgraf, U. Maas, A. Sadiki, A. Dreizler, C. Hasse, Numerical Investigation of Local Heat-Release Rates and Thermo-Chemical States in Side-Wall Quenching of Laminar Methane and Dimethyl Ether Flames, Flow, Turbul. Combust. 106 (2) (2021) 681–700.
[50] C.F. Curtiss, J.O. Hirschfelder, Transport properties of multicomponent gas mixtures, The Journal of Chemical Physics 17 (6) (1949) 550–555.
[51] B. Sforzo, J. Kim, J. Jagoda, J. Seitzman, Ignition probability in a stratified turbulent flow with a sunken fire igniter, Journal of Engineering for Gas Turbines and Power 137 (8) (2014).
[52] S. Weise, D. Messig, B. Meyer, C. Hasse, An abstraction layer for efficient memory management of tabulated chemistry and flamelet solutions, Combust. Theor. Model. 17 (3) (2013) 411–430.
[53] S. Weise, C. Hasse, Reducing the memory footprint in large eddy simulations of reactive flows, Parallel Comput. 49 (2015) 50–65.
[54] D. Messig, M. Vascellari, C. Hasse, Flame structure analysis and flamelet progress variable modelling of strained coal flames, Combust. Theor. Model. 21 (2017) 700–721.
[55] J. Galpin, A. Naudin, L. Vervisch, C. Angelberger, O. Colin, P. Domingo, Large-eddy simulation of a fuel-lean premixed turbulent swirl-burner, Combust. Flame 155 (1-2) (2008) 247–266.
[56] Z. Sun, S. Gierth, M. Pollack, C. Hasse, A. Scholtissek, Ignition under strained conditions: Unsteady flamelet progress variable modeling for diesel engine conditions in the transient counterflow configuration, Combustion and Flame 240 (2022) 111841.
[57] R. Vicquelin, B. Fiorina, S. Payet, N. Darabiha, O. Gicquel, Coupling tabulated chemistry with compressible cfd solvers, Proceedings of the Combustion Institute 33 (1) (2011) 1481–1488.
[58] S. Popp, S. Hartl, D. Butz, D. Geyer, A. Dreizler, L. Vervisch, C. Hasse, Assessing multi-regime combustion in a novel burner configuration with large eddy simulations using tabulated chemistry, Proceedings of the Combustion Institute 38 (2) (2021) 2551–2558.
[59] A. Zschutschke, D. Messig, A. Scholtissek, C. Hasse, Universal Laminar Flame Solver (ULF)(2017). doi:10.6084/m9.figshare.5119855.v2.
[60] Z. Chen, M.P. Burke, Y. Ju, Effects of lewis number and ignition energy on the determination of laminar flame speed using propagating spherical flames, Proc. Combust. Inst. 32 (1) (2009) 1253–1260.
[61] Z. Chen, On the extraction of laminar flame speed and markstein length from outwardly propagating spherical flames, Combust. Flame 158 (2) (2011) 291–300.
[62] T. Zirwes, F. Zhang, J.A. Denev, P. Habisreuther, H. Bockhorn, Automated code generation for maximizing performance of detailed chemistry calculations in openfoam, High Performance Computing in Science and Engineering 17 (2018) 189–204.
[63] T. Zirwes, F. Zhang, P. Habisreuther, M. Hansinger, H. Bockhorn, M. Pfitzner, D. Trimis, Quasi-dns dataset of a piloted flame with inhomogeneous inlet conditions, Flow, Turbulence and Combustion 104 (4) (2020).
[64] D.G. Goodwin, R.L. Speth, H.K. nd Moffat, B.L. Weber, Cantera: An object-oriented software toolkit for chemical kinetics, thermodynamics, and transport processes, Zenodo (2021).
[65] J. Li, Z. Zhao, A. Kazakov, F.L. Dryer, An updated comprehensive kinetic model of hydrogen combustion, Int. J. Chem. Kinet. 36 (10) (2004) 566–575.
[66] J.F. Grcar, J.B. Bell, M.S. Day, The soret effect in naturally propagating, premixed, lean, hydrogen-air flames, Proceedings of the Combustion Institute 32 (1) (2009) 1173–1180.
[67] F. Egolfopoulos, N. Hansen, Y. Ju, K. Kohse-Höinghaus, C. Law, F. Qi, Advances and challenges in laminar flame experiments and implications for combustion chemistry, Prog. Energy Combust. Sci. 43 (2014) 36–67.
[68] K. Seshadri, F. Williams, Laminar flow between parallel plates with injection of a reactant at high reynolds number, Int. J. Heat Mass Transfer 21 (2) (1978) 251–253.

Supplementary Material

Flamelet modeling of forced ignition and flame propagation in hydrogen-air mixtures

H. Böttler[a], X. Chen[b], S. Xie[b], A. Scholtissek[a,*], Z. Chen[b], C. Hasse[a]

[a] *Institute for Simulation of reactive Thermo-Fluid Systems, TU Darmstadt, Otto-Berndt-Straße 2, 64287 Darmstadt, Germany*
[b] *SKLTCS, CAPT, BIC-ESAT, Department of Mechanics and Engineering Science, College of Engineering, Peking University, Beijing 100871, China*

This supplementary material contains comprehensive additional validation of the proposed FPV model for all addressed flame configurations and equivalence ratios. To this end, a detailed flame structure analysis is carried out by comparing the FPV solutions against direct chemistry simulation (DC). First, freely propagating flames (FPs) are addressed to validate the closures for enthalpy and mixture fraction. This is followed by an analysis regarding cylindrical expanding flames (CEFs), spherical expanding flames (SEFs) and counterflow flames. Here, mainly additional flame structures are discussed. Additionally, the governing equations of A-SURF are given.

*Corresponding author:
Email address: scholtissek@stfs.tu-darmstadt.de (A. Scholtissek)

Preprint submitted to Combustion and Flame *April 1, 2022*

A. Flame structure analysis of planar flames

In Fig. 1, the flame structure of a lean planar unstretched flame with $\phi = 1.0$ obtained with the FPV model is compared to its direct chemistry counterpart. The profiles of the input parameters of the flamelet table and the profiles of the temperature T, velocity u, and the hydrogen source term $\dot{\omega}_{H2}$ are shown. Further, all species profiles are depicted. All the

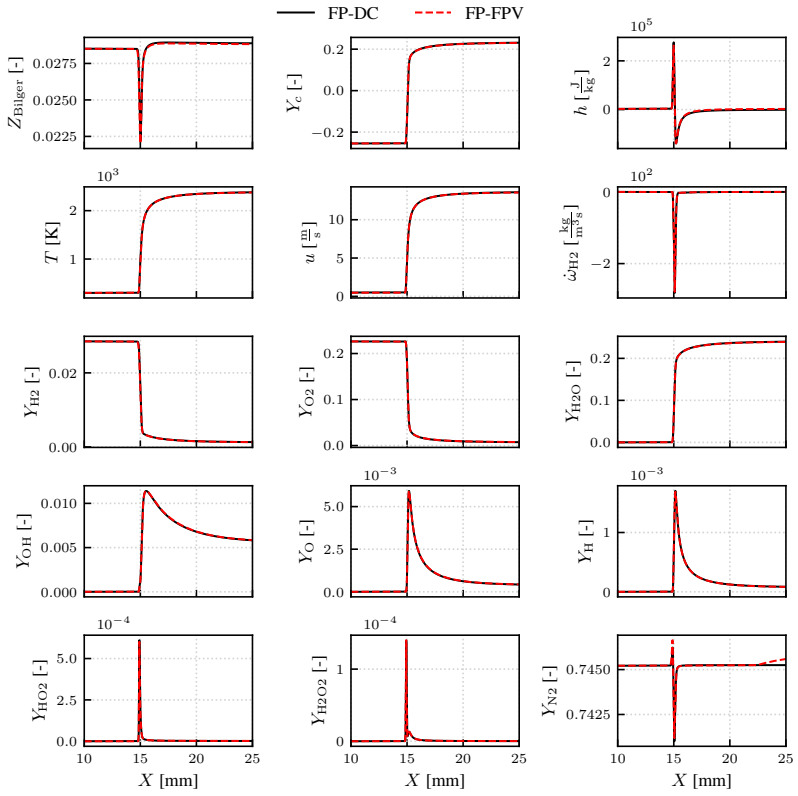

Fig. 1: Flame structure comparison of planar hydrogen-air flames with $\phi = 1.0$. The profiles along the physical space coordinate X are shown for the input parameters of the flamelet ($Z_{\mathrm{Bilger}}, h, Y_c$; top row), the temperature T, the velocity u and the hydrogen source term $\dot{\omega}_{H2}$ (second row) and all species mass fractions (bottom rows).

quantities agree very well. Only a small deviation in the enthalpy on the burned side is

visible; it is due to a minor numerical uncertainty in the direct chemistry solution. In direct chemistry calculations, the temperature equation is solved instead of the enthalpy, which is only directly solved in the FPV simulation. Therefore, the enthalpy must be calculated using the full thermo-chemical state, which leads to error accumulation since the enthalpy is not fully conserved. However, this effect is very small and shows a reasonable numerical convergence.

The same findings are found for the rich flame with $\phi = 1.4$ in Fig. 2, comparing the same variables. This suggests that the approach of approximating control variables by transporting major species is a reasonable modeling assumption. The closure used for the enthalpy equation of the flamelet model is also well suited. Moreover, these results for planar flames confirm the argument regarding stretch effects in curved flames addressed in the paper. For planar flames, no deviations in the preheat zone are found. Therefore, the deviations found for curved flames can be directly related to flame stretch caused by the change in flame topology.

Additionally, the laminar burning velocity s_l obtained with the FPV model in comparison to direct chemistry results over a range of equivalence ratios, shown in Fig. 3. The laminar flame speed is slightly overestimated by the FPV model for rich conditions, but the deviations remain below 2 % for all addressed equivalence ratios. This is considered good agreement between the FPV model and the DC reference solution and indicates that the flamelet approach can describe not only the local flame structure but also the propagation of all hydrogen-air mixtures investigated in this study.

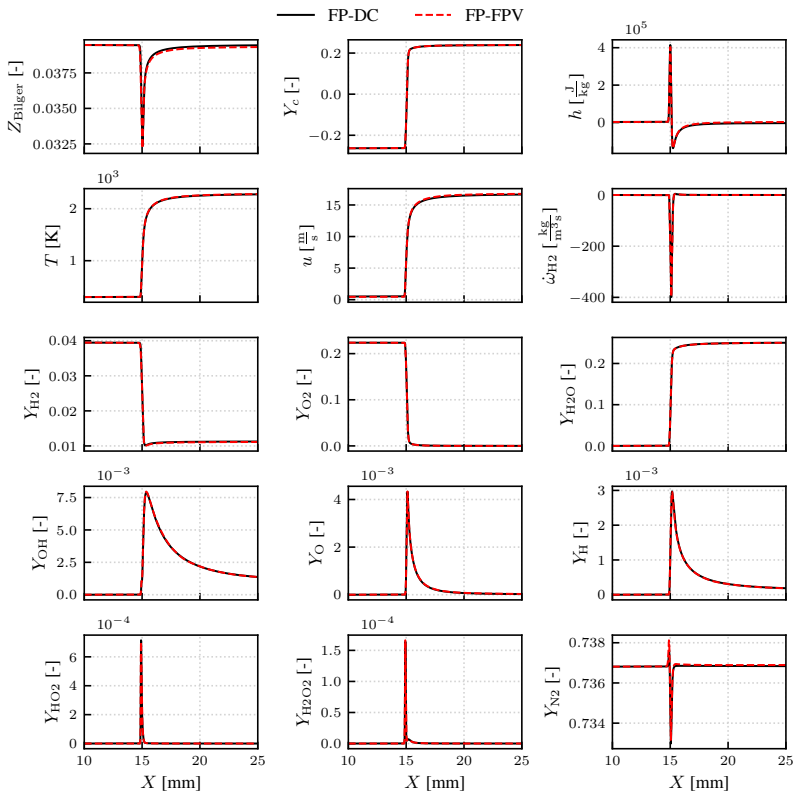

Fig. 2: Flame structure comparison of planar hydrogen-air flames with $\phi = 1.4$. The profiles along the physical space coordinate X are shown for the input parameters of the flamelet ($Z_{\mathrm{Bilger}}, h, Y_c$; top row), the temperature T, the velocity u and the hydrogen source term $\dot{\omega}_{\mathrm{H2}}$ (second row) and all species mass fractions (bottom rows).

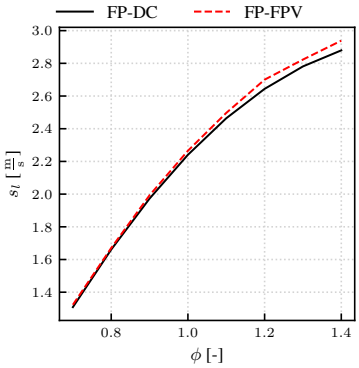

Fig. 3: Comparison of laminar burning velocity s_l of hydrogen-air mixtures ($T_u = 300\,\mathrm{K}$, $p = 1\,\mathrm{atm}$) for different equivalence ratios.

B. Flame structure analysis of cylindrical expanding flames

In Fig. 4, the detailed flame structure is analyzed. This involves comparing the profiles of the input parameters of the tabulated manifold (Z_{Bilger}, h, and Y_c) obtained by the flamelet model and the direct chemistry reference solution. Additionally, profiles of the temperature T, velocity u, and the hydrogen source term $\dot{\omega}_{\mathrm{H2}}$ and all species mass fractions are shown at a flame radius of $R_{\mathrm{f}} = 5\,\mathrm{mm}$. As for the freely propagating flame, favorable agreement is observed for all quantities. It is emphasized that the model predicts not only the overall mixture composition but also the radical mass fractions, and the local stratification in the reaction zone by differential diffusion very well. Minor discrepancies are observed in Z_{Bilger} only on the burned side and in the velocity profile (u) on the unburned side. The shift of Z_{Bilger} can be attributed to the preheat zone of the flame as the mixture fraction profile obtained by the direct chemistry result decreases slightly earlier compared to the FPV solution. This indicates that differential diffusion effects in the preheat zone are marginally underpredicted by the flamelet-based approach. Although Z_{Bilger} is sensitive to minor shifts in species mass fractions, this underlines the model's capability to account for differential diffusion effects even in flame configurations which are subject to flame stretch.

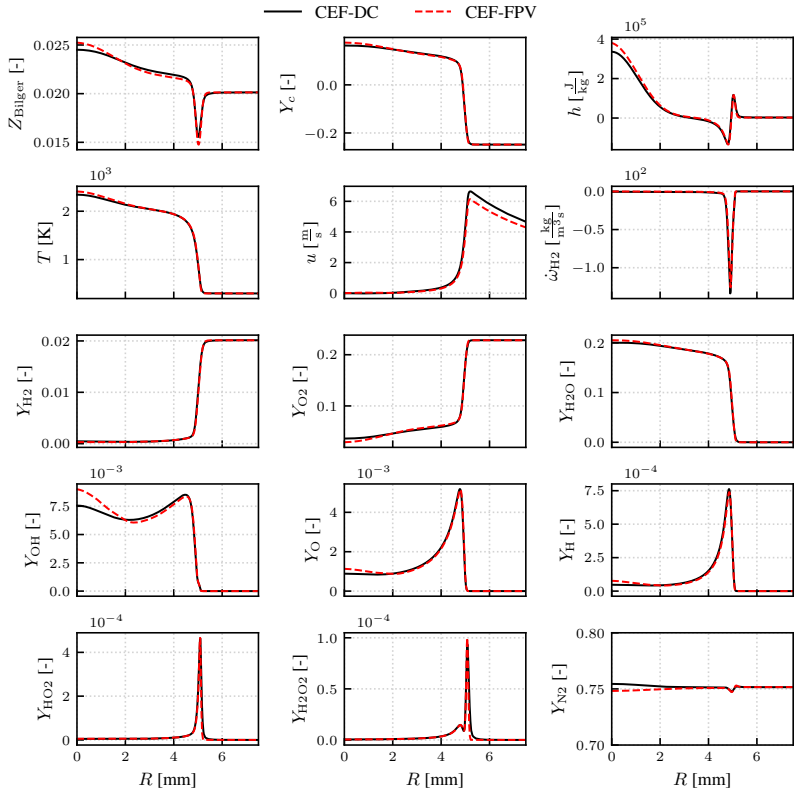

Fig. 4: Flame structure comparison of a cylindrical expanding flame with $\phi = 0.7$ ignited by an energy deposition of $E_{\mathrm{ign}} = 35\,\mathrm{nJ/m}$ at a flame radius of $R_{\mathrm{f}} = 5\,\mathrm{mm}$. The profiles along the radial coordinate R are shown for the control parameters of the flamelet manifold ($Z_{\mathrm{Bilger}}, h, Y_c$; top row), the temperature T, the velocity u and the hydrogen source term $\dot{\omega}_{\mathrm{H2}}$ (second row) and all species mass fractions (bottom rows).

The deviations in the gas velocity u_g can be traced back to the deviations in the mixture composition though the flame front, since the velocity in front of the flame is directly influenced by thermal expansion. To further illustrate the sensitivity of Z_{Bilger} to the velocity in the preheat zone, the flamelet trajectories of the two calculations are compared in Fig. 5.

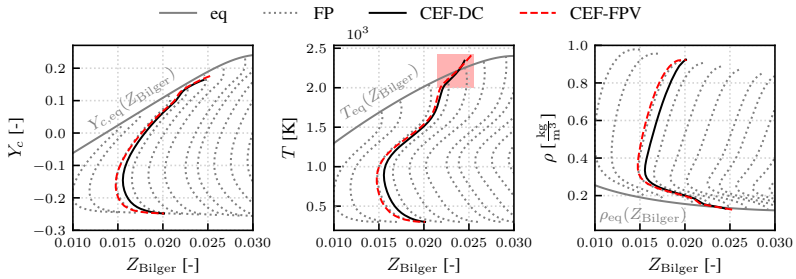

Fig. 5: Flamelet trajectories for the lean cylindrical flame ($\phi = 0.7$) at a flame radius $R_f = 5\,\text{mm}$ compared to unstretched planar flames (FP) and equilibrium conditions of various hydrogen-air mixtures at an unburned temperature of $T_u = 300\,\text{K}$ which are contained in the flamelet manifold (shown in grey). The non-adiabatic effect due to the hotspot ignition is highlighted in red shading which corresponds to higher enthalpy levels (not shown).

Here, a zoom into the reaction zone is depicted by the relation between the Bilger mixture fraction and the progress variable. Additionally, the temperature T and density ρ profiles are shown as a function of the mixture fraction, since the interplay of these quantities is relevant for thermal expansion effects. For further reference, unstretched adiabatic flamelets and equilibrium values for each mixture are shown in grey. For the CEF, temperatures above the equilibrium values of the tabulated flamelets can be found (highlighted by red shading) which are included in the manifold at higher enthalpy levels (not explicitly shown in Fig. 5). In general, the temperatures found in the FPV flame are shifted towards leaner mixtures, with the largest shift found close to the unburned side of the flame. This confirms the close link between the slightly underpredicted gas velocity and the observed deviations in mixture composition. The small deviation in Z_{Bilger} results in a shift in density, which then affects the velocity on the unburned side of the flame.

Figure 6 shows the flame structure comparison of the FPV model and the direct chemistry

solution in the stoichiometric cylindrical expanding flame. The profiles of the input parameters of the flamelet table, the temperature T, velocity u, and the hydrogen source term $\dot{\omega}_{\mathrm{H2}}$ along the radial coordinate R are investigated. Further, all species profiles are depicted. While all

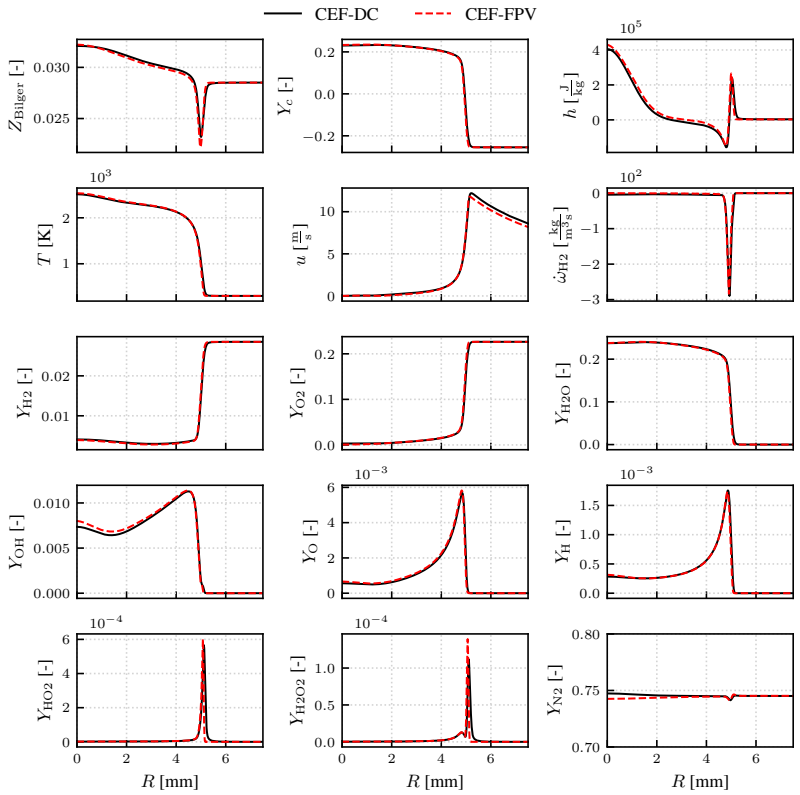

Fig. 6: Flame structure comparison between the FPV model (red) and the DC solution (black) of CEFs with $\phi = 1.0$ ignited by an energy deposition of $E_{\mathrm{ign}} = 35\,\mathrm{nJ/m}$. The profiles along the physical space coordinate X are shown for the input parameters of the flamelet ($Z_{\mathrm{Bilger}}, h, Y_c$; top row), the temperature T, the velocity u and the hydrogen source term $\dot{\omega}_{\mathrm{H2}}$ (second row) and all species mass fractions (bottom rows).

relevant effects leading to deviations between the flamelet model and the reference solution have already been discussed in detail for the lean case, similar effects are visible for the stoichiometric mixture. A slightly shifted mixture composition due to an underestimation

of diffusion effects in the preheat zone of the flame is evident. Therefore, a slightly lower hydrogen content is observed across the flame solution of the FPV model, resulting in a small shift in the enthalpy profile on the burned side of the flame. However, this shift is considered insignificant since all species including the radical mass fractions exhibit very good agreement. Moreover, the temperature profile and the hydrogen source term agree with the DC simulation. Furthermore, the deviation in the velocity profile is smaller than that found for the lean cylindrical flame (Fig. 4). This can be attributed to the increased hydrogen content in the stoichiometric mixture. Minor deviations in the hydrogen mass fraction do not affect the density of the mixture as much as in the lean case. Therefore, the gas velocity caused by thermal expansion is even better matched than in the lean mixture. Similar conclusions can be drawn from the flame structures obtained for the rich mixture, as shown in Fig. 7, investigating the same variables. The shift in the mixture composition is also visible but has an even smaller effect on the characteristics of the flame. It is further noted that the total enthalpy variation caused by differential diffusion increases with the equivalence ratio. Therefore, the hydrogen-rich mixtures place the highest demands on the closure applied to the enthalpy transport. This closure approach is shown to be robust to increasing hydrogen content, as the enthalpy gradients in the flame front are resolved well, while the minor deviation in enthalpy on the burned side of the flame is related to the overpredicted temperature.

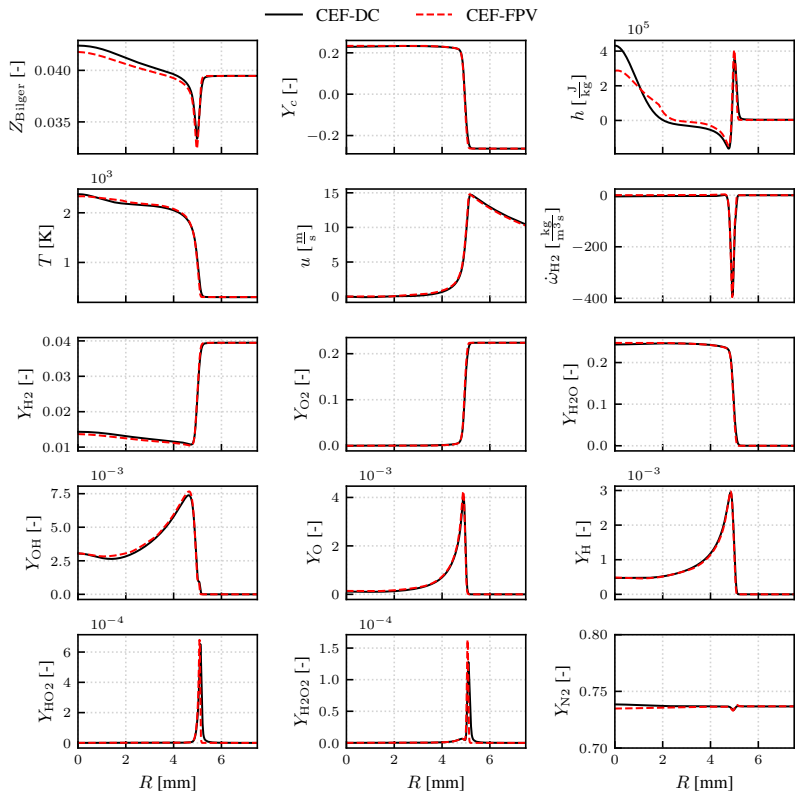

Fig. 7: Flame structure comparison between the FPV model (red) and the DC solution (black) of CEFs with $\phi = 1.4$ ignited by an energy deposition of $E_{\mathrm{ign}} = 35\,\mathrm{nJ/m}$. The profiles along the physical space coordinate X are shown for the input parameters of the flamelet ($Z_{\mathrm{Bilger}}, h, Y_c$; top row), the temperature T, the velocity u and the hydrogen source term $\dot{\omega}_{\mathrm{H2}}$ (second row) and all species mass fractions (bottom rows).

C. Flame structure analysis of spherical expanding flames

The flame structure analysis is extended to include spherical expanding flames, which are subject to increased flame stretch compared to cylindrical flames.

In Fig. 8, the spherical flame solution of the stoichiometric hydrogen-air mixture of the flamelet model is compared with that of the direct chemistry setup. The profiles of the input parameters of the flamelet table and profiles of the temperature T, velocity u, and the hydrogen source term $\dot{\omega}_{\mathrm{H2}}$ along the radial coordinate R are investigated. Further, all species profiles are depicted. In general, differential diffusion effects are predicted well by the flamelet model, where only small deviations are visible on the burned side. These are caused by an underprediction of diffusive effects in the preheat zone of the flame, as already discussed in detail for cylindrical expanding flames. The effects caused by the change of topology compared to CEFs are reproduced well by the transport of the major species, which are solved directly in the CFD setup. Here, the consideration of stretch effects in the flamelet table, which is a challenging task, is compensated by the transport of multiple scalars in the CFD application.

The flame structure of the FPV model obtained for the rich SEF with an equivalence ratio of $\phi = 1.4$ is compared to the DC solution in Fig. 9, investigating the same variables as for the discussion of the other equivalence ratios. These results show similarly good agreement to the other investigated cases, as only small deviations in mixture composition are found on the burned side of the flame.

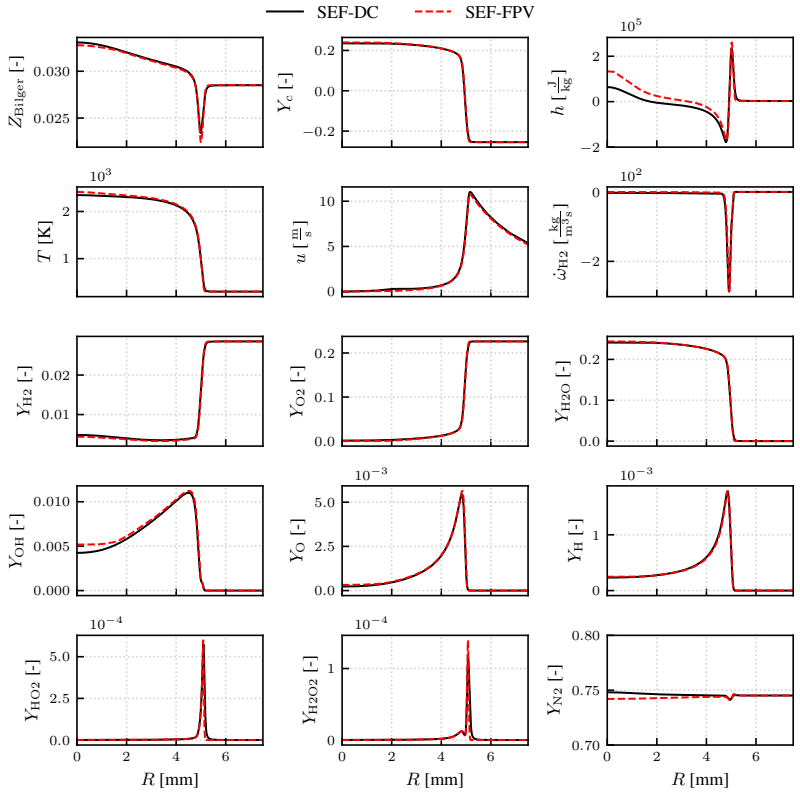

Fig. 8: Flame structure comparison between the FPV model (red) and the DC solution (black) of SEFs with $\phi = 1.0$ ignited by an energy deposition of $E_{\mathrm{ign}} = 0.15\,\mathrm{mJ}$. The profiles along the physical space coordinate X are shown for the input parameters of the flamelet ($Z_{\mathrm{Bilger}}, h, Y_c$; top row), the temperature T, the velocity u and the hydrogen source term $\dot{\omega}_{\mathrm{H2}}$ (second row) and all species mass fractions (bottom rows).

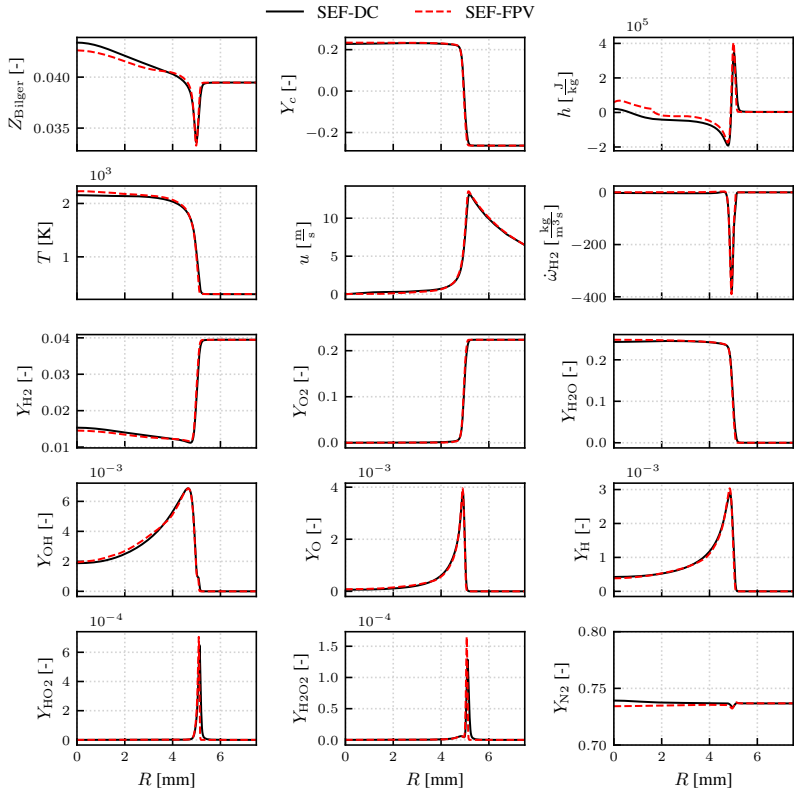

Fig. 9: Flame structure comparison between the FPV model (red) and the DC solution (black) of SEFs with $\phi = 1.4$ ignited by an energy deposition of $E_{\mathrm{ign}} = 0.15\,\mathrm{mJ}$. The profiles along the physical space coordinate X are shown for the input parameters of the flamelet ($Z_{\mathrm{Bilger}}, h, Y_c$; top row), the temperature T, the velocity u and the hydrogen source term $\dot{\omega}_{\mathrm{H2}}$ (second row) and all species mass fractions (bottom rows).

D. Flame structure analysis of igniting counterflow flames

The flame structure analysis is further extended toward igniting counterflow flames, which leads to a curvature variation compared to the expanding flames in quiescent mixtures due to the compression by the imposed flow field.

In Fig. 10, the direct chemistry counterflow solution with $\phi = 1.0$ at $t = 1\,\mathrm{ms}$ is compared to the one obtained by the FPV model. Here, the contours of the Bilger mixture fraction Z_{Bilger}, temperature T and the OH mass fraction Y_{OH} are shown. Additionally, the flow field is depicted by white arrows. In general, very good agreement is found between the DC

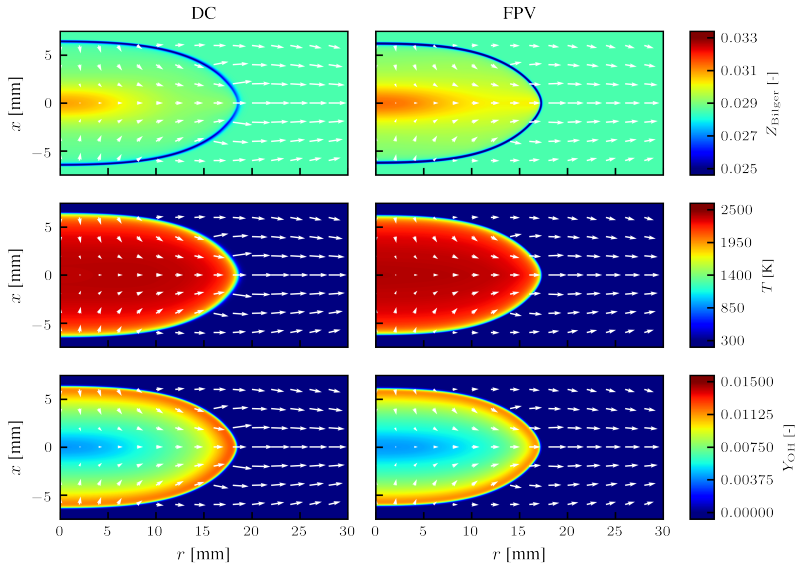

Fig. 10: Flame structure comparison of a counterflow flame flame with $\phi = 1.0$ ignited by an ignition energy of $E_{\mathrm{ign}} = 0.15\,\mathrm{mJ}$. The flame is extracted at $t = 1\,\mathrm{ms}$ and color-coded by the Bilger mixture fraction Z_{Bilger}, temperature T, and the OH mass fraction Y_{OH} with color bars given for each row. The flow field is depicted by the white arrows.

reference data and the FPV model for all quantities. Only minor deviations are found for Z_{Bilger}. The FPV model predicts slightly lower values in the reaction zone and slightly higher values on the burned side of the flame. When comparing the velocity vectors of the two

simulations, small deviations can be observed close to the flame tip ($x = 0$), since the FPV model predicts a slightly different flame shape. Considering the complexity of this flame with differential diffusion, curvature variation, unsteadiness and additional straining by the imposed flow, the agreement is quite remarkable.

In Fig. 11, the flame structure of the FPV model obtained for the rich counterflow flame with an equivalence ratio of $\phi = 1.4$ is compared to the DC solution, investigating the same variables as for the discussion of the other equivalence ratios. These results show similarly good agreement to the other investigated cases, since only small deviations in mixture composition are found on the burned side of the flame and the OH mass fraction is slightly underpredicted by the FPV model in the reaction zone.

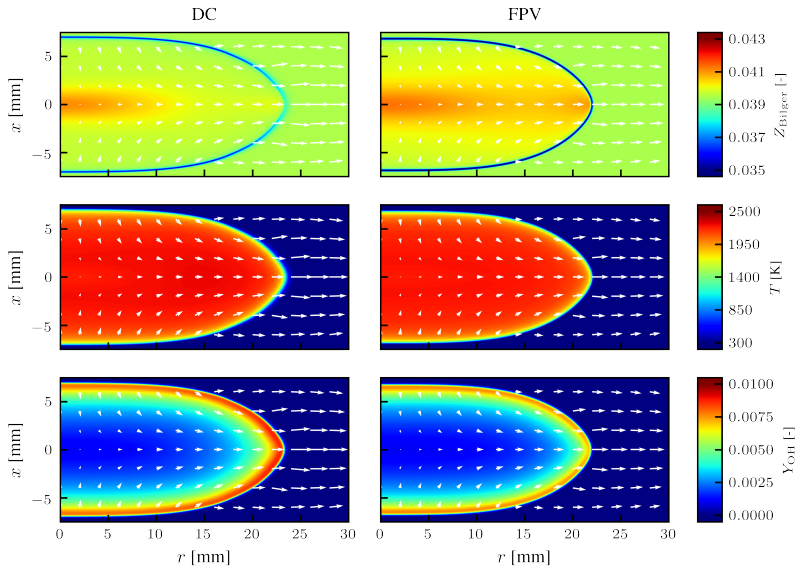

Fig. 11: Flame structure comparison of a counterflow flame flame with $\phi = 1.4$ ignited by an ignition energy of $E_{\mathrm{ign}} = 0.15\,\mathrm{mJ}$. The flame is extracted at $t = 1\,\mathrm{ms}$ and color-coded by the Bilger mixture fraction Z_{Bilger}, temperature T, and the OH mass fraction Y_{OH} with color bars given for each row. The the flow field is depicted by the white arrows.

Overall, the capabilities of the flamelet model are outlined, focusing not only on the

prediction of ignition but also on differential diffusion, including a broad variety of the effective Lewis numbers of the hydrogen-air mixtures studied. Further, the robustness of the flamelet model against varying flame topologies is emphasized.

E. Governing equations A-SURF

A-SURF has been successfully used in previous studies on premixed [1, 2] and non-premixed ignition [3]. The governing equations are revisited below for further reference.

A-SURF solves the conservation equations (including the unsteady Navier-Stokes equations as well as the energy and species conservation equations) for one-dimensional, adiabatic, multi-component, reactive flow in a planar or spherical coordinate:

$$\frac{\partial U}{\partial t} + \frac{\partial F(U)}{\partial x} + N\frac{G(U)}{x} = F_v(U) + S_R \tag{S1}$$

where N is the geometry factor ($N = 0$, 1 and 2 for planar, cylindrical and spherical coordinates, respectively. Further, t and x are respectively the temporal and spatial coordinates (x should be replaced by r for spherical configuration). In Eq. S1, the vectors U, $F(U)$, $G(U)$, $F_v(U)$, and S_R are defined as:

$$U=\begin{pmatrix}\rho Y_1\\ \rho Y_2\\ \vdots\\ \rho Y_n\\ \rho u\\ E\end{pmatrix},\quad F(U)=\begin{pmatrix}\rho u Y_1\\ \rho u Y_2\\ \vdots\\ \rho u Y_n\\ \rho u^2+P\\ (E+P)u\end{pmatrix},\quad G(U)=\begin{pmatrix}\rho u Y_1\\ \rho u Y_2\\ \vdots\\ \rho u Y_n\\ \rho u^2\\ (E+P)u\end{pmatrix}$$

$$F_v(U)=\begin{pmatrix}-x^{-N}\left(x^N\rho Y_1 V_1'\right)_x\\ -x^{-N}\left(x^N\rho Y_2 V_2'\right)_x\\ \vdots\\ -x^{-N}\left(x^N\rho Y_n V_n'\right)_x\\ x^{-N}\left(x^N\tau_1\right)_x-N\tau_2/x\\ x^{-N}q_x+\Phi\end{pmatrix}\equiv' S_R=\begin{pmatrix}\omega_1\\ \omega_2\\ \vdots\\ \omega_n\\ 0\\ 0\end{pmatrix} \tag{S2}$$

where ρ is the density, Y_k the mass fraction of species k, u the flow velocity, and E the total energy per unit mass. The subscript x in $F_v(U)$ stands for the partial derivative with respect to x. Instead of solving the continuity equation, the species conservation equations for all n species are solved in A-SURF. The continuity equation is recovered from the summation of all species conservation equations. In the species conservation equations, ω_k and V_k' are the production rate and diffusion velocity of species k, respectively. The production rate ω_k is specified via collection of elementary reactions

$$\omega_k=M_k\sum_{j=1}^{n_r}\left\{\left(v_{k,j}''-v_{k,j}'\right)\left[K_{f,j}\Pi_{k=1}^{n}\left(\frac{\rho Y_k}{M_k}\right)^{v_{k,j}'}-K_{b,j}\Pi_{k=1}^{n}\left(\frac{\rho Y_k}{M_k}\right)^{v''k,j}\right]\right\} \tag{S3}$$

where M_k is the molecular weight of species k; n_r is the total number of elementary reactions; $v_{k,j}'$ and $v_{k,j}''$ are the molar stoichiometric coefficients of species k in reaction j; and $K_{f,j}$ and $K_{b,j}$ are the forward and reverse reaction rate of reaction j. The forward reaction rate for each elementary reaction is usually modeled using the empirical Arrhenius law

$$K_{f,j} = A_{f,j} T^{\beta_j} \exp\left(-\frac{E_j}{RT}\right) \tag{S4}$$

where $A_{f,j}$ is the pre-exponential constant, β_j the temperature exponent, and E_j the activation energy. The reverse reaction rate can be obtained from chemical equilibrium constant and the forward reaction rate. These parameters ($A_{f,j}$, β_j, E_j) are given in the chemical mechanism and the reaction rates are calculated using the CHEMKIN package [4].

The diffusion velocity of species k is composed of three parts:

$$V'_k = V'_{k,Y} + V'_{k,T} + V'_{k,C} \tag{S5}$$

$V'_{k,Y}$ is the ordinary diffusion velocity given by the mixture-averaged formula [5]:

$$Y_k V'_{k,Y} = -D_{km} \frac{1}{\bar{M}} \frac{\partial \left(Y_k \bar{M}\right)}{\partial x} \tag{S6}$$

where $D_{k,m}$ is the mixture-averaged diffusion coefficient of species k and $\bar{M}$ is the mean molecular weight of the mixture. $V'_{k,T}$ is the thermal diffusion velocity, which is included only for low molecular weight species:

$$Y_k V'_{k,T} = -D_{km} \Theta_k \frac{M_k}{\bar{M} T} \frac{\partial T}{\partial x} \tag{S7}$$

where Θ_k is the thermal diffusion ratio of species k. The correction velocity $V'_{k,C}$ is included to ensure the compatibility of species and mass conservation equations [5]. It is determined by the requirement of

$$\sum_{k=1}^{n} \left(Y_k V'_k\right) = 0 \tag{S8}$$

In the momentum equation, P is the pressure and the viscous stresses, τ_1 and τ_2, are

$$\tau_1 = 2\mu \frac{\partial u}{\partial x} - \frac{2}{3}\mu \frac{1}{x^N} \frac{\partial \left(x^N u\right)}{\partial x}, \tau_2 = 2\mu \frac{u}{x} - \frac{2}{3}\mu \frac{1}{x^N} \frac{\partial \left(x^N u\right)}{\partial x} \tag{S9}$$

where μ is the dynamic viscosity of the mixture. In the energy conservation equation, the total energy, E, is defined through

$$E = -P + \rho u^2/2 + \rho h, h = \sum_{k=1}^{n} \left(Y_k h_k\right), h_k = h_{k,0} + \int_{T_0}^{T} C_{P,k}(T) dT \tag{S10}$$

where T is the temperature, h_k the enthalpy of species k, $h_{k,0}$ the species enthalpy of formation at the reference temperature T_0, and $C_{P,k}$ the specific heat of species k at constant pressure. The heat flux is

$$q = x^N \left[\lambda \frac{\partial T}{\partial x} - \rho \sum_{k=1}^{n} \left(h_k Y_k V_k'\right)\right] \tag{S11}$$

where λ is the thermal conductivity of the mixture. In the energy equation, the viscous dissipation rate is

$$\Phi = \mu \left\{ 2\left(\frac{\partial u}{\partial x}\right)^2 + 2N\left(\frac{u}{x}\right)^2 - \frac{2}{3}\left[\frac{1}{x^N}\frac{\partial\left(x^N u\right)}{\partial x}\right]^2 \right\} + u\left[\frac{1}{x^N}\frac{\partial\left(x^N \tau_1\right)}{\partial x} - N\frac{\tau_2}{x}\right] \tag{S12}$$

The pressure can be obtained from the density, temperature and mean molecular weight using the equation of state for an ideal gas

$$P = \rho R T / \bar{M} \tag{S13}$$

where $R = 8.314$ J/(mol·K) is the universal gas constant. The thermodynamic and transport properties in Eqs. S6-S13 are evaluated using the CHEMKIN and TRANSPORT packages [4, 5] interfaced with A-SURF. It is noted that the present model is simplified by not including the effects of multicomponent diffusion and bulk viscosity.

References for the supplementary material

References

[1] Y. Wang, W. Han, Z. Chen, *Effects of fuel stratification on ignition kernel development and minimum ignition energy of n-decane/air mixtures*, Proc. Combust. Inst. 37 (2019) 1623 – 1630.

[2] X. Chen, H. Böttler, A. Scholtissek, C. Hasse, Z. Chen, *Effects of stretch-chemistry interaction on chemical pathways for strained and curved hydrogen/air premixed flames*, Combustion and Flame 232 (2021) 111532.

[3] Z. Li, X. Gou, Z. Chen, *Effects of hydrogen addition on non-premixed ignition of iso-octane by hot air in a diffusion layer*, Combustion and Flame 199 (2019) 292–300.

[4] R. J. Kee, F. M. Rupley, J. A. Miller, *Chemkin-II: A Fortran chemical kinetics package for the analysis of gas-phase chemical kinetics*, in Sandia National Laboratory Report SAND89-8009B (1989).

[5] R. J. Kee, J. F. Grcar, M. D. Smooke, J. A. Miller, E. Meeks, PREMIX: a Fortran program for modeling steady laminar one-dimensional premixed flames, Technical Report SAND85-8249, Sandia National Laboratories, 1985.

P4 Proc. Combust. Inst. 39 (2023), 1567–1576

H. Böttler, H. Lulic, M. Steinhausen, X. Wen, C. Hasse, and A. Scholtissek. Flamelet modeling of thermo-diffusively unstable hydrogen-air flames. In: Proc. Combust. Inst. 39 (2023), 1567–1576. DOI: 10.1016/j.proci.2022.07.159

Author contributions

Tab. P.4: Author contributions to publication [P4] following CRediT [117]

Hannes Böttler	Conceptualization of the numerical investigation (equal) Methodology of the flamelet manifold (lead) Implementation and validation of the flamelet model (lead) Numerical investigation of flamelet-based simulations Interpretation and discussion of the results (lead) Data analysis and visualization Writing – Original draft (lead) Main and corresponding author
Haris Lulic	Numerical investigation of the dispersion relation
Matthias Steinhausen	Methodology of the flamelet manifold (supporting) Interpretation and discussion of the numerical results (supporting)
Xu Wen	Interpretation and discussion of the numerical results (supporting)
Christian Hasse	Conceptualization of the numerical investigation (supporting) Interpretation and discussion of the numerical results (supporting) Supervision of HB, HL, MS (equal) Funding acquisition
Arne Scholtissek	Conceptualization of the numerical investigation (equal) Interpretation and discussion of the numerical results (supporting) Writing – Original draft (supporting) Supervision of HB, HL, MS (equal)
All co-authors	Writing – Review & Editing

Use of publication contents in finalized and ongoing dissertations

This publication is part of the ongoing dissertation of Hannes Böttler at the Institute for Simulation of reactive Thermo-Fluid Systems at the Technical University of Darmstadt, Germany.

Available online at www.sciencedirect.com

ScienceDirect

Proceedings of the Combustion Institute 39 (2023) 1567–1576

Proceedings of the Combustion Institute

www.elsevier.com/locate/proci

Flamelet modeling of thermo-diffusively unstable hydrogen-air flames

Hannes Böttler*, Haris Lulic, Matthias Steinhausen, Xu Wen, Christian Hasse, Arne Scholtissek

Technical University of Darmstadt, Department of Mechanical Engineering, Simulation of reactive Thermo-Fluid Systems, Otto-Berndt-Str. 2, 64287 Darmstadt, Germany

Received 5 January 2022; accepted 19 July 2022
Available online 16 September 2022

Abstract

In order to reduce CO_2 emissions, hydrogen combustion has become increasingly relevant for technical applications. In this context, lean H_2-air flames show promising features but, among other characteristics, they tend to exhibit thermo-diffusive instabilities. The formation of cellular structures associated with these instabilities leads to an increased flame surface area which further promotes the flame propagation speed, an important reference quantity for design, control, and safe operation of technical combustors. While many studies have addressed the physical phenomena of intrinsic flame instabilities in the past, there is also a demand to predict such flame characteristics with reduced-order models to allow computationally efficient simulations. In this work, a H_2-air spherical expanding flame, which exhibits thermo-diffusive instabilities, is studied with flamelet-based modeling approaches both in *a-priori* and *a-posteriori* manner. A recently proposed Flamelet/Progress Variable (FPV) model, with a manifold based on unstretched planar flames, and a novel FPV approach, which takes into account a large curvature variation in the tabulated manifold, are compared to detailed chemistry (DC) calculations. Both flamelet approaches account for differential diffusion utilizing a coupling strategy which is based on the transport of major species instead of transporting the control variables of the manifold. First, both FPV approaches are assessed in terms of an *a-priori* test with the DC reference dataset. Thereafter, the *a-posteriori* assessment contains two parts: a linear stability analysis of perturbed planar flames and the simulation of the spherical expanding flame. Both FPV models are systematically analyzed considering global and local flame properties in comparison to the DC reference data. It is shown that the new FPV model, incorporating large curvature variations in the manifold, leads to improved predictions for the microstructure of the corrugated flame front and the formation of cellular structures, while global flame properties are reasonably well reproduced by both models.

Keywords: Thermodiffusive instability; Tabulated chemistry; Negative curvature; Differential diffusion; Linear stability analysis

* Corresponding author.
E-mail address: boettler@stfs.tu-darmstadt.de (H. Böttler).
https://doi.org/10.1016/j.proci.2022.07.159

1. Introduction

Due to the necessity to decarbonize modern economies, interest in hydrogen-fueled heat and power sources has increased, many of which will operate with lean premixed H_2-air flames. Despite their many advantages, lean H_2 flames can be subject to intrinsic instabilities. To allow for safe and stable operation, the mechanisms and dynamics of the instabilities need to be understood and incorporated into appropriate modeling approaches which are used to design technical combustors.

The most prominent instability mechanisms in premixed H_2 flames are the thermo-diffusive (TD) and the Darrieus-Landau (DL) instabilities. TD instabilities are caused by a disproportion of thermal and mass diffusion and can have either a stabilizing or destabilizing effect. TD-induced instabilities are only found for mixtures with Lewis numbers smaller than unity. DL instabilities on the other hand originate from thermal expansion and the associated density change across the flame front and always have a destabilizing effect for all flames. Recent studies have investigated intrinsic instabilities by means of experiments [1–4], asymptotic theory [5] and direct numerical simulations (DNSs) [6–11]. All of these studies have shown that the overall flame propagation speed is enhanced by flame surface corrugations originating from instabilities. Furthermore, thermo-diffusively unstable flames tend to exhibit characteristic cell sizes. In order to investigate such instabilities, the linear stability analysis has been utilized by determining the so-called dispersion relation from either asymptotic theory [5] or numerical simulations [6,7,9]. A comprehensive review and a theoretical introduction to intrinsic flame instabilities can be found in [11].

So far, numerical studies of intrinsic flame instabilities have usually been based on DNS. It has been shown that reliable simulations addressing flame instabilities require considerable computational resources since the formation and evolution of intrinsic instabilities can be sensitive to domain size, grid resolution, and the numerical methods employed [9,11,12]. Therefore, such investigations are restricted to academic configurations, which are also well-suited for model development. Promising modeling approaches, taking into account detailed kinetics and their interaction with transport, include flamelet-based models such as the Flamelet/Progress Variable (FPV) approach [13], Flamelet Generated Manifolds (FGM) [14], or the Flame Prolongation for ILDM (FPI) model [15]. While manifolds for non-premixed combustion are usually generated from stretched non-premixed flamelets [16], manifolds for premixed combustion can recover moderate stretch effects even when being generated from unstretched premixed flamelets [14,17–19]. Nevertheless, attempts have also been made to generate manifolds from stretched premixed flamelets [14,20,21]. Many advancements were aiming for improved predictions of the local mixture composition which has been realized via mixture fraction definitions based on elemental mass fractions, such as the Bilger mixture fraction, and efforts have been made to model its diffusivity [14,20,22]. Recently, different model extensions have been developed to improve the predictions of flamelet-based models for hydrogen combustion, where differential diffusion effects need to be captured accurately [17–19]. For TD unstable flames, which exhibit large curvature variations due to flame front corrugations, the suitability of these manifolds needs to be further investigated. A novel flamelet tabulation approach, which includes strain and curvature effects, has shown reasonable agreement with the detailed chemistry (DC) result of a lean hydrogen spherical expanding flame (SEF) [23]. The manifold was evaluated by extracting the control parameters from the DC simulation and comparing the tabulated thermochemical state to the reference (*a-priori* analysis). To the authors' knowledge, fully coupled simulations (*a-posteriori* analysis) of intrinsically unstable H_2-air flames using flamelet manifolds which incorporate large curvature variations have not been presented in the literature, yet. This gap is addressed in this work.

The objective of this study is twofold: (1) a novel flamelet tabulation approach is presented which takes into account differential diffusion and large curvature variations (positive and negative curvature range). It is studied together with a previously developed manifold constructed from unstretched premixed flames [19]. The predictive capabilities of both manifolds are first assessed by comparison to DC reference results of the unstable lean H_2-air SEF also studied by Wen et al. [23] (*a-priori* analysis). (2) The new manifold is then coupled to a CFD solver in a modified FPV approach for premixed combustion and utilized to simulate planar flames and the lean H_2-air SEF (*a-posteriori* analysis). The FPV modeling approach from our previous work [19] is employed in a similar manner. Both FPV models are examined *a-posteriori* by means of a linear stability analysis (planar flames) and the global characteristics of the SEF, as well as its cellular microstructure. These flames represent challenging cases for flamelet-based modeling approaches due to their highly unsteady nature and distinct flame front corrugations (large curvature variations).

The paper is structured as follows: the new tabulation approach and the numerical model are introduced first, followed by the *a-priori* analysis. Thereafter, fully coupled simulations are performed for the planar flames (linear stability analysis) and the SEF. The paper ends with a conclusion.

2. Numerical method

Two flamelet-based modeling approaches are investigated: (1) a recently proposed FPV approach using a three-dimensional manifold ($\psi(Z_{\text{Bilger}}, h, Y_c)$) which was created from unstretched flame solutions with varying enthalpy levels h (referred to as FPV-h) [19] and (2) a novel three-dimensional tabulation approach taking into account negative and positive curvature κ_c (referred to as FPV-κ_c). First, the novel tabulation approach is presented, followed by a description of the numerical setup of the unstable lean H_2-air SEF. Note that, in all calculations, a mixture-averaged diffusion model [24] without thermal diffusion and the detailed reaction mechanism by Varga et al. [25] are used in accordance with the DC SEF model [23].

2.1. Manifold generation (FPV-κ_c)

Flamelet-based manifolds are usually generated by performing parameter variations in simple laminar canonical flame configurations, such as freely propagating flames or counterflow flames. However, these laminar canonical flames are inherently limited regarding the attainable parameter space of stretch (strain, curvature) [26]. To overcome this limitation, a composition space model (CSM) [27] is used instead of a specific laminar canonical configuration. As shown in our previous work, the CSM recovers the characteristics of various laminar premixed flames and can further take into account arbitrary combinations of strain $K_s = \nabla_t \cdot \mathbf{u}_t - (\mathbf{u} \cdot \mathbf{n}_c)\kappa_c$, and curvature, $\kappa_c = -\nabla \cdot \mathbf{n}_c$ where $\nabla_t \cdot \mathbf{u}_t$ represents flame-tangential straining by the flow and $\mathbf{n}_c$ is the flame-normal unit vector [26]. In the model equations for the temperature, species mass fractions, and progress variable gradient are expressed and solved with respect to the progress variable Y_c, which spans the composition space. With the gradient equation, the model is self-contained, requiring only strain and curvature as external parameters [27].

In order to generate the manifold, a parameter variation is carried out for a range of equivalence ratios ($0.275 \leq \phi \leq 0.6$) and curvatures ($-1500\,1/\text{m} \leq \kappa_c \leq 5000\,1/\text{m}$). The strain rate is fixed at $K_s = 500\,1/\text{s}$ to account for the positive strain of the SEF during its outward propagation (numerical setup presented in Section 2.2). The progress variable is defined as $Y_c = Y_{H_2O} - Y_{H_2} - Y_{O_2}$. Figure 1 shows a joint probability density function (PDF) of the $\kappa_c - Y_c$ scatter which is evaluated from the DC data of the SEF.

For visual inspection, qualitative PDFs of both quantities are depicted at the respective axes. The curvature range of the FPV-κ_c manifold is indicated by dashed lines. It is noted that the curvature distribution of the DC reference is well captured, while few regions can be identified where the tabulated range is exceeded. However, no burning solutions could be generated with the CSM below $\kappa_c = -1500\,1/\text{m}$ for this type of lean H_2-air flame.

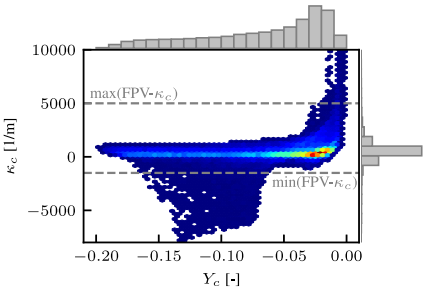

Fig. 1. Joint probability density function (PDF) of progress variable and curvature evaluated from the DC data on the SEF (presented in Section 2.2) with qualitative PDFs shown as bars at the respective edges. Dashed lines indicate the curvature range captured in the FPV-κ_c manifold.

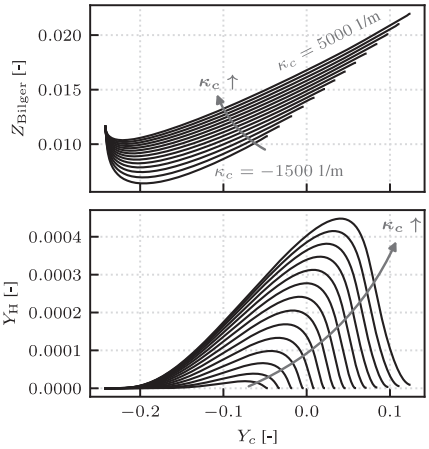

Fig. 2. Subset of the CSM solutions used for manifold generation with $\phi = 0.4$ ($Z_{\text{Bilger}} = 0.0116$) and varying curvature ($-1500\,1/\text{m} \leq \kappa_c \leq 5000\,1/\text{m}$).

Highlighting the effect of curvature variation, CSM solutions with $\phi = 0.4$ ($Z_{\text{Bilger}} = 0.0116$) are illustrated in Fig. 2.

The profiles of the Bilger mixture fraction Z_{Bilger} [22] and H radical mass fraction are shown as a function of the progress variable. Curvature variations are found to lead to different local mixture compositions and maximum values of Y_c due to pronounced differential diffusion effects. Further, the H radical profile shows a monotonic increase with curvature, which is in line with previous works

that have used this quantity to include stretch effects in flamelet-based approaches [20,21,23].

The flamelet manifold is obtained first by mapping the set of flame calculations ($\psi(\phi, Y_c, \kappa_c)$) to Z_{Bilger}, which is defined by a coupling function between the fuel (subscript 1) and oxidizer (subscript 0) [22]:

$$Z_{\text{Bilger}} = \frac{\beta - \beta_0}{\beta_1 - \beta_0} \tag{1}$$

where the coupling functions β depend on the elemental mass fractions Z_l,

$$\beta = \sum_{l=1}^{N_e} \gamma_l \sum_{k=1}^{N_s} \frac{a_{l,k} M_l Y_k}{M_k} \tag{2}$$

with the weighting factor γ_l of element l, the molecular weight M_l (M_k) of element l (species k), and $a_{l,k}$ representing the number of elements l in species k. Note that γ_l are chosen in agreement with Bilger et al. [22].

Second, the progress variable Y_c is mapped to a normalized progress variable:

$$c = \frac{Y_c - Y_{c,\min}(Z_{\text{Bilger}})}{Y_{c,\max}(Z_{\text{Bilger}}) - Y_{c,\min}(Z_{\text{Bilger}})} \tag{3}$$

Finally, the curvature dimension is mapped to a second normalized progress variable based on the H radical:

$$c_2 = \frac{Y_{\text{H}} - Y_{\text{H},\min}(Z_{\text{Bilger}}, c)}{Y_{\text{H},\max}(Z_{\text{Bilger}}, c) - Y_{\text{H},\min}(Z_{\text{Bilger}}, c)} \tag{4}$$

The tabulated manifold ($\psi(Z_{\text{Bilger}}, c, c_2)$) is coupled to the CFD solver following the approach presented in our previous work [19] by transporting the major species (H_2O, H_2, O_2) and approximating the control variables of the tabulated manifold based on these species. For the FPV-h model, the enthalpy is transported and used as a control variable for the manifold instead of the H radical. The manifold is generated with the CSM performing an enthalpy variation for unstretched flames and mapping the thermochemical state to $\psi(Z_{\text{Bilger}}, h, Y_c)$ (further details are provided in [19]). Both coupling approaches avoid the use of additional modeling assumptions which would otherwise be required to approximate the transport properties of composed quantities such as the mixture fraction or the progress variable. Finally, it is noted that these coupling approaches are flexible in number of species being transported as long as a consistent mixture fraction definition is used [19].

2.2. Numerical setup

A lean premixed spherical expanding H_2-air flame is used to investigate the performance of the FPV models in predicting cellular flame structures which evolve at larger flame radii. For this purpose, the DC reference data, which was already investigated in an *a-priori* analysis by Wen et al. [23], is used for comparison. This dataset was compared against asymptotic theory [28] showing good agreement with the reference data. It is further noted that the DC framework was validated against experimental data where only a slight under prediction of the consumption speed was observed [29]. The computational domain is a two-dimensional, axisymmetric wedge with a radius of $R = 8$ cm. In the domain center, a hot spot with a radius of 1 cm is initialized. Its conditions correspond to the equilibrium state of the fresh gases, a H_2-air mixture with an equivalence ratio $\phi = 0.4$ and an unburnt temperature $T_u = 300$ K. Outside of the hot spot, the domain is initialized with the unburned mixture at atmospheric pressure. Local grid refinement ensures that the flame is resolved with at least 20 grid points. It has been shown that computations of unstable H_2-air flames can depend significantly on the grid resolution, initialization, and numerical setup [11,12]. Therefore, the FPV calculations are based on the same numerical setup as the DC calculation. Additionally, to ensure a consistent initialization for the FPV calculations, an early time step of the DC simulation is used, where the flame front is fully developed and flame front corrugations are still below 4 % of the laminar flame thickness l_f.

3. Results and discussion

3.1. A-priori: Spherical expanding flame

An *a-priori* analysis is carried out to assess the general capability of the FPV models to capture the microstructure of the unstable H_2-air flame. Figure 3 shows a snapshot of the temperature T and the OH mass fraction Y_{OH} fields of the DC simulation (left). Further, the relative deviations of both FPV model predictions from the DC reference are shown. For both models, the highest deviations in the temperature can be found around areas of negative flame curvature (concave toward the unburned mixture), whereas smaller deviations can be found in positively curved segments (convex toward the unburned mixture). Similar, but more significant deviations are registered for the OH mass fraction. While the FPV-h model shows maximum deviations of up to 5 % for T and 40 % for Y_{OH}, the prediction of the FPV-κ_c approach exhibits smaller deviations for both quantities. The deviations at negatively curved regions are also restricted to a smaller area of the flame in comparison to the FPV-h manifold. This indicates that taking curvature effects into consideration in the FPV-κ_c approach improves the agreement for the unstable SEF, especially for fine-scale quantities such as the OH radical, which is particularly challenging for flamelet-based models due to the strong differential diffusion effects and broad curvature distribution. An *a-priori* assessment of flame-tangential diffusion effects, which supports the previous line

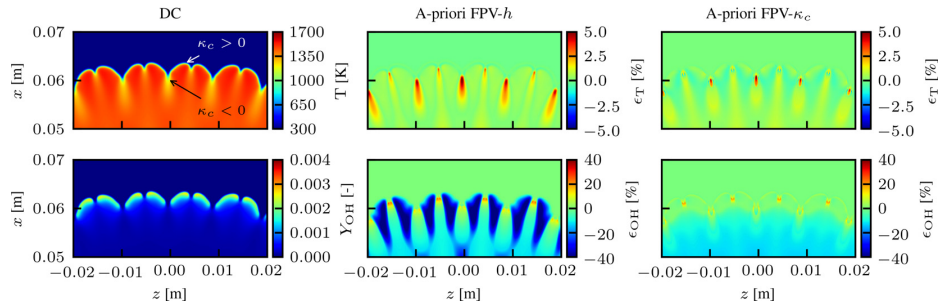

Fig. 3. *A-priori* comparison of FPV approaches based on DC SEF data. The absolute DC values are shown for the temperature T and OH mass fraction Y_{OH} (left), while deviations in the predictions of the FPV-h (middle) and the FPV-κ_c model (right) are shown relative to these values (denoted as $\epsilon_i = (i_{DC} - i_{FPV})/\max(i_{DC})$).

of argument, can be found in the supplementary material.

3.2. A-posteriori: Linear stability analysis

A comprehensive assessment of the performance of flamelet-based approaches requires *a-posteriori* analyses of fully coupled simulations, which are discussed in the following. The *a-posteriori* assessment is divided into two parts: (1) the linear stability analysis of perturbed planar flames and (2) the spherical expanding flame.

In order to examine the cell formation predicted by the different FPV models, the linear stability analysis (LSA) has proven to be a viable method for studying flame instabilities [8,9]. An LSA is performed simulating fully developed two-dimensional planar flames in a box, subject to a weak initial perturbation with an initial amplitude $A_0 = 0.04\, l_f$ and the wavelength λ. The two-dimensional domain has inflow and outflow conditions in the streamwise direction and periodic boundaries in the lateral direction.

The growth rate ω is calculated for each wavelength as $\omega = \mathrm{d}(\ln A(t)/A_0)/\mathrm{d}t$. The domain size in the direction of flame propagation is large enough to permit unconstrained flame propagation, while its lateral dimension is varied to adjust λ. The dispersion relation is obtained as $\omega = \omega(k)$, where ω is the growth rate of the initial perturbation defined by the wavelength λ and the wavenumber $k = 2\pi/\lambda$.

The dispersion relation reveals the range of unstable (and stable) wavelengths, the critical (neutral, $\omega = 0$) wavelength λ_c, and the most unstable wavelength $\lambda(\omega_{max})$ at which the growth rate reaches a maximum. The dispersion relation includes both hydrodynamic and thermo-diffusive effects similar to the unstable SEF, the main subject of this study.

The dispersion relations obtained from detailed chemistry (DC) and both FPV methods are shown in dimensionless form in Fig. 4. For normalization,

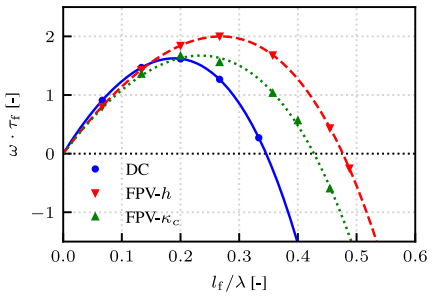

Fig. 4. Comparison of the non-dimensional dispersion relations obtained with detailed chemistry (DC) and the two FPV models, respectively.

the flame thickness $l_f = (T_b - T_u)/\max(\mathrm{d}T/\mathrm{d}x)$ and the flame time $\tau_f = l_f/s_L$ of the unperturbed freely propagating flame are used, where s_L represents the laminar burning velocity. A wider range of unstable wavelengths is recorded for both FPV models in comparison to the DC solution, with a smaller deviation for the FPV-κ_c model. The maximum growth rate is reproduced well by the FPV-κ_c approach and the peak position $\lambda(\omega_{max})$ is slightly shifted towards lower wavelengths. For the FPV-h model, the peak value of the growth rate is larger and its position is shifted to smaller wavelengths. The overall shape of the curve is captured well by both models and a good agreement is found for larger wavelengths. The shift in the peak position and range of wavelengths for the FPV models provides insights into the length scales of instabilities that will prevail and grow in premixed flame fronts.

It has been found in several studies of planar [6,9] and circular expanding flames [7] that the average cell size in these unstable flames is related to the fastest growing modes close to $\lambda(\omega_{max})$. It can therefore be concluded from the dispersion re-

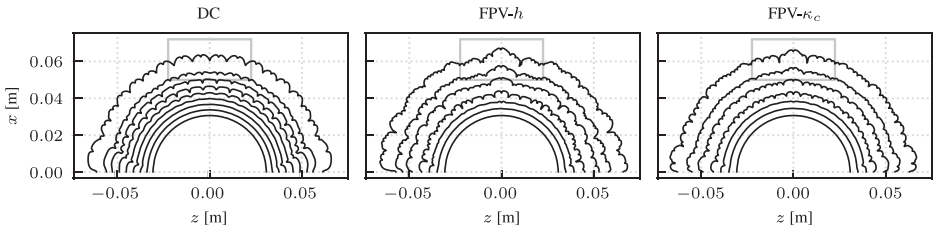

Fig. 5. Comparison of flame fronts obtained by different simulation approaches and various time steps. The flame front is defined as the progress variable iso-line $Y_c = -0.11$. The gray boxes visualize the magnified region which will be investigated in detail in Fig. 8.

lations in Fig. 4 that smaller cells are enhanced with the FPV-κ_c model and even smaller ones with the FPV-h model as compared to the detailed chemistry result. These findings are examined further for the SEF configuration in the following.

3.3. A-posteriori: Spherical expanding flame

Next, the performance of the FPV models is assessed by analyzing the growth of instabilities in the SEF configuration. The flame front evolution of the SEF for all three simulation approaches is depicted in Fig. 5. The flame front is defined based on the progress variable isoline $Y_c = -0.11$ in accordance with [23].

All calculations are performed until a flame radius of approximately 6 cm is reached. Despite having similar overall characteristics, all three approaches lead to slightly different flame shapes. In the DC simulation, cellular structures of approximately uniform size evolve. Similarly sized cells are also found in the flame front obtained from the FPV-h calculation; however, smaller secondary cellular structures are also seen to form. This leads to a more corrugated flame front at larger flame radii. The visual inspection of the results obtained with the FPV-κ_c model indicates a similar formation of secondary cells as found for the FPV-h model. Nevertheless, the flame front predicted by the FPV-κ_c model is less strongly affected by small cells compared to the FPV-h approach. Overall, this observation is in agreement with the dispersion relations in Fig. 4 since the FPV models generally predict smaller critical wavelengths, with the FPV-κ_c model showing better agreement with the DC reference.

Further, the unstable wavelengths obtained by the dispersion relation are quantitatively compared to the size of cellular structures found in the SEFs by estimating cell size distributions. The cell size is defined as $\lambda_{\text{cell}} = 2\,l_{\text{arc}}/\pi$ where the arc length l_{arc} is defined as the distance between two curvature peaks along the flame front [9].

Figure 6 shows the cell size distributions of the different SEF simulations. Note that the cell size is normalized by the laminar flame thickness l_{f} and

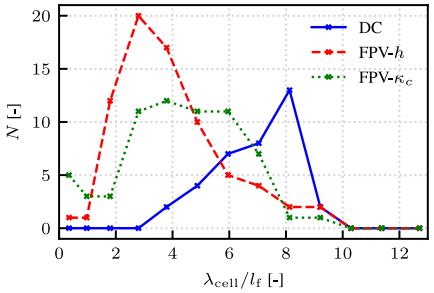

Fig. 6. Comparison of the non-dimensional cell size distributions predicted by different modeling approaches.

N represents the number of cells found in each bin. A maximum is visible in the distribution of all models which can be related to the most unstable wavelength $\lambda(\omega_{\text{max}})$ [9]. The maximum occurs at smaller cell sizes for FPV-κ_c and FPV-h in comparison to the DC reference, which is also consistent with the shift in the maximum growth rate in the corresponding dispersion relations (see Fig. 4). Similarly, the critical wavelength is shifted to smaller values for the FPV models, which is reflected by the occurrence of smaller cells in the distributions. Berger et al. [9] found that the most likely wavelength of their investigated lean H_2-air flames occurs around $6\,l_{\text{f}}$. With $7 - 8\,l_{\text{f}}$, this value is larger for the SEF computed with the DC simulation and differences are attributed to the overall curved flame configuration and the limited sample size as compared to [9].

The differently sized cells can also be explained by analyzing the temporal evolution of the maximum perturbation A_{max} along the mean flame radius $\bar{R}_{\text{f}}$ depicted in Fig. 7 (top).

Three different regimes can be identified for the DC reference. Initially, an unperturbed flame propagation, with negligible perturbations of the flame front, is identified (regime I), followed by a linear regime (regime II), which can be related to the linear stability analysis of the planar flames, and a

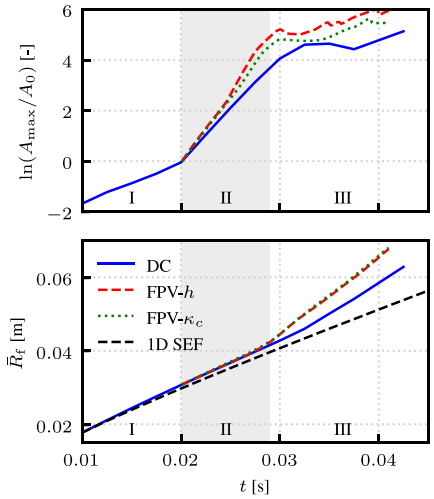

Fig. 7. Temporal evolution of the maximum amplitude of perturbation $A_{max} = R_{f,max} - R_{f,min}$ obtained from SEF simulations with respective models normalized by the initial perturbation A_0 (top). Further, the temporal evolution of the mean flame radius $\bar{R}_f$ is depicted for the respective calculations (bottom). Additionally, the regimes of unperturbed propagation (I), linear growth (II), and non-linear growth (III) are highlighted and the DC result of a one-dimensional SEF simulation is shown for reference as no instabilities can evolve due to the spatial confinement (black line).

non-linear regime (regime III), which is characterized by the interaction and chaotic superposition of different cellular structures. Note that the FPV calculations are initialized from the DC calculation at the beginning of regime II ($t = 0.02$ ms). Here, the initial amplitude of perturbation A_0 is smaller than $4\% l_f$, which is similar to the initial corrugations prescribed in the LSA. Thereby, consistency between the DC calculation and the FPV models is ensured since smaller perturbations might be sensitive to the different numerical models.

In regime II, all approaches show a linear trend, while the FPV models show a faster increase (larger growth) compared to the DC reference. This is in agreement with the overall picture obtained for the flame fronts predicted by the FPV calculations, since an increased growth of perturbation leads to a faster development of cellular structures. The final regime III is characterized by moderate growth in the amplitude of the perturbation since it is characterized by the interaction of different cells. This confirms the initial qualitative assessment of the flame front evolution (see Fig. 5).

The flame propagation speed is enhanced by the wrinkling due to intrinsic instabilities [5,7,9]. This is re-confirmed in Fig. 7 (bottom), where the temporal evolution of the mean flame radius $\bar{R}_f$ is shown for the different models. For reference, a one-dimensional SEF is shown, computed with an in-house flame solver [30]. Due to the confinement to a single dimension, no instabilities can evolve and the flame propagates in a quasi-steady manner. While the two-dimensional simulations predict a similar flame evolution as the one-dimensional model in the first two regimes, a steeper increase $d\bar{R}_f/dt = s_f$ (i.e. a higher flame speed) is observed as soon as cells of different size interact (regime III). Due to the more pronounced formation of smaller cellular structures in the FPV calculations (thus, also a larger flame surface area), a faster flame propagation is predicted by these models in comparison to the DC simulation. Considering the complexity of this particular flame with differential diffusion, curvature effects, unsteadiness, and the evolution cellular structures, this agreement is quite remarkable. Flame speed deviations of 15 % are observed for flames with the largest radius. A similar overprediction in flame propagation speed was observed in a previous study using a two-dimensional unstretched manifold ($\psi(Z, Y_c)$) [17].

So far, the results have shown that the model predictions of the instability evolution affects both global flame characteristics, such as the flame propagation speed, as well as local flame characteristics, such as the cell size distribution and visual appearance of the flame. As a next step, the results of the coupled simulations are analyzed with respect to the flame microstructure. Clear differences are found in the *a-priori* analysis (see Fig. 3) and a similar investigation is carried out for the *a-posteriori* results. The thermo-chemical states obtained with the different models are compared in Fig. 8. Here a magnified picture of the flame front is depicted (gray boxes in Fig. 5) and the scalar fields of the Bilger mixture fraction Z_{Bilger}, temperature T, and OH mass fraction Y_{OH} are shown. Richer (leaner) mixtures are found in regions of positive (negative) curvature, which is expected for lean H_2-air flames. While both FPV models show similar mixture stratification across the flame, they tend to predict richer mixtures on the burned side of the flame in comparison to the DC calculation. This also leads to a slight overprediction of the temperature on the burned side. On the other hand, areas of leaner mixtures due to negative curvature seem to be less prevalent in the FPV calculations compared to the DC simulation. However, this effect depends on the size of the cellular structures, since smaller cells lead to higher curvature variation which also amplifies differential diffusion effects. Finally, the OH mass fraction is shown, which scales with the local heat release, indicating varying local reaction intensities originating from curvature effects. From the DC snapshot, OH is seen to exhibit the highest values in the positively curved flame front while no significant OH mass fraction is found in negatively curved segments, highlight-

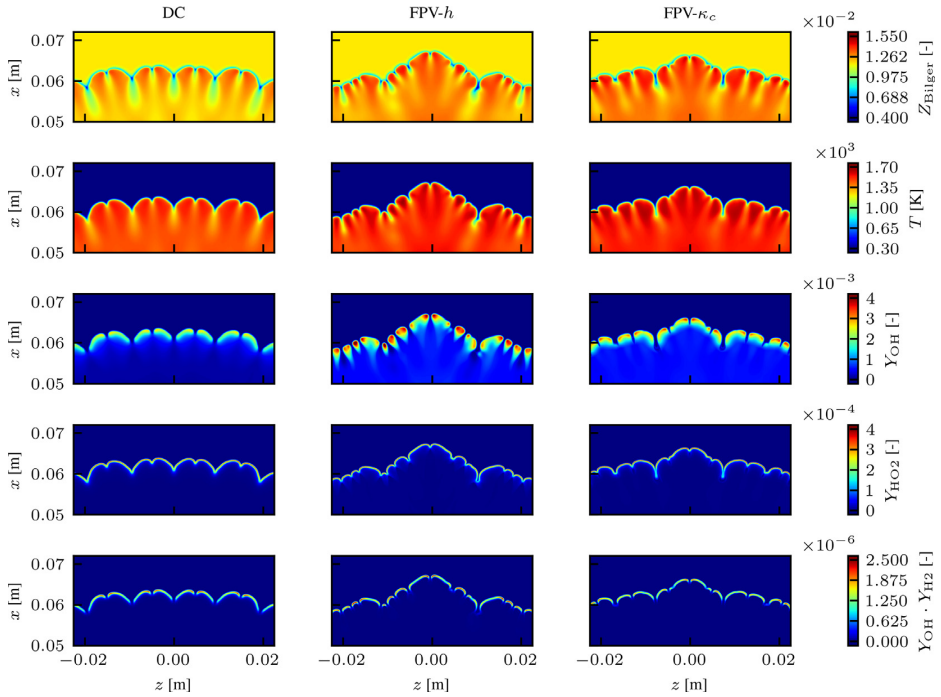

Fig. 8. Flame structure comparison for the DC reference, the FPV-h, and the FPV-κ_c model at a mean flame radius of $\bar{R}_f \approx 6$ cm. The sections of the flame front are color-coded by Z_{Bilger}, T, Y_{OH}, Y_{HO2}, and the product $Y_{\text{OH}} \cdot Y_{\text{H2}}$ with color bars given for each row.

ing its sensitivity to curvature. These characteristics are also found in the FPV simulations. The FPV-h model generally predicts higher OH mass fractions and shows a broader area with a significant OH content in comparison to the DC reference. Moreover, the FPV-κ_c result agrees better with the DC calculation. It only slightly overpredicts Y_{OH} in the positively curved flame segments and indicates the reaction zone thickness is similar to the DC reference. Further, the HO_2 mass fraction is depicted which exhibits non-negligible values also in regions of negative curvature. Similar observations were reported by Hall et al. [31]. This is consistently observed in all three modeling approaches, highlighting that weak reactions still occur in areas of negative curvature. Finally, also the product of H_2 and OH mass fractions is shown since it was found to be a suitable marker for heat release in lean unstable H_2/air flames [32]. High (low) heat release is found for areas with positive (negative) curvature for the three different modeling approaches, respectively. In general, all characteristics of the DC reference are reproduced by the FPV models, while the FPV-h model shows a slight overprediction in positively curved regions. Overall, these results are in agreement with the *a-priori* analysis performed initially. While global flame characteristics do not deviate significantly between both FPV models, the local flame characteristics and the flame's microstructure predicted by the FPV-κ_c model agrees better with the DC simulation.

4. Conclusion

In this work, a lean H_2-air spherical expanding flame (SEF), which exhibits thermo-diffusive instabilities, is studied with flamelet-based modeling approaches both in *a-priori* and *a-posteriori* manner. A recently proposed FPV-h model [19], with a manifold based on unstretched planar flames, and a novel FPV-κ_c modeling approach, which takes into account a large curvature variation in the tabulated manifold, are compared to detailed chemistry (DC) calculations of the hydrogen flame. Furthermore, a linear stability analysis (LSA) is performed in order to systematically determine and compare the growth rates of premixed flame perturbations predicted by the three modeling approaches (FPV-h, FPV-κ_c, DC).

Overall, the comparison of both FPV approaches to the DC reference shows that incor-

porating curvature in the manifold (FPV-κ_c) leads to more accurate predictions for the local characteristics and the microstructure of the flame instabilities than the manifold based on unstretched flames (FPV-*h*). The *a-priori* analysis reveals that the FPV-κ_c manifold leads to good predictions of the thermo-chemical state, especially in negatively curved flame segments, where the FPV-*h* model shows significantly larger deviations. The aspect is further confirmed from the *a-posteriori* results for the cell size distributions and the flame structure comparison of the flame with developed cellular structures. Additionally, as indicated by the dispersion relations obtained from the LSA, the coupled simulations show that the flames computed with both FPV approaches form smaller cellular structures, corresponding to smaller critical wavelengths, compared to the SEF-DC reference model. This increases the flame surface area and thereby also the flame propagation speed, an important global flame characteristic. While both FPV approaches recover the unstretched laminar burning velocity very accurately, the overall agreement of the SEF propagation speed between the FPV models and the DC simulation is still remarkable, given the challenging nature of the flame physics involving transient flame propagation, dynamic instability evolution, large curvature variation, and differential diffusion. Hence, the coupling strategy utilized in this work, which is based on the transport of major species rather than transporting the manifold control variables, shows a high potential for future applications. Additionally, an extension of this study to increased pressure levels would be a beneficial contribution to the field.

Declaration of Competing Interest

The authors declare that they have no known competing financial interests or personal relationships that could have appeared to influence the work reported in this paper.

Acknowledgments

The research leading to these results has received funding from the European Union's Horizon 2020 research and innovation program under the Center of Excellence in Combustion (CoEC) project, grant agreement No 952181 and from the German Research Foundation (DFG) - Project No. 411275182. HL acknowledges funding by the Fritz and Margot Faudi-Foundation - Project No. 55200502. Numerical simulations were conducted on the Lichtenberg II High Performance Computer of the Technical University of Darmstadt. The authors thank T. Zirwes for providing the DC dataset of the SEF.

Supplementary material

Supplementary material associated with this article can be found, in the online version, at 10.1016/j.proci.2022.07.159.

References

[1] O. Kwon, G. Rozenchan, C. Law, Cellular instabilities and self-acceleration of outwardly propagating spherical flames, Proc. Combust. Inst. 29 (2002) 1775–1783.
[2] C.A. Hall, W.D. Kulatilaka, N. Jiang, J.R. Gord, R.W. Pitz, Minor-species structure of premixed cellular tubular flames, Proc. Combust. Inst. 35 (2015) 1107–1114.
[3] C. Bauwens, J. Bergthorson, S. Dorofeev, Experimental investigation of spherical-flame acceleration in lean hydrogen-air mixtures, Int. J. Hydrog. Energy 42 (2017) 7691–7697.
[4] D. Fernández-Galisteo, V.N. Kurdyumov, P.D. Ronney, Analysis of premixed flame propagation between two closely-spaced parallel plates, Combust. Flame 190 (2018) 133–145.
[5] F. Creta, P.E. Lapenna, R. Lamioni, N. Fogla, M. Matalon, Propagation of premixed flames in the presence of Darrieus-Landau and thermal diffusive instabilities, Combust. Flame 216 (2020) 256–270.
[6] C. Altantzis, C.E. Frouzakis, A.G. Tomboulides, M. Matalon, K. Boulouchos, Hydrodynamic and thermodiffusive instability effects on the evolution of laminar planar lean premixed hydrogen flames, J. Fluid Mech. 700 (2012) 329–361.
[7] C. Altantzis, C.E. Frouzakis, A.G. Tomboulides, K. Boulouchos, Direct numerical simulation of circular expanding premixed flames in a lean quiescent hydrogen-air mixture: Phenomenology and detailed flame front analysis, Combust. Flame 162 (2015) 331–344.
[8] C.E. Frouzakis, N. Fogla, A.G. Tomboulides, C. Altantzis, M. Matalon, Numerical study of unstable hydrogen/air flames: shape and propagation speed, Proc. Combust. Inst. 35 (2015) 1087–1095.
[9] L. Berger, K. Kleinheinz, A. Attili, H. Pitsch, Characteristic patterns of thermodiffusively unstable premixed lean hydrogen flames, Proc. Combust. Inst. 37 (2019) 1879–1886.
[10] A. Attili, R. Lamioni, L. Berger, K. Kleinheinz, P.E. Lapenna, H. Pitsch, F. Creta, The effect of pressure on the hydrodynamic stability limit of premixed flames, Proc. Combust. Inst. 38 (2021) 1973–1981.
[11] T. Howarth, A. Aspden, An empirical characteristic scaling model for freely-propagating lean premixed hydrogen flames, Combust. Flame 237 (2022) 111805.
[12] J. Yu, R. Yu, X. Bai, M. Sun, J. Tan, Nonlinear evolution of 2D cellular lean hydrogen/air premixed flames with varying initial perturbations in the elevated pressure environment, Int. J. Hydrogen Energy 42 (6) (2017) 3790–3803.
[13] C.D. Pierce, P. Moin, Progress-variable approach for large-eddy simulation of non-premixed turbulent combustion, J. Fluid Mech. 504 (2004) 73–97.
[14] J.A. van Oijen, A. Donini, R.J.M. Bastiaans, J.H.M. ten Thije Boonkkamp, L.P.H. de Goey, State-of-the-art in premixed combustion modeling

using flamelet generated manifolds, Prog. Energy Combust. Sci. 57 (2016) 30–74.
[15] O. Gicquel, N. Darabiha, D. Thévenin, Liminar premixed hydrogen/air counterflow flame simulations using flame prolongation of ILDM with differential diffusion, Proc. Combust. Inst. 28 (2) (2000) 1901–1908.
[16] N. Peters, Laminar diffusion flamelet models in non-premixed turbulent combustion, Prog. Energy Combust. Sci. 10 (1984) 319–339.
[17] J. Schlup, G. Blanquart, Reproducing curvature effects due to differential diffusion in tabulated chemistry for premixed flames, Proc. Combust. Inst. 37 (2019) 2511–2518.
[18] N. Mukundakumar, D. Efimov, N. Beishuizen, J. van Oijen, A new preferential diffusion model applied to FGM simulations of hydrogen flames, Combust. Theor. Model. 25 (2021) 1245–1267.
[19] H. Böttler, X. Chen, A. Scholtissek, Z. Chen, C. Hasse, Flamelet modeling of forced ignition and flame propagation in hydrogen-air mixtures, Combust. Flame (2022) 112125.
[20] J.A. van Oijen, R.J.M. Bastiaans, L.P.H. de Goey, Modeling preferential diffusion effects in premixed methane-hydrogen-air flames by using Flamelet–Generated Manifolds, in: Proceedings Fifth ECCOMAS CFD, 2010, pp. 1–12.
[21] E. Knudsen, H. Kolla, E.R. Hawkes, H. Pitsch, LES of a premixed jet flame DNS using a strained flamelet model, Combust. Flame 160 (2013) 2911–2927.
[22] R. Bilger, S. Stårner, R. Kee, On reduced mechanisms for methane-air combustion in nonpremixed flames, Combust. Flame 80 (1990) 135–149.
[23] X. Wen, T. Zirwes, A. Scholtissek, H. Böttler, F. Zhang, H. Bockhorn, C. Hasse, Flame structure analysis and composition space modeling of thermodiffusively unstable premixed hydrogen flames' part I: Atmospheric pressure, Combust. Flame (2021) 111815 .
[24] C.F. Curtiss, J.O. Hirschfelder, Transport properties of multicomponent gas mixtures, J. Chem. Phys. 17 (1949) 550–555.
[25] T. Varga, T. Nagy, C. Olm, I.G. Zsély, R. Pálvölgyi, E. Valkó, G. Vincze, M. Cserháti, H. Curran, T. Turányi, Optimization of a hydrogen combustion mechanism using both direct and indirect measurements, Proc. Combust. Inst. 35 (2015) 589–596.
[26] H. Böttler, A. Scholtissek, X. Chen, Z. Chen, C. Hasse, Premixed flames for arbitrary combinations of strain and curvature, Proc. Combust. Inst. 38 (2021) 2031–2039.
[27] A. Scholtissek, P. Domingo, L. Vervisch, C. Hasse, A self-contained composition space solution method for strained and curved premixed flamelets, Combust. Flame 207 (2019) 342–355.
[28] X. Wen, T. Zirwes, A. Scholtissek, H. Böttler, F. Zhang, H. Bockhorn, C. Hasse, Flame structure analysis and composition space modeling of thermodiffusively unstable premixed hydrogen flames' part II: Elevated pressure, Combust. Flame (2021) 111808.
[29] F. Zhang, T. Baust, T. Zirwes, J. Denev, P. Habisreuther, N. Zarzalis, H. Bockhorn, Impact of infinite thin flame approach on the evaluation of flame speed using spherically expanding flames, Energy Technol. 5 (2017) 1055–1063.
[30] A. Zschutschke, D. Messig, A. Scholtissek, C. Hasse, Universal Laminar Flame Solver (ULF)(2017). 10.6084/m9.figshare.5119855.v2
[31] C.A. Hall, R.W. Pitz, Numerical simulation of premixed H2-air cellular tubular flames, Combust. Theory Model. 20 (2016) 328–348.
[32] G.J. Marshall, R.W. Pitz, Evaluation of heat release indicators in lean premixed H2/Air cellular tubular flames, Proc. Combust. Inst. 37 (2019) 2029–2036.

Supplementary Material

Flamelet modeling of thermo-diffusively unstable hydrogen-air flames

H. Böttler[a,*], H. Lulic[a], M. Steinhausen[a], X. Wen[a], C. Hasse[a], A. Scholtissek[a]

[a] *Technical University of Darmstadt, Department of Mechanical Engineering, Simulation of reactive Thermo-Fluid Systems, Otto-Berndt-Str. 2, 64287 Darmstadt, Germany*

This supplementary material contains an assessment of tangential diffusion effects in the thermo-diffusively unstable H_2/air spherical expanding flame in an *a-priori* manner. The diffusive fluxes of selected species are evaluated on the DC data together with corresponding predictions of the manifolds, respectively. Further, the different models are compared with respect to a coordinate measured along the corrugated flame front. In general, the FPV-κ_c model gives a more accurate prediction of the diffusive fluxes in flame-normal and flame-tangential direction compared to the FPV-h model. This is in agreement with the *a-priori* analysis provided in Section 3.1 of the manuscript, since the FPV-κ_c manifold showed also smaller deviations for the overall thermochemical state.

*Corresponding author:
Email address: boettler@stfs.tu-darmstadt.de (H. Böttler)

Preprint submitted to Proceedings of the Combustion Institute *July 4, 2022*

A. Assessment of flame-tangential diffusion effects

To provide further insights into the performance of the manifolds, diffusive fluxes of selected species are evaluated with respect to the corrugated flame front of the thermo-diffusively unstable spherical expanding flame.

For the following analysis, a segment of the flame front is considered. In Fig. 1, a subset of the flame front (DC reference result) is visualized and color-coded by temperature T. Additionally, the segment of the flame front is highlighted as black line and the arc length l_{arc} is introduced as coordinate measured along the flame front segment and subsequently used to compare tangential diffusion effects. Further, the gradient alignment between progress variable gradient ∇Y_c and diffusive flux $\mathbf{j}_k$ is depicted schematically.

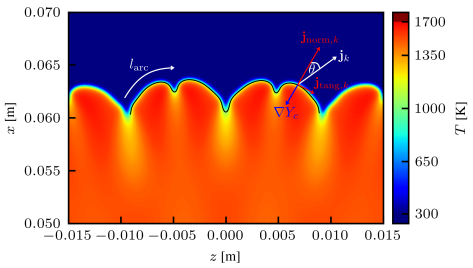

Fig. 1: Zoom into the flame front color-coded by temperature T. The subset of the flame front (progress variable iso-line $Y_c = -0.11$) is shown as black line. Additionally, the arc length $l_{\mathrm{arc}}^{n+1} = l_{\mathrm{arc}}^{n} + \sqrt{\mathrm{d}x^2 + \mathrm{d}z^2}$ is introduced as the pointwise distance of the flame front segment where n represents the point index. Further, the gradient alignment between ∇Y_c and $\mathbf{j}_k$ is schematically depicted.

The diffusive flux of species k is defined as $\mathbf{j}_k = -D_{\mathrm{m},k}\nabla Y_k$, where $D_{\mathrm{m},k}$ is the mixture-averaged diffusion coefficient of species k. It can be further decomposed into a flame-normal and a flame-tangential component by relating it to the direction of the progress variable gradient. Therefore, the angle θ between the species gradient ∇Y_k and the progress variable gradient ∇Y_c is determined by:

$$\theta = \arccos\left(\frac{\nabla Y_k \cdot \nabla Y_c}{|\nabla Y_k||\nabla Y_c|}\right). \tag{S1}$$

This information about the gradient alignment is then used to evaluate the flame-normal diffusive flux $\mathbf{j}_{\mathrm{norm},k} = \mathbf{j}_k \cos(\theta)$ and the flame-tangential diffusive flux $\mathbf{j}_{\mathrm{tang},k} = \mathbf{j}_k \sin(\theta)$ of each species, respectively.

In Fig. 2, the curvature κ_c, the OH species mass fraction Y_{OH}, and the contribution of flame-tangential diffusion for H_2 and H are shown along the arc length l_{arc} for the DC reference data and both FPV models. For the curvature profile distinct peaks towards negative curvatures are visible. As already discussed in the manuscript, these minima correlate with the different cells of the corrugated flame front. Further, areas with $\kappa_c < -1500\,\mathrm{m}^{-1}$ are highlighted by grey shading, since these highly negative curvature values exceed the curvature range captured by the FPV-κ_c manifold. Secondly, the OH mass fraction is compared between the three models. In general, the OH profile shows similar characteristics as the curvature profile. Further, the prediction of the FPV-κ_c manifold agrees better with the DC reference compared to the FPV-h manifold, while both manifolds underpredict the OH mass fraction in areas with very negative curvature. Finally, the flame-tangential diffusive fluxes of H_2 and H are shown in a normalized manner. It is clearly visible that flame-tangential diffusion becomes increasingly relevant for highly negatively curved flame segments and is negligible elsewhere. The FPV models can recover flame-tangential effects to a certain extent, but for very negative curvature regions both FPV models show notable deviations.

The analysis of the flame-tangential diffusion effects further supports the findings described in Section 3.1 of the manuscript. It can be concluded, that the manifolds' ability in recovering tangential diffusion effects correlates with its overall prediction of the thermo-chemical state. A more comprehensive analysis is conceivable in form of an *a-posteriori* assessment where deviations introduced by the reduced number of transported scalars could be systematically evaluated. This is subject to future work.

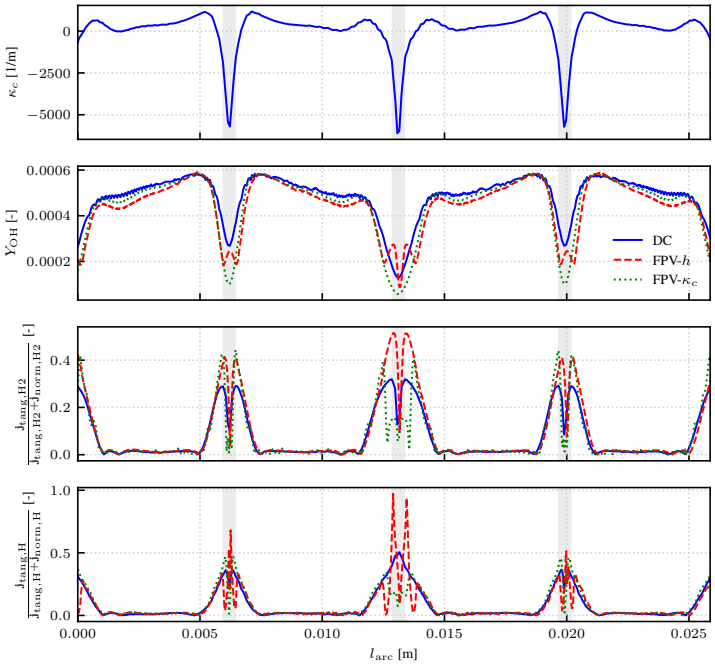

Fig. 2: A-priori assessment of flame-tangential diffusion effects along the arc length of the flame front l_{arc} of the thermo-diffusively unstable flame. The curvature κ_c, the OH species mass fraction Y_{OH}, and the normalized tangential diffusive flux for H_2 and H are shown for the DC reference and both manifold predictions. Further, areas where the curvature exceeds the range captured by the FPV-κ_c manifold, i.e. regions with $\kappa_c < -1500\,\mathrm{m}^{-1}$, are marked by grey shading.

P5 Int. J. Hydrogen Energy 56 (2024), 1397–1407

H. Böttler, D. Kaddar, T. J. P. Karpowski, F. Ferraro, A. Scholtissek, H. Nicolai, and C. Hasse. Can flamelet manifolds capture the interactions of thermo-diffusive instabilities and turbulence in lean hydrogen flames?—An a-priori analysis. In: Int. J. Hydrogen Energy 56 (2024), 1397–1407. DOI: 10.1016/j.ijhydene.2023.12.193

Author contributions

Tab. P.5: Author contributions to publication [P5] following CRediT [117]

Hannes Böttler	Conceptualization of the numerical investigation (lead) Methodology, implementation and investigation of flamelet manifolds (lead) Interpretation and discussion of the results (equal) Data analysis and visualization (lead) Writing – Original draft (lead) Shared first author and corresponding author
Driss Kaddar	Conceptualization and investigation of the fully resolved simulation (FRS) (lead) Interpretation and discussion of the results (equal) Data analysis and visualization (supporting) Writing – Original draft (supporting) Shared first author
T. Jeremy P. Karpowski	Methodology of the flamelet manifold (supporting)
Federica Ferraro	Conceptualization and investigation of the FRS (supporting) Supervision of DK, TJPK
Arne Scholtissek	Conceptualization of the numerical investigation (supporting) Supervision of HB, DK, TJPK
Hendrik Nicolai	Conceptualization of the numerical investigation (supporting) Writing – Original draft (supporting) Supervision of HB, DK
Christian Hasse	Conceptualization of the numerical investigation and the FRS (supporting) Funding acquisition Supervision of HB, DK, TJPK
All co-authors	Interpretation and discussion of the results (supporting) Writing – Review & Editing

Use of publication contents in finalized and ongoing dissertations

This publication is part of the ongoing dissertation of Hannes Böttler and Driss Kaddar at the Institute for Simulation of reactive Thermo-Fluid Systems at the Technical University of Darmstadt, Germany.

International Journal of Hydrogen Energy 56 (2024) 1397–1407

Contents lists available at ScienceDirect

International Journal of Hydrogen Energy

journal homepage: www.elsevier.com/locate/he

Can flamelet manifolds capture the interactions of thermo-diffusive instabilities and turbulence in lean hydrogen flames?—An a-priori analysis

Hannes Böttler [*,1], Driss Kaddar[1], T. Jeremy P. Karpowski, Federica Ferraro, Arne Scholtissek, Hendrik Nicolai, Christian Hasse

Technical University of Darmstadt, Department of Mechanical Engineering, Simulation of reactive Thermo-Fluid Systems, Otto-Berndt-Str. 2, 64287 Darmstadt, Germany

ARTICLE INFO

Keywords:
Turbulent premixed flames
Thermodiffusive instability
Hydrogen combustion
Preferential diffusion
Strain and curvature
Flamelet modeling

ABSTRACT

Flamelet-based methods are extensively used in modeling turbulent hydrocarbon flames. However, these models have yet to be established for (lean) premixed hydrogen flames. While flamelet models exist for *laminar* thermo-diffusively unstable hydrogen flames, for which consideration of curvature effects has resulted in improved model predictions Böttler et al. [1], it is still unclear whether these models are directly applicable to turbulent hydrogen flames. Therefore, a detailed assessment of stretch effects on thermochemical states in a turbulent lean premixed hydrogen-air slot flame through finite-rate chemistry simulations is conducted. Strain and curvature are examined individually using a composition space model, revealing their distinct influences on thermochemical states. An *a-priori* analysis confirms that the previously developed tabulated manifolds fall short of capturing all turbulent flame phenomena, necessitating a novel manifold incorporating both strain and curvature variations. These results underscore the significance of these variations in developing manifold-based combustion models for turbulent lean hydrogen flames.

1. Introduction

Hydrogen is an energy carrier of high technological relevance. Based on policies and funding programs, a variety of research directions have emerged that focus on hydrogen's economic potential, production, transport, storage, and utilization [2–7]. When generated with renewable energy sources via electrolysis, the so-called green hydrogen can be utilized directly as a fuel or further processed in chemical synthesis. One scenario is using hydrogen as a fuel in aero-engines and stationary gas turbines, however, its direct usage as a fuel presents additional challenges. Compared to conventional carbon-based fuels, hydrogen exhibits a higher diffusivity and reactivity, leading to significant changes in the combustion dynamics. Here, a lean (partially) premixed combustion mode would be desirable for low pollutant emissions but can lead to safety issues such as flashback and thermoacoustic oscillations [8–10]. To ensure the safe operation of new hydrogen-operated devices, CFD-aided design processes are desirable. To this end, predictive models for turbulent premixed flames are required that take into account the distinct characteristics of hydrogen.

One particular challenge for model development is that lean hydrogen-air flames are prone to intrinsic thermo-diffusive instabilities. Thermo-diffusive instabilities arise due to the significant difference in mass and thermal diffusive fluxes, leading to pronounced differential diffusion effects along the flame front. The ratio of the mass and thermal diffusivity is the Lewis number, which is particularly low for hydrogen ($Le_{H2} \approx 0.3$) [11]. The strong differential diffusion of hydrogen causes minor perturbations at the flame front to be amplified, resulting in highly wrinkled flame fronts which are characterized by a significantly increased flame speed and substantial fluctuations in local reaction rates. Extensive research in laminar reacting flows has explored these instabilities, revealing that the increase in the overall consumption rate can be attributed to both an enlarged flame surface area as well as an increased fuel consumption rate per unit of flame surface area [12–19].

Considering that industrial-relevant configurations generally feature turbulent flows, the question of how the turbulence-induced flame wrinkling interacts with the thermo-diffusive unstable hydrogen mixture is highly relevant. A set of recently performed DNS studies at various Karlovitz numbers suggests that thermo-diffusive instabilities persist in turbulent flames and are even amplified through synergistic effects [20–22]. Hence, in turbulent hydrogen flames, both turbulence and thermo-diffusive instabilities impact flame wrinkling and local

* Corresponding author.
E-mail address: boettler@stfs.tu-darmstadt.de (H. Böttler).
[1] Joint First Author.

https://doi.org/10.1016/j.ijhydene.2023.12.193
Received 5 November 2023; Received in revised form 14 December 2023; Accepted 19 December 2023
Available online 5 January 2024

reactivity, ultimately influencing fuel consumption rates and, consequently, turbulent flame speed. The enhancing effects of turbulence on thermo-diffusive effects are linked to higher strain and flame curvature due to turbulent wrinkling and steepened scalar gradients. Thereby, the differential diffusion of hydrogen is promoted resulting in strong mixture inhomogeneities across the flame front and super-adiabatic temperatures in the exhaust gas [20,23]. The effects of intrinsic instabilities are further enhanced with increasing pressure [21,24–26]. At high pressure and high Karlovitz numbers, diffusion of molecular and atomic hydrogen still exhibit a leading order effect on the burning rates [21]. The strong effects of molecular diffusion in turbulent hydrogen flames differ significantly from hydrocarbon fuels, where turbulence-induced flame wrinkling solely determines the turbulent flame speed.

Several numerical studies of turbulent lean premixed hydrogen-air slot flames have been based on direct numerical simulations (DNS) [20,23]. It has been outlined that these simulations require considerable computational resources. Therefore, reliable models need to be developed to investigate more complex configurations (e.g. technical combustors) at moderate computational cost. Commonly used modeling approaches are flamelet-based models that incorporate detailed kinetics using tabulated chemistry [27–29]. The detailed chemistry information of these flamelets is usually precomputed and stored as a tabulated manifold, which is parameterized by certain control variables. The control variables are related to different physical phenomena, e.g. mixing, reaction progress or non-adiabatic effects. Subsequently, the manifold is coupled to the CFD simulation, where only the transport equations for the control variables are solved and the full thermochemical state is retrieved from the manifold.

Flamelet-based modeling approaches are well established for turbulent hydrocarbon flames and have been extended to problems of increasingly physical complexity [29–37]. Recently, several model extensions have been proposed to describe laminar hydrogen-air flames capturing also differential diffusion effects and the subsequent mixture stratification [1,38–41]. It is noted that most of these models are usually based on the tabulation of one-dimensional unstretched flamelets and have been developed further with different targets. Particularly, focusing on capturing flame structures of laminar thermo-diffusively unstable hydrogen-air flames, Böttler et al. [1] reported that incorporation of curvature effects into the manifold substantially improved the results. In this work, a recently developed composition space model (CSM) [42,43] proved beneficial for computing one-dimensional flamelets with curvature variations. While flamelet-based models have been successfully applied to turbulent methane-hydrogen-air flames [44] and first attempts have been made to adapt turbulence closure models to hydrogen combustion [45,46], modeling studies on turbulent premixed hydrogen-air flames including thermo-diffusive instabilities are still scarce but highly relevant. This gap is addressed in this work.

The objective of this work is twofold: (1) A fully resolved simulation (FRS) [47] of a turbulent lean premixed hydrogen-air slot flame is performed using detailed chemistry. Based on this data, the physical phenomena that need to be captured by flamelet-based models to predict the physics of turbulent lean premixed hydrogen-air flames that exhibit thermo-diffusive instabilities are outlined. In particular, the effects of strain and curvature on the thermochemical state are studied individually. (2) Four different flamelet manifolds with increasing complexity are generated, including a novel manifold taking into account both strain and curvature variations. The performance of these manifolds is assessed based on the FRS data by means of an *a-priori* analysis.

The paper is structured as follows: first, the setup of the fully resolved simulation of the lean premixed turbulent hydrogen-air flame is described, followed by an analysis of strain and curvature effects, which are discussed concerning implications for model development. Further, an optimal estimator assessment is performed to elaborate suitable manifold parameterizations. Thereafter, differently complex flamelet-based modeling approaches are introduced. Finally, this variety of flamelet manifolds is tested against the FRS data in an *a-priori* manner. The paper ends with a conclusion.

2. Configuration and numerical methods

2.1. Configuration and operating conditions

In this work, a turbulent premixed lean hydrogen-air flame in a slot burner configuration is investigated. The unburnt mixture enters the domain through a central jet, which is separated by two walls from the hot coflows. The configuration is inspired by the works of Sankaran et al. [48] and Berger et al. [20]. Fig. 1 shows a visualization of the computational domain. It spans across $12\,L$ in streamwise (x) and crosswise (y) direction and $2\,L$ in spanwise (z) direction. The walls separating the jet from the coflows have a thickness of $L/28$, with $L = 5\,\mathrm{mm}$ being the width of the central jet. The mesh is uniform in streamwise and spanwise directions. In the crosswise direction, the mesh is uniform in the center between $-L \leq y \leq L$ and coarsened with a linear profile in the coflow region. The mesh resolution $\Delta = 30\ \mu\mathrm{m}$ is chosen to adequately resolve the Kolmogorov length scale as well as the flame front. The flame is resolved with 15 cells within the thermal flame thickness. The adopted resolution leads to a fully resolved simulation (FRS) where no compromises are present in the description of the flame structure [47]. A comprehensive listing of all simulation parameters and characteristic numbers is given in Table 1.

The unburnt hydrogen-air mixture is chosen according to the observation of strong thermo-diffusive instabilities in laminar conditions. The equivalence ratio is set to $\phi = 0.5$, the pressure is $p = 1\,\mathrm{atm}$ and the temperature of the central jet is specified as $T = 300\,\mathrm{K}$. At these conditions, the reference laminar flame speed and the laminar thermal flame thickness of a planar unstretched flame is $s_\mathrm{L} = 0.517\,\mathrm{m/s}$ and $\delta_\mathrm{L} = 0.445\,\mathrm{mm}$, respectively. The thermal flame thickness is defined by

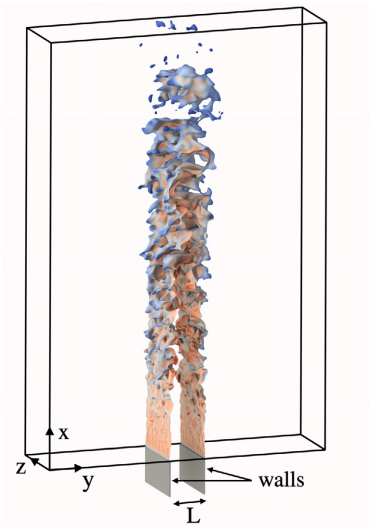

Fig. 1. Physical domain of the simulation and visualization of the flame. The flame is represented by a temperature isosurface of $T = 1100\,\mathrm{K}$ and colored by the heat release rate. (For interpretation of the references to color in this figure legend, the reader is referred to the web version of this article.)

Table 1
Parameters and characteristic numbers of the fully resolved simulation.

L [mm]	5
U_{jet} [m/s]	38
U_{coflow} [m/s]	9.5
η [µm]	80
Δ [µm]	30
s_L [m/s]	0.517
δ_L [mm]	0.445
Re	10,000
Ka	30
$(L_x, L_y, L_z)/L$	12, 12, 2
N_x, N_y, N_z	2,000, 510, 333

$\delta_L = (T_b - T_u)/\max(\nabla T)$, with T_b and T_u being the burnt and unburnt temperature, respectively, and ∇T the temperature gradient of a one-dimensional unstretched flame. The coflow composition corresponds to the burnt gas state of the central jet's mixture and the temperature of the burner walls is fixed at $T_{wall} = 300$ K. The Reynolds number of the central jet is $\mathrm{Re} = U_{jet} L/\nu = 10{,}000$, with U_{jet} being the bulk velocity, and the kinematic viscosity of the unburnt mixture ν. The coflows are laminar with an inlet velocity $U_{coflow} = 9.5$ m/s. The Kolmogorov length scale η is determined at the position of the mean flame sheet and at half the height of the mean flame length. The location inside the mean flame sheet is selected at a temperature $T = 970$ K corresponding to the mean between the fresh and burnt gas temperature in a one-dimensional unstretched flame of identical composition. For the investigated operating condition, a moderate Karlovitz number $\mathrm{Ka} = (\delta_L/\eta)^2 \approx 30$ is obtained.

The velocity data for the central jet is obtained from a precursor simulation of an inert, fully developed turbulent channel flow. In spanwise direction, periodic boundary conditions are employed. All outlets are modeled with non-reflective boundary conditions.

2.2. Governing equations and numerical methods

The simulation is performed using the finite volume method framework OpenFOAM [49,50] solving the compressible reactive Navier-Stokes equations. Second-order discretization schemes are employed in time and space. The methods have been validated for performing accurate FRS of reactive flows [51]. Chemical reactions are modeled by directly solving the chemical source terms employing the detailed reaction mechanism by Li et al. [52] containing 9 species and 21 reactions. The species diffusivities are modeled according to the mixture-averaged transport approach by Curtiss and Hirschfelder [53].

2.3. Composition space model (CSM)

In the remainder of the manuscript, a composition space model (CSM) [42,43,54,55] is used to model differential diffusion and stretch effects in a flamelet-based manner. In the CSM, conservation equations for species mass fractions Y_k, temperature T and progress variable gradient $g_c = |\nabla Y_c|$ (required for closure) are solved along progress variable Y_c which spans the composition space. The system of equations reads:

$$\rho\frac{\partial Y_k}{\partial \tau} = \underbrace{-g_c\frac{\partial}{\partial Y_c}\left(g_c\,\rho Y_k\tilde{V}_k\right) + g_c\frac{\partial}{\partial Y_c}\left(g_c\,\rho Y_c\tilde{V}_c\right)\frac{\partial Y_k}{\partial Y_c}}_{\text{Diffusion}} + \underbrace{\rho g_c\,\kappa_c\left(Y_k\tilde{V}_k - Y_c\tilde{V}_c\frac{\partial Y_k}{\partial Y_c}\right)}_{\text{Diffusion}} \underbrace{-\dot{\omega}_c\frac{\partial Y_k}{\partial Y_c}}_{\text{Drift}} + \underbrace{\rho\dot{\omega}_k}_{\text{Source}}, \tag{1}$$

$$\rho\frac{\partial T}{\partial \tau} = \underbrace{\frac{g_c}{c_p}\frac{\partial}{\partial Y_c}\left(g_c\lambda\frac{\partial T}{\partial Y_c}\right) + g_c\frac{\partial}{\partial Y_c}\left(g_c\,\rho Y_c\tilde{V}_c\right)\frac{\partial T}{\partial Y_c}}_{\text{Diffusion}} \underbrace{-\rho g_c^2\sum_k^{n_s}\frac{c_{p,k}}{c_p}Y_k\tilde{V}_k\frac{\partial T}{\partial Y_c} - \rho g_c\,\kappa_c\left(\frac{\lambda}{\rho c_p} + Y_c\tilde{V}_c\right)\frac{\partial T}{\partial Y_c}}_{\text{Diffusion}} \underbrace{-\dot{\omega}_c\frac{\partial T}{\partial Y_c}}_{\text{Drift}} + \underbrace{\frac{\dot{\omega}_T}{c_p}}_{\text{Source}}, \tag{2}$$

$$0 = \underbrace{-g_c^2\frac{\partial^2}{\partial {Y_c}^2}\left(g_c\,\rho Y_c\tilde{V}_c\right) + g_c^2\frac{\partial}{\partial Y_c}\left(\kappa_c\,\rho Y_c\tilde{V}_c\right)}_{\text{Diffusion}} \underbrace{-\dot{\omega}_c\frac{\partial g_c}{\partial Y_c}}_{\text{Drift}} + \underbrace{g_c\frac{\partial\dot{\omega}_c}{\partial Y_c} + \rho K_s g_c}_{\text{Source}}, \tag{3}$$

with the diffusion velocity of species k with respect to the composition space $\tilde{V}_k$, the heat conductivity λ, the heat capacity c_p and the heat release rate $\dot{\omega}_T$. The different terms in this set of equations can be classified as diffusion, drift, and source terms. As diffusion and source terms are well-established and known from conventional transport equations, we will not elaborate on them here for brevity. However, the drift terms are less common. These terms scale the composition space and are crucial for the CSM framework as the burned side boundary condition is coupled to the progress variable gradient which subsequently scales the computational domain. This is an important feature of these equations as stretched flame structures can be studied by supplying strain $K_s = \nabla_t \cdot \mathbf{u}_t - (\mathbf{u}\cdot\mathbf{n}_c)\kappa_c$ and curvature $\kappa_c = -\nabla\cdot\mathbf{n}_c$ as external parameters. It is well known that depending on the overall flame stretch (negative or positive) sub- or super-equilibrium states can be reached which coincide with different burned side values for the progress variable. The drift terms ensure that this behavior is accurately described and the appropriate burned side value of the progress variable is obtained by the CSM. By that, the characteristics of various canonical flame configurations are reproduced by using only one set of equations. Further, the CSM has a larger attainable strain-curvature parameter space compared to canonical configurations and flame structures for arbitrary combinations of strain and curvatures can be studied [54]. In particular, negative curvatures and strain rates can be considered for further analysis. This is important for hydrogen-air flames due to their strong sensitivity to stretch effects. It was found in our previous work that different contributions of strain and curvature to the overall flame stretch alters the flame characteristics significantly. The interested reader is referred to [54,55], where a detailed validation against several canonical flame configurations and a systematic analysis of arbitrary combinations of strain and curvature are provided. Further, the usage of the CSM to study stretch effects is also expected to be beneficial for turbulent premixed hydrogen-air flames as it was reported by Amato et al. [56] that the correlation between strain and curvature is reverted between laminar canonical flames and turbulent flames which raises the need of developing extended laminar model configurations. Note that the progress variable definition in all calculations is $Y_c = Y_{H2O} - Y_{H2} - Y_{O2}$.

3. Manifold generation

Next, stretch effects and their corresponding thermochemical states are analyzed in the FRS of the turbulent slot flame. Thereby, the parameter ranges for strain and curvature are estimated, which need to be taken into account for the subsequent flamelet modeling based on the CSM. Further, an optimal estimator assessment is performed to

confine potential sets of parameters that can be used to parameterize the manifold and to investigate the modeling error of certain parameter reductions. Finally, various flamelet manifolds are introduced which account for different physical effects and are generated based on different parameter variations using the CSM.

3.1. Analysis of stretch effects for the turbulent flame

While overall flame stretch effects are widely discussed in the literature, this study focuses on contributions of strain K_s and curvature κ_c effects to the flame stretch using following stretch decomposition [57]:

$$K = \underbrace{\nabla_t \cdot \mathbf{u}_t - \left(\mathbf{u} \cdot \mathbf{n}_c\right) \kappa_c}_{K_s} + s_d \kappa_c \,, \tag{4}$$

where s_d represents the flame displacement speed.

In Fig. 2, the joint probability density functions (PDFs) of strain and progress variable (top) and the one of curvature and progress variable (bottom) of the turbulent flame are depicted. For visual inspection, marginal PDFs are depicted at the respective axes and the equilibrium progress variable value, $Y_{c,eq}$, for an unstretched planar hydrogen-air flame (equivalence ratio of $\phi = 0.5$) is shown as a gray dashed line. Both quantities (K_s, κ_c) show a broad variation in the turbulent flame configuration. The marginal PDF for strain is symmetrical, while the one for curvature is slightly skewed toward negative values. This behavior is expected in turbulent hydrogen-air flames and in agreement with the literature as it was reported that hydrogen addition shifts the curvature distribution to negative values [58–60]. The qualitative PDF of the progress variable has a bimodal shape where a first peak occurs close to the unburned side and a second one at the burned side where the progress variable is close to the equilibrium value of the corresponding unstretched planar flame. Further, a broad scatter exists around the burned side peak. The joint PDF of strain and progress variable shows an overall symmetrical distribution between positive and negative strain rates where the strain is in the order of magnitude of 10^6 m^{-1} while approximately 50% of the values are between $\approx \pm 70\,000\,\mathrm{s}^{-1}$. However, the joint PDF of curvature and progress variable exhibits a skewed distribution. The curvature reaches values up to $\approx \pm 30\,000\,\mathrm{m}^{-1}$ but 90% of the data is located in the range of $-7000\,\mathrm{m}^{-1} \leq \kappa_c \leq 5500\,\mathrm{m}^{-1}$. Positive curvatures are found for both low and high Y_c values, while negative curvatures are predominantly found close to the unburned side and only rarely result in super equilibrium states ($Y_c > Y_{c,eq}$).

These observations indicate a link between turbulent fluctuations and the flame response. The strain distribution is symmetric since the imposed flow field does not alter the flame front in any predominant direction. However, the curvature distribution is skewed due to the flame's response. Positive curvature promotes the flame propagation and causes super equilibrium states while negative curvature weakens the flame and subsequently, sub-equilibrium states ($Y_c < Y_{c,eq}$) are found. This correlation of positive curvature with super-equilibrium states coincides with variations in the local flame structure and subsequently with altered burning rates due to the Lewis number effect. This effect was already discussed in the context of laminar thermo-diffusively unstable flames and needs to be further elaborated in turbulent flames [1,14,18].

Since the overall distributions of strain and curvature can already be related to the flame response, their impact on the thermochemical states in the turbulent flame is of interest. Therefore, the thermochemical states are depicted in composition space in Fig. 3. This figure shows the scatter of thermochemical states spanned by the enthalpy h and progress variable Y_c and is colored by the conditional mean of the Bilger mixture fraction [61], which can also be interpreted as a local equivalence ratio ϕ_{local}. In addition, CSM simulations with varying strain ($-100\,\mathrm{s}^{-1} \leq K_s \leq 28\,000\,\mathrm{s}^{-1}$; $\kappa_c = 0\,\mathrm{m}^{-1}$) are depicted as gray dashed lines in Fig. 3A and CSM results with varying curvature ($-500\,\mathrm{m}^{-1} \leq \kappa_c \leq 8000\,\mathrm{m}^{-1}$; $K_s = 0\,\mathrm{s}^{-1}$) are shown similarly in Fig. 3B. The solid black line corresponds to the unstretched planar flame solution, respectively.

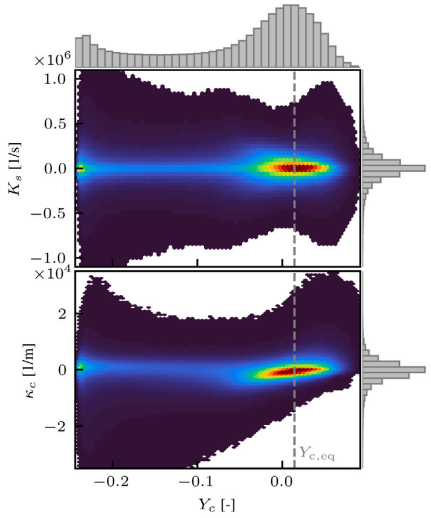

Fig. 2. Joint probability density functions (PDFs) of strain K_s and progress variable Y_c (top) and the one of curvature κ_c and progress variable (bottom) with marginal PDFs shown as bars at the respective edges. The color coding of the scatter indicates the likelihood of certain states starting from unlikely (blue) to most probable states (red). The dashed gray line corresponds to the equilibrium progress variable value $Y_{c,eq}$ of an unstretched planar flame with an equivalence ratio of $\phi = 0.5$. (For interpretation of the references to color in this figure legend, the reader is referred to the web version of this article.)

The thermochemical states in the turbulent flame scatter broadly concerning the enthalpy and the Bilger mixture fraction along the progress variable. It is noted that the enthalpy is a suitable parameter to judge the composition space since it includes the influence of all species. For low progress variable values, the enthalpy varies significantly with higher mixture fraction values located in the center of the scatter and leaner mixtures (low values of the Bilger mixture fraction) are found towards the respective edges of the scatter (lower and higher enthalpy levels). However, for high values of the progress variable, the enthalpy scatter broadens even further and significantly lower enthalpy levels are found, depicting also substantially higher mixture fraction values. When comparing the scatter of the turbulent flame against the CSM calculations with varying strain or curvature, the predominant influences of strain and curvature become visible. For higher enthalpy levels, the scatter of the turbulent flame is well captured by CSM simulations with increasing strain. It is highlighted that not only a comparable parameter space is spanned, but also the profiles of the CSM resemble the overall shape of the turbulent scatter (Fig. 3A). Similarly, for high values of progress variable and reduced levels of enthalpy, the range and shape of the scatter of the turbulent flame simulation are captured by CSM simulations with varying curvature (Fig. 3B). Only a small part of the scatter where the lowest values of Bilger mixture fraction occur are not directly captured by the CSM results. This can be either attributed to a joint interplay of strain and curvature, or multidimensional effects. It is noted that multidimensional effects cannot be captured by the CSM since these states correspond to highly negative curvatures where flame-tangential diffusion tends to become increasingly important [1]. Remarkably, the

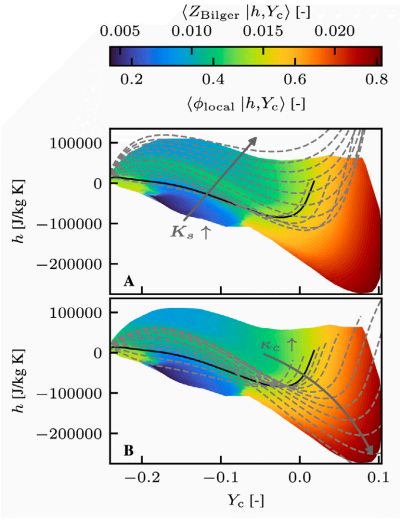

Fig. 3. Conditional mean of Bilger mixture fraction Z_{Bilger} and local equivalence ratio ϕ_{local} conditioned on enthalpy h and progress variable Y_c. Additionally, CSM solutions with varying strain ($-100\,\mathrm{s}^{-1} \leq K_s \leq 28\,000\,\mathrm{s}^{-1}$; $\kappa_c = 0\,\mathrm{m}^{-1}$) are depicted as dashed gray lines in the upper figure (A). In the bottom figure (B), the dashed gray lines correspond to CSM simulations with varying curvature ($-500\,\mathrm{m}^{-1} \leq \kappa_c \leq 8000\,\mathrm{m}^{-1}$; $K_s = 0\,\mathrm{s}^{-1}$). The solid black line corresponds to the unstretched planar flame solution. All CSM results follow the global conditions of the turbulent flame ($T = 300\,\mathrm{K}$, $p = 1\,\mathrm{atm}$, $\phi = 0.5$). (For interpretation of the references to color in this figure legend, the reader is referred to the web version of this article.)

CSM calculations capture major parts of the scatter of the turbulent flame even though nominal values for strain and curvature in the FRS significantly exceed the strain-curvature parameter space attainable with the CSM. Additionally, these findings indicate that both strain and curvature effects are important when modeling these types of flames. In the following, the relevance of these effects is further elaborated.

3.2. Optimal estimator assessment

Next, a suitable parameterization must be found to enable the construction of a suitable manifold which accounts for all relevant physical phenomena. Therefore, an optimal estimator assessment is carried out for different parameterizations [20,62]. In an optimal estimator assessment, a set of parameters ψ is used to parameterize a quantity (e.g. the progress variable source term $\dot{\omega}_c$) and is determined by an error norm known as irreducible error. Note that the progress variable source term $\dot{\omega}_c$ is used in this study since it represents an important characteristic quantity that needs to be predicted by manifold-based models and properly capturing the source term in the manifold poses usually one of the biggest challenges in flamelet-based models. Further, this error is quantified by the quadratic error norm of the scatter of $\dot{\omega}_c$ relative to the conditional mean $\langle \dot{\omega}_c | \psi \rangle$. Subsequently, this error is normalized by the maximum obtained from a respective unstretched flamelet [20]:

$$\epsilon^{\mathrm{norm}}_{\mathrm{irr},\dot{\omega}_c} = \frac{\langle (\dot{\omega}_c - \langle \dot{\omega}_c | \psi \rangle)^2 | Y_c \rangle}{\max(\dot{\omega}_c^{\mathrm{flamelet}})^2} \tag{5}$$

Thereby, low values for the normalized irreducible error $\epsilon^{\mathrm{norm}}_{\mathrm{irr},\dot{\omega}_c}$ indicate a suitable parameterization of the thermochemical states by the respective set of parameters ψ.

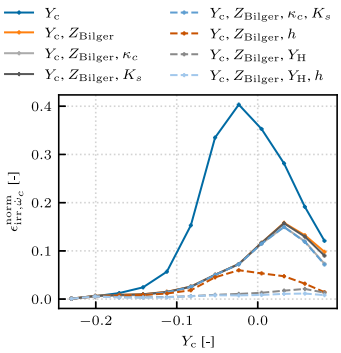

Fig. 4. Irreducible errors of $\dot{\omega}_c$ for different sets of parameters.

In Fig. 4, the irreducible error is shown for different combinations of parameters along the progress variable. High errors are obtained when parameterizing only by the progress variable Y_c. The irreducible error is reduced when adding the Bilger mixture fraction to the set of parameters. Including strain K_s, curvature κ_c, or both in the parameterization does not result in a significant error reduction. This is attributed to the fact that strain and curvature are highly instantaneous quantities that are closely linked to the flame's topology. However, they do not account for the temporal evolution of the thermochemical state [63]. Zirwes et al. [64,65] found a phase shift between stretch effects and the subsequent flame response, which depends on the local flow time scale and discussed memory effects in the local flame dynamics. Such memory effects could also play a role here. Thus, even though it was shown in Fig. 3 that the flame parameters strain and curvature induce the desired changes in the flame structure, they are not necessarily suitable control variables for manifold parameterization. However, strain and curvature effects can be represented by respective characteristic quantities to avoid any phase shift in the thermochemical states. The H-radical mass fraction Y_{H} was already used to account for curvature effects in our previous works [1,16].

Further, when revisiting the discussion concerning Fig. 3, the enthalpy was found to be suitable to distinguish between strain and curvature effects, since CSM calculations with varying strain or curvature cover different parts of the state space of the turbulent slot flame. Utilizing Y_{H} or h as markers for strain and curvature results in an additional error reduction. The lowest irreducible error and, hence, the most suitable parameterization is obtained when using $\psi(Y_c, Z_{\mathrm{Bilger}}, Y_{\mathrm{H}}, h)$. This combination of the number of scalars and obtained error is considered a good tradeoff between numerical cost (manifold size, scalars to be solved) and accuracy.

3.3. Generation of flamelet manifolds

Based on the findings of the optimal estimator assessment various flamelet-based manifolds are generated. Thereby, not only their parameterization but also the characteristics of the one-dimensional flamelets used for the manifold generation are varied. In this work, four different manifolds, which are generated from different CSM data sets and parameterized by different control variables, are used including a novel manifold based on machine learning. Thereby, the aim is to subsequently address modeling errors resulting from unstretched and stretched flamelets. The manifold parameterization follows the conceptual approach of our previous work where the manifold is coupled to the CFD by solving transport equations for the major species (H_2, O_2, H_2O) instead of Z_{Bilger} and Y_c [1,40].

Table 2
Overview of utilized manifolds classified by manifold name, parameterization of the manifold data and the set of control variables to access the respective manifold.

Manifold name	Manifold data	Number of CSM calculations	Control variables
M-1	$\psi(\phi, Y_c)$	30	Z_{Bilger}, Y_c
M-2	$\psi(\phi, h, Y_c)$	750	$Z_{\text{Bilger}}, h, Y_c$
M-3	$\psi(\phi, Y_c, \kappa_c)$	1140	$Z_{\text{Bilger}}, Y_c, Y_{\text{H}}$
M-4	$\psi(\phi, Y_c, \kappa_c, K_s)$	26 350	$Y_{\text{H}_2}, Y_{\text{O}_2}, Y_{\text{H}_2\text{O}}, Y_{\text{H}}, h$

The first manifold (M-1) is based on unstretched planar CSM calculations with varying equivalence ratio ($0.275 \leq \phi \leq 0.85$) and is parameterized by the Bilger mixture fraction Z_{Bilger} [61] and progress variable Y_c. This manifold parameterization is well established and frequently used [38,66] and captures mixture stratification.

The second manifold (M-2) is a subsequent extension of the first manifold, including also CSM calculations at different enthalpy h levels (preheating and heat loss effects) and therefore parameterized by Z_{Bilger}, h and Y_c. This parameterization is more complex than the one of M-1 but was already used in several studies [39,40] and captures both mixture stratification and non-adiabatic effects. It is noted that differential diffusion effects are captured by the Bilger mixture fraction Z_{Bilger}, but they are also partly manifested in the enthalpy. Therefore, considering enthalpy as control variable can be beneficial for the manifold parameterization which is already indicated in the previous section.

The third manifold (M-3) is based on CSM calculations with different equivalence ratios (c.f. M-1) and varying curvature ($-2500\,\text{m}^{-1} \leq \kappa_c \leq 8000\,\text{m}^{-1}$). It is parameterized by Z_{Bilger}, Y_c and the H radical mass fraction Y_{H}. The latter one correlates with the curvature variation and was already utilized to parameterize a manifold addressing laminar thermo-diffusively unstable hydrogen-air flames [1]. This manifold parameterization is even more challenging concerning its generation and was only used in our previous work since curvature can be supplied to the CSM as an external parameter [1]. It should be noted that one-dimensional flames with negative curvature cannot be easily addressed by flamelet solvers operating in physical space.

An additional novel manifold (M-4) is developed in this study to assess the joint influence of strain and curvature. The data used for M-4 is an extension of the CSM solutions used for M-3 and further includes a strain variation in the range of $-400\,1/\text{s} \leq K_s \leq 30\,000\,1/\text{s}$ as an additional dimension. It is noted that the thermochemical states are retrieved by linear interpolation in the case of M-1, M-2 and M-3, while M-4 is generated as an artificial neural network, to reduce the overall memory footprint of such high dimensional manifolds including also differential diffusion effects. A review of data-driven models in combustion research can be found in [67]. M-4 is parameterized analogously to the other manifolds using the same approach but utilizing the major species (H_2, O_2, H_2O) directly as model inputs to approximate Z_{Bilger} and Y_c. Thereby, the model inputs are the species mass fractions of H_2, O_2, H_2O, H, and enthalpy h. These control variables are found to be the most suitable to capture the effects in the turbulent flame configuration, as already shown by the optimal estimator assessment provided in Fig. 4. It is noted that the accuracy of both manifold approaches where verified for manifolds M-1, M-2 and M-3 and a comparable accuracy of both approaches is found.

An overview of the manifolds used in this study is given in Table 2. The manifold name is shown together with the parameterization of the manifold data, which represents the thermochemical states ψ spanned by various CSM simulations, the number of CSM calculations included in the parameter variation and the set of control variables that are used to access the manifold. Note that the progress variable definition in all manifolds is $Y_c = Y_{\text{H2O}} - Y_{\text{H2}} - Y_{\text{O2}}$ and the overall computational cost to generate the manifolds increases with the number of CSM calculations.

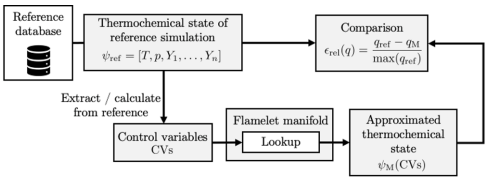

Fig. 5. Schematic overview of an *a-priori* analysis. Adapted from [33].

4. *A-priori* analysis

An *a-priori* analysis is performed to assess the general capabilities of the four manifolds to capture the microstructure of the lean turbulent hydrogen-air flame. In an *a-priori* analysis a reference database is utilized to quantify the performance of flamelet manifolds. The overall procedure is depicted schematically in Fig. 5. In this study the fully resolved simulation of the turbulent slot flame acts as reference data based on which the reduced set of control variables of the flamelet manifolds is extracted or calculated. Subsequently, these control variables are used to perform a lookup of the flamelet manifold to retrieve an approximated thermochemical state from the manifold. This approximated thermochemical state is compared to the reference data by computing a relative error ϵ_{rel} between the reference data and the manifold prediction of a quantity q.

In Fig. 6, a snapshot of the temperature T, density ρ and the species mass fractions of OH and O fields of the turbulent flame are shown along the x, y-coordinates and $z = 0\,\text{mm}$ (top row). Further, the relative deviations of all manifolds are depicted for the respective fields. The turbulent flame front is highly curved and various pockets containing unburned mixture are observed, which are detached from the main flame front and can be found for $x > 30\,\text{mm}$. Maximum temperatures higher than the equilibrium temperature of an unstretched flame are found near the flame front, indicating super equilibrium states caused by the interplay of differential diffusion and flame stretch. Further, this region is intersected by areas of lower temperatures as a consequence of turbulent fluctuations. The density and radical mass fraction fields show similar trends as the temperature field. Besides the impact of local temperature fluctuations, the amount of OH and O mass fractions also depend significantly on curvature. In areas convexly shaped towards the burned side (positive curvature), increased amounts of radicals are found, highlighting the increased burning rates due to the Lewis number effect. These characteristics highlight the relevance of differential diffusion effects in this flame configuration and indicate the interplay of turbulent wrinkling and thermo-diffusive instabilities. The prediction of M-1 and M-3 show deviations in the temperature field up to 10%. In particular, the temperatures close to positively curved flame segments are significantly underpredicted. The same observation applies to the density field. M-2 exhibits better agreement with the reference data for T and ρ, showing the highest deviations around the detached pockets of the unburned mixture. This improvement is expected since M-2 uses enthalpy as a model input and thermochemical states corresponding to preheated unstretched flames are accessed. However, the tabulation approaches based on unstretched flames cannot predict the radical species in this flame configuration. M-1 and M-2 depict high deviations for the OH and O radical mass fractions. M-3, which accounts for curvature effects, gives better predictions for the radical mass fractions. The highest deviations (up to 20–25%) are located close to negatively curved flame segments. Only the prediction of M-4, taking both strain and curvature effects into account, results in negligible errors for all quantities.

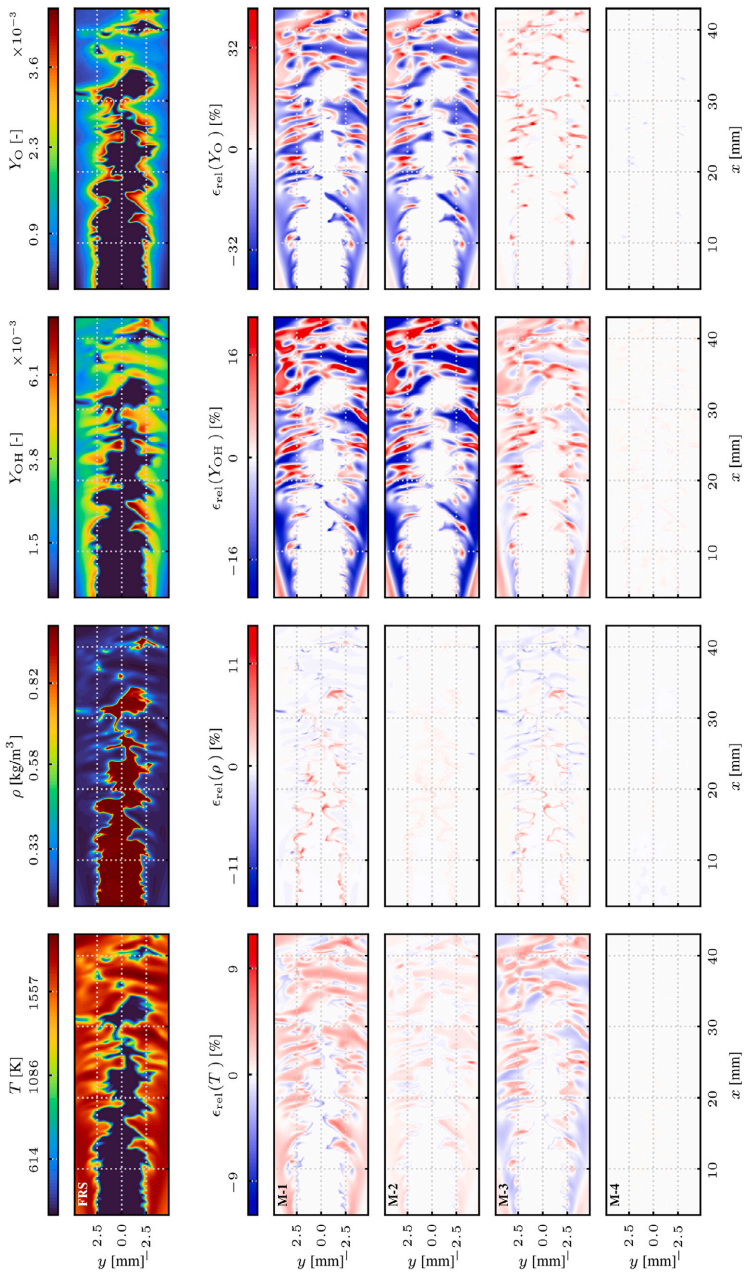

Fig. 6. *A-priori* comparison of the manifolds against the fully resolved reference solution for an instantaneous snapshot. The temperature T, density ρ and the species mass fractions of OH and O fields of the reference data are shown along the x, y-coordinates and $z = 0\,\mathrm{mm}$ (top row). The manifold predictions are depicted as relative deviations for the respective fields.

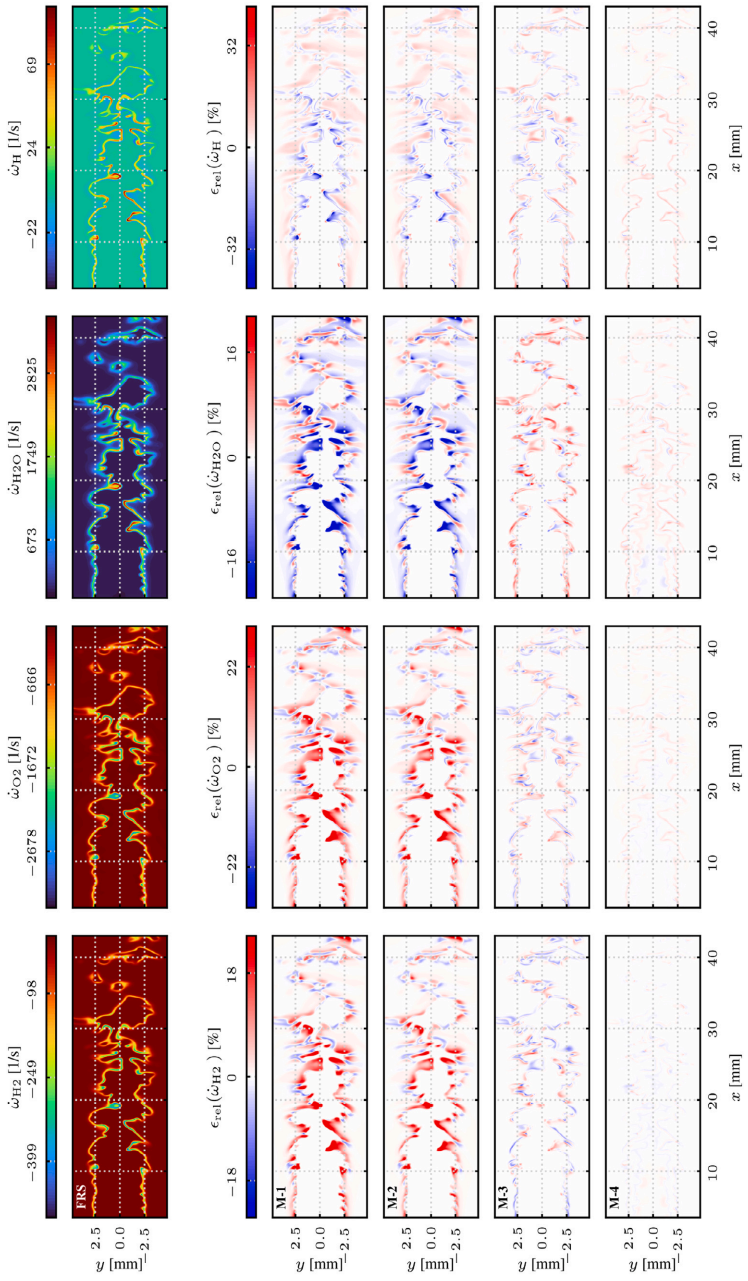

Fig. 7. *A-priori* comparison of the manifolds against the fully resolved reference solution for an instantaneous snapshot. The species source terms of H_2, O_2, H_2O and H of the reference data are shown along the x, y-coordinates and $z = 0$ mm (top row). The manifold predictions are depicted as relative deviations for the respective fields.

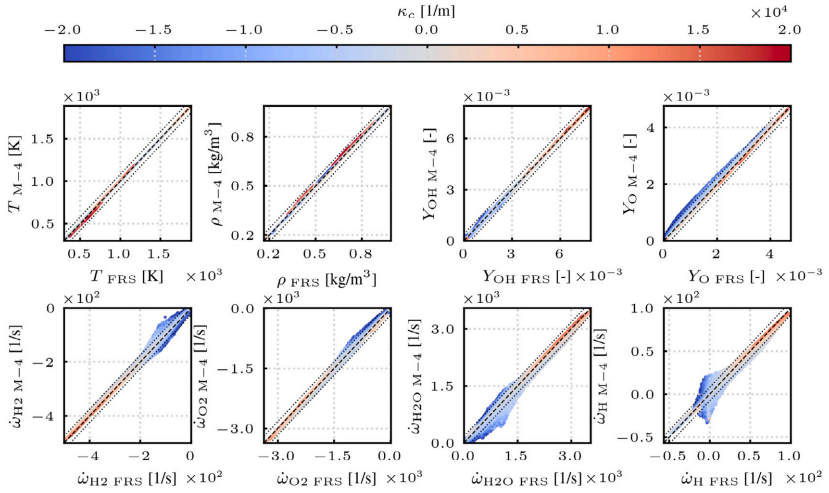

Fig. 8. Correlation of reference data and the M-4 manifold prediction for various characteristic quantities utilizing the three-dimensional data set. A perfect correlation is highlighted by the black dashed line and the dotted lines represent a 5% error margin based on the absolute variation found in the fields of the reference data, respectively. (For interpretation of the references to color in this figure legend, the reader is referred to the web version of this article.)

Besides an adequate description of the flame structure, predicting the source terms of the control variables is of utmost importance since they determine the overall transport and flame dynamics in coupled simulations. Following the coupling approach of transporting major species (as in our previous work [1,40,41]) the source terms of $Y_{\mathrm{H2}}, Y_{\mathrm{O2}}, Y_{\mathrm{H2O}}, Y_{\mathrm{H}}$ are required. These source terms are shown in Fig. 7 together with the respective relative error of the manifold predictions. The source terms of the major species follow the previously discussed Lewis number effect and their variation also indicate the locally altered burning rate of the flame. The highest source terms are found in flame segments with positive curvature. Note that this corresponds to negative source terms for H_2 and O_2 since these species get consumed. Negatively curved flame segments depict lower source terms. The source term of the H radical shows the highest production in positively curved flame segments. However, also strong consumption takes place in close vicinity of these areas. In contrast, only small source terms are found in negatively curved reaction zones. The manifold predictions of M-1 and M-2 depict errors beyond 50% for all source terms. In particular, the source terms are significantly underpredicted in positively curved flame segments. M-3 shows reduced but significant errors in the range of 20%. However, the M-4 manifold recovers the source terms of the reference data with almost negligible errors for the major species. Only small deviations are observed for the H radical source term.

Finally, the predictions of the M-4 manifold are investigated in more detail since they show the best agreement with the reference data. In Fig. 8, the previously discussed fields of the turbulent flame reference data are correlated with the respective manifold prediction, which allows for a more detailed local error assessment on the three-dimensional data set. Further, the scatter is color-coded by curvature. A full correlation of the manifold prediction and the reference data is indicated by the black dashed line. Further, the dotted lines correspond to an error margin of ±5 %. Very good agreement is found for the temperature T and density ρ prediction. The correlation is slightly weaker for the radical mass fractions of OH and O, where the scatter broadens slightly for points corresponding to negative curvature. Nevertheless, the deviations for the OH radical mass fraction do not exceed the 5% error margin. Only the prediction of the O mass fraction slightly exceeds the error margin for points corresponding to negatively curved flame segments. A similar behavior is found for the source terms of the major species. The weakest correlation is obtained for predicting the H radical source term $\dot{\omega}_{\mathrm{H}}$. Overall, the manifold prediction stays mostly within the 5% error margin. However, points with negative curvature show higher deviations. Under these conditions, the H radical source term scatters around zero. Therefore, these errors are considered insignificant since they are topologically confined and occur in areas of weak reactions.

Based on this detailed error estimation of different manifolds, it is concluded that manifold-based models based on unstretched planar flames cannot predict the thermochemical states of the lean turbulent hydrogen-air flame while including only curvature effects in the manifold leads to mediocre results. Only if both positive and negative values for strain and curvature are considered in the manifold generation good agreement with the reference data is achieved.

5. Conclusion

In this work, a fully resolved simulation of a turbulent lean premixed hydrogen-air slot flame is performed using detailed chemistry. This flame configuration is analyzed concerning stretch effects and serves as a reference database for developing flamelet-based models. The performance of various tabulated manifolds in predicting the thermochemical states in the turbulent flame is assessed in an *a-priori* manner.

The analysis of strain and curvature in the turbulent flame reveals that these effects not only alter the mixture composition but also notably influence the enthalpy. Additionally, it is shown that major parts of the scatter of thermochemical states found in the turbulent reference simulation can be captured by one-dimensional calculations with a composition space model (CSM) separately varying strain and curvature. CSM calculations with increasing strain result in higher enthalpy levels with moderate shifts in local mixture composition, while CSM calculations with increasing curvature lead to overall lower enthalpy levels and significantly richer mixtures.

Based on these findings, four different flamelet manifolds with increasing complexity are generated, including (1) a manifold generated from adiabatic unstretched flames, (2) a manifold based on

non-adiabatic unstretched flames, (3) a manifold accounting for curvature variations, and (4) a novel manifold considering strained and curved flames. The manifold predictions are discussed concerning their capability to describe the structure of the turbulent flame. It is shown that significant modeling errors are obtained when using unstretched planar flames to generate the manifold. Although including enthalpy variations in these flamelets leads to an improved temperature field prediction, significant deviations persist for species fields and source terms, indicating that these modeling approaches cannot capture the synergistic effects of turbulence and thermo-diffusive instabilities. The deviations are reduced when considering CSM calculations with varying curvature. The prediction of the manifold, taking positive and negative strain and curvature into account, shows the best agreement with the reference data. Hence, the altered reaction intensity caused by combined stretch and Lewis number effects is well recovered by the novel manifold. These results highlight the importance of stretch effects in tabulated manifolds, showing that both strain and curvature effects need to be considered when modeling the flame structure of turbulent premixed hydrogen-air flames prone to thermo-diffusive instabilities.

Future works should expand this analysis to various conditions, such as different equivalence ratios and higher turbulent intensities. Further, *a-posteriori* analysis based on fully coupled simulations should be performed. Additionally, when aiming for applications in the context of large eddy simulations, suitable sub-grid models for turbulent hydrogen combustion are of key importance.

Declaration of competing interest

The authors declare that they have no known competing financial interests or personal relationships that could have appeared to influence the work reported in this paper.

Acknowledgments

The research leading to these results has received funding from the European Union's Horizon 2020 research and innovation program under the Center of Excellence in Combustion (CoEC) project, grant agreement No 952181 and from the Federal Ministry of Education and Research (BMBF), Germany and the state of Hesse as part of the NHR4CES Program. The authors gratefully acknowledge the Gauss Centre for Supercomputing e.V. for funding this project by providing computing time on the GCS Supercomputer SuperMUC-NG at Leibniz Supercomputing Centre, Germany.

References

[1] Böttler H, Lulic H, Steinhausen M, Wen X, Hasse C, Scholtissek A. Flamelet modeling of thermo-diffusively unstable hydrogen-air flames. Proc Combust Inst 2023;39(2):1567–76. http://dx.doi.org/10.1016/j.proci.2022.07.159.

[2] Andersson J, Grönkvist S. Large-scale storage of hydrogen. Int J Hydrogen Energy 2019;44(23):11901–19. http://dx.doi.org/10.1016/j.ijhydene.2019.03.063.

[3] Dawood F, Anda M, Shafiullah G. Hydrogen production for energy: An overview. Int J Hydrogen Energy 2020;45(7):3847–69. http://dx.doi.org/10.1016/j.ijhydene.2019.12.059.

[4] Kovač A, Paranos M, Marciuš D. Hydrogen in energy transition: A review. Int J Hydrogen Energy 2021;46(16):10016–35. http://dx.doi.org/10.1016/j.ijhydene.2020.11.256, Hydrogen and Fuel Cells.

[5] Wappler M, Unguder D, Lu X, Ohlmeyer H, Teschke H, Lueke W. Building the green hydrogen market – Current state and outlook on green hydrogen demand and electrolyzer manufacturing. Int J Hydrogen Energy 2022;47(79):33551–70. http://dx.doi.org/10.1016/j.ijhydene.2022.07.253.

[6] Kohse-Höinghaus K. Combustion in the future: The importance of chemistry. Proc Combust Inst 2021;38(1):1–56. http://dx.doi.org/10.1016/j.proci.2020.06.375.

[7] Erdener BC, Sergi B, Guerra OJ, Lazaro Chueca A, Pambour K, Brancucci C, Hodge B-M. A review of technical and regulatory limits for hydrogen blending in natural gas pipelines. Int J Hydrogen Energy 2023;48(14):5595–617. http://dx.doi.org/10.1016/j.ijhydene.2022.10.254.

[8] Lopez-Ruiz G, Blanco J, Peña A, Romero-Anton N, Azkorra-Larrinaga Z. CFD study of flameless combustion in a real industrial reheating furnace considering different H2/NG blends as fuel. Int J Hydrogen Energy 2024;49:1362–74. http://dx.doi.org/10.1016/j.ijhydene.2023.11.149.

[9] Fruzza F, Lamioni R, Tognotti L, Galletti C. Flashback of H2-enriched premixed flames in perforated burners: Numerical prediction of critical velocity. Int J Hydrogen Energy 2023;48(81):31790–801. http://dx.doi.org/10.1016/j.ijhydene.2023.04.252.

[10] Zhang J, Ratner A. Experimental study on the excitation of thermoacoustic instability of hydrogen-methane/air premixed flames under atmospheric and elevated pressure conditions. Int J Hydrogen Energy 2019;44(39):21324–35. http://dx.doi.org/10.1016/j.ijhydene.2019.06.142.

[11] Law CK. Combustion physics. Cambridge University Press (CUP); 2006, http://dx.doi.org/10.1017/cbo9780511754517.

[12] Altantzis C, Frouzakis CE, Tomboulides AG, Boulouchos K. Direct numerical simulation of circular expanding premixed flames in a lean quiescent hydrogen-air mixture: Phenomenology and detailed flame front analysis. Combust Flame 2015;162:331–44. http://dx.doi.org/10.1016/j.combustflame.2014.08.005.

[13] Frouzakis CE, Fogla N, Tomboulides AG, Altantzis C, Matalon M. Numerical study of unstable hydrogen/air flames: Shape and propagation speed. Proc Combust Inst 2015;35:1087–95. http://dx.doi.org/10.1016/j.proci.2014.05.132.

[14] Berger L, Kleinheinz K, Attili A, Pitsch H. Characteristic patterns of thermodiffusively unstable premixed lean hydrogen flames. Proc Combust Inst 2019;37(2):1879–86. http://dx.doi.org/10.1016/j.proci.2018.06.072.

[15] Creta F, Lapenna PE, Lamioni R, Fogla N, Matalon M. Propagation of premixed flames in the presence of Darrieus–Landau and thermal diffusive instabilities. Combust Flame 2020;216:256–70. http://dx.doi.org/10.1016/j.combustflame.2020.02.030.

[16] Wen X, Zirwes T, Scholtissek A, Böttler H, Zhang F, Bockhorn H, Hasse C. Flame structure analysis and composition space modeling of thermodiffusively unstable premixed hydrogen flames — Part I: Atmospheric pressure. Combust Flame 2021;111815. http://dx.doi.org/10.1016/j.combustflame.2021.111815.

[17] Attili A, Lamioni R, Berger L, Kleinheinz K, Lapenna PE, Pitsch H, Creta F. The effect of pressure on the hydrodynamic stability limit of premixed flames. Proc Combust Inst 2021;38:1973–81. http://dx.doi.org/10.1016/j.proci.2020.06.091.

[18] Howarth T, Aspden A. An empirical characteristic scaling model for freely-propagating lean premixed hydrogen flames. Combust Flame 2022;237:111805. http://dx.doi.org/10.1016/j.combustflame.2021.111805.

[19] Zhang G-P, Li G-X, Li H-M, Cao J-B. Experimental study of laminar and turbulent spherical flame propagation characteristics of hydrogen-rich syngas. Int J Hydrogen Energy 2023;48(94):36955–71. http://dx.doi.org/10.1016/j.ijhydene.2023.06.056.

[20] Berger L, Attili A, Pitsch H. Synergistic interactions of thermodiffusive instabilities and turbulence in lean hydrogen flames. Combust Flame 2022;244:112254.

[21] Rieth M, Gruber A, Williams FA, Chen JH. Enhanced burning rates in hydrogen-enriched turbulent premixed flames by diffusion of molecular and atomic hydrogen. Combust Flame 2022;239:111740. http://dx.doi.org/10.1016/j.combustflame.2021.111740, A dedication to Professor Kenneth Noel Corbett Bray.

[22] Rieth M, Gruber A, Chen JH. The effect of pressure on lean premixed hydrogen-air flames. Combust Flame 2023;250:112514. http://dx.doi.org/10.1016/j.combustflame.2022.112514.

[23] Coulon V, Gaucherand J, Xing V, Laera D, Lapeyre C, Poinsot T. Direct numerical simulations of methane, ammonia-hydrogen and hydrogen turbulent premixed flames. Combust Flame 2023;256:112933. http://dx.doi.org/10.1016/j.combustflame.2023.112933.

[24] Yang S, Saha A, Liang W, Wu F, Law CK. Extreme role of preferential diffusion in turbulent flame propagation. Combust Flame 2018;188:498–504.

[25] Chu H, Berger L, Grenga T, Wu Z, Pitsch H. Effects of differential diffusion on hydrogen flame kernel development under engine conditions. Proc Combust Inst 2023;39(2):2129–38.

[26] Howarth T, Hunt E, Aspden A. Thermodiffusively-unstable lean premixed hydrogen flames: Phenomenology, empirical modelling, and thermal leading points. Combust Flame 2023;253:112811. http://dx.doi.org/10.1016/j.combustflame.2023.112811.

[27] Gicquel O, Darabiha N, Thévenin D. Liminar premixed hydrogen/air counterflow flame simulations using flame prolongation of ILDM with differential diffusion. Proc Combust Inst 2000;28(2):1901–8. http://dx.doi.org/10.1016/S0082-0784(00)80594-9.

[28] Pierce CD, Moin P. Progress-variable approach for large-eddy simulation of non-premixed turbulent combustion. J Fluid Mech 2004;504:73–97. http://dx.doi.org/10.1017/s0022112004008213.

[29] van Oijen JA, Donini A, Bastiaans RJM, ten Thije Boonkkamp JHM, de Goey LPH. State-of-the-art in premixed combustion modeling using flamelet generated manifolds. Prog Energy Combust Sci 2016;57:30–74. http://dx.doi.org/10.1016/j.pecs.2016.07.001.

[30] Fiorina B, Veynante D, Candel S. Modeling combustion chemistry in large eddy simulation of turbulent flames. Flow Turbul Combust 2015;94(1):3–42. http://dx.doi.org/10.1007/s10494-014-9579-8.

[31] Popp S, Hartl S, Butz D, Geyer D, Dreizler A, Vervisch L, Hasse C. Assessing multi-regime combustion in a novel burner configuration with large eddy simulations using tabulated chemistry. Proc Combust Inst 2021;38(2):2551–8. http://dx.doi.org/10.1016/j.proci.2020.06.098.

[32] Nicolai H, Dressler L, Janicka J, Hasse C. Assessing the importance of differential diffusion in stratified hydrogen–methane flames using extended flamelet tabulation approaches. Phys Fluids 2022;34(8):085118. http://dx.doi.org/10.1063/5.0102675.
[33] Steinhausen M, Zirwes T, Ferraro F, Scholtissek A, Bockhorn H, Hasse C. Flame-vortex interaction during turbulent side-wall quenching and its implications for flamelet manifolds. Proc Combust Inst 2023;39(2):2149–58. http://dx.doi.org/10.1016/j.proci.2022.09.026.
[34] Kircher M, Popp S, Gierth S, Pati A, Schneider J, Günther M, Hasse C. Investigation of engine combustion and auto-ignition of a multicomponent surrogate fuel with NTC behavior under knocking conditions. Flow Turbul Combust 2023;110(1):149–69. http://dx.doi.org/10.1007/s10494-022-00351-9.
[35] Tang T, Yu J, Wang Z, Yang D, Sun M, Wang H, Zhao G, Yang Y. An improved flamelet/progress variable modeling in a hydrogen-fueled scramjet. Int J Hydrogen Energy 2023. http://dx.doi.org/10.1016/j.ijhydene.2023.06.313.
[36] Vance F, de Goey L, van Oijen J. Prediction of flashback limits for laminar premixed hydrogen-air flames using flamelet generated manifolds. Int J Hydrogen Energy 2023;48(69):27001–12. http://dx.doi.org/10.1016/j.ijhydene.2023.03.262.
[37] Almutairi F, Dinesh KR, van Oijen J. Modelling of hydrogen-blended dual-fuel combustion using flamelet-generated manifold and preferential diffusion effects. Int J Hydrogen Energy 2023;48(4):1602–24. http://dx.doi.org/10.1016/j.ijhydene.2022.10.078.
[38] Schlup J, Blanquart G. Reproducing curvature effects due to differential diffusion in tabulated chemistry for premixed flames. Proc Combust Inst 2019;37(2):2511–8. http://dx.doi.org/10.1016/j.proci.2018.06.211.
[39] Mukundakumar N, Efimov D, Beishuizen N, van Oijen J. A new preferential diffusion model applied to FGM simulations of hydrogen flames. Combust Theory Model 2021;25(7):1245–67. http://dx.doi.org/10.1080/13647830.2021.1970232.
[40] Böttler H, Chen X, Xie S, Scholtissek A, Chen Z, Hasse C. Flamelet modeling of forced ignition and flame propagation in hydrogen-air mixtures. Combust Flame 2022;112125. http://dx.doi.org/10.1016/j.combustflame.2022.112125.
[41] Luo Y, Ferraro F, Breicher A, Böttler H, Dreizler A, Geyer D, Hasse C, Scholtissek A. A novel flamelet manifold parametrization approach for lean CH4–H2-air flames. Int J Hydrogen Energy 2022. http://dx.doi.org/10.1016/j.ijhydene.2022.09.233.
[42] Scholtissek A, Domingo P, Vervisch L, Hasse C. A self-contained progress variable space solution method for thermochemical variables and flame speed in freely-propagating premixed flamelets. Proc Combust Inst 2019;37(2):1529–36. http://dx.doi.org/10.1016/j.proci.2018.06.168.
[43] Scholtissek A, Domingo P, Vervisch L, Hasse C. A self-contained composition space solution method for strained and curved premixed flamelets. Combust Flame 2019;207:342–55. http://dx.doi.org/10.1016/j.combustflame.2019.06.010.
[44] Vreman A, van Oijen J, de Goey L, Bastiaans R. Direct numerical simulation of hydrogen addition in turbulent premixed Bunsen flames using flamelet-generated manifold reduction. Int J Hydrog Energy 2009;34(6):2778–88. http://dx.doi.org/10.1016/j.ijhydene.2009.01.075.
[45] Luo K, Wang H, Bushe WK, Fan J. Direct numerical simulation and reaction rate modelling of premixed turbulent flames. Int J Hydrogen Energy 2014;39(23):12158–65. http://dx.doi.org/10.1016/j.ijhydene.2014.05.144.
[46] Lapenna PE, Lamioni R, Creta F. Subgrid modeling of intrinsic instabilities in premixed flame propagation. Proc Combust Inst 2021;38(2):2001–11. http://dx.doi.org/10.1016/j.proci.2020.06.192.
[47] Domingo P, Vervisch L. Recent developments in DNS of turbulent combustion. Proc Combust Inst 2023;39(2):2055–76. http://dx.doi.org/10.1016/j.proci.2022.06.030.
[48] Sankaran R, Hawkes ER, Chen JH, Lu T, Law CK. Structure of a spatially developing turbulent lean methane–air Bunsen flame. Proc Combust Inst 2007;31(1):1291–8. http://dx.doi.org/10.1016/j.proci.2006.08.025.
[49] Weller HG, Tabor G, Jasak H, Fureby C. A tensorial approach to computational continuum mechanics using object orientated techniques. Comput Phys 1998;12:620–31.
[50] Morev I, Tekgül B, Gadalla M, Shahanaghi A, Kannan J, Karimkashi S, Kaario O, Vuorinen V. Fast reactive flow simulations using analytical Jacobian and dynamic load balancing in OpenFOAM. Phys Fluids 2022;34(2):021801. http://dx.doi.org/10.1063/5.0077437.
[51] Zirwes T, Sontheimer M, Zhang F, Abdelsamie A, Pérez FEH, Stein OT, Im HG, Kronenburg A, Bockhorn H. Assessment of numerical accuracy and parallel performance of OpenFOAM and its reacting flow extension EBIdnsFoam. Flow Turbul Combust 2023;111:567–602.
[52] Li J, Zhao Z, Kazakov A, Dryer FL. An updated comprehensive kinetic model of hydrogen combustion. Int J Chem Kinet 2004;36(10):566–75. http://dx.doi.org/10.1002/kin.20026.
[53] Curtiss CF, Hirschfelder JO. Transport properties of multicomponent gas mixtures. J Chem Phys 1949;17(6):550–5. http://dx.doi.org/10.1063/1.1747319.
[54] Böttler H, Scholtissek A, Chen X, Chen Z, Hasse C. Premixed flames for arbitrary combinations of strain and curvature. Proc Combust Inst 2021;38(2):2031–9. http://dx.doi.org/10.1016/j.proci.2020.06.312.
[55] Chen X, Böttler H, Scholtissek A, Hasse C, Chen Z. Effects of stretch-chemistry interaction on chemical pathways for strained and curved hydrogen/air premixed flames. Combust Flame 2021;232:111532. http://dx.doi.org/10.1016/j.combustflame.2021.111532.
[56] Amato A, Day M, Cheng RK, Bell J, Dasgupta D, Lieuwen T. Topology and burning rates of turbulent, lean, H2/air flames. Combust Flame 2015;162(12):4553–65. http://dx.doi.org/10.1016/j.combustflame.2015.09.010.
[57] Groot GRA, van Oijen JA, de Goey LPH, Seshadri K, Peters N. The effects of strain and curvature on the mass burning rate of premixed laminar flames. Combust Theory Model 2002;6(4):675–95. http://dx.doi.org/10.1088/1364-7830/6/4/307.
[58] Renou B, Boukhalfa A, Puechberty D, Trinité M. Local scalar flame properties of freely propagating premixed turbulent flames at various Lewis numbers. Combust Flame 2000;123(4):507–21. http://dx.doi.org/10.1016/S0010-2180(00)00180-2.
[59] Fru G, Janiga G, Thévenin D. Impact of volume viscosity on the structure of turbulent premixed flames in the thin reaction zone regime. Flow Turbul Combust 2012;88(4):451–78. http://dx.doi.org/10.1007/s10494-011-9360-1.
[60] Cecere D, Giacomazzi E, Arcidiacono N, Picchia F. Direct numerical simulation of a turbulent lean premixed CH4/H2–Air slot flame. Combust Flame 2016;165:384–401. http://dx.doi.org/10.1016/j.combustflame.2015.12.024.
[61] Bilger R, Stårner S, Kee R. On reduced mechanisms for methane-air combustion in nonpremixed flames. Combust Flame 1990;80(2):135–49. http://dx.doi.org/10.1016/0010-2180(90)90122-8.
[62] Moreau A, Teytaud O, Bertoglio JP. Optimal estimation for large-eddy simulation of turbulence and application to the analysis of subgrid models. Phys Fluids 2006;18(10):105101. http://dx.doi.org/10.1063/1.2357974, arXiv:https://pubs.aip.org/aip/pof/article-pdf/doi/10.1063/1.2357974/14042195/105101_1_online.pdf.
[63] Klimenko AY, Class AG. Propagation of nonstationary curved and stretched premixed flames with multistep reaction mechanisms. Combust Sci Technol 2002;174(8):1–43. http://dx.doi.org/10.1080/00102200290021317.
[64] Zirwes T, Zhang F, Wang Y, Habisreuther P, Denev JA, Chen Z, Bockhorn H, Trimis D. In-situ flame particle tracking based on barycentric coordinates for studying local flame dynamics in pulsating Bunsen flames. Proc Combust Inst 2021;38(2):2057–66. http://dx.doi.org/10.1016/j.proci.2020.07.033.
[65] Zirwes T, Zhang F, Bockhorn H. Memory effects of local flame dynamics in turbulent premixed flames. Proc Combust Inst 2023;39(2):2349–58. http://dx.doi.org/10.1016/j.proci.2022.07.187.
[66] Regele JD, Knudsen E, Pitsch H, Blanquart G. A two-equation model for non-unity Lewis number differential diffusion in lean premixed laminar flames. Combust Flame 2013;160(2):240–50. http://dx.doi.org/10.1016/j.combustflame.2012.10.004.
[67] Ihme M, Chung WT, Mishra AA. Combustion machine learning: Principles, progress and prospects. Prog Energy Combust Sci 2022;91:101010. http://dx.doi.org/10.1016/j.pecs.2022.101010.